

Fast Sensing and Adaptive Actuation for Robust Legged Locomotion

Dissertation

der Mathematisch-Naturwissenschaftlichen Fakultät
der Eberhard Karls Universität Tübingen
zur Erlangung des Grades eines
Doktors der Naturwissenschaften
(Dr. rer. nat.)

vorgelegt von
M.Sc. An Mo
aus Hezhou, VR China

Tübingen
2023

Gedruckt mit Genehmigung der Mathematisch-Naturwissenschaftlichen
Fakultät der Eberhard Karls Universität Tübingen.

Tag der mündlichen Qualifikation:	10.08.2023
Dekan:	Prof. Dr. Thilo Stehle
1. Berichterstatter/-in:	Dr. Alexander Badri-Spröwitz
2. Berichterstatter/-in:	Prof. Dr. Martin Giese

Abstract

Robust legged locomotion in complex terrain demands fast perturbation detection and reaction. In animals, due to the neural transmission delays, the high-level control loop involving the brain is absent from mitigating the initial disturbance. Instead, the low-level compliant behavior embedded in mechanics and the mid-level controllers in the spinal cord are believed to provide quick response during fast locomotion. Still, it remains unclear how these low- and mid-level components facilitate robust locomotion.

This thesis aims to identify and characterize the underlining elements responsible for fast sensing and actuation. To test individual elements and their interplay, several robotic systems were implemented. The implementations include active and passive mechanisms as a combination of elasticities and dampers in multi-segment robot legs, central pattern generators inspired by intraspinal controllers, and a synthetic robotic version of an intraspinal sensor.

The first contribution establishes the notion of effective damping. Effective damping is defined as the total energy dissipation during one step, which allows quantifying how much ground perturbation is mitigated. Using this framework, the optimal damper is identified as viscous and tunable. This study paves the way for integrating effective dampers to legged designs for robust locomotion.

The second contribution introduces a novel series elastic actuation system. The proposed system tackles the issue of power transmission over multiple joints, while featuring intrinsic series elasticity. The design is tested on a hopper with two more elastic elements, demonstrating energy recuperation and enhanced dynamic performance.

The third contribution proposes a novel tunable damper and reveals its influence on legged hopping. A bio-inspired slack tendon mechanism is implemented in parallel with a spring. The tunable damping is rigorously quantified on a central-pattern-generator-driven hopping robot, which reveals the trade-off between locomotion robustness and efficiency.

The last contribution explores the intraspinal sensing hypothesis of birds. We speculate that the observed intraspinal structure functions as an accelerometer. This accelerometer could provide fast state feedback directly to the adjacent central pattern generator circuits, contributing to birds' running robustness. A biophysical simulation framework is established, which provides new perspectives on the sensing mechanics of the system, including the influence of mor-

phologies and material properties.

Giving an overview of the hierarchical control architecture, this thesis investigates the fast sensing and actuation mechanisms in several control layers, including the low-level mechanical response and the mid-level intraspinal controllers. The contributions of this work provide new insight into animal locomotion robustness and lays the foundation for future legged robot design.

Zusammenfassung

Robuste Fortbewegung auf Beinen im komplexen Terrain erfordert eine rasche Erkennung von Störungen und eine zügige Reaktion des Systems. Allerdings ist die synaptische Reizübertragung in Tieren vergleichsweise langsam. Diese verzögert den Informationsfluss, was zu Regelstörungen führen kann. Um trotzdem eine schnelle Fortbewegung zu unterstützen, wird angenommen, dass speziell angepasste Mechanik auf der low-level Hardware Ebene agiert, zusammen mit mid-level Regelungsmechanismen im Rückenmark. Es blieb aber bisher unklar, wie im Detail low- und mid-level Komponenten schnelle und robuste Fortbewegung ermöglichen.

Diese Arbeit zielt darauf ab, elementare low- und mid-level Komponenten zur schnellen Erkennung und Reaktion zu identifizieren und zu charakterisieren. Um diese Teilelemente und deren Zusammenspiel zu testen, wurden mehrere robotische Vorzeige-Systeme implementiert. Die Implementierungen beinhalten aktive und passive Mechanismen als Kombination von Elastizitäten und Dämpfern in mehrsegmentischen Roboterbeinen, zentrale Mustergeneratoren inspiriert von intraspinalen Reglern, und eine synthetische robotische Version eines intraspinalen Sensors.

Im ersten Teil wird das Konzept der effektiven Dämpfung erarbeitet. Mit der Betrachtung der Dissipation von Energien während eines Schrittes wird quantifiziert, inwieweit Störungen über Dämpfung abgefangen werden können. Es stellt sich heraus, dass Dämpfer, in dieser Anwendung, idealerweise viskos und einstellbar sind. Diese Studie erarbeitete Grundlagen zur Integration effektiver Dämpfer in Roboterbeinen bei der Lokomotion.

Im zweiten Teil stellen wir einen neuartigen seriell elastischen Aktuator vor. Das System überträgt Leistung über mehrere Beinsegmente hinweg, ohne mechanische Interaktion mit den Gelenken. Es verfügt außerdem über eine intrinsische serielle Elastizität. Das Design wird an einem Hüpfroboter mit zwei weiteren elastischen Elementen getestet. Die Rückgewinnung von Bewegungsenergie und die verbesserte dynamische Leistung werden aufgezeigt.

Im dritten Beitrag erarbeiten wir einen neuartigen bioinspirierten und einstellbaren Dämpfer und beschreiben dessen Einfluss aufs robotische Hüpfen. Ein Schlaffseil-Mechanismus wurde dazu seriell zum Dämpfer und parallel zu einer Feder implementiert. Ein Mustergenerator steuert den Dämpfer-Schlaffseil Mechanismus an und aktuiert damit ein Roboterbein. Wir beobachten und beschreiben den erwarteten Kompromiss zwischen Robustheit und Effizienz beim

Vorwärtsspringen im unregelmäßigen Terrain.

Der letzte Beitrag untersucht die Hypothese eines potentiellen intraspinalen Mechanosensors in Vögeln. Wir vermuten, dass die beobachtete intraspinale Struktur als Beschleunigungsmesser funktioniert. Der spekulative Sensor könnte Signale ohne Zeitverzögerung an angrenzende intraspinale Mustergeneratoren liefern und somit zum robusten Rennen von Vögeln beitragen. Wir implementierten einen biophysikalischen Simulator, in dem die Sensormechanik einschließlich mehrerer Morphologien und Materialeigenschaften getestet und beschrieben wurden.

Die hier vorgelegte Arbeit stellt Konzepte zur hierarchischen Regelung vor und untersucht dabei Sensor und Aktuator-Prinzipien auf mehreren Ebenen. Die Beiträge dieser Arbeit liefern neue Einblicke in die Robustheit und Effizienz der Lokomotion von Tieren und erarbeiten Grundlagen für zukünftige Konstruktionen von beinigen Robotern.

Acknowledgements

I would like to express my sincere gratitude to the following individuals and groups:

My supervisor, Dr. Alexander Badri-Sprowitz, for his guidance, support, and encouragement throughout my whole PhD journey.

My advisors and collaborators, for their constructive and insightful feedback that helped me improve my work: Dr. Martin Giese, Dr. Syn Schmitt, Dr. Daniel Häufle, and Dr. Monica Daley.

My colleagues, for all the lively discussions that have inspired me and your friendship that have made this journey enjoyable: Dr. Steve Heim, Dr. Özge Drama, Dr. Felix Ruppert, Dr. Albortz Aghamaleki Sarvestani, Dr. Viktoriia Kamska, Fabio Izzi, Bernadett Kiss, Emre Cemal Gönen, Dr. Charlotte Le Mouel, Dr. Fernanda Bribiesca-Contreras, Dr. Abhishek Chatterjee, Nayan Man Singh Pradhan, Patrick Frank, Milad Shafiee-Ashtiani, Jonas Hepp, Robin Petereit, Yu-Hsiang Lin, Dr. Huanbo Sun, Gaurav Gardi, Dr. Marco Bolignari, Toshihiko Fukushima, Dr. Bernard Javot, and Hritwih Banerjee.

The MPI administration team. Your efforts have relieved many headaches for me, especially from Leila Masri, Jutta Hess, Verena Geis, and Jörg Eisfeld.

My family, for their unconditional love as always. Your faith in me has been a constant source of motivation and strength.

Lastly, my beloved Yanlin, for the endless emotional support.

List of Publications

Accepted publications:

A. Mo, F. Izzi, D. F. Haeufle, and A. Badri-Spröwitz, “Effective viscous damping enables morphological computation in legged locomotion,” *Frontiers in Robotics and AI*, vol. 7, p. 110, 2020. DOI: [10.3389/frobt.2020.00110](https://doi.org/10.3389/frobt.2020.00110)

M. Bolignari, A. Mo, M. Fontana, and A. Badri-Spröwitz, “Diaphragm ankle actuation for efficient series elastic legged robot hopping,” in *2022 IEEE/RSJ International Conference on Intelligent Robots and Systems (IROS)*, IEEE, 2022, pp. 4279–4286. DOI: [10.1109/IR0S47612.2022.9981060](https://doi.org/10.1109/IR0S47612.2022.9981060)

A. Mo, F. Izzi, E. C. Gönen, D. Haeufle, and A. Badri-Spröwitz, “Slack-based tunable damping leads to a trade-off between robustness and efficiency in legged locomotion,” *Scientific Reports*, vol. 13, no. 1, p. 3290, 2023. DOI: [10.1038/s41598-023-30318-3](https://doi.org/10.1038/s41598-023-30318-3)

Submitted manuscript:

A. Mo, V. Kamska, F. Bribiesca-Contreras, J. Hauptmann, M. Daley, and A. Badri-Spröwitz, “Biophysical simulation reveals the mechanics of the avian lumbosacral organ,” *arXiv*, Dec. 2022. DOI: [10.48550/arXiv.2212.11485](https://doi.org/10.48550/arXiv.2212.11485)

Contents

Abstract	iii
Zusammenfassung	v
Acknowledgements	vii
List of Publications	ix
Nomenclature	xiii
1 Introduction	1
1.1 Hierarchy of sensing and control	1
1.2 Morphological computation embedded in mechanics	3
1.2.1 Elasticity	4
1.2.2 Damping	4
1.3 Sensorimotor control programmed in spine	5
1.3.1 Central pattern generator	5
1.3.2 Lumbosacral organ	6
1.4 Summary and Outline	7
2 Effective Energy Dissipation	9
2.1 Topic	9
2.1.1 Abstract	9
2.1.2 Key messages	10
2.2 Classification	10
2.2.1 Venue	10
2.2.2 Contribution	10
3 Series Elastic Diaphragm Actuation	11
3.1 Topic	11
3.1.1 Abstract	11
3.1.2 Key messages	12
3.2 Classification	12
3.2.1 Venue	12
3.2.2 Contribution	12

4 Slack-based Tunable Damping	13
4.1 Topic	13
4.1.1 Abstract	13
4.1.2 Key messages	14
4.2 Classification	14
4.2.1 Venue	14
4.2.2 Contribution	14
5 Intraspinal Sensing	17
5.1 Topic	17
5.1.1 Abstract	17
5.1.2 Key messages	17
5.2 Classification	18
5.2.1 Venue	18
5.2.2 Contribution	18
6 Discussion	19
6.1 Utilizing series and parallel elasticity	19
6.2 Leveraging physical damping	20
6.3 Exploring mid-level sensing and control	21
6.4 Conclusion and outlook	23
Appendix	39

Nomenclature

- 3D** Three-Dimension. 3
- CNS** Central Nervous System. 2
- CoM** Center of Mass. 4
- CPG** Central Pattern Generator. 2, 5–8, 19, 21–23
- CPU** Central Processing Unit. 2
- CRedit** Contributor Role Taxonomy. 10, 12, 14, 18
- DoF** Degree of Freedom. 7, 20
- GRF** Ground Reaction Force. 4
- IMU** Inertia Measurement Unit. 3
- LSO** LumboSacral Organ. 6–8, 17, 19, 22, 23
- MPC** Model Predictive Control. 6, 22
- MR** Magneto-Rheological. 5
- PD** Proportional Derivative. 3
- RL** Reinforcement Learning. 22
- SEA** Series Elastic Actuator. 19
- SELDA** Series ELastic Diaphragm Actuator. 11, 12, 19, 20
- SLIP** Spring-Loaded Inverted Pendulum. 4, 19
- VMC** Virtual Model Control. 6
- ZMP** Zero Moment Point. 6

Chapter 1

Introduction

Legged animals show remarkable running agility in diverse conditions. They are capable of executing explosive maneuvers during hunting [5], resisting hidden disturbance [6], and maintaining energy efficiency [7]. These highly dynamic movements demand fast perception of environments and coordinated action of muscles.

A main challenge for fast sensing and response is the sensorimotor delays [8]. Since legged locomotion interacts with environments mainly during the stance phase, the leg loading perception and leg force actuation should be within this time frame. However, in fast running, the stance duration is typically short [9]. Assuming a nerve fiber conduction velocity of a dog is 75 m/s [10]. Action potential transmits foot-brain-foot through 2 m long nerve fibers takes 27 ms, equivalent to a 37 Hz control frequency. This nerve conduction delays can be as large as 40% of stance duration [10], making detecting and correcting ground disturbance difficult.

In comparison, state-of-the-art legged robots require much higher control rates, commonly > 1 kHz [11–13], to reduce reaction time. In addition, robot actuators are more responsive, torque-dense [14], and energy-efficient [15] than muscles. Surprisingly, despite the technological advantages mentioned above, legged robots still struggle in perturbations and can easily be outperformed by a baby pony.

However, this comparison is not fair. Is robot's control really faster than animal's? The above example demonstrates only one layer of multiple control loops. The following chapters investigate a full picture of locomotion sensing and control, in particular the low-level components leading to fast response and robust locomotion.

1.1 Hierarchy of sensing and control

Legged animals and robots share similarity in locomotion sensing and control (Figure 1.1).

Animals use a hierarchy of feedforward, feedback, and physical control mechanisms to accomplish robust locomotion at high speed [8, 16–19]. At the top layer, the brain interprets information from vision, hearing, vestibular system, etc. and send decisions through descending neurons to the spinal circuits at

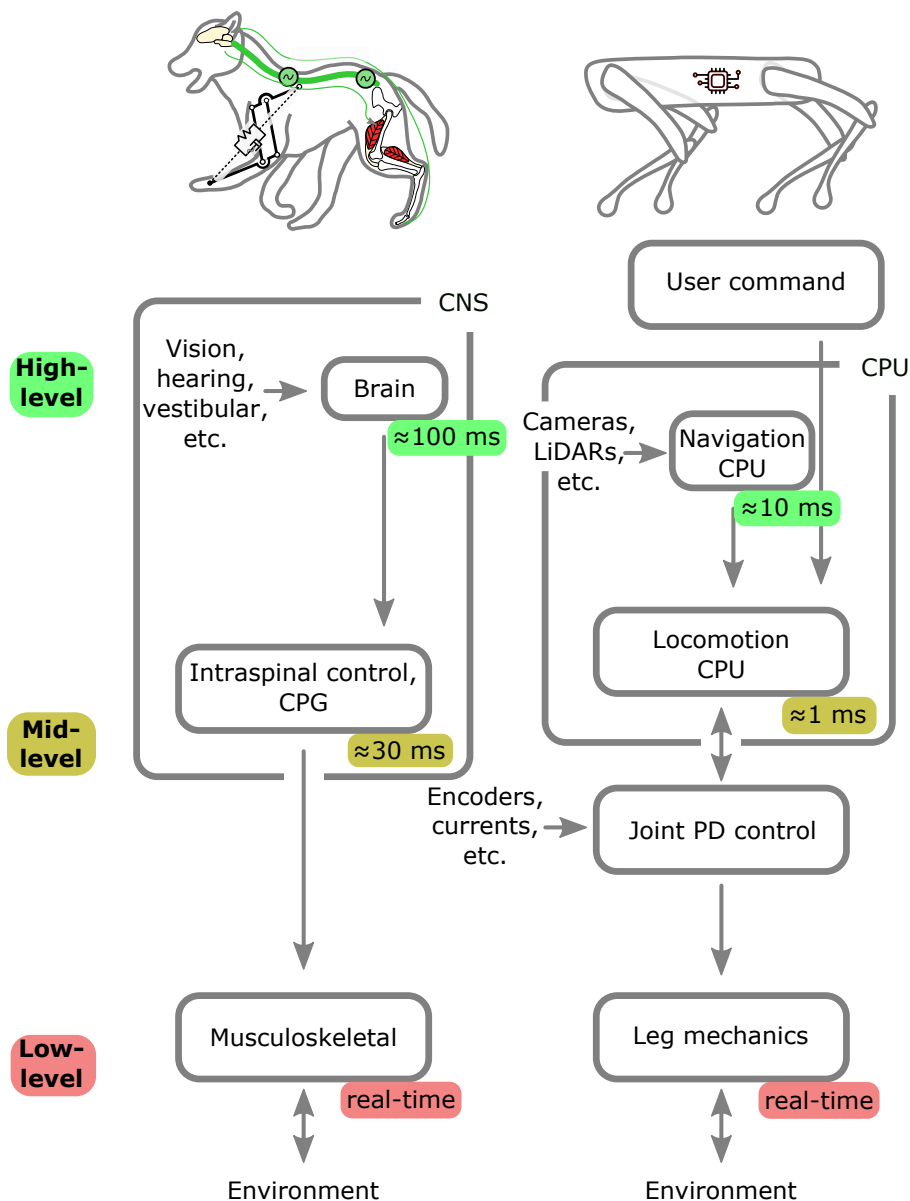


Figure 1.1: Locomotion sensing and control between legged animals and robots share similar hierarchical control architecture. For example, the Central Nervous System (CNS) is the counterpart of the Central Processing Unit (CPU), for processing higher level signals.

a timescale of ≈ 100 ms. At the middle layer, the spinal cord coordinates reflexes and generates rhythmic movement by the Central Pattern Generators (CPGs) [20] at a timescale of ≈ 30 ms. At the bottom layer, the musculoskeletal systems interact with environments through contacts. The muscles, tendons, and bones together encode compliant behavior [21, 22], such as stiffness and damping, which respond to contact loading in “real time”. Despite simplicity,

this hierarchy illustrates a fast control loop enabled by the low-level musculoskeletal systems.

Legged robots' control architecture is similar to animal's, but more centralized. A locomotion computer and a navigation computer are often needed [23, 24]. The navigation computer is responsible for understanding the environment and planning a feasible path. It reads vision data from cameras, LiDARs, radars, etc. and reconstructs Three-Dimension (3D) maps. Processing images and 3D maps is computational intensive, which reduces the control rate to ≈ 100 Hz. The locomotion computer reads high-level path commands from the user input, navigation computer, and state feedback from sensors such as encoder, force sensor, current sensor, Inertia Measurement Unit (IMU), etc. It then computes footsteps, optimizes trajectories, and sends motor commands to all actuators at a control rate ≈ 1000 Hz. A low-level Proportional Derivative (PD) controller in the actuator's drivers may exist to control the desired motor position or torque. In the end, the leg mechanics interacts with environments in real time.

Notwithstanding similarities between animals and robots (Figure 1.1), differences exist. Neural control involves millions of neuron firings that is more complex compared to lines of robot control algorithms. Hundreds of muscles are "redundant" compared to the common robot design of fully actuated or underactuated systems. The musculoskeletal system is compliant and adaptive, while the robot mechanics are often rigid and restrictive.

Animals have been perfectly engineered over millions of iterations, while the evolution of robotics has been only a few decades. Giving the similarities and discrepancies between both systems, bridging both worlds will enrich our understanding of animal locomotion and inspire future robot development.

1.2 Morphological computation embedded in mechanics

The mechanical response of a system is the fastest among other higher level control loops [16, 25]. A musculoskeletal system may produce adaptive mechanical response to external loading without any control input. This adaptive response has been termed morphological computation¹ [1, 26-29]:

"Certain processes performed by the body (and environment) that otherwise would have to be performed by the brain".

—Rolf Pfeifer, Josh Bongard

A good example of morphological computation is the insect's wing [30]. During flight, active muscular forces cannot entirely control the wing shape, which is subjected to the interaction of aerodynamic and inertial forces with the wing's own elasticity. These interactions are essentially determined by the morphology of the wing itself. When carefully modeled, morphological computation can be applied to robotic systems, such as the passive dynamic walker [31-34], a bipedal robot can walk and run in a human-like gait, even without a single actuator.

The morphological computation is embedded in the mechanics of an agent, which includes the morphologies and material properties. The morphologies are essential for interaction with environments. Material properties, such as stiffness and damping, shape the instantaneous response of the agent.

¹also called embodied intelligence, intrinsic mechanics, preflex, etc.

1.2.1 Elasticity

In locomotion studies, elastic behavior has been well observed in the limbs of animals [21, 22]. Compared to the stiff bones, the muscles and tendons are soft and elastic, acting like springs routing through joints. The muscle-tendon complex can store and release energy during rhythmic contraction in locomotion [35]. This greatly improves locomotion energy efficiency. For example, kangaroos are able to recover 70% kinetic energy during landing for lift-off [36]. In addition, the springy leg design improves running stability with ground disturbance [6, 37, 38].

The elastic elements have been well modeled. In macroscopic level, walking and running can be modelled by the Spring-Loaded Inverted Pendulum (SLIP) models [39–42]: a point mass represents the body and a massless spring describes the limb. Despite extreme simplicity, the SLIP models predict > 80% of Center of Mass (CoM) trajectory [40] and > 80% of Ground Reaction Force (GRF) [43]. In microscopic level, muscles are often described by the Hill-type muscle model [44, 45], including one contractile element and two non-linear springs, where the series elastic force is dominant in net muscle force output [46].

Mimicking the elasticity in nature, legged robots benefit from springy leg designs. Springs are implemented either physically or “virtually”. Embedding physical springs in legs reduces energy consumption [47, 48], improves stability [49, 50] and offloads control efforts [51–53]. Alternatively, spring forces can be generated from actuators with a force controller [12, 13, 54, 55]. Stiffness can be online controlled in Cartesian space, despite non-linear leg segmentation. This control flexibility necessitates strong actuators, accurate sensing, and high-frequency control.

1.2.2 Damping

Despite the dominant elastic force, an energy conservative spring-mass system can only handle small amount of perturbations [38, 56–59]. While less understood, damping likely plays a more important role in robust legged locomotion. For instance, a ground drop perturbation increases the leg impact velocity, which leads to immediate higher leg damping force to slow down the motion. Additionally, the extra gravitational energy introduced by the ground drop can be dissipated through the leg damping. Therefore, intuitively, damping produces adaptive force to regulate the system’s energy in response to perturbations.

Damping components have been identified in muscles, as muscles can do negative work like a brake [60–62]. For example, eccentric contraction of muscle exhibits a damping-like velocity adaptation to the perturbations [63–65]. Such muscle damping can suppress high-frequency oscillations [66, 67], reducing fatigue damage to tendons and bones. In legged locomotion, damping produces beneficial force output during leg impacts [68] to improve stability [69–71], mitigate ground perturbations [65, 72], regulate system’s energy [73], reduce control effort [74], and improve energy efficiency [75–77].

Damping should be tunable according to locomotion conditions [1, 3, 55, 73, 78, 79]. Since damping can be costly as it dissipates energy [1], minimizing damping during steady state locomotion, such as level running, will improve energetics without compromising stability. When robustness is prioritized in unstructured terrains, selecting a higher damping can assist mitigating pertur-

bations [3]. Also, robotic implementations confirm tunable damping in real time is fundamental towards versatility [12, 55, 80].

Legged robots commonly implement “virtual damping” through impedance control [81], in the same way as the “virtual spring” introduced in Section 1.2.1. Damping force generated from actuators is often used to stabilize landing impacts [13, 54, 82] and improve running versatility [12, 55]. To generate peak force at impacts, “virtual damping” demands precise sensing for good velocity estimation, high-frequency force control, and powerful actuator capable of high peak force and fast heat dissipation [1, 3, 12].

Alternatively, physical dampers can be integrated into leg structure, which is often overlooked. Unlike “virtual damping”, a physical damper senses instantly, requires no controller, and produces peak load instead of the actuators [3]. Despite these potential benefits, only a few implementations exist in legged machines [1, 3, 75, 83–89]. Implementing physical dampers adds additional complexity and cost to the design [84]. Due to the hysteresis and nonlinearity, damper modeling is often inaccurate, thus requires extensive testing [90, 91]. A tunable damper design is even more difficult [1]. Most tunable designs are based on Magneto-Rheological (MR) fluid, and only partially tested on legged systems [85, 87–89]. More effort is required to exploit physical tunable damping in legged dynamics.

1.3 Sensorimotor control programmed in spine

Between the fast physical response of the musculoskeletal system and the slow neural control descending from the brain, a middle layer sensorimotor control exists in the spine. This intraspinal control can be independent of the higher brain centers. For example, a driving treadmill can induce a natural-looking gait of a decerebrated cat [92], and even gait transition [93]. Similarly, electrical stimulation can induce walking and swimming of a decerebrated salamander [94]. Another example of intraspinal control is the stretch reflexes. Signals transmit through the spinal cord and back to the same muscle, leading to low-latency response. Therefore, stretch reflexes are often considered compensating for unexpected mechanical disturbance in muscles [95]. These examples are clear evidence that sensorimotor control for locomotion presents in the spinal cord.

The spinal cord connects directly to the sensor and motor roots, allowing the earliest neural response. Unlike the physically embedded response of the musculoskeletal system, the spinal neural circuits are programmable [92]. This flexibility permits adaptation to new locomotion conditions, e.g. after spinal injury [92], which is essential for survival in uncertain environments.

1.3.1 Central pattern generator

The central pattern generators (CPGs) in spinal cords are arguably the most fundamental mechanism responsible for rhythmic activities such as chewing, breathing, digesting, and locomotion [20]. Without rhythmic input from higher brain or from sensory feedback, the CPGs in the spinal cord can generate rhythmic patterns in a feedforward manner, as reported in lamprey [96, 97], salamander [98], and frog [99]. While rhythmic input is not necessary, simple electrical or chemical stimulation can trigger the CPGs [96, 97], modulate locomotion

speed [100], and even induce gait switching [94, 101]. This simple command drastically reduces the control dimensionality of the descending control signals from higher control centers. Consequently, the brain offloads the control of millions of limb muscle fibers to the CPGs of the spinal cord, making the limited bandwidth between the brain and the spinal cord feasible [20]. Likewise, the sensory feedback plays an important role in shaping the CPG output [102]. For instance, mechanical movement of the tail of the lamprey can entrain the CPG output frequency [103–105].

Different levels of CPG modelling have been proposed. Detailed biophysical models are based on the more elaborated Hodgkin-Huxley type of neuron, focusing on the generation of rhythmic activities in small neural circuits [106, 107]. Connectionist models are based on simplified leaky-integrator neurons or integrate-and-fire neurons, investigating how the network properties generate and synchronize rhythmic activities [108, 109]. Oscillator models are based on mathematical models of coupled nonlinear oscillators, studying how inter-oscillator coupling, synchronization and phase lag within a population of oscillatory centers [110, 111]. Neuromechanical models incorporate biomechanical models on top of CPG models, allowing for the study of sensory feedback and mechanical entrainment to the CPG activities [109, 112].

The advancement of the CPG modeling has inspired CPG controlled robots. CPG models have been implemented to various robots for different locomotion modes, including lamprey/eel robots [113, 114], salamander robots [111], snake robots [115, 116], quadrupedal robots [51, 117–119], bipedal robots [48, 120, 121], and single leg hopping [2, 3]. While most of these robots use CPGs to generate feedforward reference trajectories, CPGs are well suited to integrate sensory feedback. For instance, body motion feedback into CPGs tends to improve quadrupedal locomotion stability in complex terrain [118]. Pressure feedback enables automatic transition between swimming and walking [111]. Contact feedback mitigates short-term perturbations [122]. Local load sensing triggers gait transition from walking to trotting [119].

While robotics benefits from biological inspiration, robots have been increasingly used as a scientific tool to understand biological systems [20, 123, 124]. Unlike other more physics-based locomotion controllers, such as static locomotion [125], Raibert heuristic [47, 126], Zero Moment Point (ZMP) [127, 128], capture points [129, 130], Virtual Model Control (VMC) [131], hybrid zero dynamics [132, 133], Model Predictive Control (MPC) [24], ect., CPG controlled robots behave closer to their biological references. As such, these robots are ideal platforms for studying the function of morphology and sensorimotor control that are otherwise impossible with living systems.

1.3.2 Lumbosacral organ

Intraspinal sensing has been identified in several species, including lamprey [103, 134], zebrafish [135, 136], and potentially reptiles [137]. Recently, the LumboSacral Organ (LSO) in birds has been suggested as another intraspinal locomotion sensor [138–140].

The LSO exhibits unique morphology [140]. Located at the lower part of the spine, the LSO includes a pronounced spinal canal enlargement; within which a suspicious dense glycogen body wedged between the two hemispheres of the spinal cord; accessory lobes that contain mechanoreceptive neurons arranged

pairwise at the lateral side of the spinal cord; a dentate ligament network that suspends the spinal cord; and spinal fluid that fills up the rest of the spinal canal space. One could imagine a dense mass (glycogen body), hanging on elastic tissue (spinal cord and dentate ligaments) that connect to sensors (accessory lobes) and surrounded by fluid (spinal fluid).

Since the LSO first described in 1811 [141], coincidentally in University of Tübingen where this thesis is written, the precise function of the LSO remains unknown. Early research suspected a “locomotor brain” function, owing to the large accumulation of nerve cells nearby [142]. Later, the LSO was associated with secretory function, regulating the glucose through the glycogen body [143–146]. Recently, the mechanosensing hypothesis is prevailing. Schroeder and Murray proposed the strain sensing mechanism of the accessory lobes, induced by the distorted dentate ligaments during locomotion [147]. Kamska, Daley, and Badri-Spröwitz further developed this strain sensing mechanism by including gyroscopic and acceleration sensing function based on the differential topology of the accessory lobes [4, 140]. Necker suggested a balance sensing function, where the accessory lobes sense the spinal fluid flow in the narrow spinal canal, similar to the working principle of the vestibular system [138, 139, 148–151]. Still, no conclusive evidence has been found to support these hypotheses.

The hypothesized mechanosensing function of the LSO is supported by several facts: (1) Robust locomotion requires fast sensing. Birds commonly have long necks, which considerably increases the sensorimotor delays for high-level commands descending from brain to the spinal cord. An intraspinal sensor closely integrated near the CPGs will provide timely state feedback in case of perturbations. (2) LSO shares morphological similarity to known intraspinal sensors. The intraspinal mechanosensors’ arrangement in lamprey [103, 134] and zebrafish [135, 136] are similar to that of birds’ accessory lobes. (3) Neuropysiology evidence is available. A series of studies have identified the axonal projection [152, 153], the electrical activity [154–157] and the mechanosensation [158] of the accessory lobes. (4) Gyroscopic and acceleration sensing is physically possible. Since the accessory lobes are symmetrically arranged at the nodes of the dentate ligament network, 6 degrees of freedom (DoFs) motion of the LSO can stimulate different loading patterns on the accessory lobes.

Validation of the mechanosensing function of LSO has been challenging. Since the spinal soft tissue is deeply encapsulated within the fused lumbosacral vertebrae, in vivo measurement of the spinal cord movement and the accessory lobes activities has failed so far. It remains unclear how the LSO responds to locomotion acceleration and how its morphologies and material properties shape the response.

1.4 Summary and Outline

Fast sensing and control are essential for robust legged locomotion, especially in fast running, where the sensorimotor delays are predominant. Fast sensing and control exist in mechanics and spine: (1) The mechanical properties embedded in the leg structure can produce immediate and adaptive force in response to foot contact conditions. (2) The neural circuits programmed in the spine can minimize the sensorimotor delays in locomotion control. In the following chapters, I will present my work centering around these two concepts. Specifi-

cally, how these two concepts inspired robotic development and how biorobotics fosters our understanding of biology.

In Chapter 2, I investigate how the morphological computation (Section 1.2) facilitates perturbation rejection. I identified the optimal damping (Section 1.2.2) allowing for effective energy dissipation and robust locomotion.

In Chapter 3, I study how elastic elements (Section 1.2.1) in leg design improve hopping performance with CPG control (Section 1.3.1). I develop a novel series elastic actuation system based on the rolling diaphragm cylinder described in Chapter 2.

In Chapter 4, I propose a bio-inspired damping (Section 1.2.2) control concept based on tendon slack. I implement the optimal damper identified in Chapter 2 on a CPG-driven (Section 1.3.1) hopping robot and quantify the trade-off between energy efficiency and robustness.

In Chapter 5, I explore the potential intraspinal sensing organ—LSO (Section 1.3.2). I present a biophysical simulation of the LSO to analyze its entrainment behavior with configurable morphologies and material properties.

Chapter 2

Effective Energy Dissipation Enables Morphological Computation

2.1 Topic

This work is categorized in the fields of biorobotics. The paper [1] investigates how damping mitigates ground-level perturbation with a two-segment leg design, in both numerical simulation and hardware experiments.

2.1.1 Abstract

Muscle models and animal observations suggest that physical damping is beneficial for stabilization. Still, only a few implementations of physical damping exist in compliant robotic legged locomotion. It remains unclear how physical damping can be exploited for locomotion tasks, while its advantages as sensor-free, adaptive force- and negative work-producing actuators are promising. In a simplified numerical leg model, we studied the energy dissipation from viscous and Coulomb damping during vertical drops with ground-level perturbations. A parallel spring-damper is engaged between touch-down and mid-stance, and its damper auto-decouples from mid-stance to takeoff. Our simulations indicate that an adjustable and viscous damper is desired. In hardware, we explored effective viscous damping and adjustability, and quantified the dissipated energy. We tested two mechanical, leg-mounted damping mechanisms: a commercial hydraulic damper, and a custom-made pneumatic damper. The pneumatic damper exploits a rolling diaphragm with an adjustable orifice, minimizing Coulomb damping effects while permitting adjustable resistance. Experimental results show that the leg-mounted, hydraulic damper exhibits the most effective viscous damping. Adjusting the orifice setting did not result in substantial changes of dissipated energy per drop, unlike adjusting the damping parameters in the numerical model. Consequently, we also emphasize the importance of characterizing physical dampers during real legged impacts to evaluate their effectiveness for compliant legged locomotion.

Table 2.1: Individual contributions based on the CRediT system [159]

Term	AM	FI	DH	ABS
Conceptualization	x	x	x	x
Methodology	x	x		
Software		x		
Validation				
Formal analysis	x	x		
Investigation	x	x		
Resources				x
Data curation	x	x		
Writing - original draft	x	x	x	x
Writing - review and editing	x	x	x	x
Visualization	x	x	x	x
Supervision			x	x
Project administration	x		x	x
Funding acquisition	x		x	x

2.1.2 Key messages

- (1) Viscous damping is more effective than Coulomb damping in mitigating ground-level perturbation.
- (2) Adjustable damping is desired to improve energy efficiency.
- (3) The tested hydraulic damper produces more effective viscous damping than our custom-made pneumatic damper.
- (4) Adjusting damping rate does not result in substantial changes of dissipated energy due to the coupling of damper mechanics and legged dynamics.

2.2 Classification

2.2.1 Venue

Frontiers in Robotics and AI is a leading robotics journal from the Frontiers family. The journal publishes rigorously peer-reviewed theoretical and applied robotics research.

2.2.2 Contribution

I helped form the initial idea. I designed and implemented the robot leg, test bench and sensor instrumentation. I wrote the initial codes for the simulation model. I conducted all hardware experiments, wrote scripts for data processing and interpreted results. I wrote the hardware part of the paper, prepared figures and video, and helped write the rest of the paper. I helped organize regular project meetings, plan and adjust project goal.

The contributions with co-authors are classified with the Contributor Role Taxonomy (CRediT) system [159], as in Table 2.1

Chapter 3

Series Elastic Diaphragm Actuation for Efficient Robot Hopping

3.1 Topic

This work is classified in the field of compliant robot design. The paper [2] proposes a lightweight, low-friction and series elastic actuation design, allowing for efficiently actuating distal joints in legged robots.

3.1.1 Abstract

The observation of the anatomy of agile animals and their locomotion capabilities emphasizes the importance of fast and lightweight legs and confirms the intrinsic compliance integrated into muscle-tendon units as a major ingredient for energy-efficient and robust locomotion. This quality is especially relevant for distal leg segments, which are subject to aggressive dynamics. Legged robots are accordingly designed to improve dynamic performance by lightweight mechanisms combined with series elastic actuation systems. However, so far, no designs are available that feature all characteristics of a perfect distal legged locomotion actuator such as a lightweight and low-inertia structure, with high mechanical efficiency, no stick and sliding friction, and low mechanical complexity. With this goal in mind, we propose a novel robotic leg which integrates all the above features. Specifically, we develop, implement, and characterize a bioinspired robot leg that features a lightweight Series ELastic Diaphragm Actuator (SELDA) for active control of foot motion. We conducted experiments to compare two leg configurations, with and without foot actuation, to demonstrate the effectiveness of the proposed solution in agile forward hopping controlled by a central pattern generator. We studied how tuning SELDA's activation timing can adjust the robot's hopping height by 11% and its forward velocity by 14%, even with comparatively low-power injection to the distal joint.

Table 3.1: Individual contributions based on the CRediT system [159]

Term	MB	AM	MF	ABS
Conceptualization	x	x	x	x
Methodology	x	x		
Software	x	x		
Validation	x	x		
Formal analysis	x	x		
Investigation	x	x		
Resources			x	x
Data curation	x	x		
Writing - original draft	x	x		
Writing - review and editing	x	x	x	x
Visualization	x	x	x	
Supervision			x	x
Project administration	x		x	x
Funding acquisition	x		x	x

3.1.2 Key messages

- (1) The proposed SELDA system has appealing features of lightweight, low-friction, high efficiency, and truly remote actuation, which overcomes the challenge of actuating distal robot joints.
- (2) The addition of a foot segment improves the performance of the hopping robot.
- (3) The SELDA system embedded in a compliant robot leg design demonstrates effective adjustment of hopping height and forward speed.

3.2 Classification

3.2.1 Venue

The IEEE International Conference on Intelligent Robots and Systems (IROS) is one of the most important robotic conferences. The conference has a high impact and often considered a top venue for robotic research, together with the IEEE International Conference for Robotics and Automation (ICRA).

3.2.2 Contribution

I helped form the initial concept and offered the initial robot design. I designed and implemented the sensor instrumentation, control algorithm, and experimental protocol. I assisted all experiments, wrote part of the scripts for data analysis. I helped write the initial draft of the paper and the response to reviewers' feedback. I took part in regular project meetings and helped define and achieve the milestones of the project.

The contributions with co-authors are classified with the CRediT system [159], as in Table 3.1

Chapter 4

Slack-based Tunable Damping Resolves the Trade-off Between Robustness and Efficiency

4.1 Topic

This work is placed at the intersection of biomechanics, bioinspiration and legged robot design. The paper [3] overcomes the challenge of tunable damping in legged robots by the slack damper mechanism inspired from muscle tendon slack. The proposed mechanism is systematically characterized in hopping robot to investigate its effect on robustness and efficiency.

4.1.1 Abstract

Animals run robustly in diverse terrain. This locomotion robustness is puzzling because axon conduction velocity is limited to a few tens of meters per second. If reflex loops deliver sensory information with significant delays, one would expect a destabilizing effect on sensorimotor control. Hence, an alternative explanation describes a hierarchical structure of low-level adaptive mechanics and high-level sensorimotor control to help mitigate the effects of transmission delays. Motivated by the concept of an adaptive mechanism triggering an immediate response, we developed a tunable physical damper system. Our mechanism combines a tendon with adjustable slackness connected to a physical damper. The slack damper allows adjustment of damping force, onset timing, effective stroke, and energy dissipation. We characterize the slack damper mechanism mounted to a legged robot controlled in open-loop mode. The robot hops vertically and planarly over varying terrains and perturbations. During forward hopping, slack-based damping improves faster perturbation recovery (up to 170 %) at higher energetic cost (27 %). The tunable slack mechanism auto-engages the damper during perturbations, leading to a perturbation-trigger damping, improving robustness at a minimum energetic cost. With the results from the

slack damper mechanism, we propose a new functional interpretation of animals' redundant muscle tendons as tunable dampers.

4.1.2 Key messages

- (1) Adjusting tendon slack allows tunable onset timing, engage stroke, and energy dissipation of the attached damper.
- (2) Tunable damping reveals the trade-off between hopping robustness and efficiency.
- (3) The proposed slack damper mechanism allows perturbation-triggered damping to maximize both robustness and efficiency at the same time.

4.2 Classification

4.2.1 Venue

Scientific Report is a high-impact journal from the Nature family. While being young, the journal has grown to become the largest in the world by number of articles, and covers all areas of the natural science. This study is published in the special issue of "Bioinspired robotic locomotion".

4.2.2 Contribution

I conceived the initial idea. I designed and implemented the robot setup, experimental setup, sensor instrumentation, control algorithm, and test protocol. I conducted all the experiments, wrote the scripts for data analysis, and interpreted the results. I wrote the draft of the paper, prepared most of the figures, and responded to reviewers' feedback. I organized project meetings with the team, defined the milestones, distributed tasks, and adjusted the goal throughout the project.

The contributions with co-authors are classified with the CRediT system [159](#), as in Table [4.1](#).

Table 4.1: Individual contributions based on the CRediT system 159

Term	AM	FI	CG	DH	ABS
Conceptualization	x				
Methodology	x				
Software	x				
Validation	x	x	x		
Formal analysis	x	x	x		
Investigation	x		x		
Resources					x
Data curation	x	x	x		
Writing - original draft	x	x			
Writing - review and editing	x				x
Visualization	x	x	x		x
Supervision				x	x
Project administration	x				x
Funding acquisition	x				x

Chapter 5

Intraspinal Sensing in Birds—the LumboSacral Organ

5.1 Topic

This work is classified at the intersection of functional morphology, mechanosensing and biophysical simulation. The paper [4](#) studies how individual anatomical structures control the mechanical response of the avian lumboSacral organ with biophysical simulation.

5.1.1 Abstract

The LumboSacral Organ (LSO) is a lumboSacral spinal canal morphology that is universally and uniquely found in birds. Recent studies suggested an intraspinal mechanosensor function that relies on the compliant motion of soft tissue in the spinal cord fluid. It has not yet been possible to observe LSO soft tissue motion *in vivo* due to limitations of imaging technologies. As an alternative approach, we developed an artificial biophysical model of the LSO, and characterized the dynamic responses of this model when entrained by external motion. The parametric model incorporates morphological and material properties of the LSO. We varied the model's parameters to study the influence of individual features on the system response. We characterized the system in a locomotion simulator, producing vertical oscillations similar to the trunk motions. We show how morphological and material properties effectively shape the system's oscillation characteristics. We conclude that external oscillations could entrain the soft tissue of the intraspinal lumboSacral organ during locomotion, consistent with recently proposed sensing mechanisms.

5.1.2 Key messages

- (1) The biophysical model can be entrained by external oscillation, which confirms the expected mass-spring-damper behavior.

Table 5.1: Individual contributions based on the CRediT system [159]

Term	AM	VK	FBC	JH	MD	ABS
Conceptualization				x	x	x
Methodology	x	x		x		
Software	x					
Validation	x		x			
Formal analysis	x		x			
Investigation	x	x				
Resources						x
Data curation	x		x			
Writing - original draft	x	x	x			x
Writing - review and editing	x	x				x
Visualization	x	x	x			
Supervision					x	x
Project administration	x	x				x
Funding acquisition	x					x

- (2) The glycogen body density adjusts the frequency response of the spinal cord oscillation.
- (3) The narrow fluid space suppresses spinal cord oscillation amplitude.
- (4) The spinal canal morphology has a strong effect on the spinal cord entrainment response.

5.2 Classification

5.2.1 Venue

Bioinspiration & Biomimetics is a high-impact interdisciplinary journal that connects the biology with engineering. It facilitates the two-way ideas flow to extend the knowledge of different disciplines. (in submission)

5.2.2 Contribution

I helped develop the specific hypotheses to be tested in this study. I contributed to the majority of the biophysical model design and fabrication. I prepared the instrumentation of the experimental setup, including motion control, data acquisition, and test protocol. I conducted all experiments, collected and curated data for later analysis, and interpreted results. I helped write the draft of the paper and prepared figures. I planned project meetings with our team, managed the overall timeline, and adjusted the goal of the project.

The contributions with co-authors are classified with the CRediT system [159], as in Table 5.1

Chapter 6

Discussion

In this thesis, I provide insights into the fast sensing and adaptive actuation mechanisms for robust legged locomotion. Initially, my investigation starts from the morphological computation in ground perturbation rejection in Chapter 2. Subsequently, the rolling diaphragm cylinder design developed in Chapter 2 inspires the application of series elastic actuation in Chapter 3. Furthermore, the challenge of ambiguous damping dissipation in Chapter 2 leads to the bio-inspired slack damper strategy in Chapter 4. Lastly, I study the potential intraspinal sensing organ—LSO in Chapter 5 that could augment the intraspinal controller—CPG implemented in Chapter 3 and Chapter 4. For an in-depth discussion of each work, we refer to the discussion section of each paper [1-4].

6.1 Utilizing series and parallel elasticity

Traditionally, robots are built with high rigidity, as elastic deformation will impair end-effector motion precision. Also, rigid bodies are easy to model, control and manufacture compared to soft parts. In contrast, the soft robotic community often claims that robots should be soft for various motivations. In fact, rigid bones and elastic muscle-tendons worked in harmony for millions of years. Likewise, legged robots can benefit from elastic elements within a rigid structure.

In Section 1.2.1, I introduce how elasticity is modelled and utilized in legged animals and robots. The elegance of the SLIP model is to generalize all legged locomotion systems with remarkable simplicity and accuracy. Inspired by the SLIP model, early legged robots integrate springs into leg structure, aiming for elastic behavior. Later, the springs are exploited for precise force output, in the form of Series Elastic Actuator (SEA). The spring deflection between the actuator and the end effector is constantly measured and controlled for the target force output. However, in this way, the spring is an active element in the control loop, and the benefits of its passive response are basically neglected.

In Chapter 3, I present the Series ELastic Diaphragm Actuator (SELDA), a novel actuator with inherent series elasticity. Instead of a force-controlled SEA, I exploit the passive response of the SELDA with minimum control. Actuating the ankle joints of a legged robot has been challenging, due to the aggressive dynamics of leg movement and force transmission over several joints. Consequently,

there are very few actuated ankles in legged robots. The SELDA is designed to overcome the challenge of actuating distal robot joints. First, by shifting the heavy actuator next to the body of the robot, the inertia of the distal joints is effectively reduced for dynamic movement. Second, the rolling diaphragm cylinder in the SELDA eliminates the stick and sliding friction, allowing for highly transparent force transmission. Third, the air in the transmission line acts as in-series spring, improving impact resistance and energy recuperation during locomotion. Finally, I demonstrate that with simple feedforward control of the activation timing of the SELDA system, the robot's hopping height and forward velocity can be adjusted with relatively low-energy input.

The parallel elasticity is equally important as the series elasticity. The simplified 2-segment leg in Chapter 2 shows that the parallel spring at the knee joint can recover kinematic energy during drop experiments. Two parallel springs are implemented to the hopping robot in Chapter 3, at the knee joint and the bi-articular segment. In addition to energy recuperation, this parallel elasticity configuration can redirect motor power from the leg angle direction to the leg length direction. Normally, a hopping robot requires two actuated DoFs to compensate for kinematic and potential energy loss, one to swing the leg (leg angle actuator) for horizontal movement, the other to extend the leg (leg length actuator) for maintaining a certain hopping height. As a result of the power redirection, the parallel elasticity in Chapter 3 spares the leg length actuator that maintains hopping. Another advantage of the parallel elasticity in legged robot design is gravity compensation. As with conventional legged robots without parallel springs, the standing posture requires motors to actively produce leg extension force to balance the gravity, which is costly. By mimicking the quadriceps in animal anatomy, the parallel knee springs in Chapters 2 to 4 keep the leg posture while standing, without the need of energy input.

I demonstrate that the physical series and parallel elasticity in leg structure are important building blocks for efficient and agile locomotion. Nonetheless, the implementation of physical series and parallel elasticity has been controversial. The main complaint is that the physical spring often causes close-loop control instability. In my opinion, as suggested in Section 1.1, the high-level or mid-level close-loop control should not be nested with the low-level physical response of the springs. The spring itself is a complete control system with displacement sensing and force actuation. Instead of working against the springs in the control loop, the springs can be better utilized independently, with minimum control. Although the integration of series and parallel elasticity requires more profound understanding of the system's dynamics, as well as engineering efforts, the outcome will be promising towards animal-like locomotion performance.

6.2 Leveraging physical damping

Dampers often work in parallel with springs, such as in the car suspension system. It is intuitive to expect dampers in legged robots alongside the springs. However, one can hardly find any physical damper in legged robots. The realm of physical damping is almost entirely overlooked.

I observe two main obstacles that hinder the damper implementation. First, it is unclear what kinds of damping strategy can be exploited for locomotion tasks. Most studies only vaguely correlate the improved locomotion performance

with the existence of damping, without investigating the underlining mechanism. Second, the mechanical complexity of damper integration is nontrivial. Since no damper has been developed for legged robot applications, researchers often have to rely on custom-built dampers, which do not always produce the desired force output. Despite the challenges above, the potential benefits of physical damping are still promising (Section 1.2.2) and worth investigation.

I tackle the first challenge of unclear damping strategy in the work of Chapter 2 with drop tests. While the drop test is a highly simplified locomotion scenario, it highlights the underlining mechanics for the entire stance phase in one step, which is essential before implementing a complete robot system. Without energy input from actuators, dissecting and quantifying energy flow becomes viable. Through both numerical simulation and hardware experiments, I show that the viscous, tunable, hydraulic damper is the most effective damping option. Since ground perturbations often introduce additional gravitational energy into the legged system, a viscous damping strategy is capable of dissipating the excessive energy in an adaptive manner, therefore improves the robustness of the system. However, there is a third challenge—the damping tunability. Counter-intuitively, tuning a higher damping rate barely affects the magnitude of energy dissipation. Since the dissipated energy is an integral of damper force and displacement, a higher damping rate increases the force, but reduces displacement by the stronger deceleration.

Now that the desired damping strategy is identified, I tackle the tunable damping integration challenge in the work of Chapter 4. I implement a bio-inspired hopping robot similar to the one in Chapter 3, where the selected hydraulic damper from Chapter 2 is integrated at the knee for perturbation response. The robot is fully actuated and controlled by CPG (Section 1.3.1). Inspired by the muscle tendon slack in nature, I propose the slack damper mechanism for damping control. Instead of tuning the damping rate, I control the tendon slack between the damper and the knee joint. In this way, the tendon slack delays the engagement of the damper, effectively reducing both damping force and displacement at the same time. With systematic experimentation on the hopping robot, I discover the trade-off between locomotion robustness and energy efficiency with respect to damping control. As damping dissipates energy, it should be minimized when the robustness is not a priority, such as during level running without perturbations. The slack damper mechanism is able to physically disengage the damper for minimum energy loss, which is impossible with conventional tunable damper designs. Moreover, when the tendon slack is set to barely engage during level running, a ground drop perturbation will automatically engage the damper. In this way, a perturbation-triggered damping strategy maximizes both robustness and efficiency, by a purely mechanical solution. Ultimately, this slack-based physical damping is a good example of morphological computation introduced in Section 1.2, demonstrating the fastest response of low-level control leading to robust and efficient locomotion.

6.3 Exploring mid-level sensing and control

Compared to the hierarchical control architecture in nature, roboticists tend to favor centralized and modular control (Figure 1.1). Despite the simplicity and elegance of a centralized control, the counterpart in nature is never simple.

Section 1.1 suggests that the mid-level control layer could bridge the high-level commands and low-level physical responses. In this thesis, I present two mid-level mechanisms—the Central Pattern Generator (CPG) and the LumboSacral Organ (LSO), both found in the spinal circuits.

As described in Section 1.3.1, the CPG exhibits great potential for legged locomotion study. I implement a basic CPG controller for the hopping robots in Chapters 3 and 4. With only a few parameters, such as frequency, amplitude, offset and duty factor, the nominal hopping gait is defined. This exemplifies that the high-level control centers do not have to constantly monitor and control locomotion states. A mid-level control layer not only offloads the limb coordination tasks from the high-level units, but also reduces the necessary communication bandwidth in between. Unlike those widely used controllers that are based on MPC or Reinforcement Learning (RL), the CPG controller is comparatively easier to implement. This allows locomotion research to focus on the interactions of individual control layers in a control environment, e.g. focusing on the physical response as in Chapter 4.

Intraspinal sensing is able to adjust the CPG output in animals, completing the control loop for mid-level sensing and control. The LSO discussed in Section 1.3.2 is likely an unexplored accelerometer in birds.

Proving the accelerometer hypothesis of the LSO is significant for the following reasons: (1) In biomechanics, it can explain birds' exceptional running agility. Birds typically have long necks that increase the nerve fibers length, therefore the nerve conduction delays from the brains. This delay is in particular challenging for birds, as bipedalism requires balancing at all time. The LSO located in the lower part of the spine can circumvent the nerve conduction delays by providing fast state feedback directly to the CPGs, enhancing fast response to perturbations. (2) In paleontology, it elucidates the locomotion capability of the ancestors of birds—dinosaurs. Due to giant body size and therefore extended nerve length, these ancient animals may not be able to run or even walk fast. Since multiple fossil records of dinosaurs suggest a similar structure of LSO, the LSO likely plays an important role in evolutionary success. (3) In engineering, it motivates future bio-inspired accelerometer designs. Conventional accelerometers are based on the capacitance variation of a tiny moving structure in a silicon chip. In comparison, the LSO shows distinct morphology and design. Understanding its acceleration sensing mechanism can inspire new engineering solutions.

Validating the accelerometer hypothesis requires multiple difficult steps, including measurement of the LSO morphologies and material properties, quantifying the LSO mechanics during locomotion, understanding how the mechanosensing signal is produced, and learning the mapping between the mechanosensing signal and accelerations. In the work of Chapter 5, I focus on the LSO mechanics. As the spinal soft tissue is contained in the fused spinal bone canal, in vivo measurement of the spinal cord movement is extremely difficult. Alternatively, I rely on biophysical simulation. This technique allows me to study how individual LSO structure affects the spinal soft tissue entrainment in a control environment. While the biophysical simulation offers only indirect measurement, it is sufficient to provide insights on the underlining mechanics, specifically the mass-spring-damper behavior. The results from Chapter 5 confirm the strong influence of the spinal canal morphology, which differs among birds from different habitats and locomotion modalities. Hence, the living environment likely

shapes the LSO design and sensitivity.

From my perspective, for large animals and fast locomotion, the mid-level control is essential. The fastest low-level response in mechanics can partially compensate the disturbance, where the rest disturbance should be regulated over the next several steps by mid-level control. The high-level control in brain performs the best for generalizing complex tasks, rather than consciously and constantly controlling individual muscles fibers. The mid-level control loop in spine is suitable for controlling rhythmic locomotion while exploiting sensing information for improved robustness. Here, the CPG and LSO support the middle layer of the hierarchical control architecture (Section 1.1).

6.4 Conclusion and outlook

Coming back to the initial question in introduction: is robot's control really faster than animal's? By providing a full picture of hierarchical control (Section 1.1), I demonstrate that animals have fast reaction speed comparable to the robots', through low-level (intrinsic mechanics, Section 1.2) and mid-level control (spinal control, Section 1.3). Given similar reaction speed, animal legged locomotion outperforms robot's easily, indicating that robust locomotion demands not only fast response, but also the correct response to interact with the environment.

In this thesis, via biorobotic implementations, I present several key components that contribute to a fast and correct response for robust legged locomotion. The low-level components include elasticity and damping. The series and parallel elasticity embedded in the leg structure shape the passive compliant behavior, which can be leverage by a simple open-loop CPG controller to improve hopping performance (Chapter 3). After identifying the most effective damping to be viscous and tunable (Chapter 2), a bio-inspired slack-based tunable damping mechanism is proposed, which can improve hopping robustness under different perturbations (Chapter 4). The mid-level components include the CPG and the LSO. While the CPG alone can generate rhythmic limb movement, the LSO potentially provides in-time state feedback to modify the CPG output to compensate for perturbations. The work in Chapter 5 supports the accelerometer function hypothesis of the LSO.

For the further understanding of animal/robot legged locomotion, a comprehensive legged system is necessary. While this thesis highlights that elasticity, damping, CPG and LSO contribute to fast sensing and adaptive actuation individually, the interplay between these elements and different control layers remains unexplored. I believe a future system integration of all elements will foster our understanding of robust and agile legged locomotion.

Bibliography

- [1] A. Mo, F. Izzi, D. F. Haeufle, *et al.*, “Effective viscous damping enables morphological computation in legged locomotion,” *Frontiers in Robotics and AI*, vol. 7, p. 110, 2020. DOI: [10.3389/frobt.2020.00110](https://doi.org/10.3389/frobt.2020.00110).
- [2] M. Bolignari, A. Mo, M. Fontana, *et al.*, “Diaphragm ankle actuation for efficient series elastic legged robot hopping,” in *2022 IEEE/RSJ International Conference on Intelligent Robots and Systems (IROS)*, IEEE, 2022, pp. 4279–4286. DOI: [10.1109/IROS47612.2022.9981060](https://doi.org/10.1109/IROS47612.2022.9981060).
- [3] A. Mo, F. Izzi, E. C. Gönen, *et al.*, “Slack-based tunable damping leads to a trade-off between robustness and efficiency in legged locomotion,” *Scientific Reports*, vol. 13, no. 1, p. 3290, 2023. DOI: [10.1038/s41598-023-30318-3](https://doi.org/10.1038/s41598-023-30318-3).
- [4] A. Mo, V. Kamska, F. Bribiesca-Contreras, *et al.*, “Biophysical simulation reveals the mechanics of the avian lumbosacral organ,” *arxiv*, Dec. 2022. DOI: [10.48550/arXiv.2212.11485](https://doi.org/10.48550/arXiv.2212.11485).
- [5] A. M. Wilson, T. Y. Hubel, S. D. Wilshin, *et al.*, “Biomechanics of predator–prey arms race in lion, zebra, cheetah and impala,” *Nature*, vol. 554, no. 7691, pp. 183–188, 2018. DOI: [10.1038/nature25479](https://doi.org/10.1038/nature25479).
- [6] M. A. Daley, J. R. Usherwood, G. Felix, *et al.*, “Running over rough terrain: Guinea fowl maintain dynamic stability despite a large unexpected change in substrate height,” *J Exp Biol*, vol. 209, no. 1, pp. 171–187, 2006. DOI: [10.1242/jeb.01986](https://doi.org/10.1242/jeb.01986).
- [7] V. A. Tucker, “The energetic cost of moving about: Walking and running are extremely inefficient forms of locomotion. much greater efficiency is achieved by birds, fish—and bicyclists,” *American Scientist*, vol. 63, no. 4, pp. 413–419, 1975.
- [8] H. L. More and J. M. Donelan, “Scaling of sensorimotor delays in terrestrial mammals,” *Proc. R. Soc. B*, vol. 285, no. 1885, p. 20180613, Aug. 2018. DOI: [10.1098/rspb.2018.0613](https://doi.org/10.1098/rspb.2018.0613).
- [9] L. D. Maes, M. Herbin, R. Hackert, *et al.*, “Steady locomotion in dogs: temporal and associated spatial coordination patterns and the effect of speed,” *Journal of Experimental Biology*, vol. 211, no. 1, pp. 138–149, Jan. 2008. DOI: [10.1242/jeb.008243](https://doi.org/10.1242/jeb.008243), eprint: <https://journals.biologists.com/jeb/article-pdf/211/1/138/1262882/138.pdf>.

- [10] H. L. More, J. R. Hutchinson, D. F. Collins, *et al.*, “Scaling of Sensorimotor Control in Terrestrial Mammals,” *Proceedings of the Royal Society B: Biological Sciences*, vol. 277, no. 1700, pp. 3563–3568, 2010. DOI: [10.1098/rspb.2010.0898](https://doi.org/10.1098/rspb.2010.0898).
- [11] J. Van Why, C. Hubicki, M. Jones, *et al.*, “Running into a trap: Numerical design of task-optimal reflex behaviors for delayed disturbance responses,” in *2014 IEEE/RSJ International Conference on Intelligent Robots and Systems*, IEEE, 2014, pp. 2537–2542. DOI: [10.1109/IRROS.2014.6942908](https://doi.org/10.1109/IRROS.2014.6942908).
- [12] D. J. Hyun, S. Seok, J. Lee, *et al.*, “High speed trot-running: Implementation of a hierarchical controller using proprioceptive impedance control on the mit cheetah,” *The International Journal of Robotics Research*, vol. 33, no. 11, pp. 1417–1445, 2014. DOI: [10.1177/0278364914532150](https://doi.org/10.1177/0278364914532150).
- [13] F. Grimminger, A. Meduri, M. Khadiv, *et al.*, “An Open Force-Controlled Modular Robot Architecture for Legged Locomotion Research,” *The IEEE Robotics and Automation Letters*, 2020. DOI: [10.1109/LRA.2020.2976639](https://doi.org/10.1109/LRA.2020.2976639).
- [14] C. Pennycuik and M. A. REZENDE, “The specific power output of aerobic muscle, related to the power density of mitochondria,” *Journal of Experimental Biology*, vol. 108, no. 1, pp. 377–392, 1984. DOI: [10.1242/jeb.108.1.377](https://doi.org/10.1242/jeb.108.1.377).
- [15] D. Böning, N. Maassen, and M. Steinach, “The efficiency of muscular exercise,” *Dtsch Z Sportmed*, vol. 68, pp. 203–214, 2017. DOI: [10.5960/dzsm.2017.295](https://doi.org/10.5960/dzsm.2017.295).
- [16] J. C. Gordon, N. C. Holt, A. Biewener, *et al.*, “Tuning of feedforward control enables stable muscle force-length dynamics after loss of autogenic proprioceptive feedback,” *eLife*, vol. 9, K. VijayRaghavan, N. J. Cowan, and L. H. Ting, Eds., e53908, Jun. 2020. DOI: [10.7554/eLife.53908](https://doi.org/10.7554/eLife.53908).
- [17] I. E. Brown and G. E. Loeb, “A reductionist approach to creating and using neuromusculoskeletal models,” in *Biomechanics and neural control of posture and movement*, Springer, 2000, pp. 148–163. DOI: [10.1007/978-1-4612-2104-3_10](https://doi.org/10.1007/978-1-4612-2104-3_10).
- [18] T. Lam and K. G. Pearson, “The role of proprioceptive feedback in the regulation and adaptation of locomotor activity,” *Sensorimotor control of movement and posture*, pp. 343–355, 2002. DOI: [10.1007/978-1-4615-0713-0_40](https://doi.org/10.1007/978-1-4615-0713-0_40).
- [19] G. E. Loeb, I. E. Brown, and E. J. Cheng, “A hierarchical foundation for models of sensorimotor control,” *Experimental Brain Research*, vol. 126, no. 1, pp. 1–18, 1999. DOI: [10.1007/s002210050712](https://doi.org/10.1007/s002210050712).
- [20] A. J. Ijspeert, “Central pattern generators for locomotion control in animals and robots: A review,” *Neural Networks*, vol. 21, no. 4, pp. 642–653, 2008. DOI: [10.1016/j.neunet.2008.03.014](https://doi.org/10.1016/j.neunet.2008.03.014).
- [21] R. M. Alexander, *Principles of animal locomotion*. Princeton University Press, 2003.
- [22] M. H. Dickinson, C. T. Farley, R. J. Full, *et al.*, “How animals move: An integrative view,” *science*, vol. 288, no. 5463, pp. 100–106, 2000. DOI: [10.1126/science.288.5463.100](https://doi.org/10.1126/science.288.5463.100).

- [23] M. Hutter, C. Gehring, D. Jud, *et al.*, “Anymal - a highly mobile and dynamic quadrupedal robot,” *2016 Ieee/Rsj International Conference on Intelligent Robots and Systems (Iros 2016)*, pp. 38–44, 2016. DOI: [10.1109/IRoS.2016.7758092](https://doi.org/10.1109/IRoS.2016.7758092).
- [24] G. Bledt, M. J. Powell, B. Katz, *et al.*, “Mit cheetah 3: Design and control of a robust, dynamic quadruped robot,” in *2018 IEEE/RSJ International Conference on Intelligent Robots and Systems (IROS)*, IEEE, 2018, pp. 2245–2252. DOI: [10.1109/IRoS.2018.8593885](https://doi.org/10.1109/IRoS.2018.8593885).
- [25] R. J. Full and D. E. Koditschek, “Templates and anchors: Neuromechanical hypotheses of legged locomotion on land,” *Journal of experimental biology*, vol. 202, no. 23, pp. 3325–3332, 1999. DOI: [10.1242/jeb.202.23.3325](https://doi.org/10.1242/jeb.202.23.3325).
- [26] R. Pfeifer and J. Bongard, *How the body shapes the way we think: a new view of intelligence*. MIT press, 2006. DOI: [10.7551/mitpress/3585.001.0001](https://doi.org/10.7551/mitpress/3585.001.0001).
- [27] K. Zahedi and N. Ay, “Quantifying morphological computation,” *Entropy*, vol. 15, pp. 1887–1915, 2013. DOI: [10.3390/e15051887](https://doi.org/10.3390/e15051887). arXiv: [arXiv:1301.6975v1](https://arxiv.org/abs/1301.6975v1).
- [28] H. Hauser, A. J. Ijspeert, R. M. Füchslin, *et al.*, “Towards a theoretical foundation for morphological computation with compliant bodies,” *Biological cybernetics*, vol. 105, pp. 355–370, 2011. DOI: [10.1007/s00422-012-0471-0](https://doi.org/10.1007/s00422-012-0471-0).
- [29] K. Ghazi-Zahedi, D. F. B. Haeufle, G. Montúfar, *et al.*, “Evaluating Morphological Computation in Muscle and DC-motor Driven Models of Human Hopping,” *Frontiers in Robotics and AI*, vol. 3, no. July, pp. 1–10, 2016. DOI: [10.3389/frobt.2016.00042](https://doi.org/10.3389/frobt.2016.00042). arXiv: [1512.00250](https://arxiv.org/abs/1512.00250).
- [30] R. J. Wootton, “Functional morphology of insect wings,” *Annual review of entomology*, vol. 37, no. 1, pp. 113–140, 1992. DOI: [10.1146/annurev.en.37.010192.000553](https://doi.org/10.1146/annurev.en.37.010192.000553).
- [31] T. McGeer *et al.*, “Passive dynamic walking,” *Int. J. Robotics Res.*, vol. 9, no. 2, pp. 62–82, 1990. DOI: [10.1177/027836499000900206](https://doi.org/10.1177/027836499000900206).
- [32] S. Collins, A. Ruina, R. Tedrake, *et al.*, “Efficient bipedal robots based on passive-dynamic walkers,” *Science*, vol. 307, no. 5712, pp. 1082–1085, 2005. DOI: [10.1126/science.1107799](https://doi.org/10.1126/science.1107799).
- [33] P. A. Bhounsule, J. Cortell, A. Grewal, *et al.*, “Low-bandwidth reflex-based control for lower power walking: 65 km on a single battery charge,” *The International Journal of Robotics Research*, vol. 33, no. 10, pp. 1305–1321, 2014. DOI: [10.1177/0278364914527485](https://doi.org/10.1177/0278364914527485).
- [34] D. Owaki, M. Koyama, S. Yamaguchi, *et al.*, “A 2-d passive-dynamic-running biped with elastic elements,” *IEEE Transactions on Robotics*, vol. 27, no. 1, pp. 156–162, 2011. DOI: [10.1109/TR0.2010.2098610](https://doi.org/10.1109/TR0.2010.2098610).
- [35] T. J. Roberts, R. L. Marsh, P. G. Weyand, *et al.*, “Muscular force in running turkeys: The economy of minimizing work,” *Science*, vol. 275, no. 5303, pp. 1113–1115, 1997. DOI: [10.1126/science.275.5303.1113](https://doi.org/10.1126/science.275.5303.1113).
- [36] R. M. Alexander and A. Vernon, “The mechanics of hopping by kangaroos (macropodidae),” *Journal of Zoology*, vol. 177, no. 2, pp. 265–303, 1975.

- [37] A. Wu and H. Geyer, “The 3-d spring-mass model reveals a time-based deadbeat control for highly robust running and steering in uncertain environments,” *IEEE Transactions on Robotics*, vol. 29, no. 5, pp. 1114–1124, 2013. DOI: [10.1109/TR0.2013.2263718](https://doi.org/10.1109/TR0.2013.2263718).
- [38] S. Heim and A. Spröwitz, “Beyond basins of attraction: Quantifying robustness of natural dynamics,” *IEEE Transactions on Robotics*, vol. 35, no. 4, pp. 939–952, 2019. DOI: [10.1109/TR0.2019.2910739](https://doi.org/10.1109/TR0.2019.2910739).
- [39] S. Mochon and T. A. McMahon, “Ballistic walking: An improved model,” *Mathematical Biosciences*, vol. 52, no. 3-4, pp. 241–260, 1980. DOI: [10.1016/0025-5564\(80\)90070-X](https://doi.org/10.1016/0025-5564(80)90070-X).
- [40] R. Blickhan, “The spring-mass model for running and hopping,” *Journal of biomechanics*, vol. 22, no. 11-12, pp. 1217–1227, 1989. DOI: [10.1016/0021-9290\(89\)90224-8](https://doi.org/10.1016/0021-9290(89)90224-8).
- [41] R. Blickhan, A. Seyfarth, H. Geyer, *et al.*, “Intelligence by mechanics,” *Philosophical Transactions of the Royal Society of London, Series A*, vol. 365, no. 1850, pp. 199–220, 2007. DOI: [10.1098/rsta.2006.1911](https://doi.org/10.1098/rsta.2006.1911).
- [42] H. Geyer, A. Seyfarth, and R. Blickhan, “Compliant leg behaviour explains basic dynamics of walking and running,” *Proceedings of the Royal Society B: Biological Sciences*, vol. 273, no. 1603, pp. 2861–2867, 2006. DOI: [10.1098/rspb.2006.3637](https://doi.org/10.1098/rspb.2006.3637).
- [43] Z. Gan, T. Wiestner, M. A. Weishaupt, *et al.*, “Passive dynamics explain quadrupedal walking, trotting, and tölting,” *Journal of computational and nonlinear dynamics*, vol. 11, no. 2, 2016.
- [44] A. V. Hill, “The heat of shortening and the dynamic constants of muscle,” *Proceedings of the Royal Society of London. Series B*, vol. 126, no. 843, pp. 136–195, 1938. DOI: [10.1098/rspb.1938.0050](https://doi.org/10.1098/rspb.1938.0050).
- [45] A. F. Huxley, “Muscle structure and theories of contraction,” *Progress in biophysics and biophysical chemistry*, vol. 7, pp. 256–319, 1957. DOI: [10.1016/S0096-4174\(18\)30128-8](https://doi.org/10.1016/S0096-4174(18)30128-8).
- [46] M. Günther and S. Schmitt, “A macroscopic ansatz to deduce the Hill relation,” *Journal of theoretical biology*, vol. 263, no. 4, pp. 407–18, 2010. DOI: [10.1016/j.jtbi.2009.12.027](https://doi.org/10.1016/j.jtbi.2009.12.027).
- [47] M. Raibert, *Legged Robots that Balance*, ser. Artificial Intelligence Series. MIT Press, 1986. DOI: [10.1109/MEX.1986.4307016](https://doi.org/10.1109/MEX.1986.4307016).
- [48] A. Badri-Spröwitz, A. Aghamaleki Sarvestani, M. Sitti, *et al.*, “Birdbot achieves energy-efficient gait with minimal control using avian-inspired leg clutching,” *Science Robotics*, vol. 7, no. 64, eabg4055, 2022. DOI: [10.1126/scirobotics.abg4055](https://doi.org/10.1126/scirobotics.abg4055).
- [49] U. Saranli, M. Buehler, and D. E. Koditschek, “Rhex: A simple and highly mobile hexapod robot,” *The International Journal of Robotics Research*, vol. 20, no. 7, pp. 616–631, 2001. DOI: [10.1177/02783640122067570](https://doi.org/10.1177/02783640122067570).
- [50] G. Zhao, O. Mohseni, M. Murcia, *et al.*, “Exploring the effects of serial and parallel elasticity on a hopping robot,” *Frontiers in Neurorobotics*, 2022. DOI: [10.3389/fnbot.2022.919830](https://doi.org/10.3389/fnbot.2022.919830).

- [51] A. Spröwitz, A. Tuleu, M. Vespignani, *et al.*, “Towards dynamic trot gait locomotion: Design, control, and experiments with cheetah-cub, a compliant quadruped robot,” *The International Journal of Robotics Research*, vol. 32, no. 8, pp. 932–950, 2013. DOI: [10.1177/0278364913489205](https://doi.org/10.1177/0278364913489205)
- [52] C. Hubicki, J. Grimes, M. Jones, *et al.*, “Atrias: Design and validation of a tether-free 3d-capable spring-mass bipedal robot,” *The International Journal of Robotics Research*, vol. 35, no. 12, pp. 1497–1521, 2016. DOI: [10.1177/0278364916648388](https://doi.org/10.1177/0278364916648388)
- [53] M. S. Ashtiani, A. Aghamaleki Sarvestani, and A. Badri-Spröwitz, “Hybrid parallel compliance allows robots to operate with sensorimotor delays and low control frequencies,” *Frontiers in Robotics and AI*, p. 170, 2021. DOI: [10.3389/frobt.2021.645748](https://doi.org/10.3389/frobt.2021.645748)
- [54] M. Hutter, C. Gehring, M. Bloesch, *et al.*, “Starleth: A compliant quadrupedal robot for fast, efficient, and versatile locomotion,” in *Adaptive Mobile Robotics*, World Scientific, 2012, pp. 483–490. DOI: [10.1142/9789814415958_0062](https://doi.org/10.1142/9789814415958_0062)
- [55] C. Semini, V. Barasuol, T. Boaventura, *et al.*, “Towards versatile legged robots through active impedance control,” *The International Journal of Robotics Research*, vol. 34, no. 7, pp. 1003–1020, 2015. DOI: [10.1177/0278364915578839](https://doi.org/10.1177/0278364915578839)
- [56] J. Rummel and A. Seyfarth, “Stable Running with Segmented Legs,” *The International Journal of Robotics Research*, 2008. DOI: [10.1177/0278364908095136](https://doi.org/10.1177/0278364908095136)
- [57] J. Rummel, F. Iida, J. A. Smith, *et al.*, “Enlarging regions of stable running with segmented legs,” in *2008 IEEE International Conference on Robotics and Automation*, IEEE, 2008, pp. 367–372. DOI: [10.1109/ROBOT.2008.4543235](https://doi.org/10.1109/ROBOT.2008.4543235)
- [58] D. Owaki and A. Ishiguro, “Enhancing stability of a passive dynamic running biped by exploiting a nonlinear spring,” in *2006 IEEE/RSJ International Conference on Intelligent Robots and Systems*, IEEE, 2006, pp. 4923–4928. DOI: [10.1109/IR0S.2006.282452](https://doi.org/10.1109/IR0S.2006.282452)
- [59] J. D. Karssen and M. Wisse, “Running with improved disturbance rejection by using non-linear leg springs,” *The International Journal of Robotics Research*, vol. 30, no. 13, pp. 1585–1595, 2011. DOI: [10.1177/0278364911408631](https://doi.org/10.1177/0278364911408631)
- [60] A. N. Ahn and R. J. Full, “A motor and a brake: two leg extensor muscles acting at the same joint manage energy differently in a running insect.,” *The Journal of Experimental Biology*, vol. 205, no. Pt 3, pp. 379–389, Feb. 2002. DOI: [10.1242/jeb.205.3.379](https://doi.org/10.1242/jeb.205.3.379)
- [61] X. Xiong, P. Manoonpong, *et al.*, “Muscles can be brakes: The work loop technique for stable muscle-like control,” in *9th International Symposium on Adaptive Motion of Animals and Machines (AMAM 2019)*, 2019.
- [62] R. K. Josephson, “Dissecting muscle power output,” *Journal of Experimental Biology*, vol. 202, no. 23, pp. 3369–3375, 1999. DOI: [10.1242/jeb.202.23.3369](https://doi.org/10.1242/jeb.202.23.3369)

- [63] M. Araz, S. Weidner, F. Izzi, *et al.*, “Muscle reflex response to perturbations in locomotion: In-vitro experiments and simulations with realistic boundary conditions,” *bioRxiv*, 2023. DOI: [10.1101/2023.02.15.528662](https://doi.org/10.1101/2023.02.15.528662).
- [64] A. A. Biewener, “Locomotion as an emergent property of muscle contractile dynamics,” *Journal of Experimental Biology*, vol. 219, no. 2, pp. 285–294, 2016. DOI: [10.1242/jeb.123935](https://doi.org/10.1242/jeb.123935).
- [65] D. F. B. Haeufle, S. Grimmer, and A. Seyfarth, “The role of intrinsic muscle properties for stable hopping - stability is achieved by the force-velocity relation,” *Bioinspiration & Biomimetics*, vol. 5, no. 1, p. 016 004, 2010. DOI: [10.1088/1748-3182/5/1/016004](https://doi.org/10.1088/1748-3182/5/1/016004).
- [66] M. Günther, S. Schmitt, and V. Wank, “High-frequency oscillations as a consequence of neglected serial damping in Hill-type muscle models,” *Biological Cybernetics*, vol. 97, no. 1, pp. 63–79, 2007. DOI: [10.1007/s00422-007-0160-6](https://doi.org/10.1007/s00422-007-0160-6).
- [67] A. M. Wilson, M. P. McGuigan, A. Su, *et al.*, “Horses damp the spring in their step,” *Nature*, vol. 414, no. 6866, pp. 895–899, 2001. DOI: [10.1038/414895a](https://doi.org/10.1038/414895a).
- [68] R. Müller, K. Tschiesche, and R. Blickhan, “Kinetic and kinematic adjustments during perturbed walking across visible and camouflaged drops in ground level,” *Journal of Biomechanics*, vol. 47, no. 10, pp. 2286–2291, Jul. 2014. DOI: [10.1016/j.jbiomech.2014.04.041](https://doi.org/10.1016/j.jbiomech.2014.04.041).
- [69] Z. Shen and J. Seipel, “A fundamental mechanism of legged locomotion with hip torque and leg damping,” *Bioinspiration & biomimetics*, vol. 7, no. 4, p. 046 010, 2012. DOI: [10.1088/1748-3182/7/4/046010](https://doi.org/10.1088/1748-3182/7/4/046010).
- [70] G. Secer and U. Saranlı, “Control of monopedal running through tunable damping,” in *2013 21st Signal Processing and Communications Applications Conference (SIU)*, IEEE, Apr. 2013, pp. 1–4. DOI: [10.1109/SIU.2013.6531557](https://doi.org/10.1109/SIU.2013.6531557).
- [71] I. Abraham, Z. Shen, and J. Seipel, “A Nonlinear Leg Damping Model for the Prediction of Running Forces and Stability,” *Journal of Computational and Nonlinear Dynamics*, vol. 10, no. 5, 2015. DOI: [10.1115/1.4028751](https://doi.org/10.1115/1.4028751).
- [72] K. T. Kalveram, D. F. B. Haeufle, A. Seyfarth, *et al.*, “Energy management that generates terrain following versus apex-preserving hopping in man and machine,” *Biological Cybernetics*, vol. 106, no. 1, pp. 1–13, 2012. DOI: [10.1007/s00422-012-0476-8](https://doi.org/10.1007/s00422-012-0476-8).
- [73] T. Cnops, Z. Gan, and C. D. Remy, “The basin of attraction for running robots: Fractals, multistep trajectories, and the choice of control,” in *2015 IEEE/RSJ International Conference on Intelligent Robots and Systems (IROS)*, IEEE, 2015, pp. 1586–1591. DOI: [10.1109/IROS.2015.7353579](https://doi.org/10.1109/IROS.2015.7353579).
- [74] D. F. B. Haeufle, M. Günther, G. Wunner, *et al.*, “Quantifying control effort of biological and technical movements: An information-entropy-based approach,” *Physical Review E*, vol. 89, no. 1, p. 012 716, 2014. DOI: [10.1103/PhysRevE.89.012716](https://doi.org/10.1103/PhysRevE.89.012716).

- [75] E. Garcia, J. C. Arevalo, G. Munoz, *et al.*, “Combining series elastic actuation and magneto-rheological damping for the control of agile locomotion,” *Robotics and Autonomous Systems*, vol. 59, no. 10, pp. 827–839, 2011. DOI: [10.1016/j.robot.2011.06.006](https://doi.org/10.1016/j.robot.2011.06.006).
- [76] S. S. Candan, U. Saranli, and Y. Yazicioglu, “Comparison of parallel elastic and series elastic configurations of vertical hopping spring mass model controlled with virtual tuning of damping,” in *International Design Engineering Technical Conferences and Computers and Information in Engineering Conference*, American Society of Mechanical Engineers, vol. 83914, 2020, V002T02A027.
- [77] G. Secer and U. Saranli, “Energy efficient control of a 1D hopper through tunable damping,” in *Dynamic Walking*, Aland, Island, 2017, p. 281.
- [78] S. Heim, M. Millard, C. Le Mouel, *et al.*, “A little damping goes a long way: A simulation study of how damping influences task-level stability in running,” *Biology Letters*, vol. 16, no. 9, p. 20200467, 2020. DOI: [10.1098/rsbl.2020.0467](https://doi.org/10.1098/rsbl.2020.0467).
- [79] K. D. Nguyen, N. Sharma, and M. Venkadesan, “Active viscoelasticity of sarcomeres,” *Frontiers in Robotics and AI*, vol. 5, p. 69, 2018. DOI: [10.3389/frobt.2018.00069](https://doi.org/10.3389/frobt.2018.00069).
- [80] G. Secer and U. Saranli, “Control of hopping through active virtual tuning of leg damping for serially actuated legged robots,” in *2014 IEEE International Conference on Robotics and Automation (ICRA)*, IEEE, 2014, pp. 4556–4561. DOI: [10.1109/ICRA.2014.6907524](https://doi.org/10.1109/ICRA.2014.6907524).
- [81] S. Monteleone, F. Negrello, M. G. Catalano, *et al.*, “Damping in compliant actuation: A review,” *IEEE Robotics & Automation Magazine*, vol. 29, no. 3, pp. 47–66, 2022. DOI: [10.1109/MRA.2021.3138388](https://doi.org/10.1109/MRA.2021.3138388).
- [82] H. Dallali, P. Kormushev, N. G. Tsagarakis, *et al.*, “Can active impedance protect robots from landing impact?” In *2014 IEEE-RAS International Conference on Humanoid Robots*, IEEE, 2014, pp. 1022–1027. DOI: [10.1109/HUMANOIDS.2014.7041490](https://doi.org/10.1109/HUMANOIDS.2014.7041490).
- [83] V. N. M. Arelekatti, N. T. Petelina, W. B. Johnson, *et al.*, “Design of a Four-Bar Latch Mechanism and a Shear-Based Rotary Viscous Damper for Single-Axis Prosthetic Knees,” *Journal of Mechanisms and Robotics*, vol. 14, no. 3, Nov. 2021. DOI: [10.1115/1.4052804](https://doi.org/10.1115/1.4052804).
- [84] V. M. Arelekatti, N. T. Petelina, W. B. Johnson, *et al.*, “Design of a passive, shear-based rotary hydraulic damper for single-axis prosthetic knees,” in *International Design Engineering Technical Conferences and Computers and Information in Engineering Conference*, American Society of Mechanical Engineers, vol. 51807, 2018, V05AT07A064. DOI: [10.1115/DETC2018-85962](https://doi.org/10.1115/DETC2018-85962).
- [85] F. Li, H. Xie, W. Yuan, *et al.*, “The application research of mr damper in intelligent bionic leg,” in *2009 Chinese Control and Decision Conference*, IEEE, 2009, pp. 1327–1331.
- [86] J. Xiao, S. Ma, J. Mo, *et al.*, “Design and experimental validation of a shock-absorption mechanism inspired from the frog’s forelimbs,” *IEEE Robotics and Automation Letters*, vol. 7, no. 2, pp. 2079–2085, 2022. DOI: [10.1109/LRA.2022.3142845](https://doi.org/10.1109/LRA.2022.3142845).

- [87] C. Zhang, X. Li, S. Zhang, *et al.*, “Design and experiment evaluation of a magneto-rheological damper for the legged robot,” in *2018 IEEE International Conference on Real-time Computing and Robotics (RCAR)*, IEEE, 2018, pp. 687–692. DOI: [10.1109/RCAR.2018.8621745](https://doi.org/10.1109/RCAR.2018.8621745).
- [88] Y. Jiang, Q. Li, and Z. An, “Design and analysis of a single adjustable damping force robotic leg working with magnetorheological technology,” in *Journal of Physics: Conference Series*, IOP Publishing, vol. 1887, 2021, p. 012014. DOI: [10.1088/1742-6596/1887/1/012014](https://doi.org/10.1088/1742-6596/1887/1/012014).
- [89] T. Oba, H. Kadone, M. Hassan, *et al.*, “Robotic ankle-foot orthosis with a variable viscosity link using mr fluid,” *IEEE/ASME Transactions on Mechatronics*, vol. 24, no. 2, pp. 495–504, 2019. DOI: [10.1109/TMECH.2019.2894406](https://doi.org/10.1109/TMECH.2019.2894406).
- [90] J. C. Dixon, *The shock absorber handbook*. John Wiley & Sons, 2008, pp. 276–277. DOI: [10.1002/9780470516430](https://doi.org/10.1002/9780470516430).
- [91] D. Więckowski, K. Dąbrowski, and G. Ślaski, “Adjustable shock absorber characteristics testing and modelling,” in *IOP Conference Series: Materials Science and Engineering*, IOP Publishing, vol. 421, 2018, p. 022039.
- [92] S. Rossignol, “Locomotion and its recovery after spinal injury,” *Current opinion in neurobiology*, vol. 10, no. 6, pp. 708–716, 2000. DOI: [10.1016/S0959-4388\(00\)00151-3](https://doi.org/10.1016/S0959-4388(00)00151-3).
- [93] D. M. Armstrong, “The supraspinal control of mammalian locomotion,” *The Journal of physiology*, vol. 405, p. 1, 1988. DOI: [10.1113/jphysiol.1988.sp017319](https://doi.org/10.1113/jphysiol.1988.sp017319).
- [94] J.-M. Cabelguen, C. Bourcier-Lucas, and R. Dubuc, “Bimodal locomotion elicited by electrical stimulation of the midbrain in the salamander *Notophthalmus viridescens*,” *Journal of Neuroscience*, vol. 23, no. 6, pp. 2434–2439, 2003.
- [95] S. Reschechtko and J. A. Pruszynski, “Stretch reflexes,” *Current Biology*, vol. 30, no. 18, R1025–R1030, 2020. DOI: [10.1016/j.cub.2020.07.092](https://doi.org/10.1016/j.cub.2020.07.092).
- [96] A. H. Cohen and P. Wallén, “The neuronal correlate of locomotion in fish: “fictive swimming” induced in an in vitro preparation of the lamprey spinal cord,” *Experimental brain research*, vol. 41, no. 1, pp. 11–18, 1980. DOI: [10.1007/BF00236674](https://doi.org/10.1007/BF00236674).
- [97] S. Grillner, “Neural control of vertebrate locomotion—central mechanisms and reflex interaction with special reference to the cat,” *Feedback and motor control in invertebrates and vertebrates*, pp. 35–56, 1985. DOI: [10.1007/978-94-011-7084-0_3](https://doi.org/10.1007/978-94-011-7084-0_3).
- [98] I. Delvolvé, P. Branchereau, R. Dubuc, *et al.*, “Fictive rhythmic motor patterns induced by nmda in an in vitro brain stem–spinal cord preparation from an adult urodele,” *Journal of Neurophysiology*, vol. 82, no. 2, pp. 1074–1077, 1999. DOI: [10.1152/jn.1999.82.2.1074](https://doi.org/10.1152/jn.1999.82.2.1074).
- [99] S. Soffe and A. Roberts, “Tonic and phasic synaptic input to spinal cord motoneurons during fictive locomotion in frog embryos,” *Journal of Neurophysiology*, vol. 48, no. 6, pp. 1279–1288, 1982. DOI: [10.1152/jn.1982.48.6.1279](https://doi.org/10.1152/jn.1982.48.6.1279).

- [100] S. Grillner, "Selection and initiation of motor behavior," *Neurons, networks, and motor behavior*, pp. 3–19, 1997.
- [101] M. L. Shik, "Control of walking and running by means of electrical stimulation of the midbrain," *Biophysics*, vol. 11, pp. 659–666, 1966.
- [102] S. Rossignol, R. Dubuc, and J.-P. Gossard, "Dynamic sensorimotor interactions in locomotion," *Physiological reviews*, vol. 86, no. 1, pp. 89–154, 2006. DOI: [10.1152/physrev.00028.2005](https://doi.org/10.1152/physrev.00028.2005).
- [103] A. D. McClellan and W. Jang, "Mechanosensory inputs to the central pattern generators for locomotion in the lamprey spinal cord: Resetting, entrainment, and computer modeling," *Journal of Neurophysiology*, vol. 70, no. 6, pp. 2442–2454, 1993. DOI: [10.1152/jn.1994.71.6.1-a](https://doi.org/10.1152/jn.1994.71.6.1-a).
- [104] G. V. Di Prisco, P. Walle, S. Grillner, *et al.*, "Synaptic effects of intraspinal stretch receptor neurons mediating movement-related feedback during locomotion," *Brain research*, vol. 530, no. 1, pp. 161–166, 1990. DOI: [10.1016/0006-8993\(90\)90675-2](https://doi.org/10.1016/0006-8993(90)90675-2).
- [105] T. L. Williams, K. A. Sigvardt, N. Kopell, *et al.*, "Forcing of coupled nonlinear oscillators: Studies of intersegmental coordination in the lamprey locomotor central pattern generator," *Journal of neurophysiology*, vol. 64, no. 3, pp. 862–871, 1990. DOI: [10.1152/jn.1990.64.3.862](https://doi.org/10.1152/jn.1990.64.3.862).
- [106] J. Hellgren, S. Grillner, and A. Lansner, "Computer simulation of the segmental neural network generating locomotion in lamprey by using populations of network interneurons," *Biological cybernetics*, vol. 68, no. 1, pp. 1–13, 1992. DOI: [10.1007/BF00203132](https://doi.org/10.1007/BF00203132).
- [107] H. Traven, L. Brodin, A. Lansner, *et al.*, "Computer simulations of nmda and non-nmda receptor-mediated synaptic drive: Sensory and supraspinal modulation of neurons and small networks," *Journal of neurophysiology*, vol. 70, no. 2, pp. 695–709, 1993. DOI: [10.1152/jn.1993.70.2.695](https://doi.org/10.1152/jn.1993.70.2.695).
- [108] J. T. Buchanan, "Neural network simulations of coupled locomotor oscillators in the lamprey spinal cord," *Biological cybernetics*, vol. 66, no. 4, pp. 367–374, 1992. DOI: [10.1007/BF00203673](https://doi.org/10.1007/BF00203673).
- [109] Ö. Ekeberg, "A combined neuronal and mechanical model of fish swimming," *Biological cybernetics*, vol. 69, no. 5-6, pp. 363–374, 1993. DOI: [10.1007/BF01185408](https://doi.org/10.1007/BF01185408).
- [110] A. H. Cohen, P. J. Holmes, and R. H. Rand, "The nature of the coupling between segmental oscillators of the lamprey spinal generator for locomotion: A mathematical model," *Journal of mathematical biology*, vol. 13, pp. 345–369, 1982. DOI: [10.1007/BF00276069](https://doi.org/10.1007/BF00276069).
- [111] A. J. Ijspeert, A. Crespi, D. Ryczko, *et al.*, "From swimming to walking with a salamander robot driven by a spinal cord model," *Science*, vol. 315, no. 5817, pp. 1416–1420, 2007. DOI: [10.1126/science.1138353](https://doi.org/10.1126/science.1138353).
- [112] A. J. Ijspeert, "A connectionist central pattern generator for the aquatic and terrestrial gaits of a simulated salamander," *Biological cybernetics*, vol. 84, no. 5, pp. 331–348, 2001. DOI: [10.1007/s004220000211](https://doi.org/10.1007/s004220000211).

- [113] C. Stefanini, G. Orlandi, A. Menciassi, *et al.*, “A mechanism for biomimetic actuation in lamprey-like robots,” in *The First IEEE/RAS-EMBS International Conference on Biomedical Robotics and Biomechanics, 2006. BioRob 2006.*, IEEE, 2006, pp. 579–584. DOI: [10.1109/BIOROB.2006.1639151](https://doi.org/10.1109/BIOROB.2006.1639151).
- [114] A. Crespi and A. J. Ijspeert, “Online optimization of swimming and crawling in an amphibious snake robot,” *IEEE Transactions on robotics*, vol. 24, no. 1, pp. 75–87, 2008. DOI: [10.1109/TR0.2008.915426](https://doi.org/10.1109/TR0.2008.915426).
- [115] J. Conradt and P. Varshavskaya, “Distributed central pattern generator control for a serpentine robot,” in *Proceedings of the International Conference on Artificial Neural Networks (ICANN)*, 2003, pp. 338–341.
- [116] Z. Lu, S. Ma, B. Li, *et al.*, “3d locomotion of a snake-like robot controlled by cyclic inhibitory cpg model,” in *2006 IEEE/RSJ International Conference on Intelligent Robots and Systems*, IEEE, 2006, pp. 3897–3902. DOI: [10.1109/IR0S.2006.281801](https://doi.org/10.1109/IR0S.2006.281801).
- [117] P. Manoonpong, F. Pasemann, and H. Roth, “Modular reactive neuro-control for biologically inspired walking machines,” *The International Journal of Robotics Research*, vol. 26, no. 3, pp. 301–331, 2007. DOI: [10.1177/0278364906076263](https://doi.org/10.1177/0278364906076263).
- [118] Y. Fukuoka, H. Kimura, and A. H. Cohen, “Adaptive dynamic walking of a quadruped robot on irregular terrain based on biological concepts,” *The International Journal of Robotics Research*, vol. 22, no. 3-4, pp. 187–202, 2003. DOI: [10.1177/0278364903022003004](https://doi.org/10.1177/0278364903022003004).
- [119] D. Owaki and A. Ishiguro, “A quadruped robot exhibiting spontaneous gait transitions from walking to trotting to galloping,” *Scientific reports*, vol. 7, no. 1, pp. 1–10, 2017. DOI: [10.1038/s41598-017-00348-9](https://doi.org/10.1038/s41598-017-00348-9).
- [120] B. Kiss, E. C. Gonen, A. Mo, *et al.*, “Gastrocnemius and power amplifier soleus spring-tendons achieve fast human-like walking in a bipedal robot,” in *2022 IEEE/RSJ International Conference on Intelligent Robots and Systems (IROS)*, IEEE, 2022, pp. 5202–5209. DOI: [10.1109/IR0S47612.2022.9981725](https://doi.org/10.1109/IR0S47612.2022.9981725).
- [121] G. Endo, J. Morimoto, T. Matsubara, *et al.*, “Learning cpg-based biped locomotion with a policy gradient method: Application to a humanoid robot,” *The International Journal of Robotics Research*, vol. 27, no. 2, pp. 213–228, 2008. DOI: [10.1177/0278364907084980](https://doi.org/10.1177/0278364907084980).
- [122] F. Ruppert and A. Badri-Spröwitz, “Learning plastic matching of robot dynamics in closed-loop central pattern generators,” *Nature Machine Intelligence*, vol. 4, no. 7, pp. 652–660, 2022. DOI: [10.1038/s42256-022-00505-4](https://doi.org/10.1038/s42256-022-00505-4).
- [123] N. Gravish and G. V. Lauder, “Robotics-inspired biology,” *Journal of Experimental Biology*, vol. 221, no. 7, jeb138438, 2018. DOI: [10.1242/jeb.138438](https://doi.org/10.1242/jeb.138438).
- [124] J. Aguilar, T. Zhang, F. Qian, *et al.*, “A review on locomotion robotics: The study of movement at the intersection of robotics, soft matter and dynamical systems,” *Reports on Progress in Physics*, vol. 79, no. 11, p. 110 001, 2016. DOI: [10.1088/0034-4885/79/11/110001](https://doi.org/10.1088/0034-4885/79/11/110001).

- [125] J. R. Rebula, P. D. Neuhaus, B. V. Bonnländer, *et al.*, “A controller for the littledog quadruped walking on rough terrain,” in *Proceedings 2007 IEEE International Conference on Robotics and Automation*, IEEE, 2007, pp. 1467–1473. DOI: [10.1109/ROBOT.2007.363191](https://doi.org/10.1109/ROBOT.2007.363191)
- [126] M. Raibert, K. Blankespoor, G. Nelson, *et al.*, “Bigdog, the rough-terrain quadruped robot,” *IFAC Proceedings Volumes*, vol. 41, no. 2, pp. 10 822–10 825, 2008. DOI: [10.3182/20080706-5-KR-1001.01833](https://doi.org/10.3182/20080706-5-KR-1001.01833).
- [127] M. Vukobratović and B. Borovac, “Zero-moment point—thirty five years of its life,” *International journal of humanoid robotics*, vol. 1, no. 01, pp. 157–173, 2004.
- [128] S. Kajita, F. Kanehiro, K. Kaneko, *et al.*, “Biped walking pattern generation by using preview control of zero-moment point,” in *2003 IEEE international conference on robotics and automation (Cat. No. 03CH37422)*, IEEE, vol. 2, 2003, pp. 1620–1626. DOI: [10.1109/ROBOT.2003.1241826](https://doi.org/10.1109/ROBOT.2003.1241826)
- [129] T. Koolen, T. De Boer, J. Rebula, *et al.*, “Capturability-based analysis and control of legged locomotion, part 1: Theory and application to three simple gait models,” *The international journal of robotics research*, vol. 31, no. 9, pp. 1094–1113, 2012. DOI: [10.1177/0278364912452673](https://doi.org/10.1177/0278364912452673).
- [130] J. Pratt, T. Koolen, T. De Boer, *et al.*, “Capturability-based analysis and control of legged locomotion, part 2: Application to m2v2, a lower-body humanoid,” *The international journal of robotics research*, vol. 31, no. 10, pp. 1117–1133, 2012. DOI: [10.1177/0278364912452762](https://doi.org/10.1177/0278364912452762).
- [131] J. Pratt, C.-M. Chew, A. Torres, *et al.*, “Virtual Model Control: An Intuitive Approach for Bipedal Locomotion,” *The International Journal of Robotics Research*, vol. 20, no. 2, pp. 129–143, 2001. DOI: [10.1177/02783640122067309](https://doi.org/10.1177/02783640122067309).
- [132] K. Sreenath, H.-W. Park, I. Poulakakis, *et al.*, “A compliant hybrid zero dynamics controller for stable, efficient and fast bipedal walking on mabel,” *The International Journal of Robotics Research*, vol. 30, no. 9, pp. 1170–1193, 2011. DOI: [10.1177/0278364910379882](https://doi.org/10.1177/0278364910379882).
- [133] E. R. Westervelt, J. W. Grizzle, and D. E. Koditschek, “Hybrid zero dynamics of planar biped walkers,” *IEEE transactions on automatic control*, vol. 48, no. 1, pp. 42–56, 2003. DOI: [10.1109/TAC.2002.806653](https://doi.org/10.1109/TAC.2002.806653).
- [134] S. Grillner, T. Williams, and P. A. Lagerback, “The edge cell, a possible intraspinal mechanoreceptor,” *Science*, vol. 223, no. 4635, pp. 500–503, Feb. 1984. DOI: [10.1126/science.6691161](https://doi.org/10.1126/science.6691161).
- [135] U. L. Böhm, A. Prendergast, L. Djenoune, *et al.*, “CSF-contacting neurons regulate locomotion by relaying mechanical stimuli to spinal circuits,” *Nature Communications*, vol. 7, no. 1, p. 10 866, Mar. 2016. DOI: [10.1038/ncomms10866](https://doi.org/10.1038/ncomms10866).
- [136] L. D. Picton, M. Bertuzzi, I. Pallucchi, *et al.*, “A spinal organ of proprioception for integrated motor action feedback,” *Neuron*, vol. 109, no. 7, pp. 1188–1201.e7, Apr. 2021. DOI: [10.1016/j.neuron.2021.01.018](https://doi.org/10.1016/j.neuron.2021.01.018).
- [137] D. M. Schroeder, “The marginal nuclei in the spinal cord of reptiles: Intraspinous mechanoreceptors,” *The Ohio Journal of Science*, vol. 86, no. 3, pp. 69–72, 1986.

- [138] R. Necker, "Specializations in the lumbosacral vertebral canal and spinal cord of birds: Evidence of a function as a sense organ which is involved in the control of walking," *Journal of Comparative Physiology A*, vol. 192, no. 5, p. 439, 2006. DOI: [10.1007/s00359-006-0105-x](https://doi.org/10.1007/s00359-006-0105-x).
- [139] K. E. Stanchak, C. French, D. J. Perkel, *et al.*, "The Balance Hypothesis for the Avian Lumbosacral Organ and an Exploration of Its Morphological Variation," *Integrative Organismal Biology*, vol. 2, no. obaa024, 2020. DOI: [10.1093/iob/obaa024](https://doi.org/10.1093/iob/obaa024).
- [140] V. Kamska, M. Daley, and A. Badri-Spröwitz, "3D Anatomy of the Quail Lumbosacral Spinal Canal—Implications for Putative Mechanosensory Function," *Integrative Organismal Biology*, vol. 2, no. obaa037, Jan. 2020. DOI: [10.1093/iob/obaa037](https://doi.org/10.1093/iob/obaa037).
- [141] A. Emmert, "Beobachtungen über einige anatomische eigenheiten der vögel," *Reil's Arch. Physiol.*, vol. 10, pp. 377–392, 1811.
- [142] G. L. Streeter, "The structure of the spinal cord of the ostrich," *American Journal of Anatomy*, vol. 3, no. 1, pp. 1–27, 1904. DOI: [10.1002/aj.a.1000030102](https://doi.org/10.1002/aj.a.1000030102).
- [143] T. Terni, *Ricerche sulla cosiddetta sostanza gelatinosa (corpo glicogenico) del midollo lombo-sacrale degli uccelli...* L. Niccolai, 1924.
- [144] R. L. Watterson and B. E. N. Spiroff, "Development of the Glycogen Body of the Chick Spinal Cord. II. Effects of Unilateral and Bilateral Leg-Bud Extirpation," *Physiological Zoology*, vol. 22, no. 4, pp. 318–337, Oct. 1949. DOI: [10.2307/30152058](https://doi.org/10.2307/30152058).
- [145] L. D. De Gennaro, "The carbohydrate composition of the glycogen body of the chick embryo as revealed by paper chromatography," *The Biological Bulletin*, vol. 120, no. 3, pp. 348–352, 1961. DOI: [10.2307/1539536](https://doi.org/10.2307/1539536).
- [146] I. Azcoitia, J. Fernandez-Soriano, and B. Fernandez-Ruiz, "Is the avian glycogen body a secretory organ?" *Journal fur Hirnforschung*, vol. 26, no. 6, pp. 651–657, 1985.
- [147] D. M. Schroeder and R. G. Murray, "Specializations within the lumbosacral spinal cord of the pigeon," *Journal of Morphology*, vol. 194, no. 1, pp. 41–53, 1987. DOI: [10.1002/jmor.1051940104](https://doi.org/10.1002/jmor.1051940104).
- [148] R. Necker, "Head-bobbing of walking birds," *Journal of comparative physiology A*, vol. 193, no. 12, p. 1177, 2007. DOI: [10.1007/s00359-007-0281-3](https://doi.org/10.1007/s00359-007-0281-3).
- [149] R. Necker, A. Janßen, and T. Beissenhirtz, "Behavioral evidence of the role of lumbosacral anatomical specializations in pigeons in maintaining balance during terrestrial locomotion," *Journal of Comparative Physiology A*, vol. 186, no. 4, pp. 409–412, Apr. 2000. DOI: [10.1007/s003590050440](https://doi.org/10.1007/s003590050440).
- [150] R. Necker, "The structure and development of avian lumbosacral specializations of the vertebral canal and the spinal cord with special reference to a possible function as a sense organ of equilibrium," *Anatomy and Embryology*, vol. 210, no. 1, pp. 59–74, Aug. 2005. DOI: [10.1007/s00429-005-0016-6](https://doi.org/10.1007/s00429-005-0016-6).

- [151] J. Rosenberg and R. Necker, "Ultrastructural characterization of the accessory lobes of lachi in the lumbosacral spinal cord of the pigeon with special reference to intrinsic mechanoreceptors," *Journal of Comparative Neurology*, vol. 447, no. 3, pp. 274–285, 2002. DOI: [10.1002/cne.10240](https://doi.org/10.1002/cne.10240).
- [152] A. L. Eide, "The axonal projections of the Hofmann nuclei in the spinal cord of the late stage chicken embryo," *Anatomy and Embryology*, vol. 193, no. 6, pp. 543–557, Jun. 1996. DOI: [10.1007/BF00187926](https://doi.org/10.1007/BF00187926).
- [153] A. L. Eide and J. C. Glover, "Development of an Identified Spinal Commissural Interneuron Population in an Amniote: Neurons of the Avian Hofmann Nuclei," *The Journal of Neuroscience*, vol. 16, no. 18, pp. 5749–5761, Sep. 1996. DOI: [10.1523/JNEUROSCI.16-18-05749.1996](https://doi.org/10.1523/JNEUROSCI.16-18-05749.1996).
- [154] Y. Yamanaka, N. Kitamura, and I. Shibuya, "Chick spinal accessory lobes contain functional neurons expressing voltagegated sodium channels generating action potentials," *Biomedical Research*, vol. 29, no. 4, pp. 205–211, 2008. DOI: [10.2220/biomedres.29.205](https://doi.org/10.2220/biomedres.29.205).
- [155] Y. Yamanaka, N. Kitamura, H. Shinohara, *et al.*, "Analysis of GABA-induced inhibition of spontaneous firing in chick accessory lobe neurons," *Journal of Comparative Physiology A*, vol. 198, no. 3, pp. 229–237, 2012. DOI: [10.1007/s00359-011-0703-0](https://doi.org/10.1007/s00359-011-0703-0).
- [156] —, "Glutamate evokes firing through activation of kainate receptors in chick accessory lobe neurons," *Journal of Comparative Physiology A*, vol. 199, no. 1, pp. 35–43, Jan. 2013. DOI: [10.1007/s00359-012-0766-6](https://doi.org/10.1007/s00359-012-0766-6).
- [157] Y. Matsushita, N. Kitamura, M. Higuchi, *et al.*, "Neuron-like cells in the chick spinal accessory lobe express neuronal-type voltage-gated sodium channels," *Biomedical research (Tokyo, Japan)*, vol. 39, no. 4, pp. 189–196, 2018. DOI: [10.2220/biomedres.39.189](https://doi.org/10.2220/biomedres.39.189).
- [158] K. E. Stanchak, K. E. Miller, E. W. Lumsden, *et al.*, "Molecular markers of mechanosensation in glycinergic neurons in the avian lumbosacral spinal cord," *eNeuro*, Aug. 2022. DOI: [10.1523/ENEURO.0100-22.2022](https://doi.org/10.1523/ENEURO.0100-22.2022).
- [159] L. Allen, A. O'Connell, and V. Kiermer, "How can we ensure visibility and diversity in research contributions? how the contributor role taxonomy (credit) is helping the shift from authorship to contributorship," *Learned Publishing*, vol. 32, no. 1, pp. 71–74, 2019. DOI: [10.1002/leap.1210](https://doi.org/10.1002/leap.1210).

Appendix

The appendix includes the following:

Accepted publications

A. Mo, F. Izzi, D. F. Haeufle, and A. Badri-Spröwitz, “Effective viscous damping enables morphological computation in legged locomotion,” *Frontiers in Robotics and AI*, vol. 7, p. 110, 2020. DOI: [10.3389/frobt.2020.00110](https://doi.org/10.3389/frobt.2020.00110)

M. Bolignari, A. Mo, M. Fontana, and A. Badri-Spröwitz, “Diaphragm ankle actuation for efficient series elastic legged robot hopping,” in *2022 IEEE/RSJ International Conference on Intelligent Robots and Systems (IROS)*, IEEE, 2022, pp. 4279–4286. DOI: [10.1109/IR0S47612.2022.9981060](https://doi.org/10.1109/IR0S47612.2022.9981060)

A. Mo, F. Izzi, E. C. Gönen, D. Haeufle, and A. Badri-Spröwitz, “Slack-based tunable damping leads to a trade-off between robustness and efficiency in legged locomotion,” *Scientific Reports*, vol. 13, no. 1, p. 3290, 2023. DOI: [10.1038/s41598-023-30318-3](https://doi.org/10.1038/s41598-023-30318-3)

Submitted manuscript

A. Mo, V. Kamska, F. Bribiesca-Contreras, J. Hauptmann, M. Daley, and A. Badri-Spröwitz, “Biophysical simulation reveals the mechanics of the avian lumbosacral organ,” *arXiv*, Dec. 2022. DOI: [10.48550/arXiv.2212.11485](https://doi.org/10.48550/arXiv.2212.11485)

Curriculum Vitae



Effective Viscous Damping Enables Morphological Computation in Legged Locomotion

An Mo¹, Fabio Izzi^{1,2}, Daniel F. B. Haeufle^{2,3} and Alexander Badri-Spröwitz^{2*}

¹Dynamic Locomotion Group, Max Planck Institute for Intelligent Systems, Stuttgart, Germany, ²Multi-Level Modeling in Motor Control and Rehabilitation Robotics, Hertie-Institute for Clinical Brain Research, University of Tübingen, Tübingen, Germany, ³Centre for Integrative Neuroscience, University of Tübingen, Tübingen, Germany

Muscle models and animal observations suggest that physical damping is beneficial for stabilization. Still, only a few implementations of physical damping exist in compliant robotic legged locomotion. It remains unclear how physical damping can be exploited for locomotion tasks, while its advantages as sensor-free, adaptive force- and negative work-producing actuators are promising. In a simplified numerical leg model, we studied the energy dissipation from viscous and Coulomb damping during vertical drops with ground-level perturbations. A parallel spring- damper is engaged between touch-down and mid-stance, and its damper auto-deouples from mid-stance to takeoff. Our simulations indicate that an adjustable and viscous damper is desired. In hardware we explored effective viscous damping and adjustability, and quantified the dissipated energy. We tested two mechanical, leg-mounted damping mechanisms: a commercial hydraulic damper, and a custom-made pneumatic damper. The pneumatic damper exploits a rolling diaphragm with an adjustable orifice, minimizing Coulomb damping effects while permitting adjustable resistance. Experimental results show that the leg-mounted, hydraulic damper exhibits the most effective viscous damping. Adjusting the orifice setting did not result in substantial changes of dissipated energy per drop, unlike adjusting the damping parameters in the numerical model. Consequently, we also emphasize the importance of characterizing physical dampers during real legged impacts to evaluate their effectiveness for compliant legged locomotion.

OPEN ACCESS

Edited by:

Helmut Hauser,
University of Bristol, United Kingdom

Reviewed by:

Dai Owaki,
Tohoku University, Japan
Francesca Negrello,
Italian Institute of Technology (IIT), Italy

*Correspondence:

Alexander Badri-Spröwitz
sprowitz@is.mpg.de

Specialty section:

This article was submitted to
Soft Robotics,
a section of the journal
Frontiers in Robotics and AI

Received: 14 February 2020

Accepted: 16 June 2020

Published: 28 August 2020

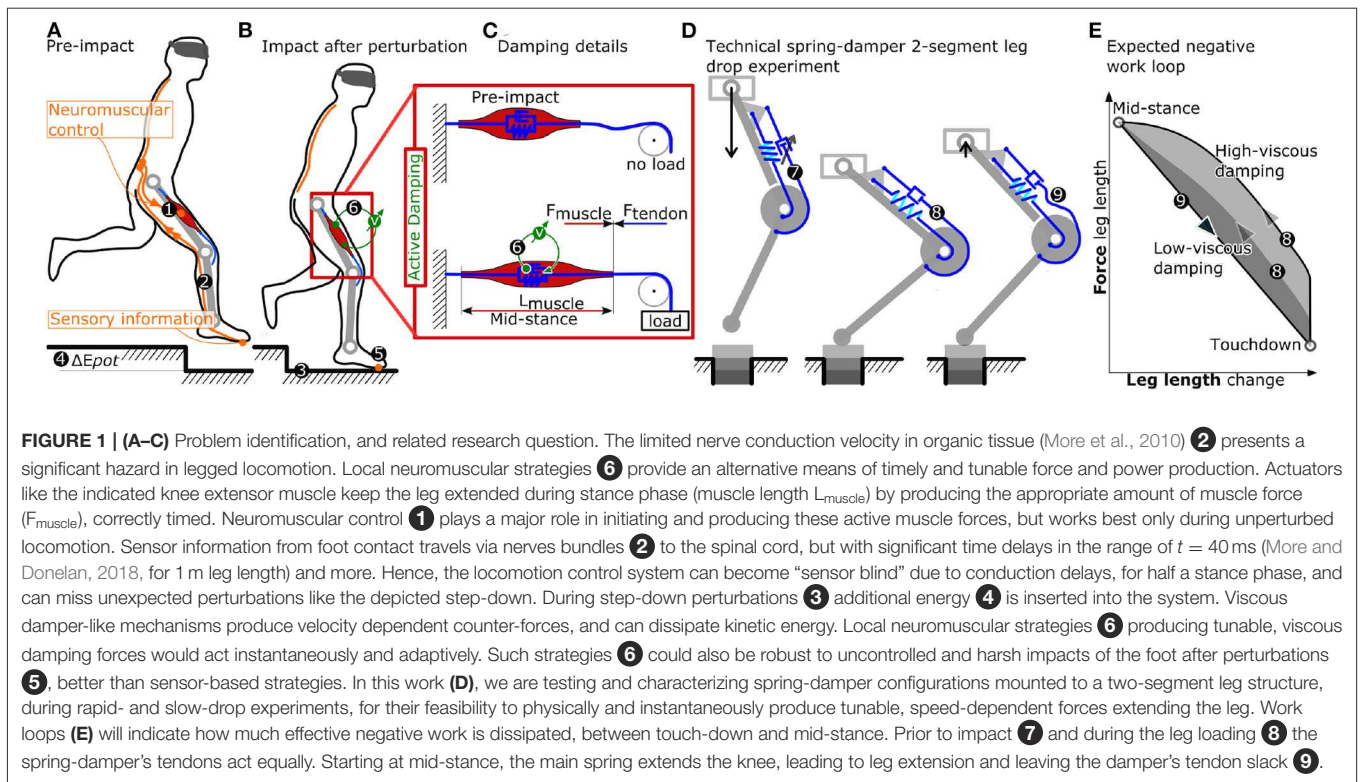
Citation:

Mo A, Izzi F, Haeufle DFB and
Badri-Spröwitz A (2020) Effective
Viscous Damping Enables
Morphological Computation in Legged
Locomotion. *Front. Robot. AI* 7:110.
doi: 10.3389/frobt.2020.00110

Keywords: damping, energy dissipation, legged locomotion, ground disturbance, drop test, rolling diaphragm

INTRODUCTION

While less understood, damping likely plays an essential role in animal legged locomotion. Intrinsic damping forces can potentially increase the effective force output during unexpected impacts (Müller et al., 2014), reduce control effort (Haeufle et al., 2014), stabilize movements (Shen and Seipel, 2012; Secer and Saranlı, 2013; Abraham et al., 2015), and reject unexpected perturbations (Haeufle et al., 2010; Kalveram et al., 2012), e.g., sudden variations in the ground level (**Figure 1**). Stiffness, in comparison, has been studied extensively in legged locomotion. Its benefits have been shown both in numerical simulations, e.g., through spring-loaded inverted pendulum (SLIP) models (Mochon and McMahon, 1980; Blickhan et al., 2007), and physical springy leg implementations (Spröwitz et al., 2013; Hutter et al., 2016; Ruppert and Badri-Spröwitz, 2019).



What combines both mechanical stiffness and intrinsic, mechanical damping is their sensor- and computational-free action. A spring-loaded leg joint starts building up forces exactly at the moment of impact. Mechanical stiffness, or damping, acts instantaneously, and are not subject to delays from post-processing sensor data (Griminger et al., 2020), delays from limited nerve conductive velocities (More and Donelan, 2018), or uncertainties in the estimation of the exact timing of swing-to-stance switching (Bledt et al., 2018).

Legged robots commonly exploit *virtual damping*: actively produced and sensory-controlled negative work in the actuators (Hutter et al., 2012; Havoutis et al., 2013; Seok et al., 2015; Kalouche, 2017; Griminger et al., 2020). Virtual damping requires high-frequency force control, and actuators mechanically and electrically capable of absorbing peaks in negative work. In comparison, mechanical damping based systems (Garcia et al., 2011; Hu et al., 2019) act instantaneously, share impact loads with the actuator when in parallel configuration, and require no sensors or control feedback. The instantaneous mechanical response of a damper is especially relevant in biological systems, where the neuronal delay may be as large as 5% to 40% of the duration of a stance phase (More et al., 2010). In such a short time-window, physical damping could help to reject the perturbation (Haeufle et al., 2010; Kalveram et al., 2012) by morphological computation, as it mechanically contributes to the rejection of the perturbation, a contribution that otherwise would need to be achieved by a (fast) controller (Zahedi and Ay, 2013; Ghazi-Zahedi et al., 2016). Hence, physical damping has the potential to contribute to the

morphological computation (Zahedi and Ay, 2013; Ghazi-Zahedi et al., 2016) of a legged system.

Compared to virtual damping with proprioceptive sensing strategies (Griminger et al., 2020), a legged robot with physical damping requires additional mechanical components, e.g., a fluidic cylinder, and the mechanics to convert linear motion to rotary output. In a cyclic locomotion task, the energy removed by any damper must also be replenished. Hence, from a naive energetic perspective, both virtual and physical damping systems are costly.

Energy dissipation in the form of negative work has been quantified in running birds, and identified as a potential strategy to “... reduce the likelihood of a catastrophic fall.” Daley and Biewener (2006, p. 185). In virtual point-based control strategies for bipedal running, positive work is inserted into hip joints, and negative work is then dissipated in equal amounts in the spring-damper leg (Drama and Spröwitz, 2020). In sum, either physical damping or virtual damping allows removing energy from a legged locomotion system. In this work, we focus on physical damping produced by a viscous damper. We aim toward an understanding of how physical damping can be exploited in legged locomotion and which requirements a damper must fulfill.

We consider two damping principles: viscous damping and Coulomb damping. Viscous damping reacts to a system motion with a force that is linearly (or non-linearly) proportional to its relative acting speed. Coulomb damping generates a constant force, largely independent from its speed (Serafin, 2004). From a control perspective, viscous damping can be beneficial for the negotiation of perturbations in locomotion as it approximates

the characteristics of a differential, velocity-dependent term. Yet it is unknown how this intuition transfers into reality, where impact dynamics and non-linearities of the leg geometry alter the stance-phase dynamics of locomotion.

Damping in legged locomotion can have other purposes, besides dissipating energy. The authors of Werner et al. (2017, p. 7) introduced a damping matrix in the control scheme, which reduced unwanted oscillations in the presence of modeling errors. Tsagarakis et al. (2013) mount compliant elements with some damping characteristics, which also could reduce oscillations of the system's springy components.

In this project, we focus our investigation on the effect of damping during the touch-down (impact) and mid-stance. We chose this simpler drop-down scenario as it captures the characteristics of roughly half a locomotion cycle. A complete cycle would require an active push off phase, and the leg's swing dynamics. Hence, we study the effectiveness of physical damping on the leg's energy dissipation within one drop (touch-down to lift-off), by quantifying its effective dissipated energy $E_{\text{effective}}$. We combine insights from numerical simulations and hardware experiments (Figure 2). By studying the response of two damping strategies (viscous and Coulomb damping) in numerical drop-down simulations, we investigate how physical damping can influence the dynamics of the impact phase. We then examine how these predictions relate to hardware experiments with two functionally different, physical dampers. Hence we explore and characterize the physical damper implementations in a robot leg for their effectiveness in drop-impacts.

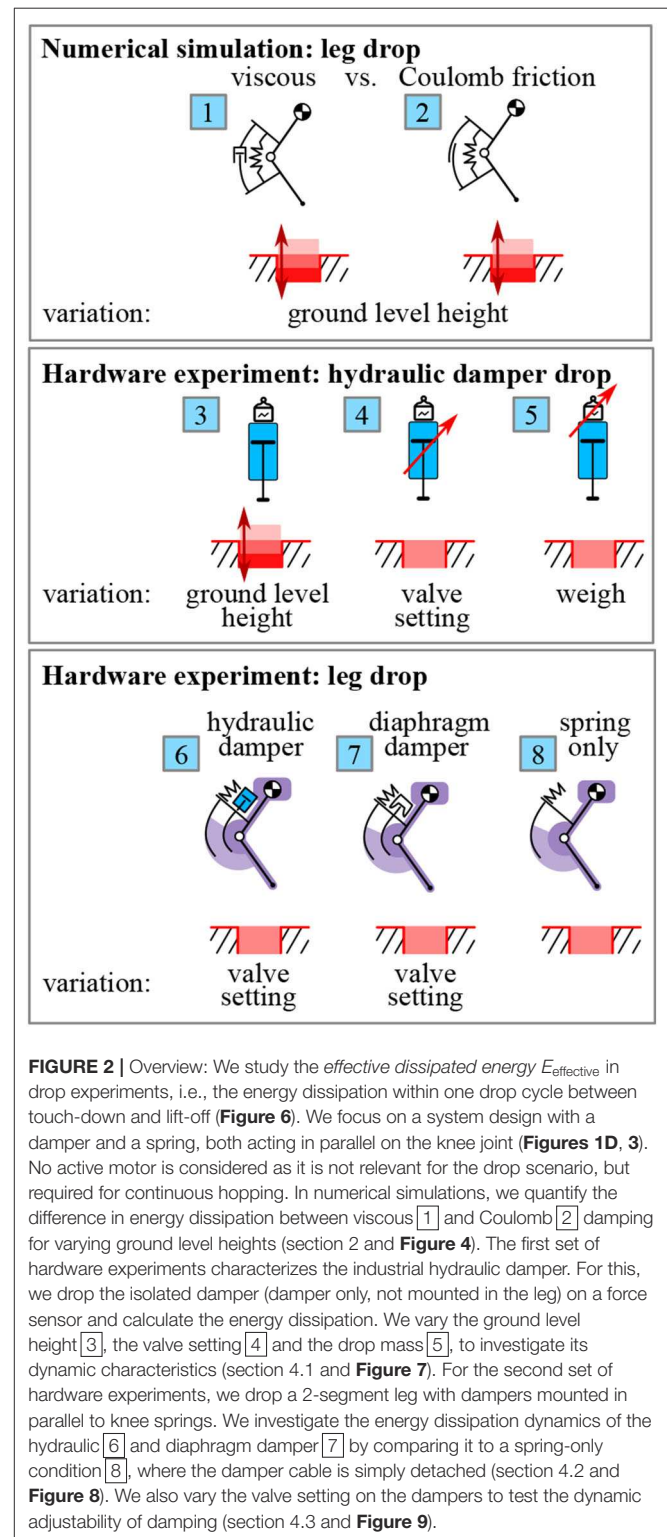
NUMERICAL SIMULATION

We use numerical simulations to investigate the energy dissipation in a leg drop scenario (Figure 2). In analogy to our hardware experiment (section 3.3), a 2-segment leg with a damper and a spring in parallel on the knee joint is dropped vertically (Figure 3A). Once in contact with the ground, the knee flexes and energy is dissipated. We compare viscous vs. Coulomb damping to investigate which of these two damping strategies may be more suited for the rejection of ground-level perturbations. Also, we investigate how the adjustment of the damping characteristics influences the dissipated energy. In all the damping scenarios investigated, the system is not energy conservative. As we investigate the potential benefit of damping in the initial phase of the ground contact, i.e., from touch-down to mid-stance, we do not consider any actuation. Without actuation or control, the model's dissipated energy is not refilled, unlike in, for example, periodic hopping (Kalveram et al., 2012).

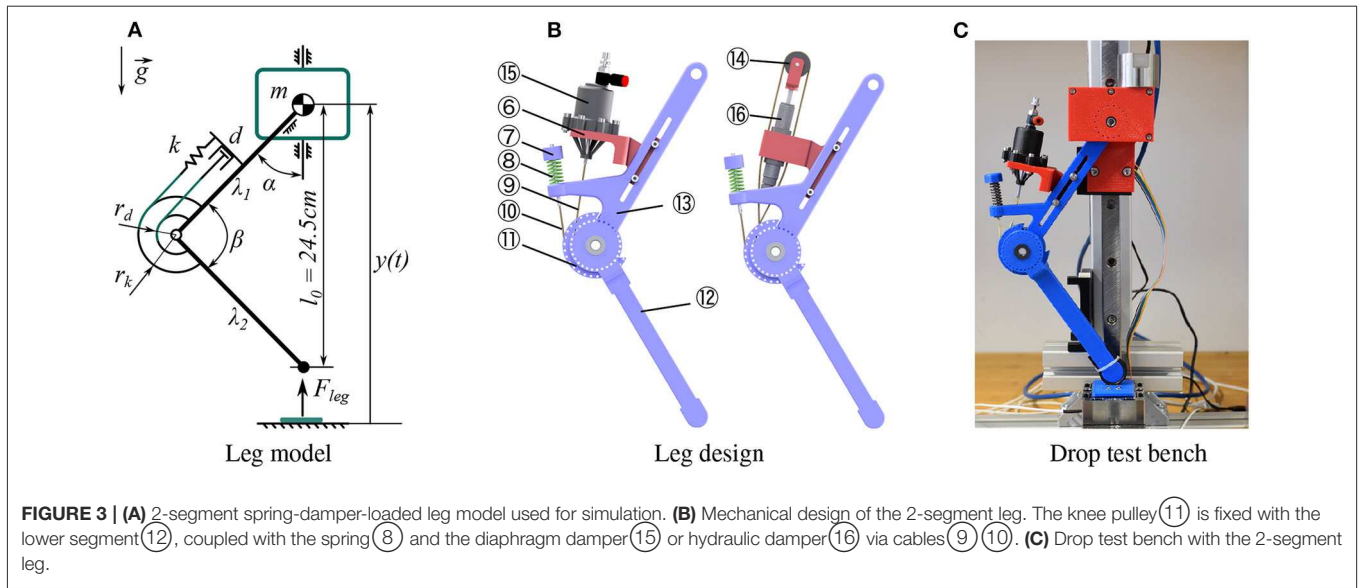
Model

The numerical model is a modified version of the 2-segment leg proposed in Rummel and Seyfarth (2008) with an additional damper mounted in parallel to the knee-spring. The equation describing our leg dynamics is:

$$\ddot{y}(t) = \frac{F_{\text{leg}}(t)}{m} - g \quad (1)$$



where g is the gravitational acceleration, m is the leg mass (lumped at the hip), and $y(t)$ is the time-dependent vertical position from the ground. $F_{\text{leg}}(t)$ is the force transmitted to the hip mass - and the ground - through the leg structure. As such,



the force depends on the current phase of the hopping cycle:

$$F_{leg}(t) = \begin{cases} 0 & , \text{ flight phase: } y(t) > l_0 \\ \frac{y(t)}{\lambda_1 \lambda_2} \frac{\tau(t)}{\sin(\beta(t))} & , \text{ ground contact: } y(t) \leq l_0 \end{cases} \quad (2)$$

with segment length λ_i and knee angle $\beta(t)$ (Figure 3A), l_0 is the leg length at impact. $\tau(t)$ is the knee torque which is produced by the parallel spring-damper element, as in

$$\tau(t) = -k r_k^2 (\beta(t) - \beta_0) + \tau_d(t) \quad (3)$$

with k and r_k being the spring stiffness coefficient and lever arm, respectively. $\tau_d(t)$ is the damping torque, which is set to zero during leg extension, i.e., the damper is only active from impact to mid-stance:

$$\tau_d(t) = 0 \quad \text{if } \dot{\beta}(t) > 0 \quad (4)$$

The modeled damper becomes inactive during leg extension, in accordance to our hardware: the tested physical dampers apply forces to the knee's cam via a tendon (Figure 1D, 9), and this tendon auto-decouples during leg extension. By choosing different definitions of the damper torque $\tau_d(t)$, we can analyse different damper concepts. The model parameters are listed in Table 1.

Simulations were performed using MATLAB (the MathWorks, Natick, MA) with ODE45 solver (absolute and relative tolerance of 10^{-5} , max step size of 10^{-5} s). When searching for appropriate settings of the numerical solver, we progressively reduced error tolerances and the maximum step size until convergence of the simulation results in Table 2 to the first non-significant digit.

Damping Characteristics

We compared two damping concepts in our numerical simulation: (1) *pure* Coulomb damping, i.e., a constant resistance

TABLE 1 | Simulation and hardware parameters.

Parameters	Symbol	Value	Unit
Mass	m	0.408	kg
Reference drop height	h_0	14	cm
Spring stiffness	k	5900	N/m
Leg segment length	λ_1, λ_2	15	cm
Leg resting length	l_0	24.6	cm
Knee resting angle	β_0	110	deg
Spring lever arm	r_k	2.5	cm
Damper lever arm	r_d	2	cm

only dependent on motion direction, and *pure* viscous damping, i.e., a damper torque linearly dependent on the knee angular velocity. Accordingly, we tested two different definitions of τ_d :

$$\tau_d(t) = \begin{cases} -d_c r_d \text{sign}(\dot{\beta}(t)) & , \text{ pure Coulomb damping} \\ -d_v r_d^2 \dot{\beta}(t) & , \text{ pure viscous damping} \end{cases} \quad (5)$$

where r_d is the damper lever arm, d_c (in N) and d_v (in Ns/m) the Coulomb damping and viscous damping coefficients, respectively.

Energy Dissipation in Numerical Drop Simulations

With this model, we investigate the difference in energy dissipation in response to step-up/down perturbations (cases 1 and 2 in Figure 2). For each drop test, the numerically modeled leg starts at rest ($\dot{y}(t) = 0$) with a drop height

$$h = y(t = 0) - l_0 \quad (6)$$

corresponding to the foot clearance at release. The total energy at release is $E_T(h) = mgh$. Given that all model parameters

TABLE 2 | Numerical simulation.

		Damping coeff.		Step-up	Reference height	Step-down
		d_v	d_c	$h = h_0 - \Delta h = 11.5 \text{ cm}$ $E_D (\Delta E_D / \Delta E_T)$	$h = h_0 = 14 \text{ cm}$ $E_{D_0} (E_{D_0} / E_{T_0})$	$h = h_0 + \Delta h = 16.5 \text{ cm}$ $E_D (\Delta E_D / \Delta E_T)$
Set 1	Viscous	29.5 Ns/m	0 N	82 mJ (15%)	97 mJ (17%)	112 mJ (15%)
	Coulomb	0 Ns/m	7.7 N	88 mJ (9%)	97 mJ (17%)	104 mJ (7%)
Set 2	Viscous	68 Ns/m	0 N	167 mJ (30%)	197 mJ (35%)	227 mJ (30%)
	Coulomb	0 Ns/m	17.3 N	178 mJ (19%)	197 mJ (35%)	214 mJ (17%)
Set 3	Viscous	119.4 Ns/m	0 N	249 mJ (46%)	295 mJ (53%)	341 mJ (46%)
	Coulomb	0 Ns/m	29.3 N	264 mJ (31%)	295 mJ (53%)	323 mJ (28%)
Set 4	Viscous	197.1 Ns/m	0 N	330 mJ (63%)	393 mJ (70%)	455 mJ (62%)
	Coulomb	0 Ns/m	46.1 N	346 mJ (47%)	393 mJ (70%)	436 mJ (43%)
Set 5	Viscous	349.4 Ns/m	0 N	411 mJ (81%)	492 mJ (88%)	572 mJ (80%)
	Coulomb	0 Ns/m	76.3 N	423 mJ (69%)	492 mJ (88%)	556 mJ (64%)

Total dissipated energy (E_D) in one drop cycle for different drop heights (h). Reference height is the reference drop height $h = h_0 = 14 \text{ cm}$. During step-up (-down) condition, the drop height is reduced (increased) by $\Delta h = 2.5 \text{ cm}$. Percentage values indicate the change in dissipated energy (ΔE_D) relative to the change in system total energy (ΔE_T) due to the height perturbations. Each set simulates two separate mechanical dampers (pure viscous or pure Coulomb damping), with damping coefficients chosen to dissipate the same energy at the reference condition, i.e., E_{D_0} . Results of set 1, 3 and 5 are further described in **Figure 4**. For all tested conditions, viscous damping outperforms Coulomb damping, as indicated by the always higher percentage values (bold).

in **Table 1** are fixed, the energy dissipated in a drop becomes a function of the drop height and the damping coefficients: $E_D = f_{E_D}(h, d_{c,v})$.

A simulated drop height h can be seen as a variation Δh from a reference value h_0 :

$$h = h_0 \pm \Delta h \quad (7)$$

Equal to the hardware experiments, we use $h_0 = 14 \text{ cm}$ as reference drop height. In the reference drop condition, i.e., $h = h_0$, the energy dissipated by damping is $E_{D_0} = E_D(h_0) = f_{E_D}(h_0, d_{c,v})$. E_{D_0} only depends on the damping level, namely the chosen damping strategy (viscous or Coulomb damping) and associated damping coefficient. We chose five different desired damping levels (set 1–5) as a means of scanning a range in which the damping could be adjusted: for each set, the amount of energy that is dissipated at the reference drop height E_{D_0} differs. The chosen E_{D_0} values (**Table 2**, column “Reference height”) correspond to proportional levels ($[0.1, 0.2, \dots, 0.5]$) of the systems potential energy in terms of the leg resting length l_0 , as in

$$E_{D_0} \approx m g [0.1, 0.2, \dots, 0.5] l_0 \quad (8)$$

This corresponds to damping configurations that dissipate between $\approx 17\%$ and $\approx 88\%$ of the system’s initial potential energy at the reference height ($E_{T_0} = E_T(h_0) = m g h_0 = 560 \text{ mJ}$), as shown in **Table 2**, column “Reference height.” To achieve these desired damping levels, we adjusted the damper parameters d_c and d_v accordingly (**Table 2**, column “Damping coeff.”). As an example: for set 3, both damping values were adjusted such that at the reference height h_0 both dampers dissipate $E_{D_0} = m g 0.3 l_0 = 295 \text{ mJ}$, which corresponds to 53% of the total energy E_{T_0} .

In the numerical simulations, we focus on the relation between a ground level perturbation Δh and the change in energy dissipation – and their dependency on the damper characteristics. A drop from a height larger than h_0 corresponds to a step-down ($\Delta h > 0$), and a drop from a height smaller than h_0 to a step-up ($\Delta h < 0$). Each condition introduces a change of the total energy of $\Delta E_T = m g \Delta h$. The change in energy dissipation due to the perturbation is defined as

$$\Delta E_D(\Delta h) = E_D(h_0 + \Delta h) - E_{D_0} \quad (9)$$

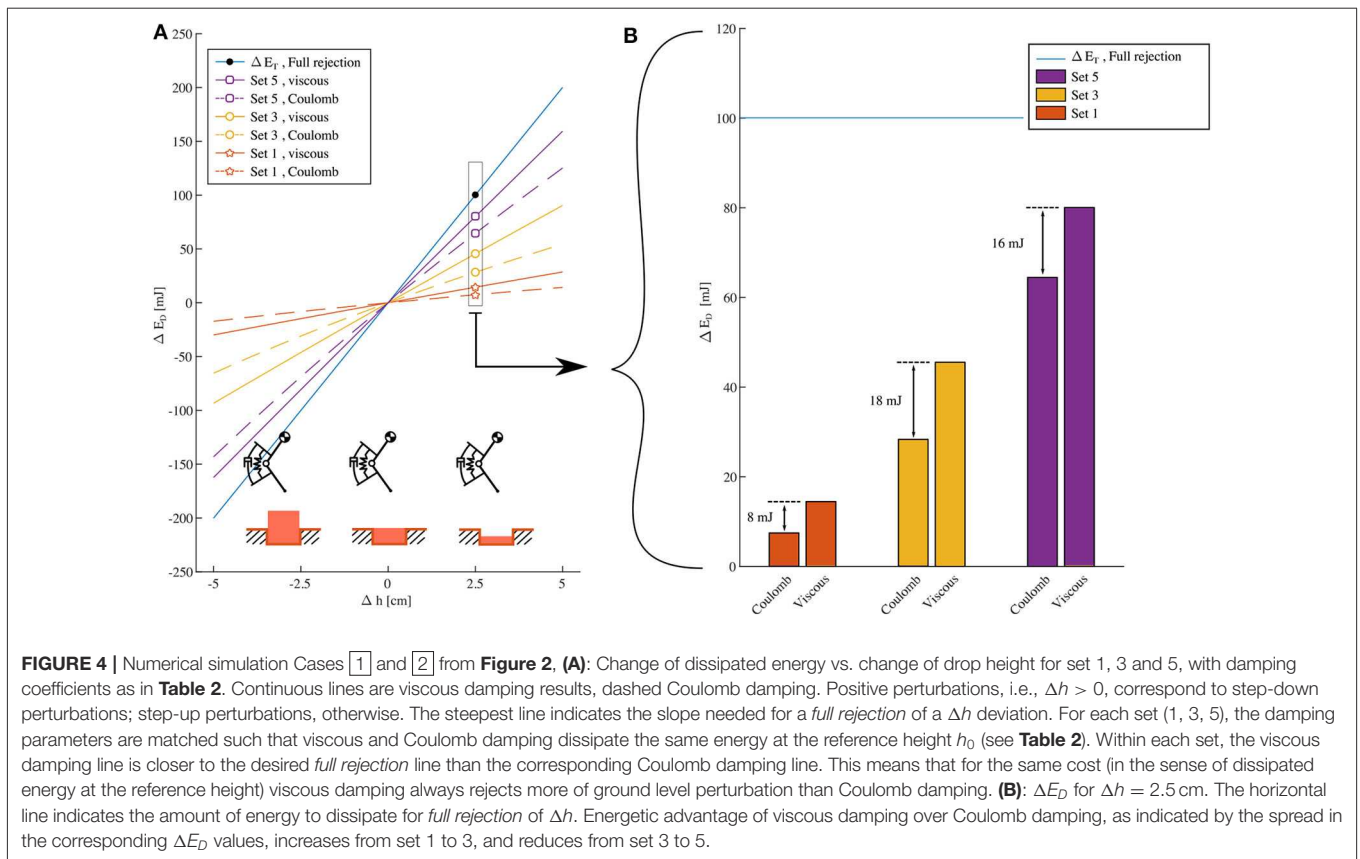
which is the difference between the dissipated energy when released from a perturbed height and the dissipated energy when released from the reference height. As a reference, we further define the *full rejection* case where

$$\Delta E_D(\Delta h) = \Delta E_T = m g \Delta h \quad (10)$$

In human hopping a full recovery within a single hopping cycle is not seen during experimental drop down perturbations. Instead, a perturbation of $\Delta h = 0.1 l_0$ is rejected in two to three hopping cycles (Kalveram et al., 2012). In our results, this corresponds to the partial rejections observed with viscous damping in sets 2 and 3 for $\Delta h = \pm 2.5 \text{ cm}$.

Simulation Results

Figure 4A shows the relation between the change in drop height and the corresponding change in dissipated energy by the simulated dampers for set 1, 3 and 5 (continuous line for pure viscous, dashed for pure Coulomb damping). For the range of simulated drop heights, pure viscous and Coulomb dampers change the amount of dissipated energy with an almost linear dependence on the drop height. However, pure viscous damping has a slope closer to the *full rejection* scenario (blue line in **Figure 4A**), regardless of the set considered. In a step-down



perturbation ($\Delta h > 0$ in Figure 4A), pure viscous damping dissipates more of the additional energy ΔE_T , while in a step-up perturbation ($\Delta h < 0$) it dissipates less energy than pure Coulomb damping. As such, the results show that a viscous damper can reject a step-down perturbation faster, e.g., within less hopping cycles, and it requires smaller correction by active energy supply during a step-up perturbation.

Adjusting the damping parameters allows to change the reaction to a perturbation (Figure 4). Increasing the damping intensity, i.e., d_v and d_c from set 1 to 5, allows to better match the full recovery behavior (blue line in Figure 4A). However, this comes at the cost of a higher energy dissipation at the reference height, i.e., in absence of a ground perturbation (Table 2, column “reference height”). Increasing the damping rate also affects the energetic advantage of viscous damping over Coulomb damping. Figure 4B shows this in detail for a specific step-down perturbation ($\Delta h = 2.5$ cm): from set 1 to set 3, the spread between the ΔE_D values of the viscous damper and the Coulomb damper increases (from 8 to 18 mJ). However, the difference in dissipated energy ΔE_D slightly reduces from set 3 to set 5 (from 18 to 16 mJ).

Table 2 quantifies the previous findings by indicating the percentage of energy perturbation ΔE_T that each damping approach dissipates for $\Delta h = \pm 2.5$ cm and for all the tested sets

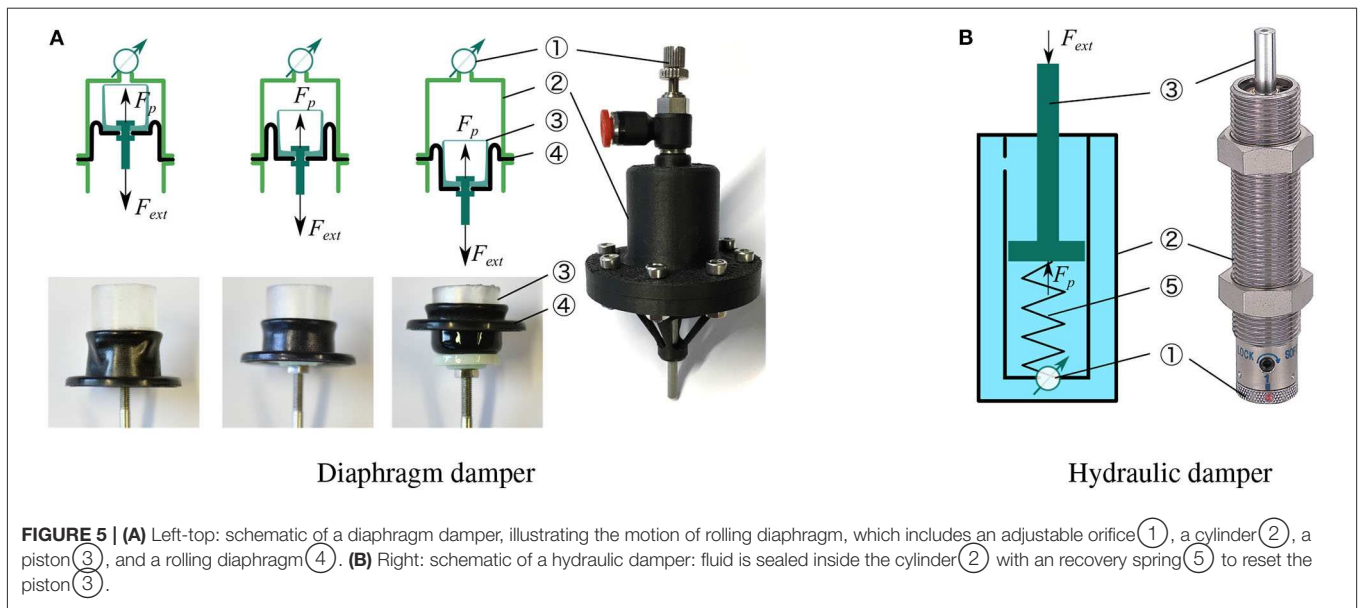
of damping coefficients d_v and d_c . The data further confirms the observations from Figure 4, showing that:

1. within each set, viscous damping outperforms Coulomb damping for all the simulated conditions - its dissipated energy is always the closest to 100 % of ΔE_T , which means the closest to full rejection;
2. the energetic benefit of viscous damping over Coulomb damping, i.e., the spread in percentage values of $\Delta E_D/\Delta E_T$, does not monotonically increase with higher damping rates, i.e., moving from set 1 to 5.

Furthermore, Table 2 shows that for small damping rates, i.e., set 1, viscous damping introduces only marginal benefits in energy management compared to Coulomb damping: < 10% spread between the corresponding $\Delta E_D/\Delta E_T$ values.

HARDWARE DESCRIPTION

With the previous results from our numerical simulation in mind, we tested two technical implementations (Figure 5) to produce adjustable and viscous physical damping. We implemented a 2-segment leg hardware (Figure 3B) and mounted it to a vertical drop test bench to investigate the role of physical damping. The drop test bench produces velocity profiles during impact and stance phase similar to continuous



hopping and allows us testing effective damping efficiently and repeatable.

Rolling Diaphragm Damper

The most common designs of viscous dampers are based on hydraulic or pneumatic cylinders (viscous damping) and can offer the possibility of regulating fluid flow by altering the orifice opening (adjustability). These physical dampers can display high Coulomb friction, caused by the mechanical design of the sliding seal mechanisms. Typically, the higher the cylinder pressure is, the higher the Coulomb friction exists. Ideally, we wanted to test one physical damper concept with the least possible amount of Coulomb friction. Inspired by the low-friction hydrostatic actuators (Whitney et al., 2014, 2016), we designed a low-Coulomb damper based on a rolling diaphragm cylinder. Its cylinder is 3D printed from Onyx material. **Figure 5A** illustrates the folding movement of this rolling diaphragm mounted on a piston. The rolling diaphragm is made of an elastomer shaped like a top hat that can fold at its rim. When the piston moves out, the diaphragm envelopes the piston. In the ideal implementation, only rolling contact between the diaphragm and the cylinder occurs, and no sliding contact. Hence, Coulomb friction between piston and cylinder is minimized. We measured $F_C \approx 0.3$ N of Coulomb friction for our rolling diaphragm cylinder, at low speed.

Our numerical simulation results promoted viscous and adjustable damping for use in vertical leg-drop. By concept, both properties are satisfied by the diaphragm damper with an adjustable valve. When an external load F_{ext} pulls the damper piston (**Figure 5A**), the fluid flows through a small orifice, adjustable by diameter. This flow introduces a pressure drop $\Delta P(t)$, whose magnitude depends on the orifice cross-section area A_o and piston speed $v(t)$. As such, for a given cylinder cross section area A_p , the diaphragm damper reacts to an external load

F_{ext} by a viscous force $F_p(t)$ due to the pressure drop $\Delta P(t)$:

$$F_p(t) = A_p \Delta P(t) = A_p f(v(t), A_o) \quad (11)$$

We mounted a manually adjustable valve (SPSNN4, MISUMI) to set the orifice size A_o . For practical reasons (weight, leakage, complexity of a closed circuit with two cylinders) we used air in the diaphragm cylinder as the operating fluid, instead of liquid (Whitney et al., 2014, 2016). Air is compressible, and with a fully closed valve the diaphragm cylinder also acts as an air spring. This additional functionality can potentially simplify the overall leg design. With the pneumatic, rolling diaphragm-based damper implementation, we focused on creating a light-weight, adjustable damper with minimal Coulomb friction, and air as operating fluid.

Hydraulic Damper

In the second technical implementation we applied an off-the-shelf hydraulic damper (1214H or 1210M, MISUMI, **Figure 5B**), i.e., a commercially available solution for adjustable and viscous damping. Tested against other hydraulic commercial dampers, we found these specific models to have the most extensive range of adjustable viscous damping and the smallest Coulomb friction ($F_C \approx 0.7$ N). Similarly to the diaphragm damper, these hydraulic dampers produce viscous damping by the pressure drop at the adjustable orifice. The operating fluid is oil, which is in-compressible. Hence, the hydraulic damper should not exhibit compliant behavior. Other than the diaphragm damper, the hydraulic damper produces damping force when its piston is pushed, not pulled. This design also includes an internal spring to recover the piston position when unloaded. In sum, the hydraulic damper features high viscous damping, no air-spring effect, and a higher Coulomb friction compared the custom-designed pneumatic diaphragm damper.

Articulated Leg Design

The characteristics of a viscous damper strongly depend on the speed- and force-loading profile imposed at its piston, because of the complex interaction of fluid pressure and compression, viscous friction, and cavitation (Dixon, 2008). We implemented a hardware leg to test our two physical dampers at loading profiles (speed, force) similar to legged hopping and running.

The 2-segment hardware leg (Figure 3B) is designed with a constant spring and damper lever arm, parameters are provided in Table 1. In all experiments with the 2-segmented leg, the leg spring provides elastic joint reaction forces. Dampers are swapped in and out in a modular fashion, depending on the experimental settings. The 2-segment leg design parameters are identical to those in our simulation model (Table 1). A compression spring (8) is mounted on the upper leg segment (13). When the leg flexes, the spring is charged by a spring cap (7) coupled to a cable (10) attached to the lower leg. Either damper (15) (16) is fixed on a support (6) on the upper segment (13). The support (6) can be moved within the upper segment (13), to adjust the cable (9) pretension. Cables (9) (10) link the damper piston (3) (Figure 5) and the spring (8) to the knee pulley (11), which is part of the lower segment (12).

During the leg flexion, the cable under tension transmits forces instantly to the spring and damper. Spring and damper forces counteract the knee flexion. During leg extension, the spring releases energy, while the damper is decoupled due to slackness of the cable. We included a hard stop into the knee joint to limit the maximum leg extension, and achieve a fixed leg length at impact. At maximum leg flexion at high leg loading, segments can potentially collide. We ensured not to hit either hard stops during the drop experiments. The hydraulic damper (16) requires a reverse mechanism (14), since its piston requires compression to work. The piston of the diaphragm damper (15) was directly connected to the knee pulley. The diaphragm damper (15) included no recovery spring (5) (Figure 5), hence we reset the piston position manually after each drop test. In sum, different spring-damper combinations can be tested with the 2-segment leg setup. Note that the here shown hardware leg has no actuation. If a motor would actuate the knee joint, in parallel mounted to the spring and the damper, the damper would share the external impact load, and consequently reduce an impact at the motor.

Experimental Set-Up, Data Sampling, and Processing

We implemented an experimental setup for repetitive measurements (Figure 3C). A drop bench was used to constrain the leg motion to a single vertical degree of freedom, and linear motion. This allowed us to fully instrument the setup (slider position, and vertical ground reaction forces, GRF), and ensured repeatable conditions over trials. Adjusting the drop height allowed us setting the touch-down speed. A linear rail (SVR-28, MISUMI) was fixed vertically on a frame. The upper leg segment was hinged to a rail slider. The rail slider was loaded with additional, external weights, simulating different robot masses. We set the initial hip angle α_0 to align the hip and foot vertically.

A hard stop ensured that the upper leg kept a minimum angle $\alpha > \alpha_0$.

Two sensors measured the leg dynamics: the body position y and the vertical ground reaction force are recorded by a linear encoder (AS5311, AMS) and a force sensor (K3D60a, ME, amplified with 9326, Burster), respectively (Figure 3C). The duration from touch-down to mid-stance is very short, typically $t \leq 100$ ms, and high-frequency data sampling was required. The encoder data was sampled by Raspberry Pi 3B+ with $f = 8$ kHz sampling rate. Force data were recorded by an Arduino Uno, with a 10-bit internal ADC at 1 kHz sampling rate. A high-speed camera (Miro Lab 110, Phantom) recorded the drop sequence at $f = 1$ kHz sampling rate. We performed ten trials for each test condition. Sensor data was processed with MATLAB (the MathWorks, Natick, MA). Data was smoothed with a moving average filter, with a filter span of 35 samples for encoder data, and 200 samples for force data. Repeated experiments of the same test condition are summarized as an envelop defined by the average $\pm 95\%$ standard deviation of the filtered signals.

HARDWARE EXPERIMENTS AND RESULTS

In the drop experiments, we characterize both the hydraulic and diaphragm dampers, and the 2-segment springy leg (Figure 6). We chose three orifice settings (labeled as a, b, and c) for each damper, and focus on the effects of viscous damping and adjustable dissipation of energy in the hardware setup. Table 3 lists an overview of the drop tests, and its settings (drop height, weight, orifice setting, damper type). To emphasize the fundamental differences between the damper designs, we compare only one model of the hydraulic damper (1214H) to the diaphragm damper (sections 4.1.–4.3), and show the potential of the second hydraulic damper (1210M) in section 4.4. Videos of the experiments can be found in the **Supplementary Material**, and online¹.

Isolated Damper Drops, Evaluation

In this experiment we characterized the hydraulic damper by dropping it under changing conditions of the instrumented drop setup, without mounting it to the 2-segment leg. The experimental setup allows differentiating effects, compared to the 2-segment leg setup, and to emphasize the viscous damper behavior of the off-the-shelf component. We also applied the results to estimate the range of damping rates available with changing orifice settings. The hydraulic damper was directly fixed to the rail slider into the drop bench (section 3.4). The piston pointed downwards. We measure the vertical ground reaction force to determine the piston force, and we recorded the vertical position of the slider over time, to estimate the piston speed after it touches the force sensor.

Figure 7 shows the force-speed profiles for drop tests with different drop heights (Figure 7A), orifice settings (Figure 7B), and drop loads (Figure 7C). Data lines in Figure 7 should be interpreted from high speed (impact, right side of each plot) to low speed (end of settling phase, 0 m/s, left). The time from

¹<https://youtu.be/F00Sma2BQ4c>

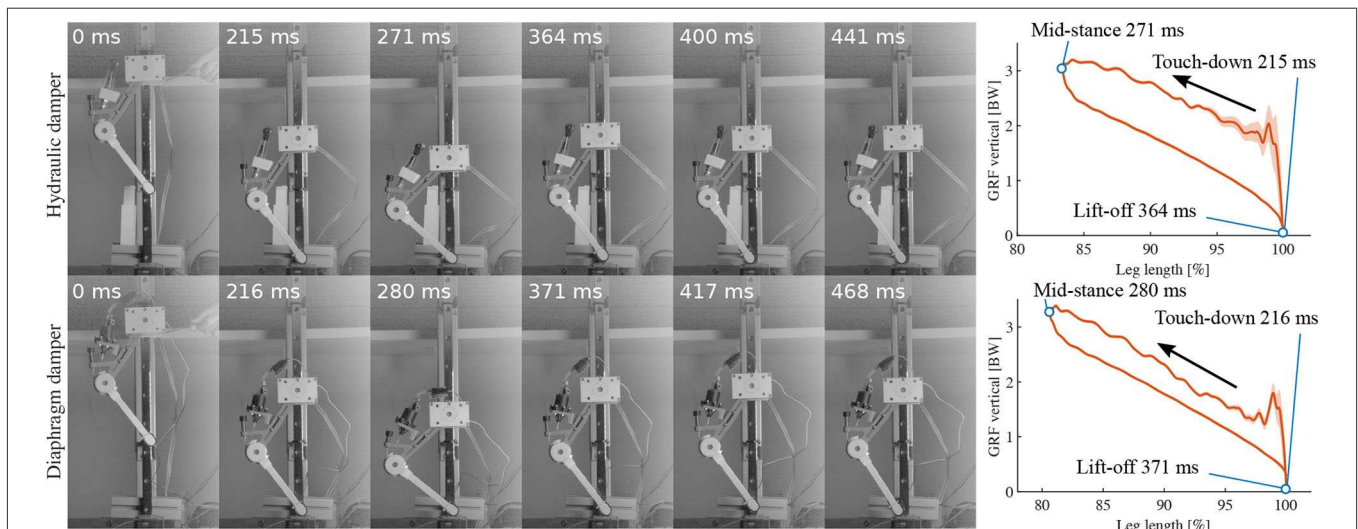


FIGURE 6 | High-speed snapshots of drop experiments starting from release to second touchdown. Leg with hydraulic damper is shown on the top row, leg with diaphragm damper the bottom row. Depicted are from left to right: release, touchdown, mid-stance, lift-off, apex, second touchdown. The right plots illustrate the timing of the events corresponding to the snapshots.

TABLE 3 | Drop test settings for experiments.

Drop test setup	Figure	Drop height [cm]	Drop weight [g]	Orifice [~]
Damper (1214H)	Figure 7A	3, 5, 7	280	b
	Figure 7B	5	280	a, b, c
	Figure 7C	3	280, 620	b
Damper (1214H, diaphragm) & leg	Figures 8A,B	14	408	c
	Figure 8C	14	408	damper detached
Damper & leg (simulation)	Figures 9A,B	14	408	a, c
	Figure 9C	14	408	viscous, Coulomb
Damper (1210M) & leg	Figure 10	14	408	a, b

Values indicated in bold indicate control parameters for these experiments.

impact to peak force (right slope of each plot) is (≈ 24 ms), while the negative work (shown in legends) was mainly dissipated along the falling slope in the much longer-lasting settling phase after the peak (left slope of each plot, ≈ 200 ms).

The results from tests with drop heights from 3 to 7 cm show viscous damping behavior in the settling phase after peak force (left slope), with higher reaction forces at higher piston speeds with higher dissipation, ranging from 45 N for maximum speeds of 0.6 m/s with 56 mJ to 65 N at 0.9 m/s with 116 mJ. The piston force almost linearly depends on the piston speed (**Figure 7A**).

Changing the orifice setting at a constant drop height resulted in different settling slopes (**Figure 7B**). Applying a least-squares fit on the left-falling settling slope, we estimate an

adjustable damping rate between 91 Ns/m and 192 Ns/m. The dissipated energy changes from 89 mJ to 81 mJ, respectively. Hence adjusting the orifice setting has an effect on the damping rate and the dissipated energy in the isolated hydraulic damper, but not as we intuitively expected.

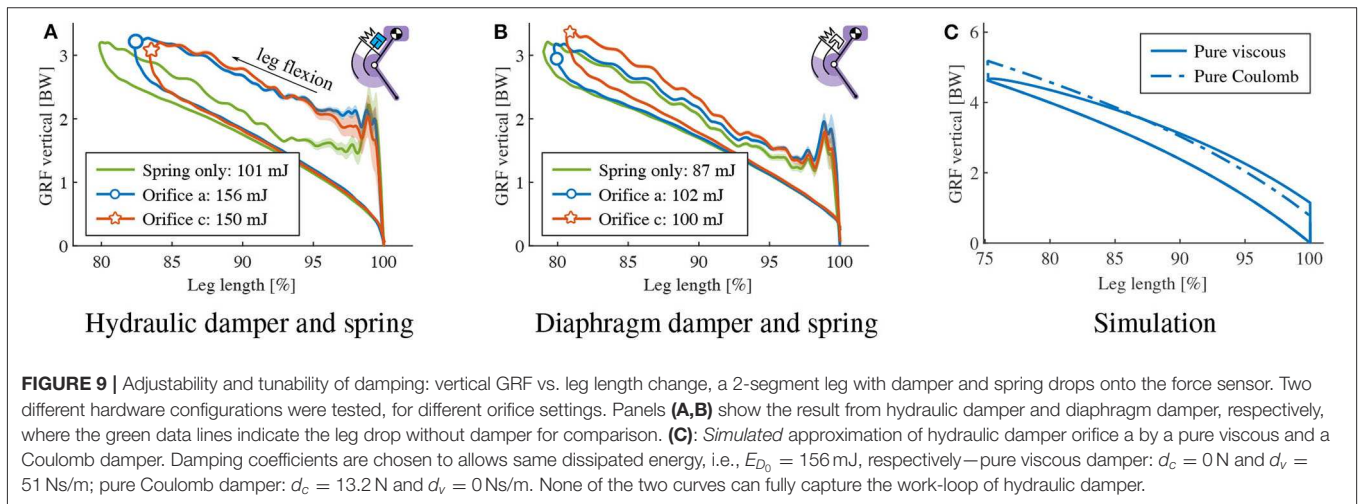
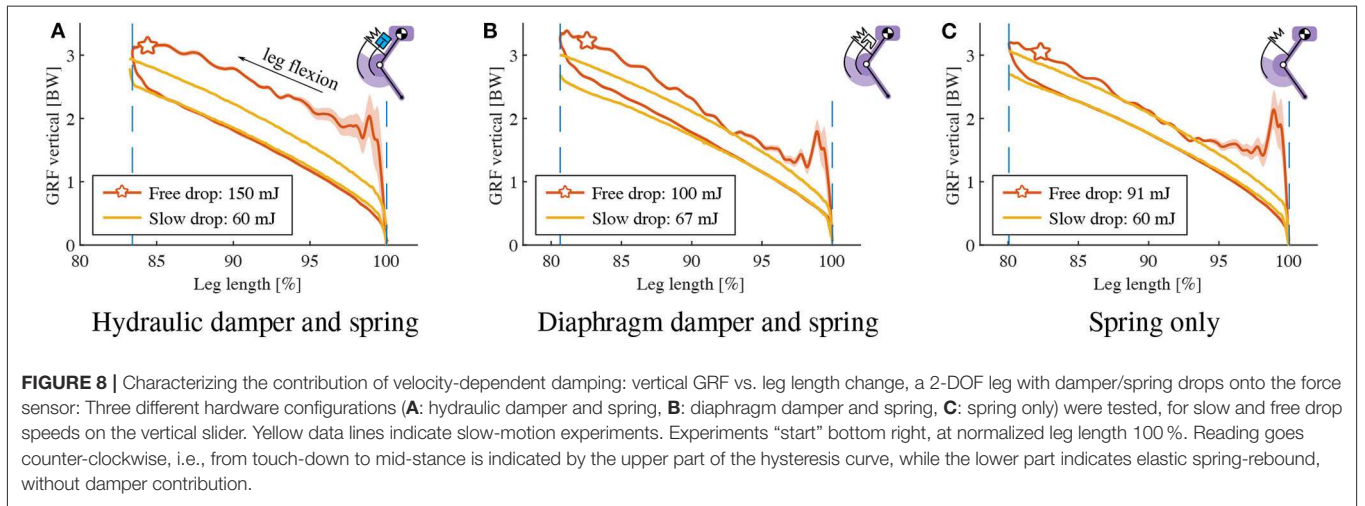
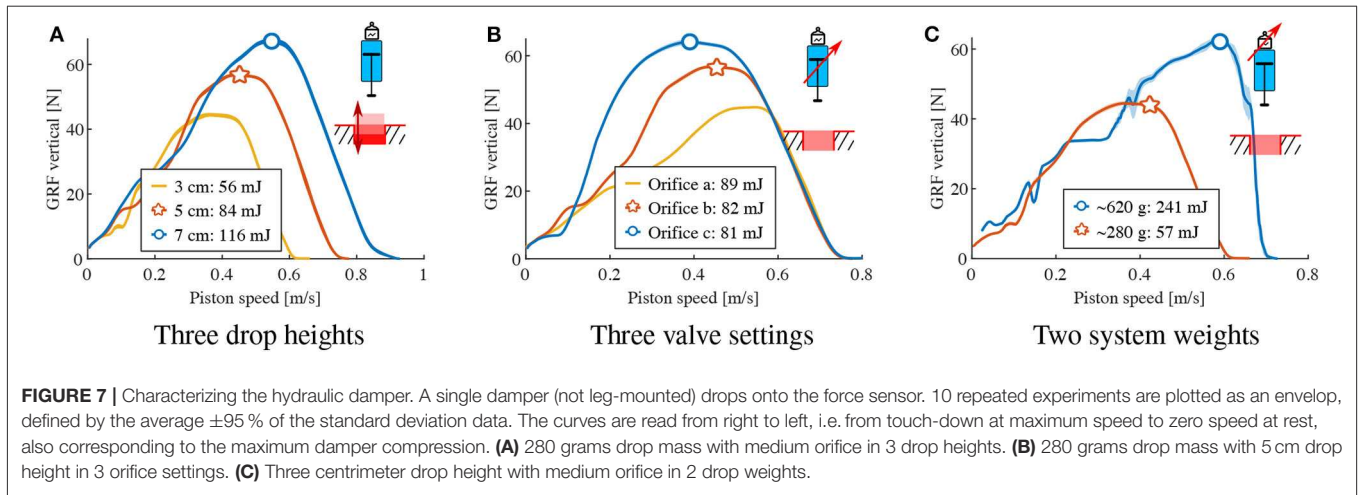
We interpret the rising slope in the impact phase (right part of each curve, **Figures 7A,B**) as a build-up phase; the hydraulic damper takes time (≈ 24 ms) to build up its internal viscous flow and the related piston movement, after the piston impact. With heavier weights (620 g = heavy, 280 g = light, **Figure 7C**), the impact phase equally lasts ≈ 24 ms. After the impact phase with heavy weight, the damper shows the same damping rate in the settling phase, in form of an equal left slope.

Similar drop tests for the evaluation of the isolated diaphragm damper were not possible since the orientation of the internal diaphragm only permits to pull the piston. In the following section, we test the diaphragm (connected by a piston reverse mechanism) and the hydraulic damper directly on the 2-segment leg structure.

Composition of Dissipated Energy

We performed drop tests of two damper configurations: one off-the-shelf hydraulic damper, and custom-made pneumatic damper, each mounted in parallel to a spring at the 2-segment leg (section 3.3, **Figure 3B**), to quantify the effect of viscous damping for drop dynamics similar to legged hopping.

For each drop, the effective dissipated energy $E_{\text{effective}}$ was computed by calculating the area enclosed by the vertical GRF-leg length curve from touch-down to lift-off (Josephson, 1985), i.e., the work-loop area. These work-loops are to be read counter-clockwise, with the rising part being the loading during leg flexion, and the falling part being the unloading, due to spring recoil. $E_{\text{effective}}$ does not only consist of the viscous loss E_{viscous} due to the damper, but also Coulomb friction loss in the leg



(E_{friction}) and the impact loss E_{impact} due to unsprung masses:

$$E_{\text{effective}} = E_{\text{friction}} + E_{\text{impact}} + E_{\text{viscous}}. \quad (12)$$

We propose a method to indirectly calculate the contribution of viscous damping, by measuring and eliminating effects from Coulomb friction, and unsprung masses.

To quantify the Coulomb friction loss E_{friction} , we conducted “slow drop” tests. The mechanical setup is identical to “free drops” test, where the leg is freely dropped from a fixed height. However, in the “slow drop” experiment the 2-segment leg is lowered manually onto the force sensor, contacting and pressing the leg-damper-spring system onto the force sensor. At slow speed only Coulomb friction in joints and damper act, but no viscous damping or impact losses occur. Consequently the dissipated energy calculated from the size of the work loop is due to Coulomb friction losses E_{friction} .

To identify the impact loss E_{impact} , we remove the viscous component first by detaching the damper cable on the setup. A “free drop” test in this spring only condition measures the contribution of friction loss E_{friction} and impact loss E_{impact} combined. A “slow drop” test of the same setup is able to quantify the friction loss E_{friction} . The impact loss E_{impact} is therefore estimated as the energy difference between “free drop” and “slow drop” in the spring-only condition (Figure 8C). Since the effective dissipated energy $E_{\text{effective}}$ is directly measured, and the friction loss E_{friction} and impact loss E_{impact} are obtained separately, the viscous loss E_{viscous} can be computed according to Equation (12).

Figures 8A,B show the “free drop” and “slow drop” results of the hydraulic damper and diaphragm damper, respectively. Both drop heights are 14 cm, at identical orifice setting. We calculated the negative work of each work-loop (range indicated by the two vertical dash lines), as shown in Figure 8. To provide an objective analysis, the work-loop area of each “slow drop” (manual movement) was cut to the maximum leg compression of the corresponding “free drop” condition. The dissipated energy of the leg-mounted hydraulic damper is 150 mJ and 60 mJ for “free drop” and “slow drop,” respectively, and 100 mJ and 67 mJ for the diaphragm damper, respectively. According to Figure 8C, the impact loss E_{impact} due to unsprung masses play a large role, accounting for 31 mJ. The viscous loss E_{viscous} of the hydraulic and the diaphragm damper are 59 mJ and 2 mJ, respectively.

Adjustability of Dissipated Energy

We tested the adjustability of energy dissipation during leg drops by the altering orifice setting for each leg-mounted damper, and quantified by calculating the size of the resulting work-loops. The drop height was fixed to 14 cm and we used 2 orifice settings. The identical same set-up but in spring-only configuration (damper cables detached) was tested for reference. Work-loop and corresponding effective dissipated energies are illustrated in Figures 9A,B. The hydraulic damper-mounted leg dissipated 156 and 150 mJ energy on its two orifice settings, the pneumatic diaphragm damper dissipated 102 and 100 mJ. In Figure 9C, we display results from the numerical model introduced in section 2 to estimate the work-loop shape that either a pure viscous or pure Coulomb damper would produce, if dissipating the same amount of energy as the hydraulic damper with orifice-a (Figure 9A). We set the damping coefficients of our numerical model to $E_{D_0} \approx 156$ mJ, so that: $(d_v, d_c) = (51 \text{ Ns/m}, 0 \text{ N})$ for pure viscous damping; and $(d_v, d_c) = (0 \text{ Ns/m}, 13.2 \text{ N})$ for pure

TABLE 4 | Leg drop experiments and their individual energetic losses per drop.

Drop test setup	$E_{\text{effective}}$ [mJ]	E_{friction} [mJ]	E_{impact} [mJ]	E_{viscous} [mJ]
Spring only	91	60	31	0
Diaphragm + spring	100	67	31	2
Hydraulic 1214H + spring	150	60	31	59
Hydraulic 1210M + spring	401	70	31	300

The system's initial potential energy is 560 mJ. $E_{\text{effective}}$, sum of all energetic losses visible as the area of the hysteresis curve; i.e., in Figure 8, E_{friction} , negative work dissipated by Coulomb friction; E_{impact} , energetic losses from impact (unsprung mass). The negative work dissipated by viscous damping in the physical damper is E_{viscous} . The corresponding work curves are provided in Figures 8–10.

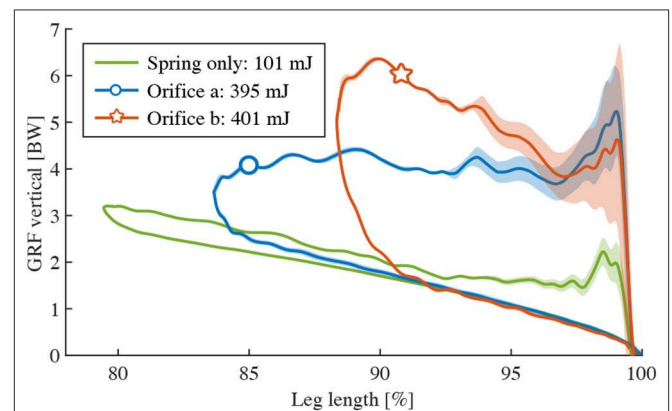
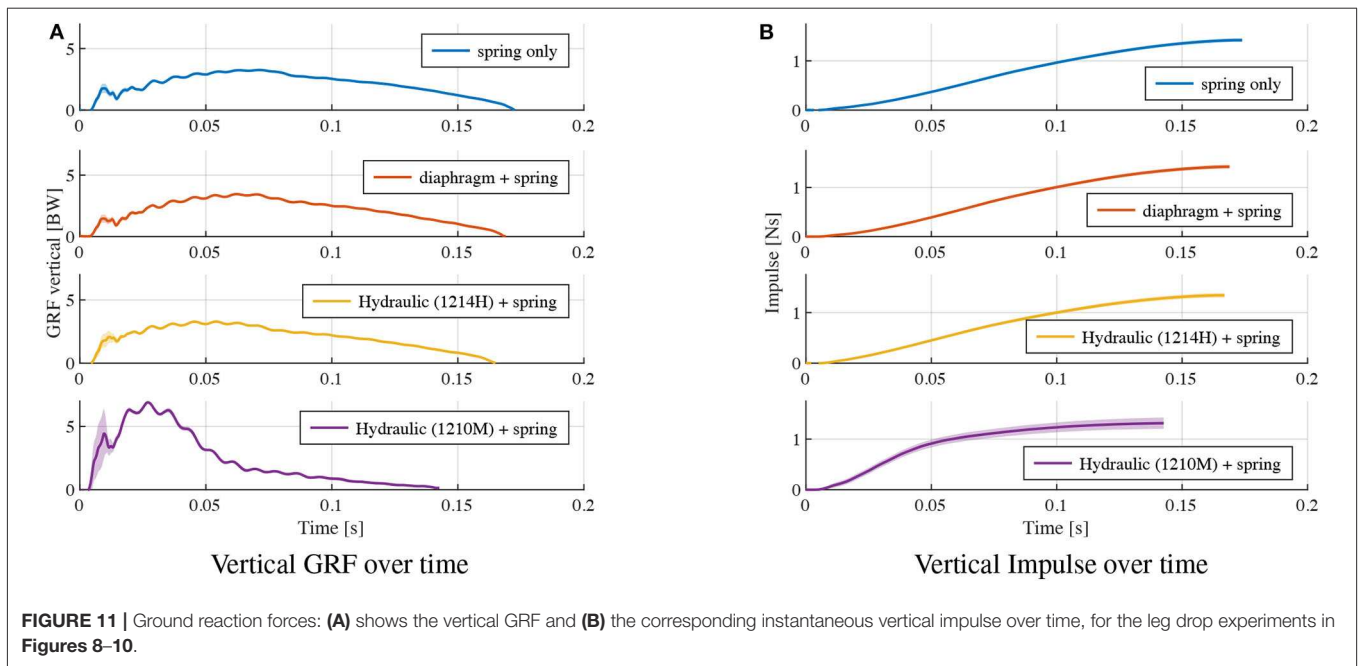


FIGURE 10 | Higher energy dissipation with a different model of the hydraulic damper (1210M): Vertical GRF vs. leg length change, a 2-DOF leg with a parallel damper and spring drops onto the force sensor. Two damper orifice settings were tested (blue, red curves). The two resulting curves are compared with the spring-only configuration, provided as reference.

Coulomb damping. Work-loops from the numerical simulation differ notably from the experimental data, suggesting that neither the hydraulic or diaphragm damper can easily be approximated as pure viscous or pure Coulomb dampers. Both work loops in Figure 9C present about equal amount of dissipated energy. Yet, both differ greatly due to their underlying damping dynamics, visible in their unique work-loop shapes. Their individual characteristics are different enough to uniquely identify pure viscous or pure Coulomb dampers, from numerical simulation.

Damper Selection Choices

In accordance with the simulation results, we aim to use a viscous damper to dissipate energy introduced by a ground disturbance. How much energy could be dissipated by the damper, depended mainly on the selected viscous damper, and only to a limited degree on the orifice setting. Results from the hydraulic damper 1214H showed significant energy dissipation capabilities: $\approx 11\%$ of the system's total energy (59 of 560 mJ) were dissipated (Figure 9A at orifice setting “c” and Table 4). At the drop, in sum 150 mJ (27%) of the leg's system energy were lost, due to Coulomb friction in the joints, impact dynamics, and viscous damping losses. Other dissipation dynamics are



feasible, by selecting appropriate dampers. We tested a second hydraulic damper (1210M, MISUMI) under equal conditions and compared it to damper-1214H. The two applied orifice settings changed the observed work loop largely by shape, and little by area (Figure 10). The damper-1210M dissipated $\approx 60\%$ system energy, and the leg lost in sum (viscous+Coulomb+impact) 72% of its system's energy during that single drop. At other orifice settings, we observed over-damping; the 1210M-spring leg came to an early and complete stop, and without rebound (data not shown here due to incomplete work loop).

For comparison, time plots of the vertical GRF and the impulse at stance phrase are shown in Figure 11. The energy composition (Equation 12) is provided in Table 4. The “spring only” data correspond the curves in Figure 8C. The diaphragm+spring data correspond to “orifice c” in Figure 9B. The hydraulic (1214H)+spring data correspond to “orifice c” in Figure 9A. The hydraulic (1210M)+spring data correspond to “orifice b” in Figure 10. Among the tested dampers, the hydraulic 1210M damper showed the largest vertical GRF; peak vertical GRF of 6.3 BW are observed, almost twice as much as the “spring only” case. The viscous dampers 1214H and 1210M shifted the peak of their legs' vertical GRF to an earlier point in time, compared to the spring-leg and the spring+diaphragm-leg (Figure 11).

DISCUSSION

A primary objective of this study was to test how physical dampers could be exploited for locomotion tasks by characterizing multiple available technical solutions. Our numerical model predicted three crucial aspects: (1) a pure viscous damper generally performs better than a pure Coulomb damper (Figure 4); (2) higher damping rates result in better

rejection of ground disturbances (Figure 4A), however at the cost of higher dissipation at reference height (Table 2); (3) characteristic work loop shapes for pure viscous and Coulomb damper during leg-drop (Figure 9C). Our hardware findings show that neither of the tested physical dampers approximates as pure viscous or pure Coulomb dampers. The experiments also suggest that the mapping between dissipated energy and damping rates is concealed by the dynamics of the impact and the non-linearity of the force-velocity characteristics of the leg in the stance phase. Therefore, it is vital to test damping in a real leg at impact because the behavior is not merely as expected from the data sheets and the simple model.

Figure 7 characterizes how the hydraulic damper dissipates energy during a free drop. The experimental results show that the dissipated energy of the hydraulic damper scales with drop height (Figure 7A) and weight (Figure 7C), but less intuitively, it reduces with increasing damping rates (Figure 7B). This can be partially interpreted in the context of an ideal viscous damper for which the effective dissipated energy $E_{\text{effective}}$ would be calculated as in,

$$E_{\text{effective}} = \int F_p(t) dy_p = \int (d_v \cdot v_p(t)) dy_p \quad (13)$$

where $F_p(t)$ is the damper piston force and y_p is the piston displacement, $v_p(t)$ the corresponding velocity. When increasing the drop height, the velocity at impact is increased, so is $v_p(t)$. With the assumption of Equation (13), this results in higher damping forces $F_p(t)$, and thus, dissipated energy $E_{\text{effective}}$, as seen in Figure 7A. The heavier drop weight leads to slower deceleration. Therefore the velocity profile $v_p(t)$ is increased, which also leads to higher dissipation $E_{\text{effective}}$ (Figure 7B). An orifice setting of high damping rate will increase the damping coefficient d_v . However, the velocity profile $v_p(t)$ is expected

to reduce due to higher resistance. This simple analogy shows that the coupling between damping coefficient d_v and velocity profile $v_p(t)$ makes it difficult to predict the energy dissipation by setting the orifice and serves as an interpretation of why adjusting the orifice generates a relatively small adjustment of 10% (81 mJ–89 mJ) of the dissipated energy. Also, the impact phase (time for the damper to output its designed damping force under sudden load) introduces additional non-linearity to the output force profile. Overall, the results in **Figure 7** indicate that we can approximate the damping force produced by the hydraulic damper to be viscous and adjustable—as such dampers are typically designed (Dixon, 2008)—, but the mapping of energy dissipation to orifice setting is difficult to predict in a dynamic scenario.

The approximation as a linear, velocity dependent damper allows us to rapidly estimate energy dissipation in simulation, over a range of parameters. However, the exact mapping of the hardware leg/spring/damper energy dissipation to orifice setting is difficult to predict, when basing the estimation only on the isolated-damper drop experiments from **Figure 7**. Instead, the leg/spring/damper experiments show that the energetic losses from the impact remove 31 mJ energy, compared to 59 mJ damper losses. The high amount of force oscillations at impact (up to 1 BW, **Figure 8A**) during the first 3% leg length change leads us to believe that these impact oscillations move the damper's dynamic working range, i.e., its resulting instantaneous force and velocity. The oscillations are likely caused by unsprung mass effects of the leg/spring/damper structure, and could not be captured in an isolated-damper setup, or—at least not easily—in a simulation.

The work loops of leg drop experiments (**Figure 8**) show the effects of our tested dampers on a legged system. From touch-down to mid-stance (*leg flexion*), the “free drop” curves show a larger negative work compared to the “slow drop” curves, illustrating that the damper absorbs extra energy. The returning curves (mid-stance to lift-off) of the hydraulic damper aligns well with the “slow drop” curve, indicating the damper is successfully detached due to slackness cable while the spring recoil. **Figure 8B** shows that the “free drop” force of the diaphragm damper is slightly higher than “slow drop” force in the first half of the leg extension phase. This discrepancy is likely caused by the elastic force component of the diaphragm damper due to sudden expansion of the air chamber volume. The elastic component seems to dominate the damper behavior, which thus acts mostly as an air spring. By separating its energetic components (Equation 12), we found that the hydraulic damper produces a viscous-like resistance higher than the diaphragm damper (59 vs. 2 mJ), indicating the hydraulic damper is more effective in dissipating energy under drop impact. Hence, the hydraulic damper shows more viscous behavior, while the diaphragm damper is more elastic.

Physical damping in the system comes at the cost of energy loss, and to maintain periodic hopping, it becomes necessary to replenish energy that is dissipated by damping (E_{D_0}). Therefore, there is a trade-off to consider: simulation results show that higher damping results in faster rejection of ground perturbation at the price of more energy consumption at reference drop

height (**Table 2, Figure 4**). An adjustable damper would partly address this problem: on level ground, the damping rate could be minimal, and on rough terrain increased. The adjustability of the two dampers is illustrated in **Figures 9A,B**. We discuss the adjustability from both energy dissipation and dynamic behavior perspectives.

Compared with the spring-only results, both the hydraulic and the diaphragm damper reduced the maximum leg flexion and dissipated more energy. The orifice setting changes the shape of the work loop differently for the two setups. For the hydraulic damper (**Figure 9A**), orifice setting-*c* shrinks the work loop from left edge, indicating more resistance is introduced by the damper to reduce leg flexion. For the diaphragm damper (**Figure 9B**), orifice setting-*c* not only shrinks the work loop, but also increases its slope. We interpret this as the elastic contribution of air: relatively fewer air enters through the smaller orifice, but instead acts as an in-parallel spring.

Concerning energy dissipation, changes of orifice settings led to relatively small changes in effective dissipated energy $E_{\text{effective}}$: 150 to 156 mJ for the hydraulic damper, and 100 to 102 mJ for the diaphragm damper. Even for the other damper model (1210M), which dissipates high amounts of energy, changes in orifice setting change the work loop shape drastically, but not the dissipated energy (395 mJ vs. 401 mJ).

Similar to the isolated damper drop, the data (**Figures 9A,B**) shows that specific orifice settings introduce more resistance, but not necessarily lead to higher energy dissipation, for both hydraulic and diaphragm damper. However, in our simplified numerical leg model, an increase in viscous damping coefficients leads to a systematic increase of dissipated energy (**Table 2**), and a sharper tip at the left side of the work loop (**Figure 9C**). The discrepancy is likely due to the non-linear coupling between the damper mechanics and the leg dynamics in the hardware setup: (1) The damping force generated by the fluid dynamics in the orifice only approximates a linear viscosity (Dixon, 2008); (2) the impact loading on both the nonlinear leg structure and the damper. This makes the prediction of the energy dissipation not straight-forward based on our simplified numerical leg model, and points toward the need of a combined approach between simulation and hardware testing to fully understand physical damping in a legged system.

Viscous, velocity dependent damping alters the leg's loading characteristics, and leads to a peak force at the instance of touch-down. As a result, the vertical GRF is increased in the early stance phase, shifting and increasing the peak vertical GRF before mid-stance (**Figure 11A**). When designing a legged system with a viscous damper, its increasing load on the mechanical structure should be considered.

The selection of viscous dampers depends on the task. High damping can fully reject disturbances in a single cycle, but lower damping could have energetic benefits. Here we looked for a damper that would dissipate significant negative work ($\frac{E_{\text{viscous}}}{E_{T_0}} \approx 10\% - 15\%$) in form of viscous damping. The air-filled diaphragm damper lead to insufficient energy losses (2%), but the hydraulic dampers dissipated 10% and 60% of the system's total energy (**Table 4**).

Drawing conclusions about animal locomotion based on the here presented leg-drop experiments is somewhat early. However, observations from Müller et al. (2014, Table 1, p.2288) indicate that leg forces can increase at unexpected step-downs during locomotion experiments. Further, Kalveram et al. (2012) suggests in a comparison of experimental human hopping and numerical simulations that damping may be the driving ingredient in passive stabilization against ground-level perturbations. We are consequently excited about the here presented results of viscous dampers mounted in parallel to a leg's spring, producing adaptive forces without the need for sensing.

CONCLUSION

We investigated the possibility to exploit physical damping in a simplified leg drop scenario as a template for the early stance phase of legged locomotion. Our results from a) numerical simulation promote the use of adjustable and viscous damping over Coulomb damping to deal with a ground perturbation by physical damping. As such, we b) tested two technical solutions in hardware: a commercial, off-the-shelf hydraulic damper, and a custom-made, rolling diaphragm damper. We dissected the observed dissipated energy from the hardware damper-spring leg drops, into its components, by experimental design. The resulting data allowed us to characterize dissipation from the early impact (unsprung-mass effects), viscous damping, Coulomb damping, and orifice adjustments *individually, and qualitatively*. The rolling diaphragm damper features low-Coulomb friction, but dissipates only low amounts of energy through viscous damping. The off-the-shelf, leg-mounted hydraulic damper did exhibit high viscous damping, and qualitatively showed the expected relationship between impact speed, output force and negative work. Changes in orifice setting showed only minor changes in overall energy dissipation, but can lead to large changes in leg length dynamics, depending on the chosen technical

damper. Hence, switching between different viscous, hydraulic dampers is an interesting future option. Our results show how viscous, hydraulic dampers react velocity-dependent, and create an instantaneous, physically adaptive response to ground-level perturbations without sensory-input.

DATA AVAILABILITY STATEMENT

The datasets generated for this study are available on request to the corresponding author.

AUTHOR CONTRIBUTIONS

AM contributed to concept, hardware design, experimental setup, experimentation, data discussion and writing. FI contributed to concept, simulation framework, experimental setup, data discussion and writing. DH and AB-S contributed to concept, data discussion and writing.

ACKNOWLEDGMENTS

The authors thank the International Max Planck Research School for Intelligent Systems (IMPRS-IS) for supporting AM and FI, the China Scholarship Council (CSC) for supporting AM, and the Ministry of Science, Research and the Arts Baden-Württemberg (Az: 33-7533.-30-20/7/2) for supporting DH, and the Max Planck Society for supporting AB-S with a Max Planck Groupleader Grant.

SUPPLEMENTARY MATERIAL

The Supplementary Material for this article can be found online at: <https://www.frontiersin.org/articles/10.3389/frobt.2020.00110/full#supplementary-material>

REFERENCES

- Abraham, I., Shen, Z., and Seipel, J. (2015). A nonlinear leg damping model for the prediction of running forces and stability. *J. Comput. Nonlinear Dyn.* 10:051008. doi: 10.1115/1.4028751
- Bledt, G., Wensing, P. M., Ingersoll, S., and Kim, S. (2018). "Contact model fusion for event-based locomotion in unstructured terrains," in *2018 IEEE International Conference on Robotics and Automation (ICRA)* (Brisbane, QLD: IEEE), 1–8. doi: 10.1109/ICRA.2018.8460904
- Blickhan, R., Seyfarth, A., Geyer, H., Grimmer, S., Wagner, H., and Günther, M. (2007). Intelligence by mechanics. *Philos. Trans. R. Soc. Lond. Ser. A* 365, 199–220. doi: 10.1098/rsta.2006.1911
- Daley, M. A., and Biewener, A. A. (2006). Running over rough terrain reveals limb control for intrinsic stability. *Proc. Natl. Acad. Sci. U.S.A.* 103, 15681–15686. doi: 10.1073/pnas.0601473103
- Dixon, J. C. (2008). *The Shock Absorber Handbook*. West Sussex: John Wiley & Sons. doi: 10.1002/9780470516430
- Drama, O., and Spröwitz, A. (2020). Trunk pitch oscillations for energy trade-offs in bipedal running birds and robots. *Bioinspir. Biomimet.* 15:036013. doi: 10.1088/1748-3190/ab7570
- Garcia, E., Arevalo, J. C., Munoz, G., and Gonzalez-de Santos, P. (2011). Combining series elastic actuation and magneto-rheological damping for the control of agile locomotion. *Robot. Auton. Syst.* 59, 827–839. doi: 10.1016/j.robot.2011.06.006
- Ghazi-Zahedi, K., Haeufle, D. F. B., Montúfar, G., Schmitt, S., and Ay, N. (2016). Evaluating morphological computation in muscle and DC-motor driven models of human hopping. *Front. Robot. AI* 3:42. doi: 10.3389/frobt.2016.00042
- Grimminger, F., Meduri, A., Khadiv, M., Viereck, J., Wuthrich, M., Naveau, M., et al. (2020). An open torque-controlled modular robot architecture for legged locomotion research. *IEEE Robot. Automat. Lett.* 5, 3650–3657. doi: 10.1109/LRA.2020.2976639
- Haeufle, D. F. B., Grimmer, S., and Seyfarth, A. (2010). The role of intrinsic muscle properties for stable hopping - stability is achieved by the force-velocity relation. *Bioinspir. Biomimet.* 5:016004. doi: 10.1088/1748-3182/5/1/016004
- Haeufle, D. F. B., Günther, M., Wunner, G., and Schmitt, S. (2014). Quantifying control effort of biological and technical movements: an information-entropy-based approach. *Phys. Rev. E* 89:012716. doi: 10.1103/PhysRevE.89.012716
- Havoutis, I., Semini, C., Buchli, J., and Caldwell, D. G. (2013). "Quadrupedal trotting with active compliance," in *2013 IEEE International Conference on Mechatronics (ICM)* (Vicenza: IEEE), 610–616. doi: 10.1109/ICMECH.2013.6519112
- Hu, C.-J., Wang, T.-K., Huang, C.-K., and Lin, P.-C. (2019). A torque-actuated dissipative spring loaded inverted pendulum model with rolling contact

- and its application to hexapod running. *Bioinspir. Biomimet.* 14:026005. doi: 10.1088/1748-3190/aafc4e
- Hutter, M., Gehring, C., Bloesch, M., Hoepflinger, M. A., Remy, C. D., and Siegwart, R. (2012). "Starleth: a compliant quadrupedal robot for fast, efficient, and versatile locomotion," in *Adaptive Mobile Robotics*, eds A. K. M. Azad, N. J. Cowan, M. O. Tokhi, G. S. Virk (Baltimore, MD: World Scientific), 483–490. doi: 10.1142/9789814415958_0062
- Hutter, M., Gehring, C., Jud, D., Lauber, A., Bellicoso, C. D., Tsounis, V., et al. (2016). "Anymal - a highly mobile and dynamic quadrupedal robot," in *2016 IEEE/RSJ International Conference on Intelligent Robots and Systems (IROS 2016)* (Daejeon), 38–44. doi: 10.1109/IROS.2016.7758092
- Josephson, R. K. (1985). Mechanical power output from striated muscle during cyclic contraction. *J. Exp. Biol.* 114, 493–512.
- Kalouche, S. (2017). "Goat: a legged robot with 3D agility and virtual compliance," in *2017 IEEE/RSJ International Conference on Intelligent Robots and Systems (IROS)* (Vancouver, BC), 4110–4117. doi: 10.1109/IROS.2017.8206269
- Kalveram, K. T., Haeufle, D. F. B., Seyfarth, A., and Grimmer, S. (2012). Energy management that generates terrain following versus apex-preserving hopping in man and machine. *Biol. Cybernet.* 106, 1–13. doi: 10.1007/s00422-012-0476-8
- Mochon, S., and McMahon, T. A. (1980). Ballistic walking: an improved model. *Math. Biosci.* 52, 241–260. doi: 10.1016/0025-5564(80)90070-X
- More, H. L., and Donelan, J. M. (2018). Scaling of sensorimotor delays in terrestrial mammals. *Proc. R. Soc. B* 285:20180613. doi: 10.1098/rspb.2018.0613
- More, H. L., Hutchinson, J. R., Collins, D. F., Weber, D. J., Aung, S. K. H., and Donelan, J. M. (2010). Scaling of sensorimotor control in terrestrial mammals. *Proc. R. Soc. B Biol. Sci.* 277, 3563–3568. doi: 10.1098/rspb.2010.0898
- Müller, R., Tschiesche, K., and Blickhan, R. (2014). Kinetic and kinematic adjustments during perturbed walking across visible and camouflaged drops in ground level. *J. Biomech.* 47, 2286–2291. doi: 10.1016/j.jbiomech.2014.04.041
- Rummel, J., and Seyfarth, A. (2008). Stable running with segmented legs. *Int. J. Robot. Res.* 2, 919–934. doi: 10.1177/0278364908095136
- Ruppert, F., and Badri-Spröwitz, A. (2019). Series elastic behavior of biarticular muscle-tendon structure in a robotic leg. *Front. Neurobot.* 13:64. doi: 10.3389/fnbot.2019.00064
- Secer, G., and Saranlı, U. (2013). "Control of monopodal running through tunable damping," in *2013 21st Signal Processing and Communications Applications Conference (SIU)* (Haspolat: IEEE), 1–4. doi: 10.1109/SIU.2013.6531557
- Seok, S., Wang, A., Chuah, M. Y. M., Hyun, D. J., Lee, J., Otten, D. M., et al. (2015). Design principles for energy-efficient legged locomotion and implementation on the MIT cheetah robot. *IEEE/ASME Trans. Mechatron.* 20, 1117–1129. doi: 10.1109/TMECH.2014.2339013
- Serafin, S. (2004). *The sound of friction: real time models, playability and musical applications* (Thesis). Department of Music, Stanford University, Stanford, CA, United States.
- Shen, Z., and Seipel, J. (2012). A fundamental mechanism of legged locomotion with hip torque and leg damping. *Bioinspir. Biomimet.* 7:046010. doi: 10.1088/1748-3182/7/4/046010
- Spröwitz, A., Tuleu, A., Vespignani, M., Ajallooeian, M., Badri, E., and Ijspeert, A. J. (2013). Towards dynamic trot gait locomotion: design, control, and experiments with cheetah-cub, a compliant quadruped robot. *Int. J. Robot. Res.* 32, 932–950. doi: 10.1177/0278364913489205
- Tsagarakis, N. G., Morfey, S., Dallali, H., Medrano-Cerda, G. A., and Caldwell, D. G. (2013). "An asymmetric compliant antagonistic joint design for high performance mobility," in *2013 IEEE/RSJ International Conference on Intelligent Robots and Systems* (Tokyo: IEEE), 5512–5517. doi: 10.1109/IROS.2013.6697155
- Werner, A., Turlej, W., and Ott, C. (2017). "Generation of locomotion trajectories for series elastic and viscoelastic bipedal robots," in *2017 IEEE/RSJ International Conference on Intelligent Robots and Systems (IROS)* (Vancouver, BC: IEEE), 5853–5860. doi: 10.1109/IROS.2017.8206476
- Whitney, J. P., Chen, T., Mars, J., and Hodgins, J. K. (2016). "A hybrid hydrostatic transmission and human-safe haptic telepresence robot," in *Proceedings of ICRA* (Stockholm: IEEE), 690–695. doi: 10.1109/ICRA.2016.7487195
- Whitney, J. P., Glisson, M. F., Brockmeyer, E. L., and Hodgins, J. K. (2014). "A low-friction passive fluid transmission and fluid-tendon soft actuator," in *Proceedings of IROS* (Chicago, IL: IEEE), 2801–2808. doi: 10.1109/IROS.2014.6942946
- Zahedi, K., and Ay, N. (2013). Quantifying morphological computation. *Entropy* 15, 1887–1915. doi: 10.3390/e15051887

Conflict of Interest: The authors declare that the research was conducted in the absence of any commercial or financial relationships that could be construed as a potential conflict of interest.

Copyright © 2020 Mo, Izzi, Haeufle and Badri-Spröwitz. This is an open-access article distributed under the terms of the Creative Commons Attribution License (CC BY). The use, distribution or reproduction in other forums is permitted, provided the original author(s) and the copyright owner(s) are credited and that the original publication in this journal is cited, in accordance with accepted academic practice. No use, distribution or reproduction is permitted which does not comply with these terms.

Diaphragm Ankle Actuation for Efficient Series Elastic Legged Robot Hopping

Marco Bolignari^{1,2}, An Mo³, Marco Fontana² and Alexander Badri-Spröwitz³

Abstract—The observation of the anatomy of agile animals and their locomotion capabilities emphasizes the importance of fast and lightweight legs and confirms the intrinsic compliance integrated into muscle-tendon units as a major ingredient for energy efficient and robust locomotion. This quality is especially relevant for distal leg segments which are subject to aggressive dynamics. Legged robots are accordingly designed to improve dynamic performance by lightweight mechanisms combined with series elastic actuation systems. However, so far no designs are available that feature all characteristics of a perfect distal legged locomotion actuator such as a lightweight and low-inertia structure, with high mechanical efficiency, no stick and sliding friction, and low mechanical complexity. With this goal in mind, we propose a novel robotic leg which integrates all above features. Specifically, we develop, implement, and characterize a bioinspired robot leg that features a lightweight Series ELastic Diaphragm distal Actuator (SELDA) for active control of foot motion. We conducted experiments to compare two leg configurations, with and without foot actuation, to demonstrate the effectiveness of the proposed solution in agile forward hopping controlled by a central pattern generator. We studied how tuning SELDA’s activation timing can adjust the robot’s hopping height by 11% and its forward velocity by 14%, even with comparatively low power injection to the distal joint.

I. INTRODUCTION

Lightweight actuation of distal joints is proven effective by animals and humans, which can run, jump, and hop with agility, robustness and efficiency based on muscle-tendon structures embedded in multi-segment legs. Animals feature low mass and moment of inertia at distal locations, with heavy actuators (muscles) mounted proximally [1], [2], [3]. These muscle-tendon units can be presented as series elastic actuators [2], [4]. The exact functionality of the leg segment architecture, networks of muscle-tendon units, and their mechanical and control coupling are not yet understood and are the focus of ongoing research [5], [6], [7], [8]. In human walking, much research focuses on ankle kinematics and dynamics, the coupling of proximal and distal leg joints through elastic structures and control [9], [10], and the resulting impact on locomotion efficiency, agility, and robustness [11], [12], [13]. In this context, catapult-like power

This work was supported by Department of Excellence grant of Scuola Superiore Sant’Anna, the International Max Planck Research School for Intelligent Systems, the China Scholarship Council, and the Max Planck Society. Gefördert durch die Deutsche Forschungsgemeinschaft (DFG)-449912641.

¹ Department of Industrial Engineering, University of Trento, 38123 Trento, Italy. [marco.bolignari]@unitn.it

² Institute of Mechanical Intelligence, Scuola Superiore Sant’Anna, 56127 Pisa, Italy. [marco.fontana]@santannapisa.it

³ Dynamic Locomotion Group, Max Planck Institute for Intelligent Systems, 70569 Stuttgart, Germany. [mo] [sprowitz]@is.mpg.de

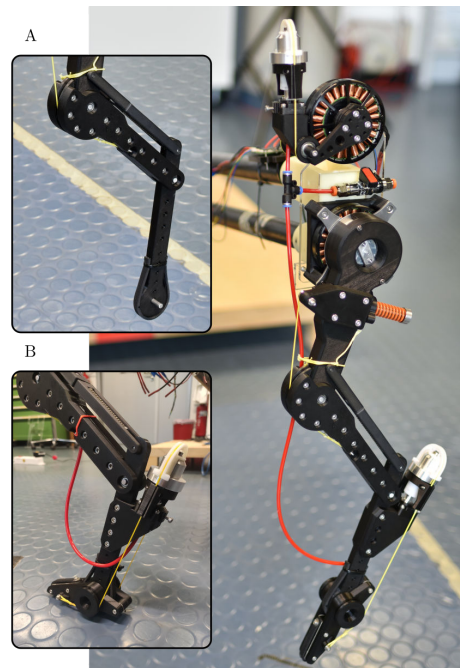


Fig. 1. Experimental prototype of the bio-inspired leg. Detail figures on the left show the two configurations compared in this work. *Configuration-A*: traditional bio-inspired layout. *Configuration-B*: novel configuration with ‘foot’ segment remotely actuated by a compliant pneumatic transmission.

output rooted in lower-leg muscle-tendon structures has been observed that exceeds the muscle’s power output, by charging and discharging lower-leg series elasticities favourably [14], [15], [8]. These examples from biomechanics emphasize the potential to reduce energetic losses, simplify control and mechanics, and increase robustness and agility by leveraging on distally acting series elastic actuators in legged machines.

In robotic legs, the actuation of distal joints is often avoided because combinations of motors and gearboxes, perhaps combined with mechanical series elasticity [16], [17], come with high mass, moment of inertia, and mechanical complexity. Heavy actuators placed distally are energetically costly to be accelerated and decelerated through leg swing. For this reason, several power transmissions have been proposed for the remote actuation of distal joint with proximally located motors, Tab. I. Such transmissions can be achieved with cable (tendon), chain, and belt systems [7], [18], [19], but the design and control complexity of these systems increases notably when transferring the actuation over multiple joints. Simpler systems are possible when remote actuation bypasses joints by transmitting power di-

rectly into the target location. For this reason, Bowden-cable power transmissions have been explored [20], however, high friction between the inner cable and the outer sheath leads to control difficulties and power losses that are prohibitive for mobile application [20]. Alternatively, hydraulic [21], [22] or pneumatic [23] cylinders and pneumatic artificial muscles (PAMs) [24] can be employed for distal actuation. Generally, fluidic actuation is less energy efficient and is associated with complex and bulky parts such as heavy pumps, manifolds, and accumulators that can be only integrated into large-scale robotic systems.

Rolling diaphragm transmissions [25], [26] are novel passive devices that allow the proximal placement of electrical motors with low-friction actuation. Rolling diaphragm actuation of distal joints combines the efficient power transmission of cable/tendon mechanisms with the flexibility of Bowden cables. Both hydraulic and pneumatic configurations are feasible [25]; high bandwidth and stiffness are achieved in the former case, and compliance and energy-storage capabilities are offered in the latter. Promising characteristics of high power, efficiency, mechanical transparency, excellent backdrivability, and simplified control and mechanical design [27] lead to robotic applications such as MRI-compatible backdrivable arms [28], fluid dampers [29], bio-inspired robots [26], and interactive robots [30].

TABLE I
MULTI LEG-JOINT ACTUATION SYSTEMS FOR LEGGED ROBOTS.

Technology	Weight	Design complexity	Force transparency
Coupled multi-joint motion			
Linkage [31]	fair	fair*, poor†	good
Tendon [7], chain [18], belt [19]	good	fair*, poor†	good
Decoupled multi-joint motion			
PAM [24]	good	poor	poor
Bowden cable [20]	good	good	poor
Hydraulic piston [22]	fair	fair	poor
Rolling diaphragm transmission	good	good	good

*in planar transmission, †in 3D transmission or over multiple joints.

In this work, we developed a first proof of concept of Series ELastic Diaphragm for distal Actuation (SELDA) that integrates the positive attributes of diaphragm transmission with a purposely tuned stiffness that provides the sought series elastic actuation (SEA) behaviour. With SELDA, we aim to develop hardware for agile legged hopping that is easy to control, is uncoupled from neighboring joint's movements and loads, is easy and flexible to mount, features a remote motor placement and a distal power output, is distally lightweight, inherently compliant, and mechanically efficient. To test our design, we built a lightweight bio-inspired leg with a remotely actuated foot segment. The foot's actuator is placed in the robot's torso and its torque is reflected at the ankle joint using a pneumatic rolling-diaphragm transmission with intrinsic compliance characteristics.

In the following sections, we present the mechanical design and controller details of SELDA, our series elastic diaphragm for ankle actuation. We present experiment-based characterizations of the pneumatic transmission and actuation, and a comparison of hopping performances between

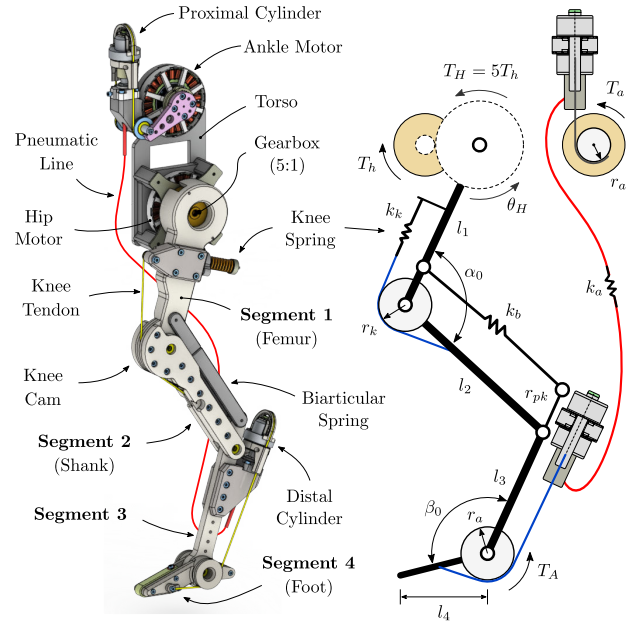


Fig. 2. Drawing of the proposed robotic leg equipped with the SELDA-actuated foot. *Left*: computer-aided design (CAD) picture. *Right*: schematic drawing.

two leg configurations (Fig. 1): configuration-A is a leg without a foot segment, inspired by our previous work [32], while configuration-B is a leg with a foot segment, actuated by SELDA. We compare both configurations by recording locomotion data of both robot legs when hopping forward. Configuration-B is tested a) in passive mode, i.e. without foot-motor actuation, to assess its compliance features, and b) in active mode, i.e., the ankle motor is actively controlled, to explore the effects of foot-actuation timing during the step cycle.

II. ROBOT DESIGN

Lightweight, under-actuated, compliant design of bio-inspired robotic legs proved effective for achieving agile locomotion with low control complexity [23], [33], [32]. However, previous leg designs have not explored the opportunity of introducing ankle actuation which is typically avoided due to the difficulty of independently actuating distal joints with low additional mechanical complexity and inertia.

In this work, we present a bio-inspired leg that is inspired by the design presented in [32] and further enriched by introducing a remotely-actuated, active ankle joint.

A. Leg architecture

Detailed schematics of the proposed robot leg are shown in Fig. 2. The robot features four-segment planar kinematics that mimics the compliant behavior of mammalian quadruped legs. In our design, two joints are active (hip and ankle) and two joints are passive (knee and biarticular mechanism). Segments 1, 2 and 3 are arranged in a pantograph configuration. Segment 1 is driven by the hip motor, which is the main actuation of the robot. The hip motor, equipped

TABLE II
ROBOT DESIGN PARAMETERS.

Parameters		Value
Robot mass (config. A)*	m_A	1.05 kg
Robot mass (config. B)	m_B	1.20 kg
Leg resting length	l_0	408 mm
Segment 1 length	l_1	150 mm
Segment 2 length	l_2	150 mm
Segment 3 length	l_3	140 mm
Segment 4 length	l_4	70 mm
Knee pulley radius	r_k	30 mm
Knee spring stiffness	k_k	10.9 N/mm
Bi-articular insertion radius	r_{pk}	32 mm
Bi-articular spring stiffness	k_b	9.8 N/mm
Ankle pulley radius	r_a	15 mm
Ankle stiffness (air spring)	k_a	0.2 Nm/rad
Knee resting angle	α_0	130°
Ankle resting angle	β_0	175°
Hip swing amplitude	A	18°
Hip oscillation frequency	f	1.65 Hz

*the ankle motor is not removed from the robot torso.

with a 5:1 gearbox, swings the leg forward and backwards during locomotion. Segments 2 and 3 are passive, instead. The knee joint is passively extended to a resting angle of $\alpha_0 = 130^\circ$ by the knee spring k_k acting on the knee cam. Segment 3 is passively constrained by the spring-loaded biarticular segment k_b that acts over two joints, parallel to the shank, which replicates the lower leg muscle-tendon apparatus of gastrocnemius muscle and Achilles tendon. The overall under-actuated pantograph-like leg can be modeled as a non-linear spring that stores elastic energy during deceleration following the touch-down and converts spring energy back to kinetic energy which accelerates the robot in the second half of the stance phase. The proposed design parameters, which are summarized in Tab. II, are selected to meet the requirement of $\approx 10\%$ leg compression at three times body weight loading, similar to running dogs [34].

The design introduces our novel SELDA system to remotely actuate the foot (segment 4) for enhanced control of the interaction with the ground. SELDA exploits a second source of actuation, which is the proximally-mounted ankle motor. The motor torque is delivered to the ankle utilizing a lightweight pneumatic transmission, which also provides series elastic compliance and thus additional energy storage capabilities to the robot. Details of the working principle and the design of the SELDA system are provided in the following sections.

B. SELDA working principle

Starting from the concept of hydrostatic transmissions developed for the remote actuation of high-performance robots [35], we introduce a pneumatic rolling-diaphragm transmission (called SELDA) for the actuation of distal joints of a compliant robotic leg. The use of air instead of liquids, employed in other applications [27], makes it possible to merge functionalities of remote and series-elastic actuation in a single lightweight, efficient and compact device, showing convenient attributes such as low static friction, zero backlash, reduced complexity, and low-cost. A detailed scheme of the system is shown in Fig. 3 (left

and center). To minimize weight, we take advantage of the asymmetrical torque requirements of locomotion at the ankle joint, which provides large torques during the push-off phase and small torques for backward flexion during the swing phase. According to this consideration, the SELDA system is conceived as a single-acting device, able to transmit torques to the foot in the direction of the push-off. The flexion of the foot is passively actuated during the touch-down phase, when landing on the ground, as a result of the robot's weight/inertia. This allows the use of a single pneumatic cylinder placed distally, where mass reduction is critical, and one single cylinder placed in the proximal actuation group. Identical cylinders and pulleys (with radius r_a) are chosen at proximal and distal sides to determine a 1:1 static torque reflection between the remote motor and the ankle joint. The proposed cylinder units (i.e. cylinder, piston, rolling diaphragm and supporting frame) weight 42 g each, adding relatively low inertia distally.

The system is initially pressurized up to a bias pressure p_0 that acts on both cylinders in the direction of expansion (notice that diaphragms require the internal pressure to be always higher than the atmospheric pressure in any working condition to prevent the membrane jamming [25]). Torque T_a , generated by the motor, causes the proximal cylinder to compress and the air pressure p to increase. The pressure propagates through the pneumatic line up to the distal cylinder along the direction of expansion, generating a torque

$$T_A = r_a A_e p = T_0 + r_a A_e \Delta p \quad (1)$$

where constant A_e is the equivalent area of the diaphragm, $T_0 = r_a A_e p_0$ is the preload torque generated by the initial pressurization and Δp is the pressure increment due to volume variation $\Delta V = A_e r_a (\theta_A - \theta_a)$ generated by motor and ankle rotations. Experimental evidence in Sec. II-E shows that the assumption of adiabatic process well describes the response of SELDA, thus

$$T_A = r_a A_e p_0 V_0^\gamma / (V_0 + \Delta V)^\gamma, \quad (2)$$

where $\gamma = 1.4$ is the adiabatic index of air. A simpler description of the system is offered by the following linearised equation in the case of sufficiently small volume variations for the initial volume V_0 :

$$T_A \approx r_a A_e p_0 + \gamma r_a^2 A_e^2 \frac{p_0}{V_0} (\theta_a - \theta_A) = T_0 + k_a (\theta_a - \theta_A) \quad (3)$$

Indeed, the pneumatic transmission can be modeled as a linear spring with $k_a = \gamma r_a^2 A_e^2 p_0 / V_0$ stiffness and T_0 preload torque. Notice that (3) provides the lower bound of k_a , since the nonlinear response of air makes linearised stiffness larger for higher compression. In general, the system can be approximately modelled as a typical series-elastic system with 2-dof (Fig. 3 center), namely θ_a and θ_A . I_a and I_A are the inertia of proximal and distal bodies, which are connected by a torsional spring with stiffness k_a . It is worth noticing that this model offers a conservative estimation of the torque bandwidth of the actuation system, which is limited by the natural frequency $\omega_n = \sqrt{k_a / I_A}$.

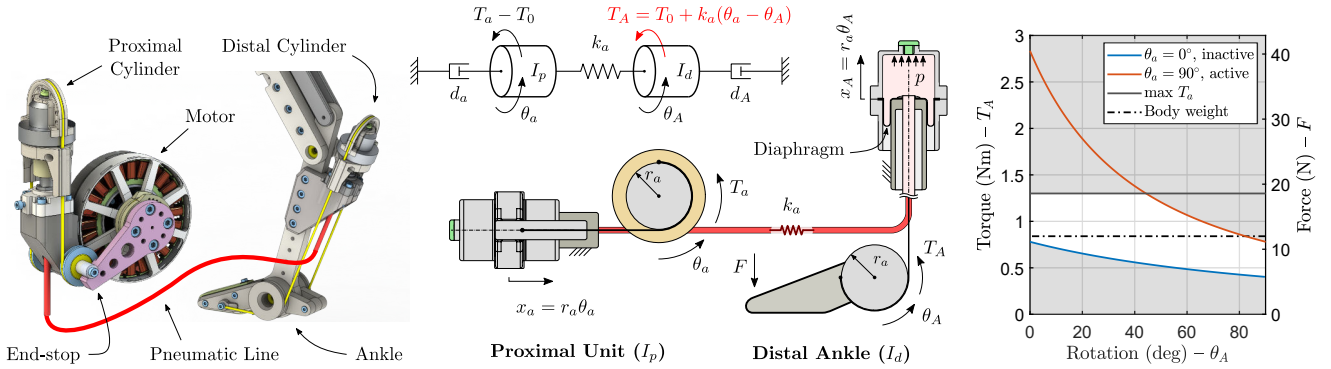


Fig. 3. SELDA system. *Left:* details of the proximal and distal units. *Center:* scheme and linearized description of the transmission system. *Right:* representation of the feasible range (in white background) of ankle torque T_A and foot force F as function of motor and ankle position.

C. SELDA dimensioning and details of implementation

Starting from kinematics observations, then confirmed by experiments in Fig. 6, we firstly impose a requirement on the minimum ankle rotation range of $\theta_A^m = 90^\circ$. With this choice, the use of rolling diaphragms poses an intrinsic design trade-off between added distal mass and transmission stiffness. Equation (3) suggests that the selection of membranes with large effective area A_e and thus longer stroke x_A^m (which allows for larger values of r_a) would produce higher stiffness and bandwidth. However, large-diameter cylinders come with larger distal mass, which degrades the locomotion dynamical properties. According to the relation between the diaphragm stroke, the required ankle rotation angle and the pulley radius, which reads as $\theta_A^m = x_A^m / r_a$, the choice of a small pulley radius r_a allows the use of smaller diaphragms (which have a limited stroke), leading to a lighter distal cylinder. However, the transmission stiffness (as well as the transmissible torque, for a given maximum motor torque) decreases. In this regard, an under-dimensioned low-stiffness air tendon is pursued, i.e., the torque T_A , which is transmitted to the foot, is not supposed to fully sustain the peak ground reaction force during stance (three times body weight, 36 N in our case). Thus, the presented design lets the inertial forces be absorbed by the heel, which touches the ground during stance like in many natural runners. Specifically, we set as a target the generation of a foot force F that is about able to balance the body weight in static conditions; ≈ 12 N. Because ground reaction forces drop to zero between mid-stance and lift-off, even small ankle torques from the active ankle actuation are expected to effectively alter the timing of the energy transfer to the ground during push-off and influence the hopping dynamics in terms of forward speed and hopping height. To meet these requirements, we select DM3-20-20 rolling diaphragms by Fujikura Composites (268.8 mm² effective area, 24 mm full stroke, 20 mm cylinder diameter). A pulley radius $r_a = 15$ mm guarantees a rotation range larger than 90° . A stiffness $k_a = 0.12$ Nm/rad and a torque bandwidth larger than 6 Hz (considered enough for open loop hopping) are obtained by selecting an initial pressure $p_0 = 0.1$ MPa. In the

passive configuration, i.e., the inactive SELDA-motor at the end-stop ($\theta_a = 0^\circ$), the force on the foot tip varies from $F = 6$ N when extended ($\theta_A = 90^\circ$), to $F = 11$ N when fully flexed ($\theta_A = 0^\circ$). This is also the force profile that is delivered when the foot lands on the ground. In the active configuration, when the SELDA motor fully compresses the proximal cylinder, the foot should generate a force of $F = 11$ N when extended and a force of $F = 42$ N when flexed. However, both are limited to 19 N by the maximum available motor torque. The workspace of feasible forces is highlighted in Fig. 3 (right), where achievable distal torques/forces are represented at different values of θ_a .

Hip and ankle joints are actuated by brushless motors (model MN7005-KV115) by *T-Motor* with 1.3 Nm maximum rated torque. The hip motor is equipped with an RS3505S planetary gearbox by *Matex* with 5:1 gear ratio. The motor positions are measured by AEAT8800-Q24 rotary encoders by *Broadcom* with 12 bit resolution. We use open-source drivers (Micro-Driver, [36]) for motor control, current sensing, and encoder reading. The Micro-Driver board is capable of dual motor Field Oriented Control (FOC) at 10 kHz. We implemented our controller on a single board computer (Raspberry Pi 3B+) with a control frequency of 1 kHz. The pneumatic line is implemented with a 70 mm long polyurethane hose with a $\phi 1.5$ mm inner diameter. The internal air volume of the transmission in the non-deformed configuration is 16.2 cm³. The knee and biarticular springs are implemented with SWS14.5-45 and UBB10-60 springs, respectively (*MISUMI*).

D. Experimental configurations

To investigate the influence of ankle actuation, i.e., power injection at distal joints on locomotion performances, two different leg configurations have been designed for testing and comparison (Fig. 1). 1) a configuration-A leg without actuated ankle and related components, which is equipped with a rubber foot directly connected to the segment 3; 2) a configuration-B leg which is fully equipped with the SELDA ankle actuation system described previously. The

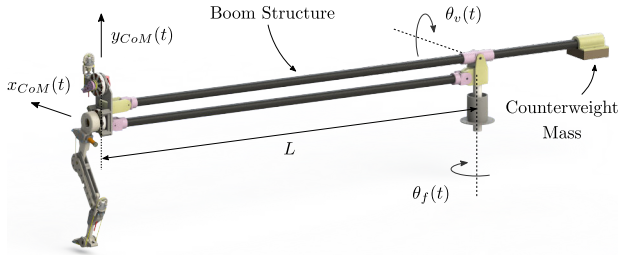


Fig. 4. Experimental test bench: the leg is constrained to a rotating boom to allow horizontal and vertical displacement only. Torso rotation and lateral displacement are prevented. The boom setup allows the robot to hop continuously over long distances.

configuration-A leg weighs less, i.e., in total 1.05 kg, due to the lack of the distal cylinder-ankle unit.

A custom setup that allows comparing both leg configurations and their locomotion patterns fairly was used for testing. The robot legs are minimally instrumented—torque and position measurements of distal joints are not used for control—and each actuator is controlled with feedforward reference trajectories, since locomotion stability and robustness are supported by compliant leg mechanics. Please see Sec. III for details. Initially, experiments of configuration-A are compared to those of the passive configuration-B. Configuration-B implements the SELDA system but its proximal ankle motor is inactive, to analyse the elastic foot contribution. Then, configuration-B is tested in the active mode to investigate the different activation timings of the ankle motor during the step cycle.

The trunk of the robot is mounted to a boom structure, Fig. 4 that prevents torso rotations, eliminating the need for trunk pitch control. The boom arm rotates around a vertical axis by angle θ_f , which allows the robot to jump along a circular path. The length of boom rods L is 1.55 m and the travelled distance over a complete revolution is 9.73 m. A counterweight balances the mass of boom rods. The position of the robot center of mass, x_{CoM} and y_{CoM} , are evaluated as a function of θ_f and θ_v angles. The boom rotation angles θ_f and θ_v are measured by two 102-V rotary encoders by AMT with 11 bit resolution.

E. Transmission characterization

To verify the SELDA model introduced in (2), we measured the motor torque while the foot segment was fixed at $\theta_A = 90^\circ$ and the actuator was progressively rotated along its full stroke. We manually applied a full-stroke rotation to the actuator rotor with an instrumented lever arm. A load cell (model 3133.0, *Phidgets*) was mounted to measuring the applied torque. Fig. 5 shows the measured data compared to model data (2), at a pre-pressurization of 0.1 MPa. Globally, the analytical model (2) well describes the behaviour of the experimental data, with observable mismatches due to hysteresis (Fig. 5). In separated experiments, we measured a motor friction/hysteresis of approximately 15 mNm to 25 mNm and a transmission friction/hysteresis due to diaphragms, cables and bearings of approximately

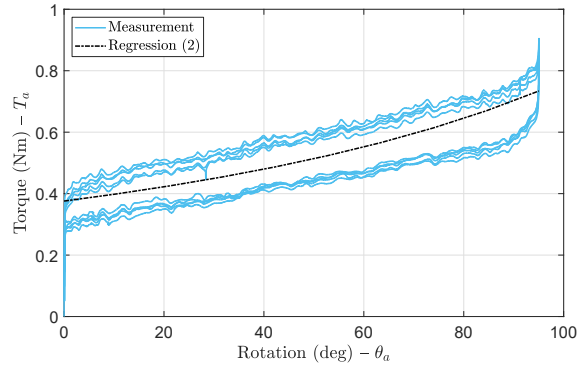


Fig. 5. Characterization of the input-actuation response of the SELDA system. The experimental data and the analytical model (2) are compared.

35 mNm to 50 mNm, explaining the observed hysteresis loop.

III. HOPPING EXPERIMENTS

This section presents our hopping experiments. Sec. III-A describes the experimental configuration chosen for gait analysis; Sec. III-B compares the performance of the leg with and without the foot segment, i.e., configuration-A and passive configuration-B; Sec. III-C presents our first investigation of the effect of distal actuation, mainly focusing on kinematic effects in terms of gait velocity, step length and step height. A typical gait obtained during the experiments with SELDA system is shown in Fig. 6.

A. Experimental configuration

The robot response is characterized in case of simple control strategies in order to emphasize intrinsic self-stabilizing response through compliant design. The hip joint is position controlled along a sinusoidal trajectory:

$$\hat{\theta}_H = A \sin(2\pi f t) \quad (4)$$

where constant A is the hip trajectory amplitude and constant f defines the hopping frequency. Hip oscillation amplitude $A = 18^\circ$ and locomotion frequency $f = 1.65$ Hz are common for all of our experiments. Note that the chosen parameter set is likely not optimal for both configurations; we expect that each configuration has its dynamics. Nevertheless, we keep the parameter common for a consistent comparison between leg configurations. An example hip trajectory is shown in Fig. 7. The trajectory tracking is performed through a PD controller $T_H = k_p e(t) + k_d \dot{e}(t)$, where T_H is the commanded torque to the hip joint and variable $e(t)$ is the tracking error $e(t) = \hat{\theta}_H - \theta_H$. The controller behaves like a virtual spring-damper element acting between the reference trajectory $\hat{\theta}_H$ and the hip joint with stiffness value k_p and damping coefficient k_d . Parameters $k_p = 40$ and $k_d = 0.35$ are fixed for all experiments.

To investigate the influence of the distal actuation, we focus on the actuation timing of the foot segment during the step cycle. A step torque reference of 1 Nm is commanded to the ankle motor: the initial actuation instant varies in the range 5% to 30% of the step cycle, as shown by the

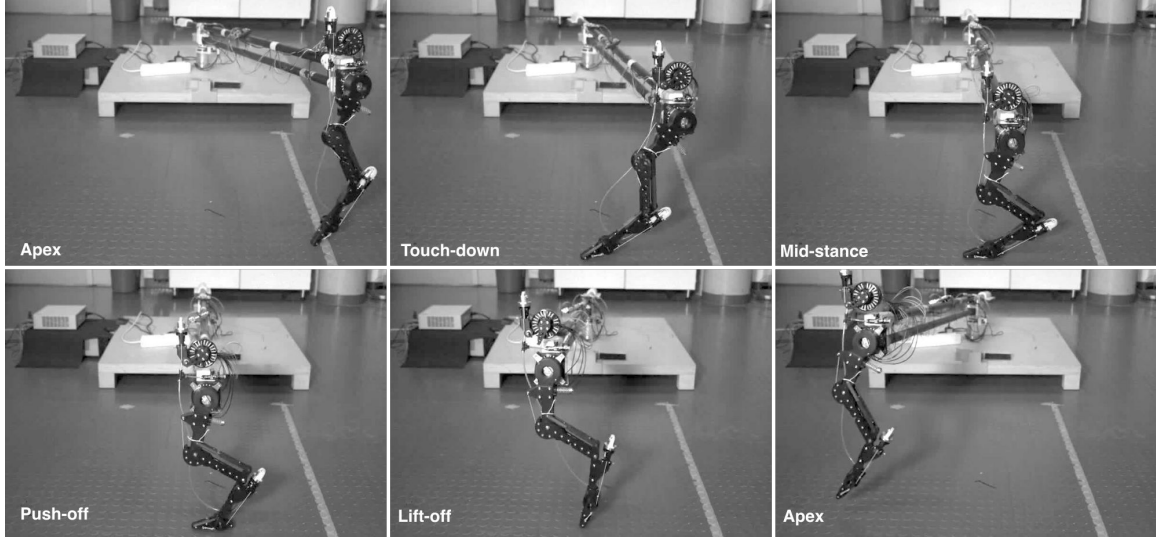


Fig. 6. Gait cycle snapshots from apex to apex, taken from high-speed video footage. A *delay* was programmed to trigger push-off actuation. Step cycle time ($T = 1/f$, f is frequency) is 606 ms, or 1.65 Hz hopping frequency.

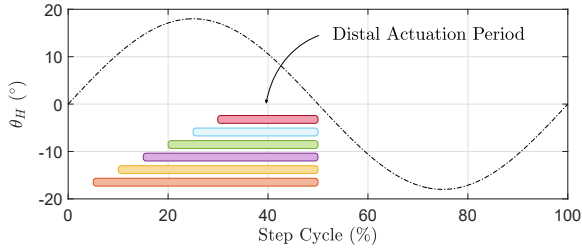


Fig. 7. Distal actuation timing with respect to the hip reference trajectory (black dashed line). The colored rectangles indicate the distal actuation period. Varying initial timing t_T values are considered: $t_T = 5\%$, 10% , 15% , 20% , 25% and 30% of the step cycle. Distal actuation stops at 50% of the step cycle, during the swing phase. Positive angles indicate a leg position behind the vertical axis (Fig. 2).

colored bars in Fig. 7; the ankle actuation is then ended at 50% of the step cycle, during the swing phase when the leg is not in contact with the ground. The compliance features of the pneumatic transmission allow driving a simple step torque-reference to the ankle motor so that we can focus on analyzing the influence of actuation timing only.

B. Analysis of passive foot

In this section, leg configuration-B is tested in passive mode, i.e., without activating the ankle motor, and its performance is compared to configuration-A to assess the benefits of the additional compliant foot. Fig. 8 shows this comparison evaluated on data sets corresponding to a complete revolution of the circular trajectory around the boom. The top plot shows that the distance of 9.7 m is traveled in 15.7 s by robot configuration-A and in 8.1 s by the configuration-B in SELDA passive mode. In this experiment, SELDA increases the forward velocity \dot{x}_{CoM} from 0.62 m/s to 1.20 m/s; an almost two-fold increase. The higher-speed locomotion is also visible in terms of step length, Fig. 8 (bottom-left), which increases of 93% from 378 mm to 730 mm. The foot

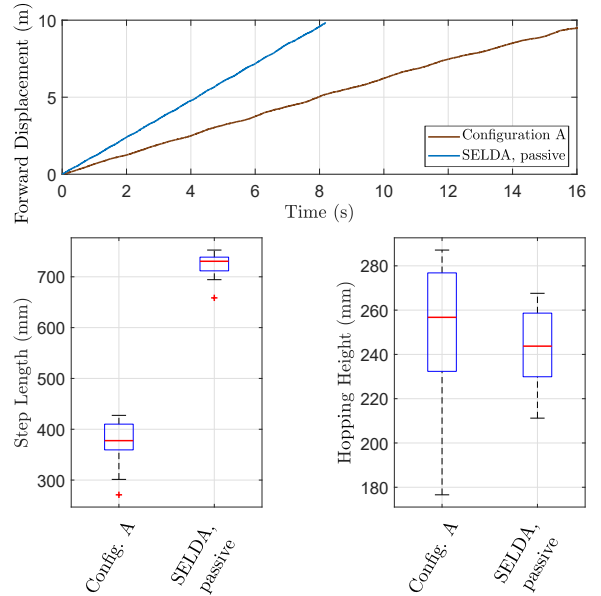


Fig. 8. Performance comparison between configurations-A and -B, (Fig. 1). In this experiment the distal segment is not actuated and the pneumatic transmission behaves like an air spring. *Top*: time to travel a complete turn around the boom. *Left*: statistical analysis of the maximum step height over one full boom revolution. *Right*: statistical analysis of the step length over one full revolution.

slightly affects the robot's maximum hopping height (Fig. 8 bottom-right), but it leads to a more repeatable hopping height and more stable hopping motion. Based on the ankle's stiffness characterization of Fig. 5, we estimate 67 mJ of peak energy stored in the ankle joint. In comparison, we calculate the hip's virtual spring peak energy of 250 mJ.

C. Analysis of active foot

This section investigates the effect of the SELDA activation timing, also in comparison with the passive foot

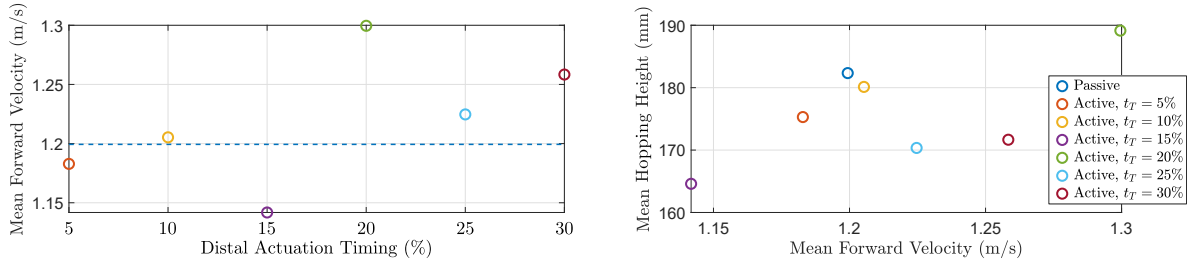


Fig. 9. Investigation of the effect of different distal actuation timing t_T . *Left*: mean velocity of the center of mass achieved for different values of timing t_T . The blue dashed line refers to measurements obtained with the passive-mode system. *Right*: mean step height with respect to mean forward velocity. Step height is the difference between the highest and the lowest vertical position of the robot’s center of mass at each step. Mean values refer to the dataset corresponding to one full revolution around the boom (9.7 m travelled distance) during steady state locomotion.

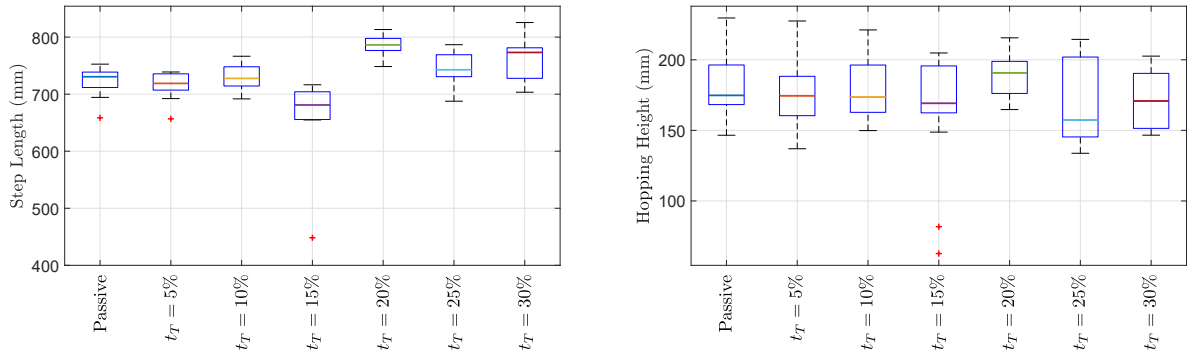


Fig. 10. Box plot statistical representation of the influence of distal actuation timing t_T on step length and maximum step height. The dataset of this analysis corresponds to samples collected during one full revolution around the boom in steady state gait. The minimum number of steps for one revolution is 13.

configuration. The initial timing t_T of the ankle actuation varies in the range 5% to 30% of the step cycle; a timing of 5% means that the ankle is actuated right after the touch-down, while the timing of 30% means that the ankle is actuated right before the lift-off. Fig. 9 (left) shows that, in general, the center-of-mass velocity \dot{x}_{CoM} can be increased by activating the ankle after mid-stance, while it is slowed down by actuating the ankle before mid-stance. In particular, the active SELDA achieves the highest forward velocity of 1.30 m/s with an actuation timing of $t_T = 20\%$ versus a speed of $\dot{x}_{CoM} = 1.20$ m/s for the passive SELDA. The lowest performance is observed with an actuation timing of $t_T = 15\%$ leading to an average forward speed of $\dot{x}_{CoM} = 1.14$ m/s. Fig. 9 (right) illustrates the energy transfer between hopping height and forward velocity \dot{x}_{CoM} . The hopping height is calculated at each step as the difference between the highest and the lowest vertical position y_{CoM} reached by the robot’s center of mass. By tuning the activation timing, we can effectively adjust the hopping height by 11% and the forward velocity by 14%. Note that our diaphragm actuation produces a torque of (≈ 1 Nm) from the motor side, which also compensates for the internal pressure of the pneumatic line. Albeit the limited actuator output torque, we observe that locomotion speed and hopping height are effectively altered (Fig. 9 left and right). We quantify the effect of the activation timing in terms of step length and hopping height over a minimum number of 13 steps, i.e. one revolution, during steady state locomotion

(Fig. 10). Narrow bands in the box plot indicate a more stable hopping gait. We observed period-2 hopping in some experiments, which expands the confidence interval in the plot. Once gait parameters such as frequency and amplitude are tuned to match the robot’s dynamic, we expect to further reduce the variation of step length and hopping height.

The supplementary video of the robot leg with SELDA actuated ankle joint can also be found at this YouTube link.

IV. CONCLUSIONS

This work proposes distal actuation of the foot segment in a bio-inspired hopping robot with a compliant rolling diaphragm pneumatic transmission. Diaphragm actuation has appealing features of lightweight, low-friction, high efficiency, and truly remote actuation. We found self-stabilizing gaits with comparatively simple, open-loop position control. We show that the addition of a foot segment improves the locomotion performance of the robot, already in its passive elastic mode, with an increase in forward velocity of 93%. With the actuated foot, we observed that actuation timing effectively influences the hopping gait. By tuning the ankle actuation timing from 5% to 30% of the gait cycle, we observed a 11% change in hopping height and 14% change in forward velocity, with its currently underdimensioned actuator. Based on these first results, our future developments will focus on providing the proximal cylinder with an antagonistic action to reduce the actuation effort that is required to balance the hose’s internal pressure. An

additional gearbox mounted to the ankle motor will increase output torque at reduced electrical power requirements. The proposed experiments are not yet based on optimal control strategies, and we expect SELDA to achieve higher performance in the future. Gait patterns will be optimized for energy efficient and agile locomotion, by tuning control parameters and type, and by introducing online feedback.

REFERENCES

- [1] R. M. Alexander, "Elastic Energy Stores in Running Vertebrates," *American Zoologist*, vol. 24, no. 1, pp. 85–94, Jan. 1984.
- [2] R. Alexander, "Three Uses for Springs in Legged Locomotion," *The International Journal of Robotics Research*, vol. 9, no. 2, pp. 53–61, Apr. 1990.
- [3] H. Witte, H. Hoffmann, R. Hackert, C. Schilling, M. S. Fischer, and H. Preuschoft, "Biomimetic robotics should be based on functional morphology," *Journal of Anatomy*, vol. 204, no. 5, pp. 331–342, May 2004.
- [4] J. Pratt and G. Pratt, "Intuitive control of a planar bipedal walking robot," in *1998 IEEE International Conference on Robotics and Automation, 1998. Proceedings*, vol. 3, 1998, pp. 2014–2021 vol.3.
- [5] M. S. Fischer, N. Schilling, M. Schmidt, D. Haarhaus, and H. Witte, "Basic limb kinematics of small therian mammals," *J Exp Biol*, vol. 205, no. 9, pp. 1315–1338, May 2002.
- [6] A. J. Ijspeert, "Central pattern generators for locomotion control in animals and robots: A review," *Neural Networks*, vol. 21, no. 4, pp. 642–653, May 2008.
- [7] A. Badri-Spröwitz, A. Aghamaleki Sarvestani, M. Sitti, and M. A. Daley, "Birdbot achieves energy-efficient gait with minimal control using avian-inspired leg clutching," *Science Robotics*, vol. 7, no. 64, p. eabg4055, 2022.
- [8] B. Kiss, E. C. Gonen, A. Mo, A. Buchmann, D. Renjewski, and A. Badri-Spröwitz, "Gastrocnemius and power amplifier soleus spring-tendons achieve fast human-like walking in a bipedal robot," no. arXiv:2203.01588, Mar. 2022.
- [9] Y. P. Ivanenko, R. E. Poppele, and F. Lacquaniti, "Five basic muscle activation patterns account for muscle activity during human locomotion," *The Journal of Physiology*, vol. 556, no. 1, pp. 267–282, 2004.
- [10] F. De Groot, I. Jonkers, and J. Duysens, "Task constraints and minimization of muscle effort result in a small number of muscle synergies during gait," *Frontiers in Computational Neuroscience*, vol. 8, p. 115, 2014.
- [11] J. M. Caputo and S. H. Collins, "Prosthetic ankle push-off work reduces metabolic rate but not collision work in non-amputee walking," *Scientific Reports*, vol. 4, no. 1, May 2015.
- [12] G. S. Sawicki and D. P. Ferris, "A pneumatically powered knee-ankle-foot orthosis (KAFO) with myoelectric activation and inhibition," *Journal of NeuroEngineering and Rehabilitation*, vol. 6, no. 1, p. 23, Jun. 2009.
- [13] O. B. Farah, Z. Guo, C. Gong, C. Zhu, and H. Yu, "Power analysis of a series elastic actuator for ankle joint gait rehabilitation," in *2015 IEEE International Conference on Robotics and Automation (ICRA)*, May 2015, pp. 2754–2760.
- [14] M. Ishikawa, P. V. Komi, M. J. Grey, V. Lepola, and G.-P. Brüggemann, "Muscle-tendon interaction and elastic energy usage in human walking," *Journal of Applied Physiology*, vol. 99, no. 2, pp. 603–608, Aug. 2005.
- [15] S. W. Lipfert, M. Günther, D. Renjewski, and A. Seyfarth, "Impulsive ankle push-off powers leg swing in human walking," *The Journal of experimental biology*, vol. 217, no. 8, pp. 1218–1228, 2014.
- [16] P. Cherele, V. Grosu, M. Cestari, B. Vanderborcht, and D. Lefeber, "The AMP-Foot 3, new generation propulsive prosthetic feet with explosive motion characteristics: design and validation," *BioMedical Engineering OnLine*, vol. 15, p. 285, 2016.
- [17] H. Mineshita, T. Otani, K. Hashimoto, M. Sakaguchi, Y. Kawakami, H. O. Lim, and A. Takanishi, "Robotic Ankle Mechanism Capable of Kicking While Jumping and Running and Adaptable to Change in Running Speed," in *2019 IEEE-RAS 19th International Conference on Humanoid Robots (Humanoids)*, Oct. 2019, pp. 505–510.
- [18] M. Hutter, C. D. Remy, M. A. Hoepflinger, and R. Siegwart, "Efficient and versatile locomotion with highly compliant legs," *IEEE/ASME Transactions on Mechatronics*, vol. 18, no. 2, pp. 449–458, 2012.
- [19] B. Katz, J. Di Carlo, and S. Kim, "Mini cheetah: A platform for pushing the limits of dynamic quadruped control," in *2019 International Conference on Robotics and Automation (ICRA)*. IEEE, 2019, pp. 6295–6301.
- [20] S. Rutishauser, A. Spröwitz, L. Righetti, and A. Ijspeert, "Passive compliant quadruped robot using central pattern generators for locomotion control," in *Proceedings of 2nd IEEE RAS & EMBS International Conference on Biomedical Robotics and Biomechatronics (Biorob)*. Scottsdale, AZ, USA: IEEE Biorob 2008, Oct. 2008.
- [21] M. H. Raibert, "Trotting, pacing and bounding by a quadruped robot," *Journal of Biomechanics*, vol. 23, no. Supplement 1, pp. 79–81, 1990.
- [22] C. Semini, N. G. Tsagarakis, E. Guglielmino, M. Focchi, F. Cannella, and D. G. Caldwell, "Design of HyQ—a hydraulically and electrically actuated quadruped robot," *Proceedings of the Institution of Mechanical Engineers, Part I: Journal of Systems and Control Engineering*, vol. 225, no. 6, pp. 831–849, 2011.
- [23] K. Narioka, A. Rosendo, A. Spröwitz, and K. Hosoda, "Development of a Minimalistic Pneumatic Quadruped Robot for Fast Locomotion," in *Proceedings of IEEE International Conference on Robotics and Biomimetics (ROBIO)*, Guangzhou, China, 2012, pp. 307–311.
- [24] R. Niyama, A. Nagakubo, and Y. Kuniyoshi, "Mowgli: A Bipedal Jumping and Landing Robot with an Artificial Musculoskeletal System," in *2007 IEEE International Conference on Robotics and Automation*, 2007, pp. 2546–2551.
- [25] J. P. Whitney, M. F. Glisson, E. L. Brockmeyer, and J. K. Hodgins, "A low-friction passive fluid transmission and fluid-tendon soft actuator," in *Intelligent Robots and Systems (IROS 2014), 2014 IEEE/RSJ International Conference on*. IEEE, 2014, pp. 2801–2808.
- [26] J. Hepp and A. Badri-Spröwitz, "A Novel Spider-Inspired Rotary-Rolling Diaphragm Actuator with Linear Torque Characteristic and High Mechanical Efficiency," *Soft Robotics*, Jun. 2021.
- [27] M. Bolognari and M. Fontana, "Design and experimental characterization of a high performance hydrostatic transmission for robot actuation," *Meccanica*, vol. 55, no. 5, pp. 1169–1179, 2020.
- [28] S. Frishman, R. D. Ings, V. Sheth, B. L. Daniel, and M. R. Cutkosky, "Extending reach inside the mri bore: A 7-dof, low-friction, hydrostatic teleoperator," *IEEE Transactions on Medical Robotics and Bionics*, vol. 3, no. 3, pp. 701–713, 2021.
- [29] A. Mo, F. IZZI, D. F. B. Haeuffe, and A. Badri-Spröwitz, "Effective Viscous Damping Enables Morphological Computation in Legged Locomotion," *Frontiers in Robotics and AI*, vol. 7, 2020.
- [30] J. P. Whitney, T. Chen, J. Mars, and J. K. Hodgins, "A hybrid hydrostatic transmission and human-safe haptic telepresence robot," in *Robotics and Automation (ICRA), 2016 IEEE International Conference on*. Stockholm, Sweden: IEEE, 2016, pp. 690–695.
- [31] C. Hubicki, J. Grimes, M. Jones, D. Renjewski, A. Spröwitz, A. Abate, and J. Hurst, "Atrias: Design and validation of a tether-free 3d-capable spring-mass bipedal robot," *The International Journal of Robotics Research*, vol. 35, no. 12, pp. 1497–1521, 2016.
- [32] F. Ruppert and A. Badri-Spröwitz, "Series Elastic Behavior of Biarticular Muscle-Tendon Structure in a Robotic Leg," *Frontiers in Neurobotics*, vol. 13, p. 64, Aug. 2019.
- [33] A. Spröwitz, A. Tuleu, M. Vespignani, M. Ajallooeian, E. Badri, and A. Ijspeert, "Towards Dynamic Trot Gait Locomotion: Design, Control and Experiments with Cheetah-cub, a Compliant Quadruped Robot," *Int. J. of Robotics Research*, vol. 32, no. 8, pp. 932–950, 2013.
- [34] R. M. Walter and D. R. Carrier, "Ground forces applied by galloping dogs," *Journal of Experimental Biology*, vol. 210, no. 2, pp. 208–216, 2007.
- [35] M. Bolognari, G. Rizzello, L. Zaccarian, and M. Fontana, "Smith-predictor-based torque control of a rolling diaphragm hydrostatic transmission," *IEEE Robotics and Automation Letters*, vol. 6, no. 2, pp. 2970–2977, 2021.
- [36] F. Grimmering, A. Meduri, M. Khadiv, J. Viereck, M. Wüthrich, M. Naveau, V. Berenz, S. Heim, F. Widmaier, T. Flayols, J. Fiene, A. Badri-Spröwitz, and L. Righetti, "An open torque-controlled modular robot architecture for legged locomotion research," *IEEE Robotics and Automation Letters*, vol. 5, no. 2, pp. 3650–3657, 2020.



OPEN

Slack-based tunable damping leads to a trade-off between robustness and efficiency in legged locomotion

An Mo¹✉, Fabio Izzi^{1,2}, Emre Cemal Gönen¹, Daniel Haeufle^{2,3} & Alexander Badri-Spröwitz^{1,4}

Animals run robustly in diverse terrain. This locomotion robustness is puzzling because axon conduction velocity is limited to a few tens of meters per second. If reflex loops deliver sensory information with significant delays, one would expect a destabilizing effect on sensorimotor control. Hence, an alternative explanation describes a hierarchical structure of low-level adaptive mechanics and high-level sensorimotor control to help mitigate the effects of transmission delays. Motivated by the concept of an adaptive mechanism triggering an immediate response, we developed a tunable physical damper system. Our mechanism combines a tendon with adjustable slackness connected to a physical damper. The slack damper allows adjustment of damping force, onset timing, effective stroke, and energy dissipation. We characterize the slack damper mechanism mounted to a legged robot controlled in open-loop mode. The robot hops vertically and planarly over varying terrains and perturbations. During forward hopping, slack-based damping improves faster perturbation recovery (up to 170%) at higher energetic cost (27%). The tunable slack mechanism auto-engages the damper during perturbations, leading to a perturbation-trigger damping, improving robustness at a minimum energetic cost. With the results from the slack damper mechanism, we propose a new functional interpretation of animals' redundant muscle tendons as tunable dampers.

Animals run dynamically over a wide range of terrain (Fig. 1). The unevenness and changing compliance of natural terrain demand the capability for fast and dynamic adaptation to unexpected ground conditions. However, animals' neurotransmission delays slow down sensorimotor information propagation², rendering a neuronal response impossible for as much as 5 to 40% of the stance phase duration, depending on the animal size¹. How animals are able to produce and maintain highly dynamic movements despite delayed sensorimotor information is, therefore, a central question in neuroscience and biorobotics^{1,3-5}.

Inherent mechanical properties of muscles facilitate the rejection of unexpected perturbations⁶⁻⁹. Muscular tissue possesses nonlinear elastic and viscous-like mechanical properties, which adapt the muscle force instantly to changes in the length or contraction velocity of the muscle-tendon fibers. These mechanical properties enable the neuro-musculoskeletal system to react to external perturbations with zero delay, a capacity termed "preflex"^{10,11}.

Intrinsic elasticity and its role in legged locomotion have been studied extensively¹²⁻¹⁶. For instance, tendons, which behave like nonlinear serial springs, store and release mechanical energy during ground contact¹² and improve shock tolerance¹⁷. Inspired by this, parallel and series elastic actuators have successfully been implemented in the design of legged robots¹⁸⁻²¹, demonstrating improved robustness at low control effort. In contrast, the functional role that damping plays in legged locomotion is less studied and understood.

Damping can produce a force outcome that is adaptive to the impact velocity. This adaptive force output enhances the effective force output during impacts²², minimize control effort²³, stabilize motion²⁴⁻²⁶ and reject unexpected disturbances^{27,28}. Nevertheless, damping is usually minimized in the design of (bio)robotic systems, as it can lead to increased energy consumption. Interestingly, vertebrates seem capable of tuning the damping produced by their muscle fibers²⁹. This suggests that tunable damping can be a solution for regulating damping forces and dissipating energy depending on the terrain conditions.

¹Dynamic Locomotion Group, Max Planck Institute for Intelligent Systems, 70569 Stuttgart, Germany. ²Hertie Institute for Clinical Brain Research and Center for Integrative Neuroscience, University of Tübingen, 72076 Tübingen, Germany. ³Institute for Modelling and Simulation of Biomechanical Systems, Computational Biophysics and Biorobotics, University of Stuttgart, 70569 Stuttgart, Germany. ⁴Department of Mechanical Engineering, KU Leuven, 3001 Leuven, Belgium. ✉email: mo@is.mpg.de

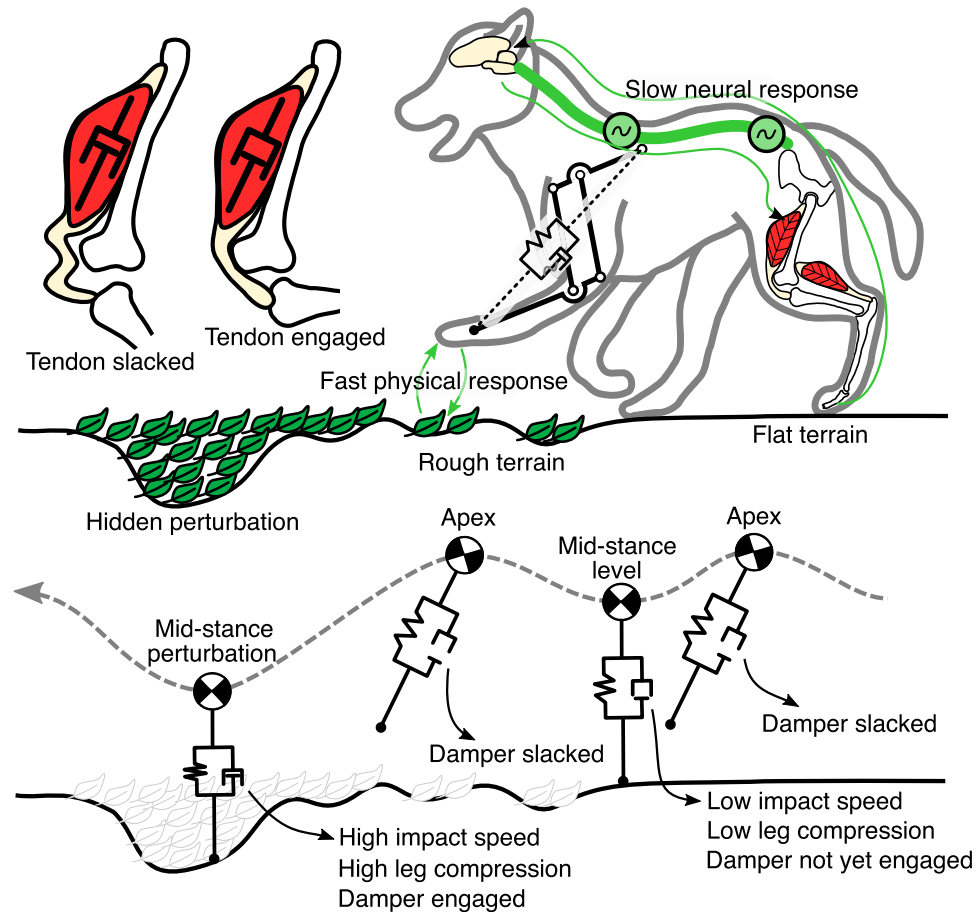


Figure 1. Top: Fast running over ground perturbation is challenging. Due to sensorimotor delays up to 50 ms, the central nervous system struggles to perceive and react to sudden ground disturbances¹. In contrast, the intrinsic mechanics of the musculoskeletal system act like a spring damper. They produce a physical and, therefore, immediate (< 5 ms) reaction when in contact with the environment. We hypothesize that the leg damping mitigates ground disturbance through adaptive force production and energy dissipation. The tendon's slack, coupled with the joint's motion, auto-engages the damper. This creates a trade-off between locomotion robustness and energetic efficiency. Bottom: The damper slack enables perturbation-triggered damping. Sufficiently slacked, the damper does not engage during stance, and only spring-based torque is produced. When encountering a perturbation, the leg's compression increases further, removing all damper slack, and the damper engages in parallel to the spring.

Tunable damping in biorobotics can be implemented through control^{30,31}, i.e., virtual damping. Virtual damping poses substantial design constraints. It requires precise velocity estimation, high-frequency control (> 1 kHz), strong actuators to produce sufficient peak forces, and means to dissipate the resulting heat effectively^{32–36}. Alternatively, physical dampers can be mounted in parallel to the robot's joints³⁷. A physical damper perceives and responds physically and instantly, requires no controller or computation, shares peak load of actuators, and thus has the potential for fast adaptation to terrain perturbations³⁸. Tuning damping with a physical damper mounted to a legged robot proved challenging. Setting a higher damping rate resulted in the expected higher forces, but at reduced leg compression and effective damper stroke³⁸. Consequently, the dissipated energy indicated by the work loop area did not increase. Additionally, fix-mounted physical dampers operate continuously and dissipate energy during unperturbed level running. Instead, physical tunable damping should ideally be triggered by the perturbation itself. The damper should engage and self-adjust according to the presence and severity of the ground disturbance experienced during running.

The tendon slack observed in muscle-tendon units^{39,40} and animal-inspired robots⁴¹ provided us with a design template for implementing tunable damping in a legged system (Fig. 1 Top). Tendon slack length is defined as the "...length beyond which the tendons associated with a muscle begin resisting stretch and producing force"⁴⁰. In other work, the "tendon is strained up to 2%, representing the "stretching out" of the crimped tendon fibrils, before starting to transfer considerable force"³⁹. Badri-Spröwitz *et al.* show tendon slack in the flexing motion of the digits of large birds, and implement tendon slack in the related robot⁴¹. By disengaging the damper from its joint via controlled tendon slack, we expect to adjust the onset, timing, and amount of damper engagement. Moreover, the tendon slack allows for a perturbation-trigger strategy (Fig. 1 Bottom). During steady-state running, for example, on flat terrain, the leg compresses without saturating the tendon slack. Once an

unperceived ground perturbation increases leg compression further, the tendon displacement will exceed the tendon's slack and start to auto-engage the damper. This strategy enables adaptive force output triggered by ground perturbations.

We implemented and tested a bio-inspired, physical tunable damping strategy based on tendon slack in this work. We aimed at producing perturbation-triggered damping and improving robustness against ground perturbations. We evaluated this design concept on a robotic leg during vertical and forward hopping, both in steady-state and perturbed conditions. Unlike earlier designs³⁸, our slack damper mechanism enabled straightforward adjustment of the damper engagement and energy dissipation. We observed improved hopping robustness due to the adaptive characteristics of our physical damping design, whereas the energetic cost increases. The perturbation-triggered capacity of our slack damper mechanism allows for a more favorable trade-off between robustness and efficiency.

Results

We designed three experiments to study the proposed design with a hydraulic damper mounted to a robotic leg joint (Table 1). We tested damper slack values of 10, 6, 3, and 0 mm for all conditions. These settings span from full slack (10 mm, minimum effective damping) to no slack (0 mm, maximum effective damping). An open-loop controller produced the robot leg's locomotion pattern. Without feedback, ground perturbations were invisible to this high-level control (neural circuits), and perturbations could only be compensated by low-level mechanics in the form of a physical response.

We used the vertical hopping setup to investigate the vertical component of locomotion, allowing ground reaction force (GRF) measurement in all steps (Fig. 5e). We introduced step-down perturbation to evaluate the robustness of the system. We used the forward hopping setup, which mounts the leg on a boom structure, to simulate more realistic locomotion dynamics (Fig. 5f). We analyzed forward hopping performance on rough terrain and robustness against ramp-up-step-down perturbation.

All data can be found in Supplementary Table S3–5.

Vertical hopping with step-down perturbation. With feed-forward control, the leg hopped in the vertical setup for two perturbation levels and four slack values. Figure 2a shows an example of a time-series of 10 repetitions. The test condition included a perturbation of 15% leg length (LL) and tendon slack of 3 mm (Supplementary Movie S1). At the perturbed step 1, the leg impacted the ground at a higher speed, compressing more. This resulted in higher damper and spring forces than during pre-perturbation levels. We noticed that the damper force did not drop to zero at mid-stance due to the damper's internal recovery spring.

We found that the tunable slack mechanism was effective in tuning damping. Damper slack adjustments of 0 to 6 mm resulted in a delayed engagement of the damper: from 0 to 50 ms after the onset of the spring force during level hopping (Fig. 2b). The damper's force-displacement work loops during level hopping confirmed the controllable onset of the damper force (Fig. 2c). The enclosed work loop areas represent the damper's standby dissipated energy. Damper slack values of 0, 3, 6, and 10 mm can be mapped to standby dissipation of 152, 86, 29, and 1 mJ. At the perturbation step, the damper dissipated more energy (65% to 190%) compared to level hopping standby dissipation (Fig. 2d). The extra dissipated energy is associated with the height of the ground drop, showing an adaptive energy dissipation to terrain disturbance. In all tested conditions, the extra dissipated energy converged to 0 in the following steps, indicating recovery to steady-state hopping.

The robustness of the hopping system can be qualitatively assessed by the phase plot of the hip height (Fig. 2e and Supplementary Movie S1). With a 10 mm slack setting, the hopping behavior was the most variable, as shown by the overlay of gray lines, representing 200 steps in 10 repetitions. With a 6 mm slack setting, the phase plot was clean, and the hopping converged to a new 'limit cycle' in fewer steps than other settings. A quantitative robustness measurement is the number of steps required to bring the system back to its original hopping height after the perturbation (Fig. 2f). The system's robustness was highest with the 6 mm slack setting, requiring on average 1.7 and 2.5 steps to recover for 10% and 15% LL perturbation, respectively (Fig. 2g). At stronger perturbations, the robot needed more steps to recover. We measure the energetics of the hopping system by its cost of hopping (CoH, equation (4)). The CoH increased from 6.3 to 7.6 with higher damping or stronger perturbations (Fig. 2h). With a damper slack of 6 mm at 10% LL perturbation, we found 47% faster perturbation recovery in combination with 5% higher CoH compared to 10 mm damper slack (Fig. 2i).

Experiment	Terrain	Perturbation Height	No. of perturbation steps	No. of repetitions
Vertical hopping	Step-down	10% LL	1	10
		15% LL		
Forward hopping	Flat terrain	0 mm	15	4
	Rough terrain	±5 mm		
	Rough terrain	±10 mm		
Forward hopping	Ramp-up-step-down	15% LL	1	10
		30% LL		

Table 1. Experiment design, all experiments are repeated with damper slack values of 10, 6, 3, and 0 mm, from maximum slack to no slack.

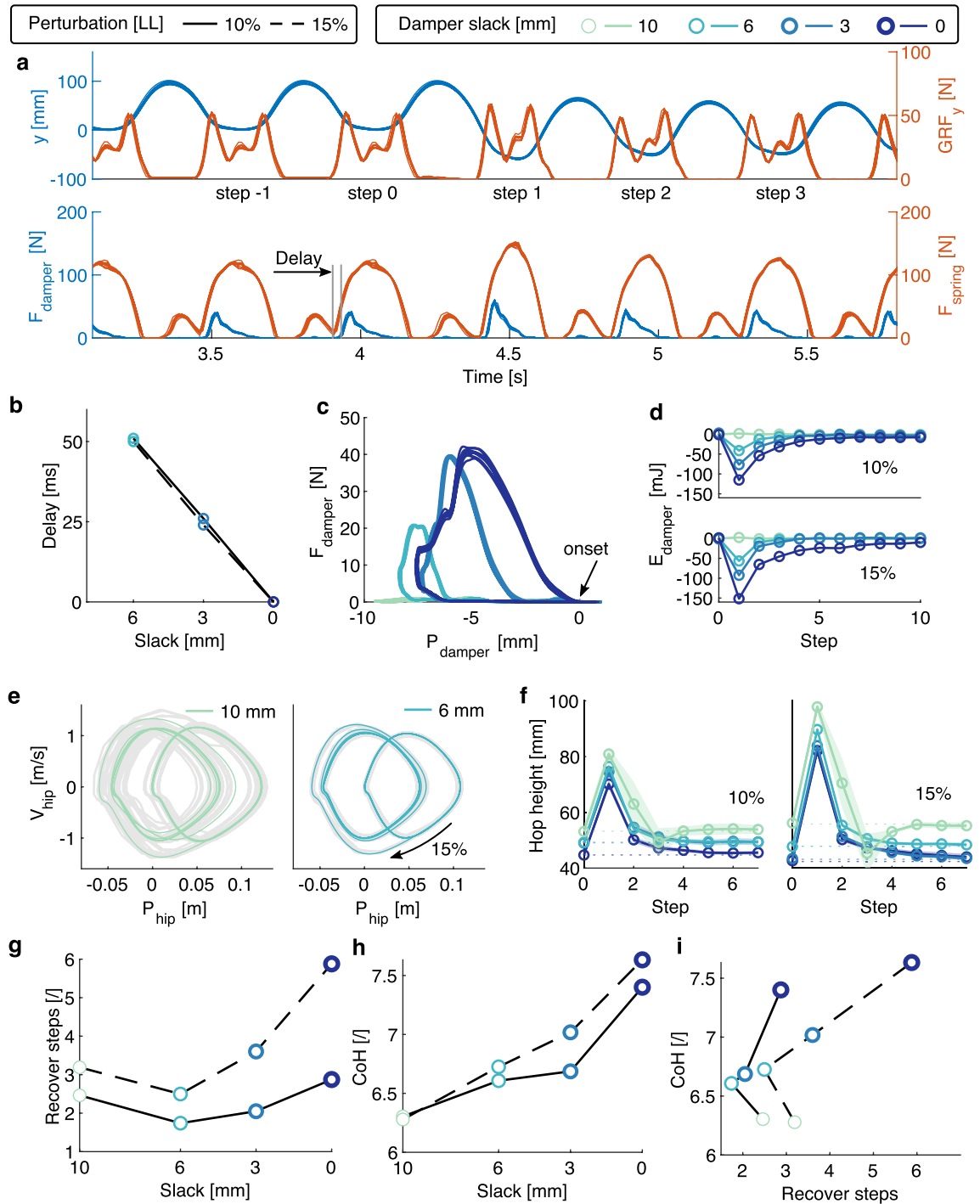


Figure 2. Vertical hopping with step-down perturbation: (a) 10-repetition-overlay time-series of hip position y , GRF, spring, and damper forces. 15% LL perturbation at step 1 increases the GRF, spring and damper forces due to higher impact speed. The damper starts to produce force with a delay to touchdown due to the 3 mm slack setting. (b) This damper engagement delay is adjustable by the damper slack setting. (c) The 10-repetition-overlay damper work loop in unperturbed periodic steps shows that the onset position can be reliably tuned and the standby dissipated energy (enclosed area) adjustable. (d) The average extra damper dissipated energy during perturbation steps. (e) Phase plot of hip position with 10 mm and 6 mm damper slack under 15% LL perturbation. The grey overlay shows the overlap of 10 repetitions of 20 steps, while the darker line is the averaged trajectory. (f) The average hopping apex height during perturbation steps. The transparent overlay represents the 95% confidence boundary. (g) The relationship between the number of steps to recovery after perturbation and the damper slack settings. (h) The relationship between the cost of hopping and the damper slack settings. (i) The relationship between the number of steps to recovery to the cost of hopping under different damper slack settings and perturbation levels.

Forward hopping with continuous perturbation. During forward hopping on the sinusoidal ground, the standard deviation of the step cycle time quantifies the hopping periodicity. In the flat terrain, the standard deviation of the step cycle time decreased from 27 ms to 2 ms with less damper slack, showing improved hopping periodicity with more damping (Fig. 3a). This tendency was less apparent in ± 5 and ± 10 mm rough terrain, as the step cycle time variation increased first for the damper slack value 6 mm, then decreased with less damper slack. The energetic cost of forward hopping was measured as the cost of transport⁴² (CoT, equation (5)). The CoT increased from a minimum of 0.75 to 1.35 with increasing damping (Fig. 3b). Both hopping periodicity and CoT were affected by the terrain's roughness. In flat terrain, increasing damping was associated with improved periodicity and increased CoT (Fig. 3c). At ± 5 mm terrain roughness, data for damper slack values of 0, 3, and 6 mm show similar tendency. The 10 mm damper slack shows the best performance with a CoT of 0.75 and a standard deviation of 2 ms cycle time (Fig. 3d). With ± 10 mm terrain roughness, the cycle time standard deviation was clustered around 2 mm to 3 mm for all slack settings, while the CoT varied from 0.79 to 1.32. Among these three tested terrains, the strongest damping, i.e., the setting with a slack of 0 mm, showed better periodicity with a cycle time standard deviation of ≈ 2 ms, but with the highest CoT, ranging from 1.24 to 1.35.

Forward hopping with ramp-up-step-down perturbation. We evaluated the system's robustness during forward hopping by testing its response to unexpected, sudden perturbations. Thus, we analyzed the robotic leg's behavior with step-down perturbations in its hopping path. As robustness measurement, we counted the number of steps required for the hopper to recover after the step perturbation. The second measurement of robustness is the number of failures out of ten perturbation attempts. By reducing the damper slack from 10 to 0 mm, the average recovery steps needed by the robotic leg decreased from 2.7 to 1.0 for the 15% LL perturbation and from 2.6 to 2.3 for the 30% LL perturbation (Fig. 4a). Similarly, with more damping, the number of failed trials decreased from 7 to 0 for the 15% LL perturbation and 10 to 3 for the 30% LL perturbation (Fig. 4b). The legged robot was less robust against a stronger perturbation, as it required on average 0.7 more recovery steps or failed, on average, four times more for the two tested perturbation levels. Similar to the other two experiments, the energetic cost of the system increased with more damping, as the CoT increased from 0.95 to 1.44 (Fig. 4c). With a damper slack of 0 mm at 15% LL perturbation, we found 170% faster perturbation recovery in combination with 27% higher CoH compared to 10 mm damper slack (Fig. 4d). With both measurements of robustness, we observed a tendency of increasing robustness at the expense of more energetic cost with higher damping settings (Fig. 4d and e).

Discussion

The slack damper mechanism allows effective tunable damping. This has three consequences: First, depending on the slack setting, the damper produces an immediate or delayed response to ground impacts (Fig. 2b). Second, the onset of the damper stroke can be reliably set by the tendon slack (Fig. 2c). Third, the mechanical work generated by the damper is tunable, as shown by the change in the size of the enclosed work loops (Fig. 2c). Such a level

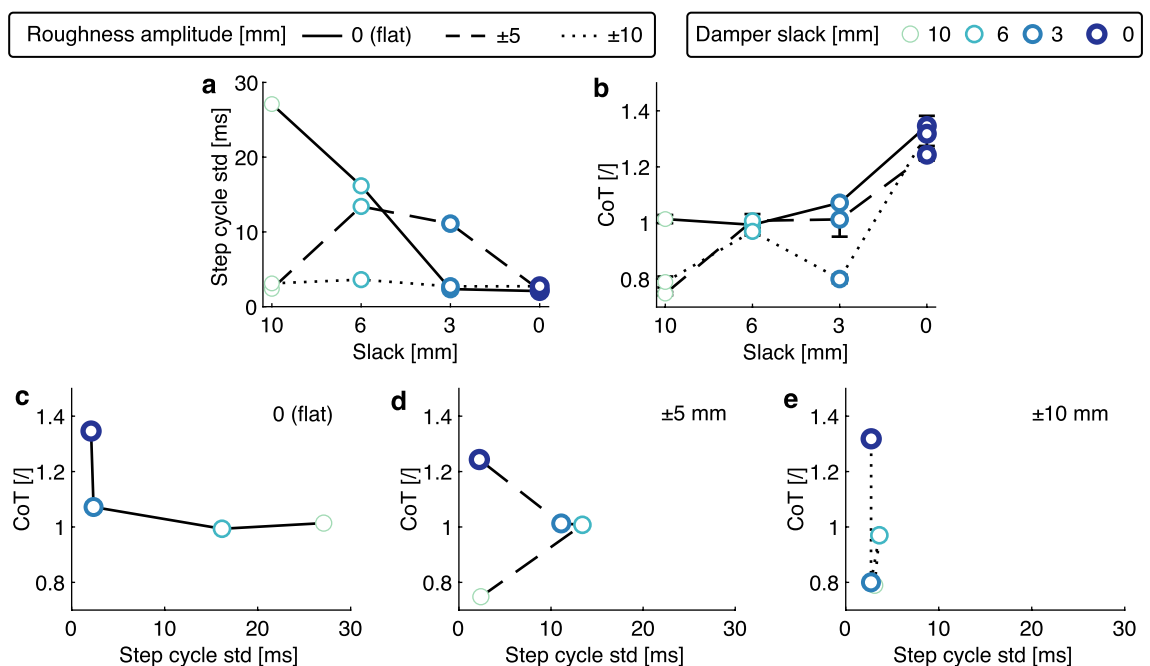


Figure 3. Forward hopping with continuous perturbation: (a) The standard deviation of the step cycle time shows that the hopping periodicity is improved with higher damping (less slack). (b) The relationship between the CoT and the damper slack settings. (c) In flat terrain, the robot's ability to maintain periodic hopping is improved by higher damping at the cost of CoT. (d,e) In the continuous perturbation terrain, high damping is also associated with high CoT and good periodicity.

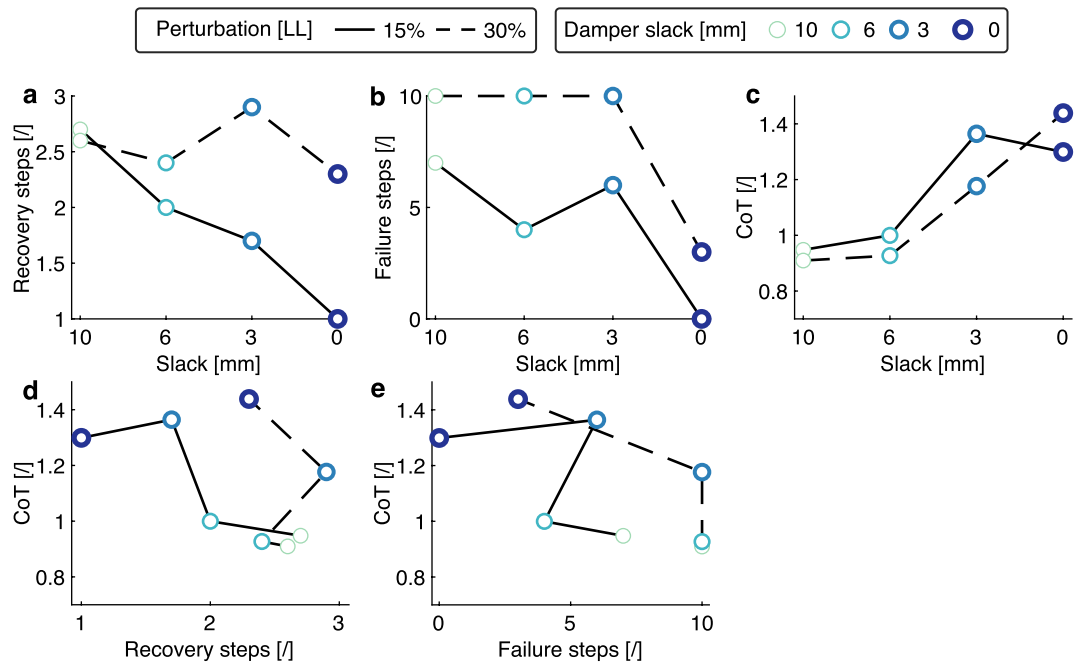


Figure 4. Forward hopping with ramp-up and step-down perturbation: The robustness of the robot system is quantified with the number of steps needed to recover stable hopping (a) and the number of failed trials in 10 attempts (b). (c) The relationship between the CoT and the damper slack settings. (d,e) show the trade-off between robustness and CoT.

of tunability of the damper response was not possible in our previous, more canonical approach of controlling the damping rate of the same damper model (implemented in a two-segment leg) via orifice adjustment³⁸. In contrast, adjusting the slack of the damper tendon provides an effective strategy for tuning embedded damping in the robotic leg. The slack in the damper tendon system allows the parallel spring to soften the damper impact within tens of milliseconds after the foot touchdown. As a result, the damper produced less force and effective stroke than scenarios with less slack (Eq. (1), Fig. 2c).

In the steps following a sudden drop in ground height, the additional gravitational energy results in 20% to 30% higher touchdown speeds. The damper force and negative work increase accordingly, providing a beneficial mechanical reaction to compensate for the perturbation (Fig. 2d). Therefore, our damper implementation produces mechanical work in an adaptive manner that is consistent with the perturbation level and tunable by just one parameter; the damper tendon slack.

Legged system robustness is required due to the system's inherent sensor- and control-noise and the imprecision of its motor-control^{1,43,44}. Heim *et al.*⁴⁵ quantified task-level stability in a modified spring-loaded inverted pendulum (SLIP) model that includes perturbation-triggered damping, suggesting that increased damping contributes to improved robustness. Legged locomotion simulation studies^{24,26} and muscle experiments⁴⁶ revealed the stabilizing effect of damping. This theoretical evidence motivated our biorobotic setup to explore and characterize damping and its effect on locomotion robustness.

In general, damping improves system robustness. In the vertical hopping experiments, adding a small amount of damping (6 mm slack) led to the fastest recovery from step perturbations (Fig. 2e and g). Above a certain amount of damping, the robotic leg appears to be “over-damped”, as shown by the hopping height over steps. For example, with more damping (slack < 6 mm), the convergence to the pre-perturbation behavior is smoother (Fig. 2f) but requires more steps (Fig. 2g). In forward hopping experiments, more damping improved hopping periodicity (Fig. 3a) and robustness (Fig. 4a and b) without the emergence of an over-damping threshold. Our system performed well in this perturbed condition. It overcame the perturbation 64 times out of 80 trials, despite using the simple feed-forward open-loop controller for forward hopping motion. Although no electronic sensors are utilized to perceive the perturbations, the passive compliance embedded in the leg acts as an intrinsic system of mechanical sensors and actuators, which detect and respond immediately to external disturbances. We believe the adaptive force output from damping plays a key role. A reflex-control mammalian quadruped of similar size to our robot has a total sensorimotor delay of 60 ms³. In comparison, the delay of damping force production in the robotic leg is less than 50 ms (Fig. 2b). This confirms that the physical damping force effectively acts faster than reflex control in response to a perturbation.

The improved robustness introduced by the damper system comes at an energetic cost. Higher damping settings (less slack) result in higher energy costs for all the experiments (Figs. 2i, 3b, and 4c). This occurs because the actuators need to produce more power to compensate for the lost energy by damping (Fig. 2c,d) and achieve a steady-state hopping behavior. Tunable damping leads to a trade-off between the robustness and energy cost of the system (Fig. 4d,e). This trade-off implies that hopping can be either robust against perturbations but with

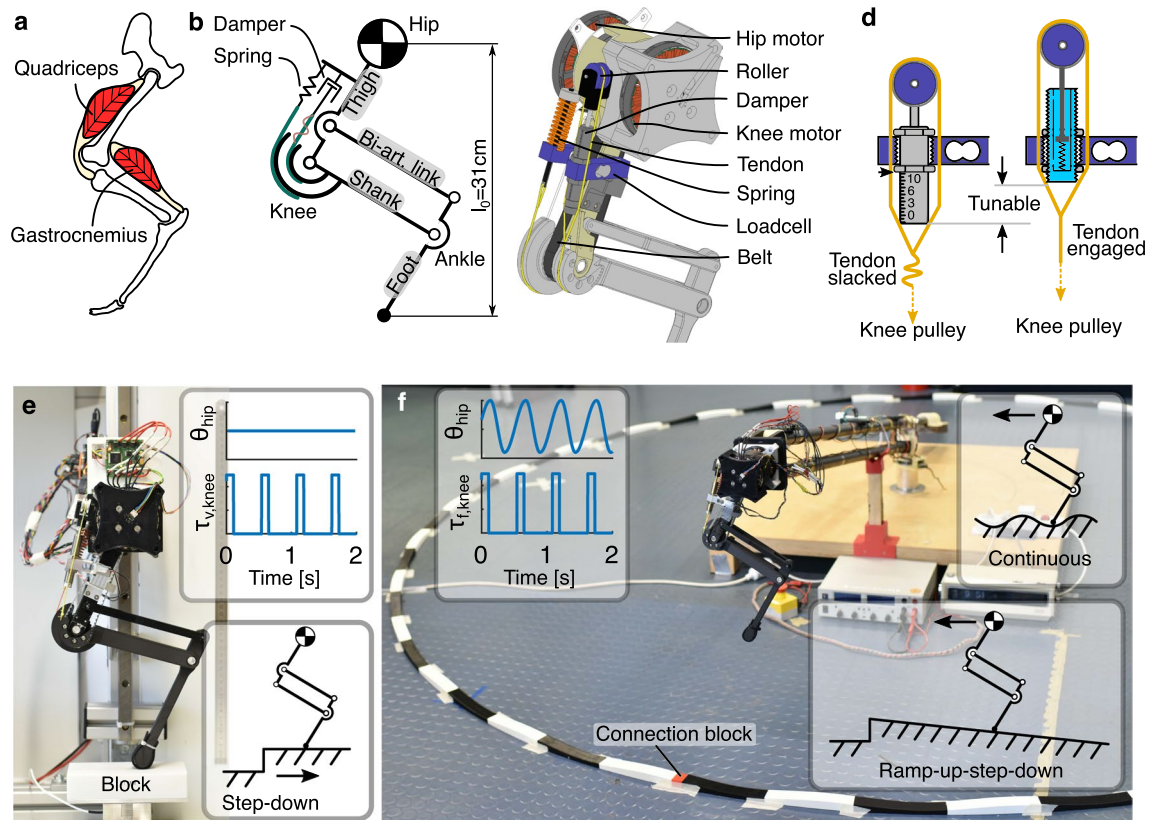


Figure 5. Experiment setup overview. (a) Our leg design is inspired by the leg anatomy of mammalian quadrupeds. (b) We implement a pantograph leg design with spring and damper representing the passive compliance of the quadriceps and a biarticular segment, simplifying the gastrocnemius muscle and the Achilles tendon. (c) The rendering of the leg design shows that the knee joint is coupled to the linear spring, the linear damper through tendons, and the knee motor through a timing belt. (d) The slack damper mechanism is realized by the threaded connection between the damper and the loadcell. By rotating the damper, the damper will travel up and down, thus allowing tunable tendon slack. The left schematics illustrates the lowest position of the damper in maximum tendon slack, and the right schematics demonstrates the inner mechanics of the hydraulic damper with minimum tendon slack. (e) The vertical hopping setup fixes the robot leg on a vertical slider to test step-down perturbation, which is introduced by removing the perturbation block on top of the force sensor. The top right shows a feed-forward control pattern for hip position and knee torque. (f) The forward hopping setup fixes the robot leg on a rotary boom to test continuous perturbation (in photo) and ramp-up-step-down perturbation (Supplementary Movie S3). The top right shows a feed-forward CPG control pattern for hip position and knee torque.

a penalty in energy consumption, or be energy efficient but vulnerable to disturbance. Adjusting tendon slack allows for selecting a suitable compromise depending on the terrain.

The benefit of damping for legged systems remains a debate in the field^{24,45,47}. Most research on legged locomotion focuses on optimizing a single aspect, such as robustness, stability, or energy consumption. On the contrary, evolution in biology is likely not a single-objective optimization process. Instead, we argue that a more holistic perspective is required to understand the interaction among the many performance metrics characterizing legged locomotion. Therefore, we argue that the locomotion priority can change. As Fig. 1 suggests, less damping is desired to minimize energy consumption during level terrain locomotion. In case of rough terrain, higher damping is preferred to improve the robustness against ground disturbances. Hence, damping is a key to balance the trade-off between robustness and energy consumption.

The advantage of our slack damping mechanism concerning energy consumption is that it allows a perturbation-trigger strategy. The damper tendon slack can be tuned to barely engage at level hopping. It will then engage once a ground perturbation induces higher impact velocities. In this way, the absence of a damper minimizes the dissipating energy during level hopping, while the engagement of the damper improves robustness at ground perturbation steps. This automatic on-off control was impossible with previous damper implementations^{48,49}, because damping generated from friction, rheology, eddy currents, and fluid dynamics are hard to switch off completely³⁷. Instead of optimizing the adjustment of the nonlinear damping coefficient, our mechanism features a fixed damping coefficient but exploits a slack tendon to create a tunable on-off damping. The proposed slack tendon could also be applied to selectively engage springs. Hence, the tunable tendon slack mechanism offers a new mechanism for adaptive compliant actuator applications.

Besides the adaptive force output of damping, we expect the tunability of damping to provide better hopping behavior, such as transitioning into new terrain. When expecting a more uneven terrain, the damper slack can be adjusted accordingly to gain more robustness against the stronger perturbation. This requires an online slack tuning mechanism and its feedback control strategy. Possibly, a feed-forward controller can be sufficient to produce highly robust running in an uncertain environment⁵⁰. Limited by the hardware implementation, we did not thoroughly investigate an online tuning design. Nevertheless, the four damper slack settings demonstrate the proof-of-concept of online tunable damping.

We consider extending our system with stiffness control in the future. Tunable spring designs have been studied extensively³⁷, but a combination with tunable damping is rare. Software online tuning of stiffness and damping has been realized^{51,52}, but relies on precise sensing, high-frequency control and strong actuation. Virtual feedback impedance control^{53,54} combined with physical springs and dampers provide software control flexibility and fast physical response⁵. With these improvements, we can readily implement controllers and hardware for versatile and robust locomotion in natural terrains such as gravel.

In summary, this work aims at understanding the tunable damping mechanism in legged locomotion. We proposed the slack damper strategy inspired by muscle tendon slack and tested it in robotic legged hopping. The slack damper mechanism allows effective tunable damping regarding onset timing, engaged stroke, and energy dissipation. This study provides novel insights into the trade-off between energetics and robustness under different damping levels. Additionally, the slack damper design allows for perturbation-trigger damping, resolving the trade-off during locomotion with unexpected perturbation. Our results could inspire future robotic locomotion hardware and controller design.

Methods

Biorobotic leg implementation. The 3-segment leg design was inspired and simplified from the leg anatomy of small mammalian quadrupeds (Fig. 5a). It consisted of four links forming a pantograph structure (Fig. 5b). A spring and a damper coupled to the knee joint mimicked the passive compliance of the quadriceps muscles. The gastrocnemius muscle and Achilles tendon were simplified as a rigid link to reduce parameter space. The two-degrees-of-freedom leg was fully actuated by two motors (hip and knee). The key design parameters are provided in the supplementary materials (Fig. S1 and Table S1).

The leg was fabricated mostly from off-the-shelf components and 3D-printing (Fig. 5c). The main structural components were 3D-printed using polylactic acid (PLA), except for the foot segment, which was 3D-printed using carbon-fiber-reinforced nylon to improve strength and impact resistance. The hip and knee motors (MN7005-KV115, *T-motor*, 1.3Nm maximum rated torque) were placed co-axially at the hip to reduce leg swing inertia, using a 5:1 planetary gearbox (lgu35-s, *Matex*) to gear them down. The knee torque was transmitted by a timing belt (SYNCHROFLEX 10/T5/390, *Contitech*) with an additional 25:12 gear ratio. We mounted two loadcells (model 3134, *Phidgets*, 20kg) to the spring and the damper to measure forces. The knee spring (SWS14.5-15, *MISUMI*) was designed to hold the leg in stance. Its stiffness of 10.9N/mm was empirically determined to generate three times the body weight of the robot at 10% leg length deflection^{55,56}. The knee damper (1210M, *MISUMI*) was selected as the most effective damper from our previous study³⁸. Both the spring and the damper were coupled to the knee joint through Dyneema tendons (Climax Combat Speed 250/150, *Ockert*), with a cam radius of 30 mm and 20 mm, respectively. A roller (VMRA20-4, *MISUMI*) was attached to the piston of the damper to transform the tendon tension (“muscle lengthening”) in knee flexion to a push motion on the damper piston. The whole leg weighs 0.94kg, with a resting leg length of 31 cm.

Slack damper mechanism. Tuning an adjustable damper when operating within a legged system is challenging. Higher damping settings make the damper produce larger forces, which in turn can reduce the piston displacement, compromising the projected change in dissipated energy³⁸. Therefore, it is difficult to anticipate how adjusting the orifice of the damper internal valve affects the dissipated energy. Instead of regulating the damper’s force by adjusting the orifice size, we propose damping control by adjustment of the damper tendon slack. Tendon slack has been observed in biology, with tendon stretch up to 2% of the nominal tendon length before starting to produce considerable force^{39–41}. This is known as the ‘toe region’ in the tendon’s stress-strain diagram.

Inspired by this observation, we set a defined tendon slack length when connecting the damper to the knee pulley (Fig. 5d). For our mechanism, the damper body and the loadcell are machined with external and internal threading, respectively. By screwing the damper’s body into the loadcell, we set the damper’s position with a resolution of ± 1 mm per turn. The adjustable threading allows for a precise slack control in the range of 0 to 10 mm. Before each experiment, we lock the damper in place with two nuts to prohibit damper body movement.

This slack damper mechanism permitted tunable damping. The damper energy dissipation E_{damper} , calculated as the integration of damper force F_{damper} and damper piston displacement x , can be controlled by the tendon slack s because of two concomitant effects (equation (1)). First, when the ground impact flexes the leg, the parallel spring decelerates leg flexion. At the same time, the tendon slack saturates, thereby softening the engagement conditions for the damper’s piston (more slack $s \hat{=}$ less damper force F_{damper}). Second, the tendon slack reduces the effective damper piston stroke Δx (more slack $s \hat{=}$ less piston stroke Δx). The combination of these two mechanisms—softened (less F_{damper}) and delayed (less Δx) damper engagement—predicts an inverse relationship between the tendon slack s and the integrated damper energy dissipation E_{damper} .

$$\left. \begin{aligned} E_{damper} &= \int F_{damper} dx \\ F_{damper} &\propto \frac{1}{s}, \Delta x \propto \frac{1}{s} \end{aligned} \right\} \Rightarrow E_{damper} \propto \frac{1}{s} \quad (1)$$

Experimental setup. We designed two experimental setups and three perturbation types to evaluate the proposed design in four slack settings.

The vertical hopping setup (Fig. 5e) investigates only the vertical component of locomotion. Such a reduced-order experiment reduced system complexity, allowing ground reaction force (GRF) measurement in all steps. The forward hopping setup (Fig. 5f) fixed the leg on a boom structure, simulating more realistic locomotion dynamics and allowing for more perturbation types.

We focus the investigation on the mechanical response produced by the passive damping embedded in the leg design. Hence, we designed an open-loop locomotion controller such that it could not detect ground perturbation. We tested three types of ground perturbations: step-down perturbation representing a sudden, unexpected disturbance during fast running; continuous perturbation simulating rough terrain conditions, and ramp-up-step-down perturbation combining gradual and sudden disturbance.

We tested damper tendon slack of 10, 6, 3, and 0 mm for each test condition. The damper engaged synchronously with the spring in the 0 mm slack setting. With the 10 mm slack setting, the damper never engaged. Hence, we investigated a wide range of possible slack conditions, from complete to zero tendon slack.

Vertical hopping. In the vertical hopping setup (Fig. 5e), the hip of the robot leg was fixed to a vertical rail (SVR-28, MISUMI). A force sensor (K3D60a, ME) was used to measure the ground reaction force during hopping. The step-down perturbation was realized using a 3D-printed block (PLA) and an automatic block-removal device. The block was placed on top of the force sensor to elevate the ground. Magnets were inserted into the block and the top plate of the force sensor to prevent relative sliding during the leg impact. The block-removal device was a lever arm actuated by a servo motor (1235M, Power HD). The arm pushed away the block during the aerial phase of a hopping cycle (Supplementary Movie S1). This automatic block-removal device was needed to remove the perturbation block within the aerial hopping phase reliably (200 ms in our experiments).

The vertical hopping setup was instrumented as follows. The hip position was measured by a linear encoder (AS5311, AMS). The loadcells (spring and damper) and the ground reaction force sensor readings were amplified (9326, Burster) and then recorded by a microcontroller (Due, Arduino) with internal 12-bit ADC. The motor position was measured by a 12-bit rotary encoder (AEAT8800-Q24, Broadcom). We used an open-source motor driver (Micro-Driver³⁶) for motor control, current sensing, and encoder reading, which runs dual motor field-oriented control at 10 kHz. We monitored the motor driver current with a current sensor (ACS723T-AB, Allegro Microsystems). A second microcontroller (Uno, Arduino) was implemented to control the servo motor for automatic block removal. A single-board computer (Raspberry Pi 4B) was used to centralize and synchronize all sensor readings and motor commands in 1 kHz.

We implemented a Raibert-like⁵⁷ open-loop controller for vertical hopping. The hip was position controlled with a PD controller to keep a vertical posture. The knee was torque controlled to produce a defined torque at a given duty cycle, typically during the second half of the stance phase. Motor commands are illustrated in the inserted plots in Fig. 5e. Control parameters for a stable hopping gait were found through manual tuning, resulting in a 450 ms cycle time with 100 ms knee motor push-off. The knee torque was tuned for each setting of the damper tendon slack to maintain the same hopping heights across tested conditions (Supplementary Table S2).

We tested two perturbation levels: 31 mm and 47 mm, equivalent to 10% and 15% of the leg length, respectively. For each hopping trial, the robot hopped for 1 min. We analyzed ten steps before and after the perturbation. Each hopping condition was repeated ten times. We recorded in total 80 trials; two perturbations \times four slack settings \times ten repetitions.

Forward hopping. In the forward hopping setup (Fig. 5f), the robot leg was mounted on a boom in a four-bar design. This mount permits only horizontal and vertical motion in the robot's sagittal plane. The length of the boom was 1.613 m, and the travel distance of a complete revolution was around 10 m. The boom design is openly available⁵⁸.

The instrumentation of the forward hopping setup was similar to that of the vertical hopping setup. The force measurement and the automatic block-removal device were incompatible with the boom setup and were removed. All the other sensors remained. Horizontal and vertical motions of the rotating boom were measured by two 11-bit rotary encoders (102-V, AMS).

We generated the forward motion of the robot leg using a feed-forward central pattern generator (CPG). In most vertebrates, CPGs contribute to controlling rhythmic motion⁵⁹, such as locomotion. We implemented a CPG controller for the hip angle trajectory θ_{hip} :

$$\theta_{hip} = A_{hip} \cos(\Phi) + O_{hip} \quad (2)$$

$$\Phi = \begin{cases} \frac{\phi}{2D} & \phi < 2\pi D_{vir} \\ \frac{\phi + 2\pi(1 - 2D_{vir})}{2(1 - D_{vir})} & \text{else} \end{cases} \quad (3)$$

where A_{hip} is the hip angle amplitude, Φ the hip angle phase, O_{hip} the hip angle offset, D_{vir} the virtual duty factor as the fraction of time when the leg moves forward, and ϕ the oscillator's linearly progressing phase. The knee motor was torque controlled to generate push-off force in the late stance, following a fixed square-wave pattern as in the vertical hopping with the same frequency as the hip CPG. The motor commands are shown in the overlay plots of Fig. 5f. For ease of comparison, the control parameters (Supplementary Table S2) remained the same for all forward-hopping experiments.

To replicate rough terrain in a controlled way, we designed 3D-print tracks with a sinusoidal profile (Fig. 5f). The circular track was built from 3D-printed blocks. These were serially connected and taped to the floor. Each block is 360 mm long, and 27 blocks fit the circumference of the hopping path. A single, shorter connection block was added (red, Fig. 5f). This connection block prevents the hopping cycle from being entrained by the terrain harmonic perturbation pattern, e.g., repeatedly stepping onto the exact position of a cycle length of the track. We tested two rough terrains, with the amplitude of the sinusoidal perturbation being 5 mm and 10 mm. In addition, we also tested hopping on flat terrain. For each trial, the robot performed a total of six revolutions. We cropped the first and the last revolution from the recorded data and analyzed the remaining four revolutions (60 steps per condition).

Further, we designed ramp-up-step-down perturbations to disturb stable hopping during forward locomotion. Within a revolution's 10m hopping path, we built a slope of 3m length for the robot leg to gradually climb and jump off. We tested two perturbation heights: 47 mm and 93 mm, equivalent to 15% and 30% of leg length, respectively. For each trial, the robot leg performed 12 revolutions. We cropped the first and the last revolution from the recorded data and analyzed the remaining ten revolutions (150 steps per condition).

Data analysis. The ground reaction force and vertical position data were filtered for the vertical hopping experiments with a 4th-order zero-lag Butterworth filter. The loadcells were calibrated to output force reading only at leg flexion. The spring and damper force data were smoothed using a moving average filter with a filter span of 5 samples. The boom encoder data were filtered with a 4th-order zero-lag Butterworth filter for the forward hopping experiments. The cutoff frequencies (9–19 Hz) of the Butterworth filter were determined by residual analysis⁶⁰.

The recovery steps in the vertical hopping experiment were calculated by first computing the average hop height before perturbation as a reference height (dotted lines in Fig. 2f) and then finding the post-perturbation hop height that intersected with the $\pm 4\%$ boundary of the reference height²¹. The cost of hopping was calculated by normalizing the electric energy consumption E_{elec} of one hopping step to the system's gravitational potential energy at the apex.

$$CoH = \frac{E_{elec}}{m \cdot g \cdot h_{apex}} \quad (4)$$

where m is the robot mass, g the gravitational acceleration, h_{apex} the apex height position.

We defined two measurements for evaluating the robustness of forward hopping after the ramp-up-step-down perturbation. The recovery steps were defined as the number of steps needed by the robot leg to recover its stable hopping after the step-down perturbation. This metric quantified how fast the robot system can recover from perturbation, and it was measured by visual inspection of the video recordings and kinematic data. The failure step metric quantified the number of failures after a perturbation was applied. We identified two failure modes from the video recordings: the robot leg could slip or stop after the perturbation (Supplementary Movie S3). The number of failures was visually counted from the video recordings. The CoT was calculated by the electric energy consumption per distance traveled d , normalized by the robot weight.

$$CoT = \frac{E_{elec}}{m \cdot g \cdot d} \quad (5)$$

All data were processed with Matlab (R2021b, *MathWorks*).

Data availability

All data needed to evaluate the conclusions of the paper are available in the paper or the Supplementary Information. Additional data and the computer-aided design model of the robot leg are available from <https://doi.org/10.1038/s41598-023-30318-3>.

Received: 8 December 2022; Accepted: 20 February 2023

Published online: 25 February 2023

References

- More, H. L. *et al.* Scaling of Sensorimotor Control in Terrestrial Mammals. *Proc. R. Soc. B: Biol. Sci.* **277**, 3563–3568. <https://doi.org/10.1098/rspb.2010.0898> (2010).
- Gordon, J. C., Holt, N. C., Biewener, A. & Daley, M. A. Tuning of feedforward control enables stable muscle force-length dynamics after loss of autogenic proprioceptive feedback. *eLife* **9**, e53908. <https://doi.org/10.7554/eLife.53908> (2020).
- More, H. L. & Donelan, J. M. Scaling of sensorimotor delays in terrestrial mammals. *Proc. R. Soc. B* **285**, 20180613. <https://doi.org/10.1098/rspb.2018.0613> (2018).
- Kamska, V., Daley, M. & Badri-Spröwitz, A. 3D Anatomy of the Quail Lumbosacral Spinal Canal-Implications for Putative Mechanosensory Function. *Integr. Org. Biol.* **2**, 1. <https://doi.org/10.1093/iob/obaa037> (2020).
- Ashtiani, M. S., Aghamaleki Sarvestani, A. & Badri-Spröwitz, A. Hybrid parallel compliance allows robots to operate with sensorimotor delays and low control frequencies. *Front. Robot. AI* **170**, 1. <https://doi.org/10.3389/frobt.2021.645748> (2021).
- Loeb, G. E., Brown, I. E. & Cheng, E. J. A hierarchical foundation for models of sensorimotor control. *Exp. Brain Res.* **126**, 1–18. <https://doi.org/10.1007/s002210050712> (1999).
- Wagner, H. & Blickhan, R. Stabilizing function of skeletal muscles: An analytical investigation. *J. Theor. Biol.* **199**, 163–179. <https://doi.org/10.1006/jtbi.1999.0949> (1999).
- Grillner, S. The role of muscle stiffness in meeting the changing postural and locomotor requirements for force development by the ankle extensors. *Acta Physiol. Scand.* **86**, 92–108. <https://doi.org/10.1111/j.1748-1716.1972.tb00227.x> (1972).

9. Daley, M. A., Voloshina, A. & Biewener, A. A. The role of intrinsic muscle mechanics in the neuromuscular control of stable running in the guinea fowl. *J. Physiol.* **587**, 2693–2707. <https://doi.org/10.1113/jphysiol.2009.171017> (2009).
10. Brown, I. E., Scott, S. H. & Loeb, G. E. Reflexes—Programmable high-gain zero-delay intrinsic responses of perturbed musculoskeletal systems. *Soc. Neurosci. Abst.* **21**, 562 (1995).
11. Brown, I. E. & Loeb, G. E. A reductionist approach to creating and using neuromusculoskeletal models. In *Biomechanics and Neural Control of Posture and Movement*, 148–163. https://doi.org/10.1007/978-1-4612-2104-3_10 (Springer, 2000).
12. Alexander, R., Maloiy, G., Ker, R., Jayes, A. & Warui, C. The role of tendon elasticity in the locomotion of the camel (*Camelus dromedarius*). *J. Zool.* **198**, 293–313. <https://doi.org/10.1111/j.1469-7998.1982.tb02077.x> (1982).
13. Alexander, R. M. Energy-saving mechanisms in walking and running. *J. Exp. Biol.* **160**, 55–69. <https://doi.org/10.1242/jeb.160.1.55> (1991).
14. Hof, A. L. Effects of Muscle Elasticity in Walking and Running. In *Multiple Muscle Systems*, 591–607. https://doi.org/10.1007/978-1-4613-9030-5_38 (Springer New York, New York, NY, 1990).
15. Biewener, A. A. & Roberts, T. J. Muscle and tendon contributions to force, work, and elastic energy savings: a comparative perspective. *Exerc. Sport Sci. Rev.* **28**, 99–107 (2000).
16. Robertson, B. D. & Sawicki, G. S. Exploiting elasticity: Modeling the influence of neural control on mechanics and energetics of ankle muscle-tendons during human hopping. *J. Theor. Biol.* **353**, 121–132. <https://doi.org/10.1016/j.jtbi.2014.03.010> (2014).
17. Roberts, T. J. & Azizi, E. The series-elastic shock absorber: tendons attenuate muscle power during eccentric actions. *J. Appl. Physiol. (Bethesda, Md.: 1985)* **109**, 396–404. <https://doi.org/10.1152/jappphysiol.01272.2009> (2010).
18. Spröwitz, A. *et al.* Towards dynamic trot gait locomotion: Design, control, and experiments with cheetah-cub, a compliant quadruped robot. *Int. J. Robot. Res.* **32**, 932–950. <https://doi.org/10.1177/0278364913489205> (2013).
19. Grizzle, J., Hurst, J., Morris, B., Park, H.-W. & Sreenath, K. MABEL, a new robotic bipedal walker and runner. In *2009 American Control Conference*, 2030–2036, <https://doi.org/10.1109/ACC.2009.5160550> (IEEE, 2009).
20. Hubicki, C. *et al.* Atrias: Design and validation of a tether-free 3d-capable spring-mass bipedal robot. *Int. J. Robot. Res.* **35**, 1497–1521. <https://doi.org/10.1177/0278364916648388> (2016).
21. Zhao, G., Mohseni, O., Murcia, M., Seyfarth, A. & Sharbafi, M. A. Exploring the effects of serial and parallel elasticity on a hopping robot. *Front. Neurobot.* <https://doi.org/10.3389/fnbot.2022.919830> (2022).
22. Müller, R., Tschiesche, K. & Blickhan, R. Kinetic and kinematic adjustments during perturbed walking across visible and camouflaged drops in ground level. *J. Biomech.* **47**, 2286–2291. <https://doi.org/10.1016/j.jbiomech.2014.04.041> (2014).
23. Haeufle, D. F. B., Günther, M., Wunner, G. & Schmitt, S. Quantifying control effort of biological and technical movements: An information-entropy-based approach. *Phys. Rev. E* **89**, 012716. <https://doi.org/10.1103/PhysRevE.89.012716> (2014).
24. Shen, Z. & Seipel, J. A fundamental mechanism of legged locomotion with hip torque and leg damping. *Bioinspir. Biomimet.* **7**, 046010. <https://doi.org/10.1088/1748-3182/7/4/046010> (2012).
25. Secer, G. & Saranlı, U. Control of monopodal running through tunable damping. In *2013 21st Signal Processing and Communications Applications Conference (SIU)*, 1–4. <https://doi.org/10.1109/SIU.2013.6531557> (IEEE, 2013).
26. Abraham, I., Shen, Z. & Seipel, J. A nonlinear leg damping model for the prediction of running forces and stability. *J. Comput. Nonlinear Dyn.* **10**, 1. <https://doi.org/10.1115/1.4028751> (2015).
27. Haeufle, D. F. B., Grimmer, S. & Seyfarth, A. The role of intrinsic muscle properties for stable hopping - stability is achieved by the force-velocity relation. *Bioinspir. Biomimet.* **5**, 016004. <https://doi.org/10.1088/1748-3182/5/1/016004> (2010).
28. Kalveram, K. T., Haeufle, D. F. B., Seyfarth, A. & Grimmer, S. Energy management that generates terrain following versus apex-preserving hopping in man and machine. *Biol. Cybern.* **106**, 1–13. <https://doi.org/10.1007/s00422-012-0476-8> (2012).
29. Günther, M. & Schmitt, S. A macroscopic ansatz to deduce the Hill relation. *J. Theor. Biol.* **263**, 407–18. <https://doi.org/10.1016/j.jtbi.2009.12.027> (2010).
30. Monteleone, S., Negrello, F., Catalano, M. G., Garabini, M. & Grioli, G. Damping in compliant actuation: A review. *IEEE Robot. Autom. Mag.* **29**, 47–66. <https://doi.org/10.1109/MRA.2021.3138388> (2022).
31. Candan, S. Ş., Karagöz, O. K., Yazıcıoğlu, Y. & Saranlı, U. Design of a parallel elastic hopper with a wrapping cam mechanism and template based virtually tunable damping control. In *Dynamic Systems and Control Conference*, vol. 84270, V001T05A009. <https://doi.org/10.1115/DSCC2020-3278> (American Society of Mechanical Engineers, 2020).
32. Seok, S. *et al.* Design principles for energy-efficient legged locomotion and implementation on the MIT cheetah robot. *IEEE/ASME Trans. Mechatron.* **20**, 1117–1129. <https://doi.org/10.1109/TMECH.2014.2339013> (2015).
33. Hutter, M. *et al.* Starleth: A compliant quadrupedal robot for fast, efficient, and versatile locomotion. In *Adaptive Mobile Robotics*, 483–490, https://doi.org/10.1142/9789814415958_0062 (World Scientific, 2012).
34. Havoutis, I., Semini, C., Buchli, J. & Caldwell, D. G. Quadrupedal trotting with active compliance. In *2013 IEEE International Conference on Mechatronics (ICM)*, 610–616, <https://doi.org/10.1109/ICMECH.2013.6519112> (IEEE, 2013).
35. Kalouche, S. Goat: A legged robot with 3d agility and virtual compliance. In *2017 IEEE/RIS International Conference on Intelligent Robots and Systems (IROS)*, 4110–4117. <https://doi.org/10.1109/IROS.2017.8206269> (2017).
36. Grimminger, F. *et al.* An Open Force-Controlled Modular Robot Architecture for Legged Locomotion Research. *The IEEE Robot. Autom. Lett.* <https://doi.org/10.1109/LRA.2020.2976639> (2020).
37. Vanderborght, B. *et al.* Variable impedance actuators: A review. *Robot. Auton. Syst.* **61**, 1601–1614. <https://doi.org/10.1016/j.robot.2013.06.009> (2013).
38. Mo, A., Izzı, F., Haeufle, D. F. & Badri-Spröwitz, A. Effective viscous damping enables morphological computation in legged locomotion. *Front. Robot. AI* **7**, 110. <https://doi.org/10.3389/frobot.2020.00110> (2020).
39. Robi, K., Jakob, N., Matevz, K. & Matjaz, V. The physiology of sports injuries and repair processes. *Current Issues in Sports and Exercise Medicine* 43–86, <https://doi.org/10.5772/54234> (2013).
40. Heers, A. M., Rankin, J. W. & Hutchinson, J. R. Building a bird: musculoskeletal modeling and simulation of wing-assisted incline running during avian ontogeny. *Front. Bioeng. Biotechnol.* **6**, 140. <https://doi.org/10.3389/fbioe.2018.00140> (2018).
41. Badri-Spröwitz, A., Aghamaleki Sarvestani, A., Sitti, M. & Daley, M. A. Birdbot achieves energy-efficient gait with minimal control using avian-inspired leg clutching. *Sci. Robot.* **7**, eabg4055. <https://doi.org/10.1126/scirobotics.abg4055> (2022).
42. Tucker, V. A. The energetic cost of moving about: walking and running are extremely inefficient forms of locomotion. much greater efficiency is achieved by birds, fish-and bicyclists. *Am. Sci.* **63**, 413–419 (1975).
43. Faisal, A. A., Selen, L. P. & Wolpert, D. M. Noise in the nervous system. *Nat. Rev. Neurosci.* **9**, 292–303. <https://doi.org/10.1038/nrn2258> (2008).
44. Eliasmith, C. & Anderson, C. H. *Neural Engineering: Computation, Representation, and Dynamics in Neurobiological Systems* (MIT Press, 2003).
45. Heim, S., Millard, M., Le Mouel, C. & Badri-Spröwitz, A. A little damping goes a long way: a simulation study of how damping influences task-level stability in running. *Biol. Lett.* **16**, 20200467. <https://doi.org/10.1098/rsbl.2020.0467> (2020).
46. Wilson, A. M., McGuigan, M. P., Su, A. & Van den Bogert, A. J. Horses damp the spring in their step. *Nature* **414**, 895–899 (2001).
47. Cham, J. G. & Cutkosky, M. R. Dynamic Stability of Open-Loop Hopping. *J. Dyn. Syst. Meas. Contr.* **129**, 275–284. <https://doi.org/10.1115/1.2718237> (2006).
48. Garcia, E., Arevalo, J. C., Munoz, G. & Gonzalez-de Santos, P. Combining series elastic actuation and magneto-rheological damping for the control of agile locomotion. *Robot. Auton. Syst.* **59**, 827–839, <https://doi.org/10.1016/j.robot.2011.06.006> (2011).

49. Arelekatti, V. N. M., Petelina, N. T., Johnson, W. B., Major, M. J. & Winter, V. A. G. Design of a Four-Bar Latch Mechanism and a Shear-Based Rotary Viscous Damper for Single-Axis Prosthetic Knees. *J. Mech. Robot.* **14**, 1. <https://doi.org/10.1115/1.4052804> (2021).
50. Wu, A. & Geyer, H. The 3-d spring-mass model reveals a time-based deadbeat control for highly robust running and steering in uncertain environments. *IEEE Trans. Rob.* **29**, 1114–1124. <https://doi.org/10.1109/TRO.2013.2263718> (2013).
51. Huerta, C. V., Xiong, X., Billeschou, P. & Manoonpong, P. Adaptive neuromechanical control for robust behaviors of bio-inspired walking robots. In *Neural Information Processing: 27th International Conference, ICONIP 2020, Bangkok, Thailand, November 23–27, 2020, Proceedings, Part II* 27, 775–786. https://doi.org/10.1007/978-3-030-63833-7_65 (Springer, 2020).
52. Roberts, S. & Koditschek, D. E. Mitigating energy loss in a robot hopping on a physically emulated dissipative substrate. In *2019 International Conference on Robotics and Automation (ICRA)*, 6763–6769, ICRA.2019.8793781 (IEEE, 2019).
53. Bogdanovic, M., Khadiv, M. & Righetti, L. Learning variable impedance control for contact sensitive tasks. *IEEE Robot. Autom. Lett.* **5**, 6129–6136. <https://doi.org/10.1109/LRA.2020.3011379> (2020).
54. Xiong, X. & Manoonpong, P. Adaptive motor control for human-like spatial-temporal adaptation. In *2018 IEEE International Conference on Robotics and Biomimetics (ROBIO)*, 2107–2112. <https://doi.org/10.1109/ROBIO.2018.8665222> (IEEE, 2018).
55. Bobbert, M. F., Yeadon, M. R. & Nigg, B. M. Mechanical analysis of the landing phase in heel-toe running. *J. Biomech.* **25**, 223–234. [https://doi.org/10.1016/0021-9290\(92\)90022-S](https://doi.org/10.1016/0021-9290(92)90022-S) (1992).
56. Walter, R. M. & Carrier, D. R. Ground forces applied by galloping dogs. *J. Exp. Biol.* **210**, 208–216. <https://doi.org/10.1242/jeb.02645> (2007).
57. Raibert, M. *Legged Robots that Balance*. Artificial Intelligence Series (MIT Press, 1986).
58. Ruppert, F., Aghamaleki Sarvestani, A., Heim, S., Mo, A. & Badri-Spröwitz, A. Instrumented boom, CAD data. <https://doi.org/10.17617/3.RSO2AG> (2022).
59. Ijspeert, A. J., Crespi, A., Ryczko, D. & Cabelguen, J.-M. From swimming to walking with a salamander robot driven by a spinal cord model. *Science* **315**, 1416–1420. <https://doi.org/10.1126/science.1138353> (2007).
60. Winter, D. *Biomechanics and Motor Control of Human Movement* (Wiley, 2009).

Acknowledgements

The authors thank the International Max Planck Research School for Intelligent Systems (IMPRS-IS) for supporting An Mo, Fabio Izzì, Emre Cemal Gönen, and the China Scholarship Council (CSC) for supporting An Mo. The authors thank Felix Ruppert and Alborz Aghamaleki Sarvestani for assisting the robot development. The authors also thank Prof. Syn Schmitt and Prof. Martin Giese for inspiring discussions on the project.

Author contributions

A.M., F.I., D.H., and A.B.-S. conceptualized the project, A.M., D.H., and A.B.-S. conceived the experiments, A.M. designed and implemented the robot and experimental setups, A.M. and E.C.G. conducted experiments and analyzed the data, all authors interpreted and discussed the data, A.M., F.I. and E.C.G. prepared the manuscript, all authors reviewed the manuscript.

Funding

Open Access funding enabled and organized by Projekt DEAL. This work was funded by the Deutsche Forschungsgemeinschaft (DFG, German Research Foundation) - 449912641, HA 7170/3.

Competing interests

The authors declare no competing interests.

Additional information

Supplementary Information The online version contains supplementary material available at <https://doi.org/10.1038/s41598-023-30318-3>.

Correspondence and requests for materials should be addressed to A.M.

Reprints and permissions information is available at www.nature.com/reprints.

Publisher's note Springer Nature remains neutral with regard to jurisdictional claims in published maps and institutional affiliations.



Open Access This article is licensed under a Creative Commons Attribution 4.0 International License, which permits use, sharing, adaptation, distribution and reproduction in any medium or format, as long as you give appropriate credit to the original author(s) and the source, provide a link to the Creative Commons licence, and indicate if changes were made. The images or other third party material in this article are included in the article's Creative Commons licence, unless indicated otherwise in a credit line to the material. If material is not included in the article's Creative Commons licence and your intended use is not permitted by statutory regulation or exceeds the permitted use, you will need to obtain permission directly from the copyright holder. To view a copy of this licence, visit <http://creativecommons.org/licenses/by/4.0/>.

© The Author(s) 2023

Supplementary Materials for **Slack-based tunable damping leads to a trade-off between robustness and efficiency in legged locomotion**

**An Mo^{1,*}, Fabio Izzzi^{1,2}, Emre Cemal Gönen¹, Daniel Haeufle^{2,3}, and Alexander
Badri-Spröwitz^{1,4}**

¹Dynamic Locomotion Group, Max Planck Institute for Intelligent Systems, Stuttgart, 70569, Germany

²Hertie Institute for Clinical Brain Research and Center for Integrative Neuroscience, University of Tübingen,
Tübingen, 72076, Germany

³Institute for Modelling and Simulation of Biomechanical Systems, Computational Biophysics and Biorobotics,
University of Stuttgart, Stuttgart, 70569, Germany

⁴Department of Mechanical Engineering, KU Leuven, Leuven, 3001, Belgium

*Corresponding author: An Mo, mo@is.mpg.de

The PDF file includes:

Figure S1
Tables S1 to S5
Legends for movies S1 to S3

Other Supplementary Material for this manuscript includes the following:

Movies S1 to S3: <https://youtu.be/Sa-q-5NucGY>
CAD model of the robot leg and data analysis: <https://doi.org/10.17617/3.THJWG8>

1 Leg design parameters

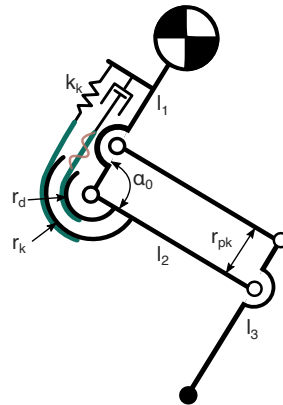


Figure S1. Schematics of the leg with the key design parameters.

Parameters	Value
Robot mass - vertical hopping	m_v 1.94 kg
Robot mass - forward hopping	m_f 0.94 kg
Leg resting length	l_0 310 mm
Segment 1 length	l_1 150 mm
Segment 2 length	l_2 150 mm
Segment 3 length	l_3 150 mm
Knee spring pulley radius	r_k 30 mm
Knee damper pulley radius	r_d 20 mm
Knee spring stiffness	k_k 10.9 N/mm
Bi-articular insertion radius	r_{pk} 32 mm
Knee resting angle	α_0 100°

Table S1. Robot design parameters.

2 Robot control parameters

Parameters		Value
Vertical hopping		
Hopping frequency	f_v	2.2 Hz
Knee torque amplitude	τ_v	4.0 - 4.3Nm
Knee duty cycle	—	0.22
Forward hopping		
Hip amplitude	θ_{hip}	18°
Hip offset	O_{hip}	2°
Hopping frequency	f_f	1.85 Hz
Hip virtual duty factor	D_{vir}	0.4
Knee torque amplitude	τ_f	1.3 Nm
Knee phase shift	—	0.75
Knee duty cycle	—	0.2

Table S2. Robot control parameters

3 Experimental results

Perturbation [LL]	Damper slack [mm]	Hop height [mm]	CoH [l]	Recovery steps [l]	Delay [ms]	E_d [mJ]
10%	10	53.3	6.3	2.5	-	1
10%	6	49.3	6.6	1.7	51	26
10%	3	49.1	6.7	2.0	26	117
10%	0	44.7	7.4	2.9	0	186
15%	10	55.8	6.3	3.2	-	1
15%	6	47.8	6.7	2.5	50	29
15%	3	43.2	7.0	3.6	24	86
15%	0	42.4	7.6	5.9	0	152

Table S3. Experimental results of vertical hopping with step-down perturbation. The energy dissipated by the damper (E_d) is calculated by integrating the damping force with respect to the damper compression (Fig. 2c).

Roughness amplitude [mm]	Damper slack [mm]	Speed [m/s]	CoT [l]	Step cycle std [ms]
0	10	0.80	1.01	27.1
0	6	0.79	0.99	16.2
0	3	0.71	1.07	2.4
0	0	0.67	1.35	2.1
±5	10	0.76	0.75	2.4
±5	6	0.76	1.01	13.4
±5	3	0.74	1.01	11.1
±5	0	0.68	1.24	2.2
±10	10	0.76	0.79	3.1
±10	6	0.71	0.97	3.6
±10	3	0.72	0.80	2.7
±10	0	0.66	1.32	2.7

Table S4. Experimental results of forward hopping with continuous perturbation.

Perturbation [LL]	Damper slack [mm]	Speed [m/s]	CoT [l]	Recovery steps [l]	Failure steps [l]
15%	10	0.81	0.95	2.7	7
15%	6	0.78	1.00	2.0	4
15%	3	0.72	1.36	1.7	6
15%	0	0.68	1.30	1.0	0
30%	10	0.80	0.91	2.6	10
30%	6	0.75	0.93	2.4	10
30%	3	0.73	1.18	2.9	10
30%	0	0.64	1.44	2.3	3

Table S5. Experimental results of forward hopping with ramp-up-step-down perturbation.

4 Supplementary Videos

Movie-S1: Vertical hopping with step-down perturbation. The leg is hopping on a block whose height is 15% of the leg length. The slack of the damper is set to 3 mm. The first part of the video shows the experiment in real-time. In the second part, slow motion of the same experiment is repeated. In both cases, hip position y , GRF, spring and damper forces are plotted synchronized to the video. In the last part, the phase plots of the all experiments show the relation between hopping speed and the hopping position.

Movie-S2: Forward hopping with continuous perturbation. The leg moves forward by hopping on the sinusoidal terrain with ± 10 mm amplitude. The damper is fully engaged, i.e., the slackness is 0 mm. After the leg completes one full rotation on the terrain, the video shows frames taken by the high-speed video camera.

Movie-S3: Failure modes of forward hopping with ramp-up-step-down perturbation. The leg moves on the flat surface, and it gradually climbs on the ramp to jump off. The perturbation height is 30% of the leg length, and the damper slack is set to 3 mm. The bottom-right plot shows the synchronized hip position in planer motion. The video shows three cases: slipping, stopping, and the good response after the step-down perturbations. The slipping case can be identified by audio irregularity.

Biophysical Simulation Reveals the Mechanics of the Avian Lumbar Sacral Organ

An Mo¹, Viktoriia Kamska¹, Fernanda Bribiesca-Contreras¹, Janet Hauptmann^{1,3}, Monica Daley², Alexander Badri-Spröwitz^{1,4}

¹Dynamic Locomotion Group, Max Planck Institute for Intelligent Systems, Stuttgart, Germany

²Department of Ecology and Evolutionary Biology, University of California, Irvine, USA

³Harz University for Applied Sciences, Wernigerode, Germany

⁴Department of Mechanical Engineering, KU Leuven, Leuven, Belgium

Keywords: lumbar sacral organ, intraspinal mechanosensing, physical model, biophysical simulation, spinal cord, avian locomotion

The lumbar sacral organ (LSO) is a lumbar sacral spinal canal morphology that is universally and uniquely found in birds. Recent studies suggested an intraspinal mechanosensor function that relies on the compliant motion of soft tissue in the spinal cord fluid. It has not yet been possible to observe LSO soft tissue motion *in vivo* due to limitations of imaging technologies. As an alternative approach, we developed an artificial biophysical model of the LSO, and characterized the dynamic responses of this model when entrained by external motion. The parametric model incorporates morphological and material properties of the LSO. We varied the model's parameters to study the influence of individual features on the system response. We characterized the system in a locomotion simulator, producing vertical oscillations similar to the trunk motions. We show how morphological and material properties effectively shape the system's oscillation characteristics. We conclude that external oscillations could entrain the soft tissue of the intraspinal lumbar sacral organ during locomotion, consistent with recently proposed sensing mechanisms.

1 Introduction

Birds are exceptional bipedal runners capable of robust running over unexpected disturbance [1]. Robust locomotion requires a sense that informs the central nervous system about the environment and the system's internal state. Such sensing is essential to coordinate limbs [2, 3], balance [4], manipulate the environment [5], for entrainments [6–9], and protect from excessive loading or untimely muscle stretching [10]. Rapid sensing and response is crucial, especially during fast locomotion. When stance phases are brief, a sensorimotor delay [11] will cause a temporal blind spot in the control loop, potentially leading to detrimental falls. Interestingly, birds generally have long necks, contributing to increased sensorimotor delays from higher brain centers, as well as from the balance-sensing vestibular system [12]. The immediate physical response of the musculoskeletal [13] system alone cannot fully explain birds' agility.

Birds' outstanding locomotion abilities might be supported by an unexplored and uniquely avian intraspinal mechanosensor: the lumbar sacral organ (LSO, Figure 1) [14]. It has been suggested that the LSO could act as a second vestibular-like sensing organ, independent of the head's orientation [14]. The LSO is located at the lower spine, right next to the sciatic nerves that communicate motor commands for locomotion [15]. The short distance between intraspinal mechanosensors and spinal motor-control units could minimize sensorimotor delays, and effectively reduce response times [16].

The LSO is a collection of unique anatomical features (Figure 2A). A glycogen body is dorsally wedged between both spinal cord hemispheres, spanning over three segments [16]. At the LSO's centre, the glycogen body ventrally reaches the central canal [17, 18]. Accessory lobes ("Hofmann nuclei" or "major marginal nuclei", [19]) are found pairwise, segmentally, and laterally to the lateral side of the spinal cord. Potentially, they contain mechanoreceptors [14, 20–25]. Hofmann nuclei processes project into ipsilateral and contralateral hemispheres [19, 26]. The spinal cord is supported

ventrally by a complex dentate ligament network, comprised of lateral longitudinal, ventral longitudinal, and transverse ligaments [16]. The vertebrae in the LSO region are fused with fusion zones formed as transverse semi-circular grooves (“semi-circular canals” [22]). Between the LSO soft tissue (spinal cord, glycogen body, dentate ligament network, accessory lobes) and the spinal canal walls exists a significant fluid space with a prominent dip ventral to the LSO central region [16].

Since its first discovery in 1811 [27], the exact function of the LSO remains an enigma. Early research suggested metabolic energy supply and myelin synthesis as potential functions for the glycogen body and accessory lobes [17, 28, 29]. Schroeder, Murray and Eide [19, 20] were the first to propose a mechanoreceptive function. They had found mechanoreceptor-like tissue in accessory lobes and therefore theorized that dentate ligament strain is transmitted to and sensed by the adjacent accessory lobes. Later, Necker proposed that semicircular grooves and spinal fluid are integral parts of the sensor organ’s function. He hypothesized that lumbosacral organ spinal fluid flow could excite mechanoreceptive accessory lobes [14, 30, 31]. Besides, he was the first to point to morphological similarities between the lumbosacral organ and the vestibular system [14]. Otherwise, possible mechanical functions of the LSO are largely unexplored. While conclusive evidence for the LSO sensing function is still missing, intraspinal mechanosensing has been found in a few animals; lampreys [32, 33], zebrafish [34, 35], and potentially in reptiles [36]. Despite the difference between these animals and birds, the similar location of their intraspinal mechanosensors is intriguing [25, 32, 35, 37], and suggests a homologous connection.

Based on our own observation of morphologies and material properties [16], we hypothesize a locomotion state sensing function of the LSO (Figure 1). We suspect that the viscoelastic properties of the spinal cord and ligaments allow these structures to physically deflect and oscillate within the enlarged fluid space [16]. During locomotion, the trunk oscillation, such as pitching, will entrain the spinal cord oscillation. The resulting soft tissue motion could resemble a mass-spring-damper system; the dense glycogen body as the mass, the elasticity of the spinal cord and the dentate ligament network as the spring, and the spinal fluid as the damper. The relative motion between the spinal cord and the spinal canal would stretch the mechanoreceptors contained in the accessory lobes, then accelerations and postural changes could be measured, leading to a fast state feedback of locomotion.

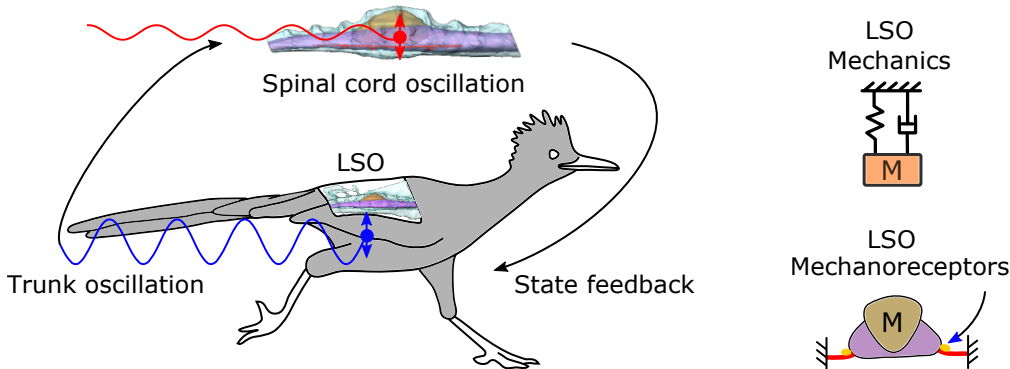


Figure 1: The LSO located at the lower spine of birds is hypothesized as an accelerometer. During locomotion such as running, the trunk oscillation will entrain the spine cord like a mass-spring-damper system. The morphology of LSO tunes the mass-spring-damper behavior. The entrained LSO stimulates the mechanoreceptors to provide fast state feedback of locomotion.

In this work, we focus on the mass-spring-damper properties of the LSO. Since birds feature the highest number of locomotion modes within species; they swim, dive, walk, and fly; their habitats and locomotion modalities may shape the LSO response through mass-spring-damper property variation. Structures like the glycogen body with densities higher than the spinal fluid will tend to sink, exerting forces on the dentate ligament network. The glycogen body are subject to growth [38], allowing for lifelong tuning and adaptation. The microfluidic environment of the spinal canal implies an effective flow resistance (Hagen–Poiseuille equation) to dampen high-frequency oscillation, similar to a mechanical low-pass filter. Neural tissue is fragile, with a reported maximum strain up to 7% for uni-axial fibre strain [39]. Likely, the combined structure of ligaments, spinal fluid, and glycogen body protects the spinal cord from excessive strain.

While the spinal soft tissue entrainment is likely, observing such entrainment within a running bird is a grand challenge. In birds, the spinal cord is well protected within the dense, fused bone structure. Imaging the soft tissue motion in vivo has failed so far. As an alternative approach, we developed a parametric, biophysical lumbosacral organ model, which we based on previously reported data [16]. In sum, we suggest three hypotheses related to the mass-spring-damper properties of the LSO. 1) The glycogen body tunes the LSO measurement range. 2) The narrow spinal canal dampens soft tissue oscillation. 3) The fine structure of the spinal canal diversifies the LSO response.

2 Materials and Methods

First, We developed a configurable biophysical model of the lumbosacral organ in birds (Figure 2). We parameterized the biophysical model’s morphology and varied its material properties to investigate the individual influence of each part and its associated hypothesis (Table 2). Then, the biophysical models were tested on a custom-built locomotion simulator (Figure 3), which emulates vertical locomotion patterns of running birds. Lastly, the biophysical model’s response to external accelerations was recorded and characterized (Figure 4).

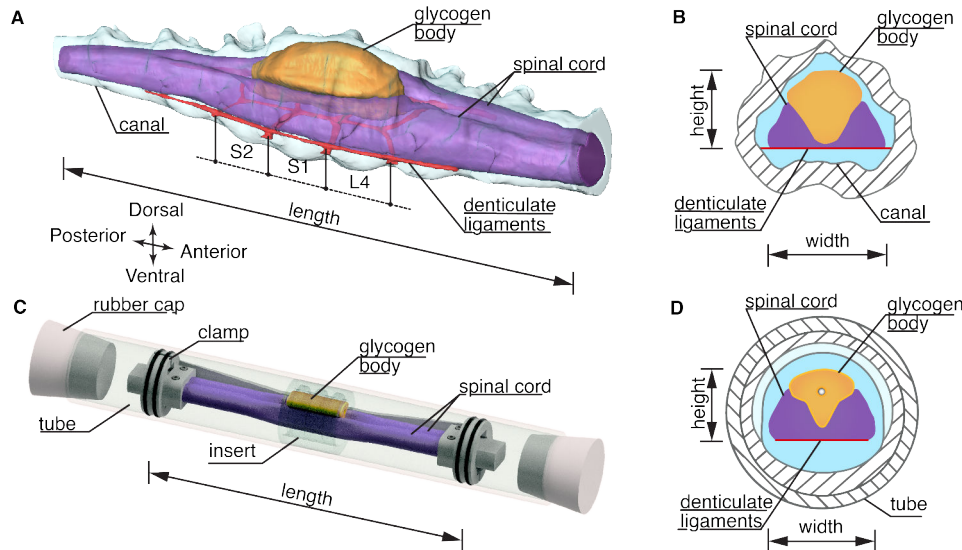


Figure 2: Lumbosacral soft tissue in the spinal canal, and its biophysical model developed here to simulate soft tissue motion. (A) Perspective view of the lumbosacral region of a common quail [16]. Shown are spinal cord (purple), glycogen body (orange), and dentate ligament network (red). (B) Transverse section through the vertebral column at vertebra fusion S1 and L4. (C) Biophysical model with spinal cord, glycogen body and semi-circular grooves mounted as a water-filled glass tube. In this configuration, the modelled spinal cord is clamped at its both ends. Transverse semi-circular grooves are cut into the insert as indentations. (D) Cross-cut view of the biophysical model at the position of a semi-circular groove.

2.1 Biophysical model

We aimed at these goals to implement and test the biophysical model of birds’ LSO: 1. Develop a simplified, parametric model for physical testing, with a low, appropriate number of design parameters. In contrast, a one-to-one replicated LSO geometry would lead to a large parameter number, which is infeasible for physical testing. 2. Select model parameters according to their relevance for the LSO’s physical functionality according to our hypotheses. 3. Create an LSO model of appropriate size for fabrication and instrumentation. 4. The ratio of volumes, material densities, and soft material stiffness approximates to data from the literature.

To replicate the geometry, we simplified and linearly scaled up the three-dimensional common quail model (*Coturnix coturnix*) made available by Kamska et al. [16]. Its main components were simplified as in the biophysical model: an spinal cord, a dentate ligament network, a glycogen body, the surrounding spinal fluid, the spinal canal morphology between spine segments L4 to S2 (Figure 2). We linearly scaled up the LSO soft parts, leading to model parameters documented in Table 1. The length of the biophysical model is 140 mm between proximal and distal anchor points (Figure 2C), which is roughly the size of the lumbosacral region of an emu [40]. We kept the volume ratio constant for the spinal cord, the glycogen body, and the spinal fluid (Table 1). We implemented model morphologies mimicking dorsal grooves and a ventral dip found in birds; both features were volume scaled.

To approximate the material properties, we fabricated the biophysical model with soft robotics techniques. The spinal cord and the glycogen body were moulded from silicone rubber, with dentate ligament network made from fabric attached. The glycogen body density is adjustable. A custom clamp holds the spinal soft tissue in a water-filled glass tube, simulating the fluid environment. A configurable insert existed in some biophysical models to implement the spinal canal morphologies. Detail fabrication steps are provided in the supplementary section S1. In sum, we prepared seven configurations of the biophysical model as shown in Table 2.

The resulting biophysical model allows for characterizing its compliant parts responding to external motions while interacting with the surrounding fluid and complex canal morphologies.

Table 1: Biophysical model design parameters. Volume percentages of the biophysical model are in reference to the quail model [16], for the sum of volumes at L4-S2 region.

Unit	Parameter	Reference	Design
Length [mm]	Width, w	3.5	21
	Length, l	20	140
	Height, h	5.0	30
Volume [mm ³]	Spinal cord, V_{SpC}	25 (36%)	4761 (35%)
	Spinal fluid, V_{SpF}	31 (45%)	6323 (47%)
	Glycogen body, V_{GB}	13 (19%)	2487 (18%)
Density [g/cm ³]	Spinal cord, ρ_{SpC}	1.0	1.0
	Spinal fluid, ρ_{SpF}	1.0	1.0
	Glycogen body, ρ_{GB}	1.4 – 1.5	1.0, 1.5, 2.0

Table 2: Biophysical model schematic overview. Cross-section views are made at the model centre. Blue areas represent fluid space; contours indicate canal shapes. Triangles with varying background colour/patterns represent spinal cord tissue with varying glycogen body density ρ_{GB} from 1.0 g/cm³ to 2.0 g/cm³. The canal diameter indicates the inner $\varnothing_{\text{canal}}$. Semi-circular grooves are located on the dorsal canal inside; dips are ventral to the spinal cord. Dips and semi-circular grooves are tested in models with narrow canals only (model 4-7). All models feature a fibre-reinforced spinal cord (short horizontal red line).

Model number	1	2	3	4	5	6	7
GB density [g/cm ³]	1.0	1.5	2.0	1.5	1.5	1.5	1.5
Canal diameter [mm]	51	51	51	24	24	24	24
Canal morphology	large	large	large	grooves+dip	dip	grooves	narrow

2.2 Locomotion simulation

We developed a locomotion simulator to produce the up-down motion of the bird’s trunk during running (Figure 3). The locomotion simulator generates vertical motions in a controlled manner and records the biophysical model’s compliant response. A stepper motor① (103H7823-1740, *Sanyo Denki*) drives a ball screw② (KUHC1205-340-100, *MISUMI*) mounted to a frame made of 20 mm plywood③, moving a motion platform④ vertically. The 3D-printed (PLA) motion platform holds the biophysical model⑥, an LCD screen⑧ (model 1602) and a video camera⑤ (Hero 5 Black, *GoPro*). The camera and the biophysical model move together. Hence, the camera observes the model’s compliant response within the local coordinate system. A rotary encoder⑦ (AS5045, *AMS*) counts spindle rotations, and the slider displacement is the product of spindle rotation and pitch.

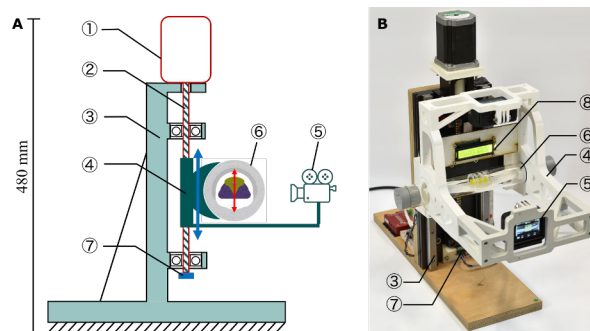


Figure 3: The locomotion simulator, schematic (A) and photo (B). The biophysical model⑥ is mounted to the platform④ of a linear drive③. A stepper motor① moves the slider vertically (blue) with a spindle②. An encoder⑦ records the spindle position. A camera⑤ mounted on the moving platform④ measures the biophysical model’s response (red). Video and encoder data are synchronized visually by observing the LCD screen⑧.

The locomotion simulated is instrumented. A motor driver (G201X, *geckodrive*) drives the stepper motor. A micro-controller (Teensy 4.0, *PJRC*) controls the stepper motor driver and an LCD screen. The LCD shows the setup’s status. Encoder data was sampled by a single board computer (Raspberry Pi, v.4B), with 10 μm resolution at 1 kHz update frequency. Biophysical model movement was camera-recorded at a sampling frequency of 240 Hz. Both data lines were synchronized by a programmed LCD backlight flash. The locomotion simulator produces oscillations up to a maximum frequency of 4.5 Hz at an amplitude of ± 5 mm.

We found only a few off-the-shelf motion simulators capable of highly dynamic motion (3 Hz to 5 Hz), all of which

were expensive. With this project, we are open-sourcing¹ our locomotion simulator design and control for barrier-free research; which is capable, easy to replicate, and comparably low-cost.

Testing protocols were identical for all models. Glass tubes were mounted to the locomotion simulator and vertically driven to oscillate with an amplitude of ± 5 mm. We stopped the motor after 5 s. The resulting damped model motion was recorded for another 3 s. Each model was driven at four ‘drive’ frequencies: 3.0, 3.5, 4.0 and 4.5 Hz. Trials were repeated eight times, resulting in a total of 224 trials; 4 drive frequencies with 8 repetitions and 7 models.

We extracted the biophysical model’s movement from the recorded videos with the Tracker software [41]. An example trial is shown in Figure 4. We divide the experiment’s time series into three phases:

1. Entrainment phase with settling time τ ;
2. Steady phase with peak-to-peak amplitude A , phase shift ϕ ;
3. Damping phase with decay rate ζ , damped oscillation frequency f_d .

The definitions of the measured parameters in each phase are documented in the supplementary section S2.

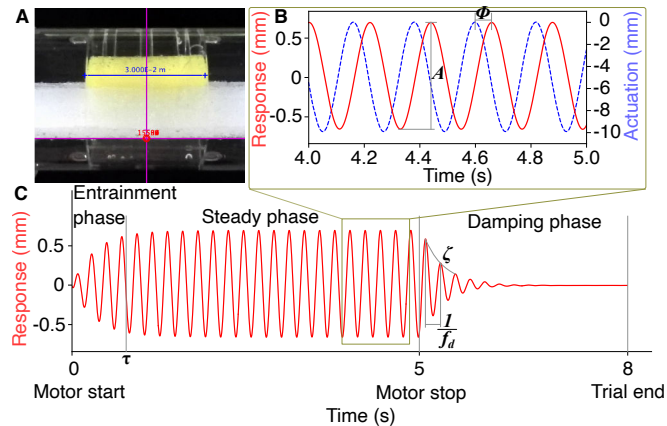


Figure 4: Typical model response to external motion. The data shown is extracted from trial 1, model-2, at 4.5 Hz external oscillation frequency. Each experiment shows three phases; (1) The entrainment phase, with a settling time τ spanning from start until the model reaches 90 % of the steady state amplitude. (2) In the steady phase we measure the model’s peak-to-peak amplitude A , and the phase shift ϕ between the external actuation and the model’s response. (3) The damping phase starts when the motor is switched off (5 s). We calculate the model’s decay rate ζ and the damped oscillation frequency f_d .

2.3 Functional parameter hypotheses

We tested three hypotheses with seven biophysical models (Table 3):

Table 3: Hypotheses and the corresponding control variables for model-1 to 7.

Hypothesis	Model #	Controlled variable
1	1 - 3	Density
2	2, 7	Canal size
3	4 - 7	Canal morphology

1) **The glycogen body tunes the LSO measurement range.** The glycogen body is unique in birds and unexplained. Since its density is notably higher than the surrounding spinal fluid and the spinal cord, we expect the glycogen body presents an effectively larger mass leading to higher soft tissue oscillation caused by external movements, compared to a neutrally buoyant glycogen body. We compare amplitude response and settling time of three glycogen body densities: 1.0, 1.5, and 2.0 g/cm³, and expect high glycogen body density associates with high amplitude.

2) **The narrow spinal canal dampens soft tissue oscillation.** The fluid space that allows for spinal cord oscillation is relatively small. Flow resistance increases in the proximity of walls according to the Hagen–Poiseuille equation. Hence, we expect that a narrow spinal canal increases flow resistance compared to a wide one, leading to reduced soft tissue oscillations. We investigate the effect of large and narrow canal size on the model’s response amplitude and decay rate.

3) **The spinal canal fine structure diversifies the LSO response.** Previous observations [16, 24, 42] hint the distinct spinal canal morphologies of different birds may be associated with habitats and locomotion modalities. We








¹www.github.com/moanan/1_dof_motion_simulator

expect the dorsal grooves and the ventral dip [16] both have an effect on spinal fluid flow and soft tissue oscillations. To test this, we map the combinations of the dorsal grooves and the ventral dip, and study the models' response amplitude and decay rate.

3 Results

Table 4 shows all results obtained, ordered by model and drive frequency, symbols are identical to Table 2.

Table 4: Results for all models depending on drive frequency, showing settling time during entrainment phase, peak-to-peak amplitude, phase shift between drive signal and model oscillation, damped oscillation frequency and decay rate during damping phase. Values are mean values \pm standard error (SE). SEs are not shown if smaller than the rounding digit.

Model	Freq. [Hz]	Settling time τ [s]	Amp. A [mm]	Phase shift ϕ [deg]	Damped freq. f_d [Hz]	Decay rate ζ [/]
1 	3.0	0.55 ± 0.07	0.11	25 ± 1	4.8	0.77 ± 0.03
	3.5	0.39	0.25	28 ± 1	4.8	0.69 ± 0.02
	4.0	0.37 ± 0.02	0.62	49 ± 1	4.7	0.79
	4.5	0.67	1.06	106 ± 1	4.7	0.83
2 	3.0	0.63 ± 0.05	0.13	20 ± 1	4.8	0.52 ± 0.02
	3.5	0.38	0.28	25 ± 1	4.8	0.59 ± 0.01
	4.0	0.36	0.66	40 ± 1	4.7	0.67 ± 0.01
	4.5	0.78 ± 0.01	1.33	92 ± 1	4.7	0.73
3 	3.0	0.47 ± 0.04	0.19	21 ± 1	4.5	0.58 ± 0.02
	3.5	0.39	0.44	24 ± 1	4.4	0.66 ± 0.01
	4.0	0.61	1.03	62 ± 1	4.4	0.72
	4.5	0.56	1.32	120 ± 1	4.4	0.74 ± 0.01
4 	3.0	0.48	0.25	46 ± 1	3.7	0.82 ± 0.02
	3.5	0.72 ± 0.02	0.57	80 ± 1	3.6	0.87 ± 0.01
	4.0	0.52	0.66	130 ± 1	3.6	0.87 ± 0.01
	4.5	0.36	0.56	154 ± 1	3.6	0.87 ± 0.01
5 	3.0	0.78 ± 0.16	0.06	152 ± 1	4.3 ± 0.3	1.28 ± 0.15
	3.5	0.45	0.11	123 ± 1	4.5 ± 0.1	1.53 ± 0.16
	4.0	0.40	0.19	127 ± 1	4.3 ± 0.2	1.50 ± 0.09
	4.5	0.42 ± 0.02	0.28	147 ± 1	4.4 ± 0.1	1.42 ± 0.14
6 	3.0	0.48	0.25	56 ± 1	3.5	0.88 ± 0.01
	3.5	0.70 ± 0.02	0.5	103 ± 1	3.5	0.92 ± 0.01
	4.0	0.40	0.5	138 ± 1	3.5	0.93 ± 0.02
	4.5	0.37	0.48	155 ± 1	3.5	0.89 ± 0.02
7 	3.0	0.88 ± 0.22	0.07	152 ± 1	4.4 ± 0.2	0.88 ± 0.11
	3.5	0.48 ± 0.04	0.12	127 ± 1	5.0 ± 0.2	1.24 ± 0.18
	4.0	0.42 ± 0.02	0.19	137 ± 1	4.6 ± 0.2	1.25 ± 0.21
	4.5	0.37	0.26	154 ± 1	4.5 ± 0.2	1.02 ± 0.13

3.1 Entrainment

All models showed an entrainment response similar to Figure 4. Within 1s models transitioned into steady-state oscillations. We observed steady-state peak-to-peak amplitude up to 1.3mm.

We observed a distinct frequency peak for each model processed with spectrum analysis. The damped oscillation frequency measured from damping phase was independent of the drive frequency for the same model, but differed between models (Table 4). Damped oscillation frequencies ranged from 3.5 Hz to 5.0 Hz. Albeit a different calculation method, damped oscillation frequencies of model 5 and 7 showed a similar dependency.

3.2 Influence of glycogen body density

In general, a denser glycogen body produced a larger peak-to-peak amplitude in the steady phase. The peak-to-peak amplitude increased with increasing drive frequency (Figure 5A). The peak-to-peak amplitude significantly differed between glycogen body densities in all models at all drive frequencies (t -test; p values $< 1e-4$) except for densities of

1.5 g/cm³ to 2.0 g/cm³ at 4.5 Hz. Model-2 with a glycogen body density of 1.5 g/cm³ showed the highest peak-to-peak amplitude of 1.33 mm. Independent of glycogen body density, models took between 0.36 s to 0.78 s to entrain, and we found no clear tendency for settling time for different glycogen body densities (Figure 5B).

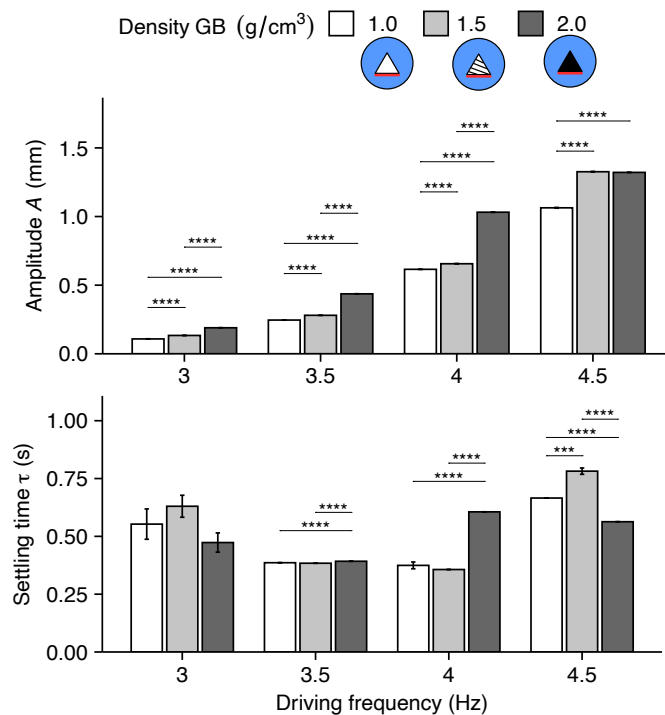


Figure 5: Influence of glycogen body density and drive frequency to peak-to-peak amplitude (A) and settling time (B). Values shown are for model-1, 2, and 3 with density of 1.0, 1.5, and 2.0 g/cm³, respectively. Drive frequencies tested were 3.0, 3.5, 4.0 and 4.5 Hz. Here and in all following figures, standard error shown as error bar, significant p -values from t -test pairwise comparisons as '****', 0; '***', 0-0.001; '**', 0.001-0.01, '*', 0.1-0.05. Error bars are not shown if the standard error is smaller than the measurement resolution.

3.3 Influence of canal size

The canal size had an effect on the soft tissue response amplitude and its decay rate (Figure 6). The larger canal of model-2 yielded a significant higher peak-to-peak amplitude of 1.33 mm at 4.5 Hz. In comparison, the narrow canal of model-7 yielded a maximum amplitude of 0.26 mm at 4.5 Hz (t -test; p values $<1e-4$). For both canal sizes, amplitudes increased with increasing drive frequency. A narrow canal produced damped oscillations with higher decay rate ζ of 0.88 to 1.25, compared to a large canal with decay rates between 0.52 to 0.73. However, the difference was only significant at 3.0 Hz and 3.5 Hz (t -test; p values <0.05). The narrow canal decay rate did not increase monotonically with drive frequency as the large canal model did.

3.4 Influence of canal morphology

Varying canal morphologies were implemented by simulating dorsal grooves or a ventral dip (model-4 to 7, Figure 7). The peak-to-peak amplitude significantly differed between these models at all drive frequencies (t -test; p values <0.05) and it was larger in the presence of grooves+dip with values ranging from 0.25 mm to 0.66 mm, followed by dorsal grooves with values from 0.25 mm to 0.5 mm. Decay rates were lower, between 0.82 to 0.93, for models with grooves and grooves+dip. Decay rates were highest between 1.28 to 1.53 for model-5 with its ventral dip. Decay rates differed significantly only when comparing grooves+dip versus ventral dip and ventral dip versus grooves at 4.0 Hz (t -test; p values <0.05). Note that the decay rate for the narrow canal and ventral dip models showed comparatively large standard errors due to low peak-to-peak amplitude, with lower signal quality.

4 Discussion

We developed a reconfigurable biophysical model of the lumbosacral organ to investigate its physical response during simulated locomotion. The biophysical model includes the spinal soft tissue, the surrounding spinal fluid, and the spinal

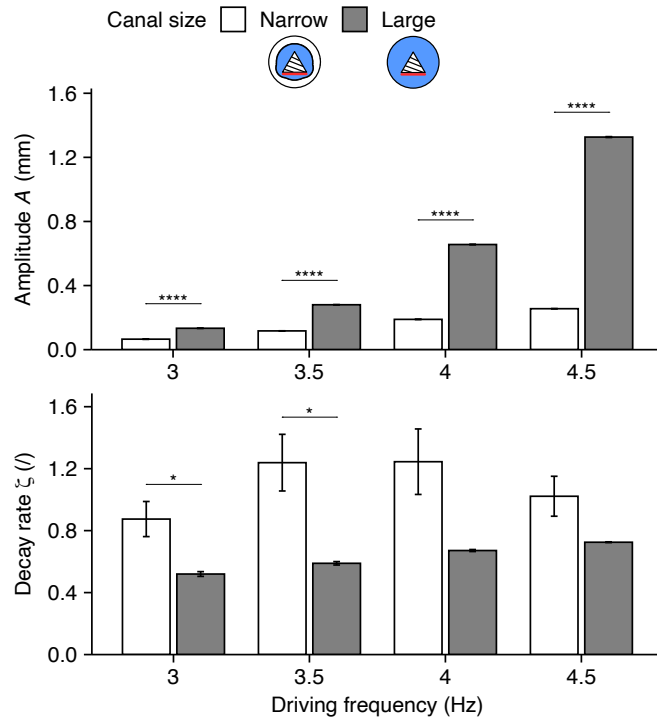


Figure 6: Influence of spinal canal size and drive frequency on mean values of peak-to-peak amplitude (A) and decay rate (B). Data is shown for eight trials at 3.0, 3.5, 4.0, and 4.5 Hz for model-7 with its narrow-size and model-2 with its large-size canal.

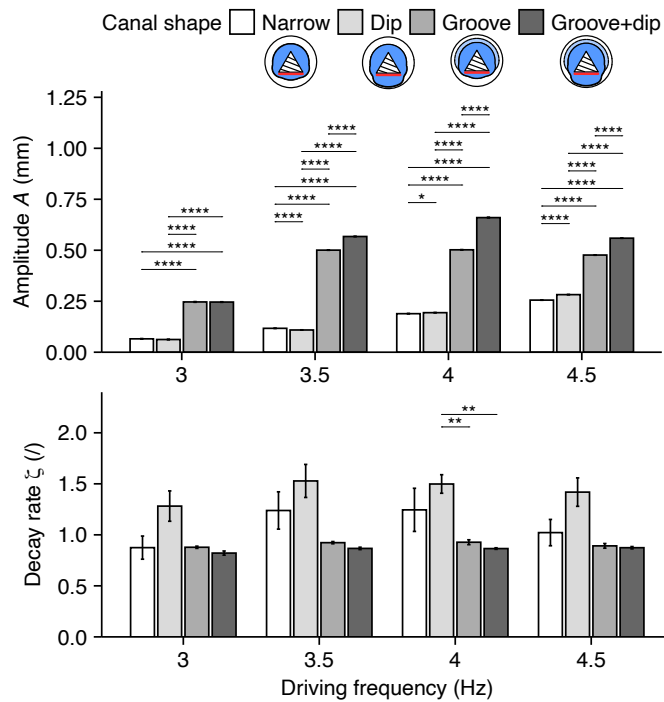


Figure 7: Influence of canal morphology and drive frequency on mean values of peak-to-peak amplitude(A) and decay rate (B). Data is shown for eight trials at 3.0, 3.5, 4.0, and 4.5 Hz for model-7 with a narrow canal, model-5 with a ventral dip, model-6 with a dorsal groove and model-4 with groove+dip.

canal, with a focus on replicating the key morphologies and material properties relevant to potential mechanosensing functions. The goal of this work is to produce quantitative results to understand the mechanics of the LSO, especially the influence of the glycogen body and the spinal canal. We observed typical mass-spring-damper behavior of the soft tissue oscillation, which supports the strain-based accelerometer hypothesis of the LSO [16].

The function of the LSO remains a debate in the field. The glycogen body within an enlarged spinal canal is suspicious, and can be only found in birds. Early studies assumed a “locomotor brain” function, due to the large accumulation of nerve cells nearby [43]. The glycogen body was further hypothesized to have a nutritional or secretory function [38, 44–46], or relate to myelin synthesis [17, 28]. However, these early studies failed to provide a holistic understanding of the LSO, since the specialized morphologies, such as the spinal canal and the dentate ligament network, were ignored.

Recently, new evidence has supported the mechanosensing function hypothesis of the LSO (Figure 1). The discovery of mechanoreceptive neurons within the accessory lobes laid the foundation for the potential mechanosensing function [19, 20, 22, 25, 26, 30, 31]. The enlarged spinal canal at the LSO region allows for the spinal soft tissue motion [16], which is essential for stimulating the mechanoreceptors. During locomotion, the spinal soft tissue is entrained by external acceleration, which forces the spinal fluid to circulate and the dentate ligament network to strain. Necker hypothesized that the fluid flow, guided by the spinal canal morphology, may stimulate the mechanoreceptors for a balance function [22, 24, 47, 48]. Instead of the fluid flow, Schroeder and Murray proposed that the ligament strain will transfer to the attached accessory lobes and therefore stimulate the mechanoreceptors [20]. Biological mechanoreceptors are well suited to detect the smallest strain values; they are sensitive in the angstrom range on a cellular level [49, 50]. Based on our own observations [16], the ligament strain can be up to 7.9%, which is large enough to produce consistent signals. Although none of these hypotheses have provided conclusive evidence, there were separate studies supported the LSO intraspinal sensing function. Intraspinal sensing has been identified in lamprey [32, 33] and zebrafish [34, 35], where their mechanosensors' arrangement is similar to birds' accessory lobes. Another study suggested that balance sensing exists in the bird's body. After labyrinthectomy and spinal cord transection, birds can still reflexively compensate for body rotations without the vision and vestibular sensing [51]. Here, the mechanosensing function of the LSO is a potential explanation.

The hypothesized LSO sensing mechanism can be essential for birds' exceptional locomotion agility. As agile locomotion requires fast sensing and action, the LSO potentially provides fast state feedback by minimizing the time required for detecting accelerations and sending the corresponding signals (Figure 1). On one hand, the body accelerations, as a result of contact with environments, can be transmitted to the spinal canal and the LSO through bones in the form of shock wave. The shock wave transmitted through bones [52, 53] is at least one order of magnitudes faster than the nerve conduction speed [54], allowing for fast acceleration detection. On the other hand, the close integration of LSO to the spinal cord greatly reduces the nerve conduction delays, and the output signals are likely integrated to the central pattern generator circuits for limb coordination [19, 25, 26]. Moreover, the fast state feedback is increasingly important for larger birds. An extreme example is the ancestor of birds—dinosaur, as the extended nerve fiber may prohibit in-time muscle response. Coincidentally, recent fossil records of dinosaurs have identified a lumbosacral canal enlargement similar to the birds' [55], suggesting the importance of the LSO for evolutionary success.

While the mechanosensing hypothesis has been well established [16, 20, 22, 24], several key processes remain unsolved. First, whether the spinal soft tissue can move relative to the spinal canal is still questionable. So far, we have been able to observe only a small amount of soft tissue motion in chicken [42]. Second, assuming the soft tissue can move, can truck movement entrain the spinal soft tissue motion? Further, how the morphologies and material properties shape the LSO response? In this work, we aim to understand this entrainment behavior. Third, supposing the soft tissue entrainment exists, how the neural circuits process the mechanoreceptors' signals and how the signals can be mapped to what kinds of sensing modalities is still unknown.

To answer the above questions, the main challenge is the inaccessibility of the LSO. Birds' spinal canal is densely fused, making in vivo measurement of the soft tissue movement and the mechanosensor activity almost impossible. Numerical simulation is not viable due to the complex interaction among the viscoelastic tissue, the spinal fluid, and the rigid spinal canal. Moreover, large deformation of viscoelastic materials are poorly predicted in simulation. Alternatively, we propose using biophysical simulation to study the entrainment mechanics of the LSO. Biophysical models are effective tools for testing the underlying mechanisms of biological systems [56, 57]. Benefiting from soft robotic techniques, our LSO biophysical model is parametric, modular, and based on precise anatomical data [16] (Figure 2). Testing different configurations of the biophysical model on our custom-developed locomotion simulator (Figure 3) revealed how individual morphology and material property affect the LSO response (Table 4).

The biophysical model confirmed the mobility of the soft tissue. Although the model is not a one-to-one copy of its biological reference, the underlining physics is the same. The models were carefully crafted to account for the appropriate physical forces acting on the model, such as the gravitational forces, buoyant forces, locomotion accelerations. As long as we are able to measure notable soft tissue motion, we can trust a similar soft tissue motion will exist in the biological LSO. As expected, all models have shown typical mass-spring-damper response (Figure 4). In entrainment phase, the settling time conveys how fast a model responds to external oscillation and provides an intuition of the model's temporal sensitivity. In steady phase, assuming the soft tissue displacement is in proportional to the mechanosensing signal intensity, the peak-to-peak amplitude indicates the signal strength. In damping phase, the decay rate shows how fast the LSO resets after a locomotion stop. We consider that an effective mechanosensor rapidly fades out oscillations through fluid damping and lossy tissue deformations. Here, we observed a distinct damped oscillation frequency, ranged between 3.5 Hz to 4.5 Hz, which overlaps with locomotion frequencies of running birds of 3 Hz to 5 Hz [58–60]. Note that the damped oscillation frequency is an approximation of the resonant frequency [61]. A resonating LSO will increase the oscillation amplitude, potentially increasing the sensor signal intensity. We did not perform a system identification test to determine the precise mass-spring-damper parameters, as our goal was to understand the impact of morphological variations to the LSO response, rather than systematically investigate an artificial system. In particular, we focus on the glycogen body density, the spinal canal size and morphology.

The glycogen body density showed notable influence on the soft tissue oscillation (Figure 5). We implemented the glycogen body denser than the spinal cord and the spinal fluid. In simplified mass-spring-damper systems, higher masses tend to oscillate at lower frequencies. We indeed observed a small reduction in the damped oscillation frequency between model-2 and 3 with higher glycogen body densities; from averaged 4.8 Hz to 4.4 Hz, which again confirmed the mass-spring-damper behavior. The increased glycogen body density is associated with higher peak-to-peak amplitude (Figure 5A). Since the peak-to-peak amplitude is assumed to connect with signal strength, the denser glycogen body could act as a signal amplifier. Consequently, running birds that experience higher vertical accelerations could feature a low-density glycogen body, leading to a signal intensity similar to flying or swimming birds with low-acceleration locomotion modes. As such, the glycogen body density could adjust the acceleration measurement range, i.e., amplifying small acceleration with high density, or suppressing excessive acceleration with low density. Varying glycogen body densities could have developed as a trade-off between LSO responsiveness and protection. Sudden perturbations during locomotion can lead to high accelerations, potentially damaging the spinal cord tissue. Spinal fluid and ligaments would reduce soft tissue motions through fluid buoyancy, damping, and ligament elasticity [62]. We think buoyancy could protect the best if tissue densities are similar to the surrounding fluid. Too high or low density would lead to sinking or flotation. Hence, two or more opposing motivations exist; feature a neutrally buoyant density to protect the spinal cord, and increase glycogen body density for sufficiently high peak-to-peak amplitude.

The spinal canal dimensions with submillimeter flow classifies as a micro-fluid environment, with high fluid resistance slowing the flow and dampening oscillations. The dimension of lumbosacral canal expansion has been a central question in the functional hypothesis of the LSO [14, 16, 24, 27, 63]. As expected, a narrow spinal canal led to smaller peak-to-peak amplitude and higher decay rate as a result of high damping, in contrast to a large-diameter spinal canal (Figure 6). The high damping has two main effects on the LSO sensing mechanism. First, it suppresses excessive spinal cord deflection during high acceleration events, such as strong perturbations, protecting the spinal cord tissue. Second, the resulting high decay rate enhances fast sensor reset. When locomotion stops, the damped oscillation will continue simulating the mechanosensors and generating signals. In this scenario, these signals may become noise and should be minimized as soon as possible. Therefore, the spinal canal expansion could have been optimized for the damping term of a mass-spring-damper system.

Additionally, the spinal canal enlargement features different fine structure among different birds [16, 24, 42]. From our preliminary scanning data of swan, pigeon, quail and chicken, selected to represent diverse locomotion modalities, we observed different shape of semi-circular grooves and ventral dip. We studied whether these fine structures would play an important role in the LSO response by testing the combinations of semi-circular grooves and ventral dip (Figure 7). Vertical spinal cord motions will displace fluid inside the volume-constant spinal canal; when the spinal cord moves up, the spinal fluid is pushed down. We can assume that fluid of the same volume is moved against the spinal cord motion. Lateral gaps and, possibly, semi-circular grooves will guide the flow between the spinal cord and the inner spinal canal [22, 24]. In quails [16], only small flow space is available laterally—between 0.3 mm to 0.8 mm—which we mimicked in model-4 to 7 (Table 2). Models with extra dorsal structures showed larger peak-to-peak amplitude and lower decay rates, compared to canals without (Figure 7). Hence, the laterally and dorsally extending semi-circular grooves could act as fluid reliefs or flow channels [16, 24, 48]. Model-5 featuring the ventral dip behaved somewhat unexpectedly. Albeit a larger fluid space, it caused a higher decay rate compared to the narrow-canal model-7 (Figure 7). We conclude that model-5’s ventral dip might have dampened the oscillations. Although the spinal canal we developed is highly simplified compared to our reference quail model (Figure 2), small modifications to the canal morphology has already led to considerable different responses (Figure 7). Hence, the spinal canal fine structure diversifies the LSO response, likely associated with the locomotion modality of birds. For example, we expect more pronounced semi-circular grooves and ventral dip for swimmers and divers, since the lack of visual cues and low body acceleration might require higher sensitivity. To better understand the function of spinal canal fine structure in relation to locomotion modality and LSO response, a more realistic spinal canal modelling is required.

While our three hypotheses have been validated, there are several directions for future improvement. Our locomotion simulator (Figure 3) is limited to only one degree of freedom (DoF), while real-world locomotion acceleration is in 3D space and has six DoFs. This was because suitable motion simulators capable of highly dynamic motion in six DoFs were not affordable. As a starting point, we custom-developed our own motion simulator, and open sourced the design for barrier-free research. Nevertheless, this platform was sufficient to prove the feasibility of our biophysical simulation framework. In the future, a 6-DoF motion simulator [64] will allow testing the LSO response under rolling, yawing, pitching, etc. We also expect to improve the biophysical model design by instrumentation. By adding strain or pressure sensors at the location of the mechanoreceptors (Figure 1), testing the differential mechanosensing mechanism [16] will be possible. If we can successfully map the strain or pressure signals to the body accelerations in six DoFs, we close the loop of the mechanosensing hypothesis as shown in Figure 1. More importantly, the improved and instrumented framework will permit the correlation of LSO sensitivity on specific DoF. For instance, the topology of the mechanosensors in LSO may have been optimized to predict heaving, pitching, and rolling, which are the dominant motions for most birds.

Overall, our biophysical simulation framework emphasizes the notion of understanding through creation, also known

as “What I cannot create, I do not understand.” We expect creating the “physical twins” of the LSO will be a powerful tool to improve our understanding of it.

5 Conclusions

We developed a simplified, modular, biophysical model of the lumbosacral organ of birds to advance our understanding of this system. Models were mounted to an instrumented setup that simulated vertical oscillations and recorded the model response. We presented results that support the central hypothesis that external motion, such as running, leads to measurable LSO spinal cord movement. The glycogen body density has a strong impact on the LSO response intensity. We found that narrow spinal canal reduces soft tissue motions through the effects of damping, effectively protecting the spinal cord. The spinal canal fine structure potentially associated with locomotion modalities of different birds. In this work, we focus on understanding the mechanics of the LSO. In the future, we expect to test the mechanosensing mechanism with a more elaborate LSO model and a 6-DoF locomotion simulator.

Acknowledgements: This work was supported by the China Scholarship Council (CSC) and the International Max Planck Research School for Intelligent Systems (IMPRS-IS).

Data availability: The biophysical model design has been uploaded as part of the supplementary material.

References

1. Daley MA and Biewener AA. Running over rough terrain reveals limb control for intrinsic stability. *Proceedings of the National Academy of Sciences* 2006;103:15681–6.
2. Knuesel J and Ijspeert AJ. Effects of muscle dynamics and proprioceptive feedback on the kinematics and CPG activity of salamander stepping. *BMC Neuroscience* 2011;12:P158.
3. Conway BA, Hultborn H, and Kiehn O. Proprioceptive input resets central locomotor rhythm in the spinal cat. *Experimental Brain Research* 1987;68:643–56.
4. Mouel CL and Brette R. Anticipatory coadaptation of ankle stiffness and sensorimotor gain for standing balance. *PLOS Computational Biology* 2019;15. Publisher: Public Library of Science:e1007463.
5. Kuchenbecker KJ, Gewirtz J, McMahan W, et al. VerroTouch: High-Frequency Acceleration Feedback for Telerobotic Surgery. In: *Haptics: Generating and Perceiving Tangible Sensations*. Ed. by Kappers AML, Erp JBFv, Tiest WMB, and Helm FCTvd. Springer Berlin Heidelberg, 2010:189–96.
6. Goldfield EC, Kay BA, and Warren WH. Infant Bouncing: The Assembly and Tuning of Action Systems. *Child Development* 1993;64:1128.
7. Taga G. Emergence of bipedal locomotion through entrainment among the neuro-musculo-skeletal system and the environment. *Physica D: Nonlinear Phenomena* 1994;75:190–208.
8. Berthouze L and Goldfield EC. Assembly, tuning, and transfer of action systems in infants and robots. *Infant and Child Development* 2008;17:25–42.
9. Ruppert F and Badri-Spröwitz A. Learning Neuroplastic Matching of Robot Dynamics in Closed-loop CPGs. *Nature Machine Intelligence* 2022;4:652–60.
10. Haen Whitmer K. *A Mixed Course-Based Research Approach to Human Physiology*. 2021.
11. More HL and Donelan JM. Scaling of sensorimotor delays in terrestrial mammals. *Proceedings of the Royal Society B* 2018;285:20180613.
12. Urbina-Meléndez D, Jaleddini K, Daley MA, and Valero-Cuevas FJ. A physical model suggests that hip-localized balance sense in birds improves state estimation in perching: implications for bipedal robots. *Frontiers in Robotics and AI* 2018;5:38.
13. Daley MA, Voloshina A, and Biewener AA. The role of intrinsic muscle mechanics in the neuromuscular control of stable running in the guinea fowl. *The Journal of physiology* 2009;587:2693–707.
14. Necker R. Specializations in the Lumbosacral Spinal Cord of Birds: Morphological and Behavioural Evidence for a Sense of Equilibrium. *European Journal of Morphology* 1999;37:211–4.
15. Bekoff A, Stein PS, and Hamburger V. Coordinated motor output in the hindlimb of the 7-day chick embryo. *Proceedings of the National Academy of Sciences* 1975;72:1245–8.
16. Kamska V, Daley M, and Badri-Spröwitz A. 3D Anatomy of the Quail Lumbosacral Spinal Canal—Implications for Putative Mechanosensory Function. *Integrative Organismal Biology* 2020;2.

17. De Gennaro LD and Benzo CA. Ultrastructural characterization of the accessory lobes of Lachi (Hofmann's nuclei) in the nerve cord of the chick. I. Axoglial synapses. *Journal of Experimental Zoology* 1976;198:97–107.
18. Möller W and Kummer W. The blood-brain barrier of the chick glycogen body (corpus gelatinosum) and its functional implications. *Cell and Tissue Research* 2003;313:71–80.
19. Eide AL. The axonal projections of the Hofmann nuclei in the spinal cord of the late stage chicken embryo. *Anatomy and Embryology* 1996;193:543–57.
20. Schroeder DM and Murray RG. Specializations within the lumbosacral spinal cord of the pigeon. *Journal of Morphology* 1987;194:41–53.
21. Rosenberg J and Necker R. Ultrastructural characterization of the accessory lobes of Lachi in the lumbosacral spinal cord of the pigeon with special reference to intrinsic mechanoreceptors. *Journal of Comparative Neurology* 2002;447:274–85.
22. Necker R. Specializations in the lumbosacral vertebral canal and spinal cord of birds: evidence of a function as a sense organ which is involved in the control of walking. *Journal of Comparative Physiology A* 2006;192:439.
23. Yamanaka Y, Kitamura N, and Shibuya I. Chick spinal accessory lobes contain functional neurons expressing voltagegated sodium channels generating action potentials. *Biomedical Research* 2008;29:205–11.
24. Stanchak KE, French C, Perkel DJ, and Brunton BW. The Balance Hypothesis for the Avian Lumbosacral Organ and an Exploration of Its Morphological Variation. *Integrative Organismal Biology* 2020;2.
25. Stanchak KE, Miller KE, Lumsden EW, et al. Molecular markers of mechanosensation in glycinergic neurons in the avian lumbosacral spinal cord. *eNeuro* 2022.
26. Eide AL and Glover JC. Development of an Identified Spinal Commissural Interneuron Population in an Amniote: Neurons of the Avian Hofmann Nuclei. *The Journal of Neuroscience* 1996;16:5749–61.
27. Emmert A. Beobachtungen über einige anatomische Eigenheiten der Vögel. *Reil's Arch. Physiol.* 1811;10:377–92.
28. Benzo CA and De Gennaro LD. Glycogen metabolism in the developing accessory lobes of Lachi in the nerve cord of the chick: Metabolic correlations with the avian glycogen body. *Journal of Experimental Zoology* 1981;215:47–52.
29. Benzo CA and De Gennaro LD. An hypothesis of function for the avian glycogen body: A novel role for glycogen in the central nervous system. *Medical Hypotheses* 1983;10:69–76.
30. Yamanaka Y, Kitamura N, Shinohara H, Takahashi K, and Shibuya I. Analysis of GABA-induced inhibition of spontaneous firing in chick accessory lobe neurons. *Journal of Comparative Physiology A* 2012;198:229–37.
31. Yamanaka Y, Kitamura N, Shinohara H, Takahashi K, and Shibuya I. Glutamate evokes firing through activation of kainate receptors in chick accessory lobe neurons. *Journal of Comparative Physiology A* 2013;199:35–43.
32. Grillner S, Williams T, and Lagerback PA. The edge cell, a possible intraspinal mechanoreceptor. *Science* 1984;223:500–3.
33. McClellan AD and Jang W. Mechanosensory inputs to the central pattern generators for locomotion in the lamprey spinal cord: resetting, entrainment, and computer modeling. *Journal of Neurophysiology* 1993;70:2442–54.
34. Böhm UL, Prendergast A, Djenoune L, et al. CSF-contacting neurons regulate locomotion by relaying mechanical stimuli to spinal circuits. *Nature Communications* 2016;7:10866.
35. Picton LD, Bertuzzi M, Pallucchi I, et al. A spinal organ of proprioception for integrated motor action feedback. *Neuron* 2021;109:1188–1201.e7.
36. Schroeder DM. The marginal nuclei in the spinal cord of reptiles: intraspinal mechanoreceptors. *The Ohio Journal of Science* 1986;86:69–72.
37. Viana Di Prisco G, Walle'n P, and Grillner S. Synaptic effects of intraspinal stretch receptor neurons mediating movement-related feedback during locomotion. *Brain Research* 1990;530:161–6.
38. Watterson RL and Spiroff BEN. Development of the Glycogen Body of the Chick Spinal Cord. II. Effects of Unilateral and Bilateral Leg-Bud Extirpation. *Physiological Zoology* 1949;22:318–37.
39. Tamura A, Nagayama K, Matsumoto T, and Hayashi S. Variation in nerve fiber strain in brain tissue subjected to uniaxial stretch. *Stapp car crash journal* 2007;51:139–54.
40. Bausch P. Die Spezialisierungen des lumbosakralen Wirbelkanals beim Großen Emu (*Dromaius novaehollandiae*). Tech. rep. 2014.
41. Software T. Tracker Video Analysis and Modeling Tool for Physics Education.
42. Kamska V, Mo A, Pohmann R, Karakostis FA, Daley MA, and Badri-Spröwitz A. Imaging the soft tissues motion inside the canal, submitting.
43. Streeter GL. The structure of the spinal cord of the ostrich. *American Journal of Anatomy* 1904;3:1–27.

44. Terni T. Ricerche sulla cosiddetta sostanza gelatinosa (corpo glicogenico) del midollo lombo-sacrale degli uccelli... L. Niccolai, 1924.
45. De Gennaro LD. The carbohydrate composition of the glycogen body of the chick embryo as revealed by paper chromatography. *The Biological Bulletin* 1961;120:348–52.
46. Azcoitia I, Fernandez-Soriano J, and Fernandez-Ruiz B. Is the avian glycogen body a secretory organ? *Journal fur Hirnforschung* 1985;26:651–7.
47. Necker R. Head-bobbing of walking birds. *Journal of comparative physiology A* 2007;193:1177.
48. Necker R, Janßen A, and Beissenhirtz T. Behavioral evidence of the role of lumbosacral anatomical specializations in pigeons in maintaining balance during terrestrial locomotion. *Journal of Comparative Physiology A* 2000;186:409–12.
49. Hudspeth AJ. How the ear’s works work. *Nature* 1989;341. Publisher: Nature Publishing Group:397–404.
50. Barth FG. Mechanics to pre-process information for the fine tuning of mechanoreceptors. *Journal of Comparative Physiology. A, Neuroethology, Sensory, Neural, and Behavioral Physiology* 2019;205:661–86.
51. Biederman-Thorson M and Thorson J. Rotation-compensating reflexes independent of the labyrinth and the eye. *Journal of comparative physiology* 1973;83:103–22.
52. Pelker RR and Saha S. Stress wave propagation in bone. *Journal of Biomechanics* 1983;16:481–9.
53. Miller TE and Mortimer B. Control vs. constraint: understanding the mechanisms of vibration transmission during material-bound information transfer. *Frontiers in Ecology and Evolution* 2020;8:587846.
54. More HL, Hutchinson JR, Collins DF, Weber DJ, Aung SK, and Donelan JM. Scaling of sensorimotor control in terrestrial mammals. *Proceedings of the Royal Society B: Biological Sciences* 2010;277:3563–8.
55. Wedel M, Atterholt J, Dooley A, et al. Expanded neural canals in the caudal vertebrae of a specimen of *Haplocanthosaurus*. *Acad. Lett* 2021;911.
56. Panjabi MM. Cervical spine models for biomechanical research. *Spine* 1998;23:2684–99.
57. Poel R, Belosi F, Albertini F, et al. Assessing the advantages of CFR-PEEK over titanium spinal stabilization implants in proton therapy—a phantom study. *Physics in Medicine & Biology* 2020;65:245031.
58. Gatesy S and Biewener A. Bipedal locomotion: effects of speed, size and limb posture in birds and humans. *Journal of Zoology* 1991;224:127–47.
59. Smith NC, Jespers KJ, and Wilson AM. Ontogenetic scaling of locomotor kinetics and kinematics of the ostrich (*Struthio camelus*). *Journal of Experimental Biology* 2010;213:1347–55.
60. Daley MA and Birn-Jeffery A. Scaling of avian bipedal locomotion reveals independent effects of body mass and leg posture on gait. *Journal of Experimental Biology* 2018;221:jeb152538.
61. Morin D. Oscillations. In: *Waves*. 2021. Chap. 1.2:15.
62. Telano LN and Baker S. Physiology, Cerebral Spinal Fluid. In: Treasure Island (FL): StatPearls Publishing, 2022.
63. Necker R. The structure and development of avian lumbosacral specializations of the vertebral canal and the spinal cord with special reference to a possible function as a sense organ of equilibrium. *Anatomy and Embryology* 2005;210:59–74.
64. Pradhan NMS, Frank P, Mo A, and Badri-Spröwitz A. Upside down: affordable high-performance motion platform. arXiv preprint arXiv:2303.17974 2023.

Supplementary Materials for Biophysical Simulation Reveals the Mechanics of the Avian Lumbosacral Organ

The PDF file includes:

Figure S1
Section S1 to S2
Time series of all biophysical models (phantoms)

Other Supplementary Material for this manuscript includes the following:

Computer-aided design model of the biophysical model: <https://doi.org/10.17617/3.VTH081>
Locomotion simulator design: https://github.com/moanan/1_dof_motion_simulator

S1 Biophysical model fabrication

We mimicked soft tissue material properties. Spinal cord is gel-like and soft, with little inherent stiffness [1], and it stretches only minimally [2]. We chose extra-soft silicone rubber (Ecoflex 00-10, *Smooth-On*) to mimic the spinal cord's high compliance and bendability. A single layer of microfiber cloth (MSC-00014-S, *Stratasys*) at the ventral side reinforced the spinal cord to increase its tensile strength [3], acting as a replacement of the dentate ligament network at the same time. As a result, the spinal cord model made is easily bendable, but with high tensile stiffness. We simulated the spinal fluid with water; both fluids feature similar density and viscosity [4, 5].

We fabricated the biophysical models as follows(Figure S1): First, we laser-cut microfiber cloth (PLS6 150D, *Universal Laser Systems*) into the desired shape (Figure S1A) and embedded it directly into the spinal cord moulds. The moulds were 3d-printed from polycarbonate/acrylonitrile butadiene styrene (PC-ABS) in fused deposition model printer (FDM, *Stratasys Fortus 450mc*). The glycogen body and the spinal cord were cast in separate moulds (Figure S1B) with the help of release agent (Ease Release 200, *Smooth-On*) and degassed silicone rubber. In addition, we coloured the glycogen body with yellow pigments (Silc Pig, *Smooth-On*) for visual contrast. Then, we inserted short aluminium rods into the glycogen body to increase density yet keep the glycogen body bendable (Figure S1C). Adjusted glycogen body densities were 1.5 g/cm^3 and 2.0 g/cm^3 :

$$\begin{cases} V_{\text{GB}} = V_{\text{SR}} + V_{\text{AL}} \\ \rho_{\text{GB}}V_{\text{GB}} = \rho_{\text{SR}}V_{\text{SR}} + \rho_{\text{AL}}V_{\text{AL}} \end{cases} \quad (1)$$

ρ_{SR} and ρ_{AL} are the density of silicone rubber (1.0 g/cm^3) and aluminium (2.7 g/cm^3), respectively. V_{SR} and V_{AL} are the volume of the silicone rubber structure and the aluminium rod, respectively. After curing and removing parts from the moulds, we wedged the glycogen body into the spinal cord, connected by a thin layer of uncured silicone rubber. Next, we implemented two spinal canals made from borosilicate glass tubes; a large canal with an inner diameter of 51 mm (model 1-3), and a narrow canal with an inner diameter of 34 mm (model 4-7). Additional inserts at the centre of the narrow tube reduced the inner diameter further to 24 mm (Figure S1). The inserts were fabricated from polymethyl methacrylate (PMMA) and polished for optical transparency. We carved the inside of the inserts (Figure S1D), mimicking the ventral dip [4, 6] and dorsal semi-circular grooves [7] of birds' spinal canal. Finally, we prepared clamps to hold compliant parts and inserts in position (Figure S1E). To reduce spinal cord sagging, we tensioned the spinal cord to 103% of its resting length before clamping. We fully immersed glass tubes in water, removed air bubbles and closed the tube with rubber caps on both ends (Figure S1F). Consequently, the biophysical model is configurable in terms of glycogen body density, spinal canal size, and spinal canal morphology.

S2 Data analysis

We extracted the biophysical model's movement from the recorded videos. We removed lens distortion with the single camera calibrator app (Matlab v. 2019a), then cropped to a region of interest for better tracking performance,

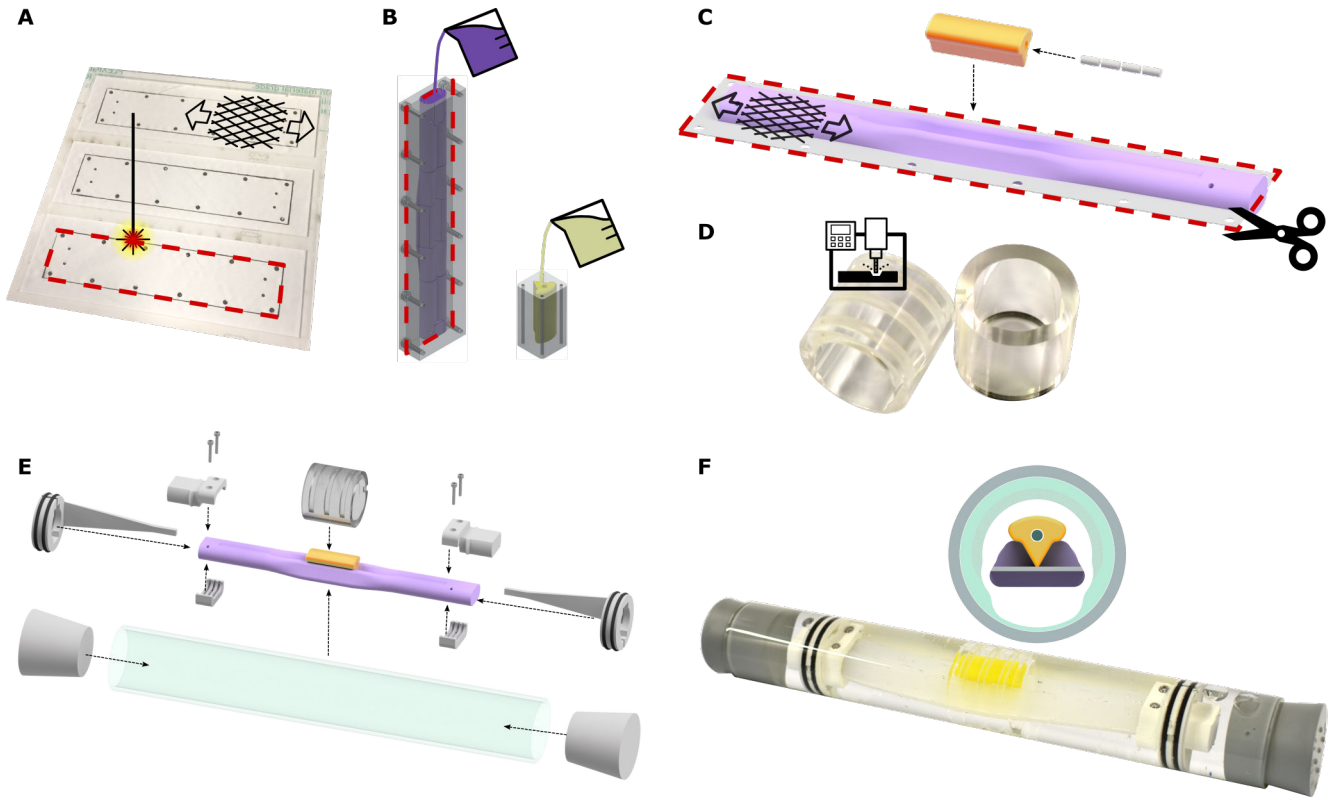


Fig. S1: Lumbar organ model fabrication. (A) Laser-cutting microfiber cloth. Arrows indicate the high-stiffness direction of the microfiber cloth, orthogonal is its low-stiffness direction. (B) The spinal cord and the glycogen body are moulded with silicone rubber individually. The microfiber cloth is embedded into the spinal cord mould. (C) After de-moulding, we insert aluminium rods into the glycogen body to adjust its density. We trim excess microfiber cloth before gluing the glycogen body to the spinal cord. (D) Some biophysical models are equipped with a modular cylindrical insert featuring the dorsal semi-circular grooves or the ventral dip. (E) Parts and canal inserts are clamped into a glass tube with custom fixtures. (F) Photo of the model-4 and rendering of its cross-section.

and applied contrast-enhancing filter. In the processed videos, the movements were software tracked (Tracker, [8]). Extracted model position data were filtered with 4th-order zero-lag Butterworth filter and interpolated to 1 kHz, with a cutoff frequency of 9 Hz.

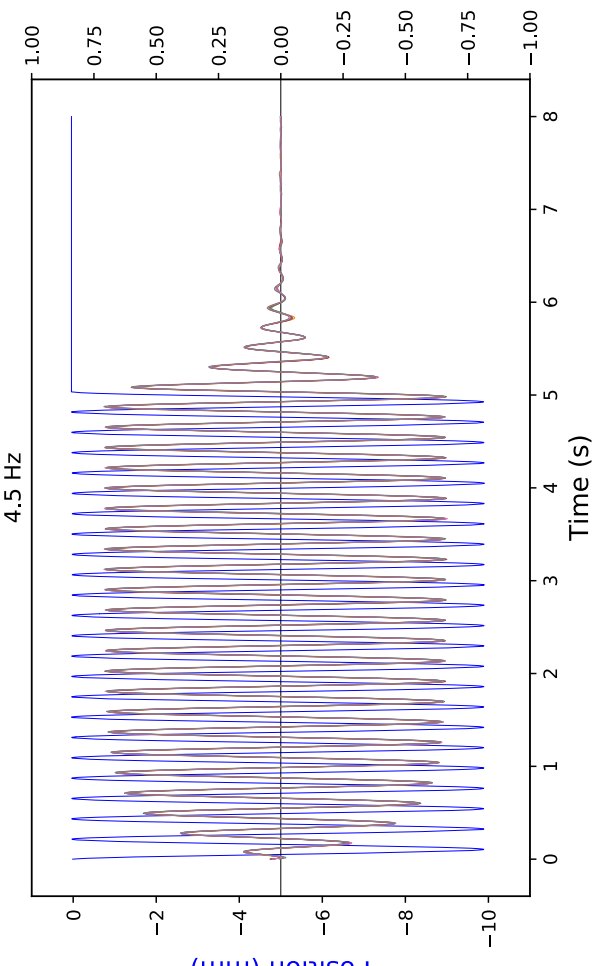
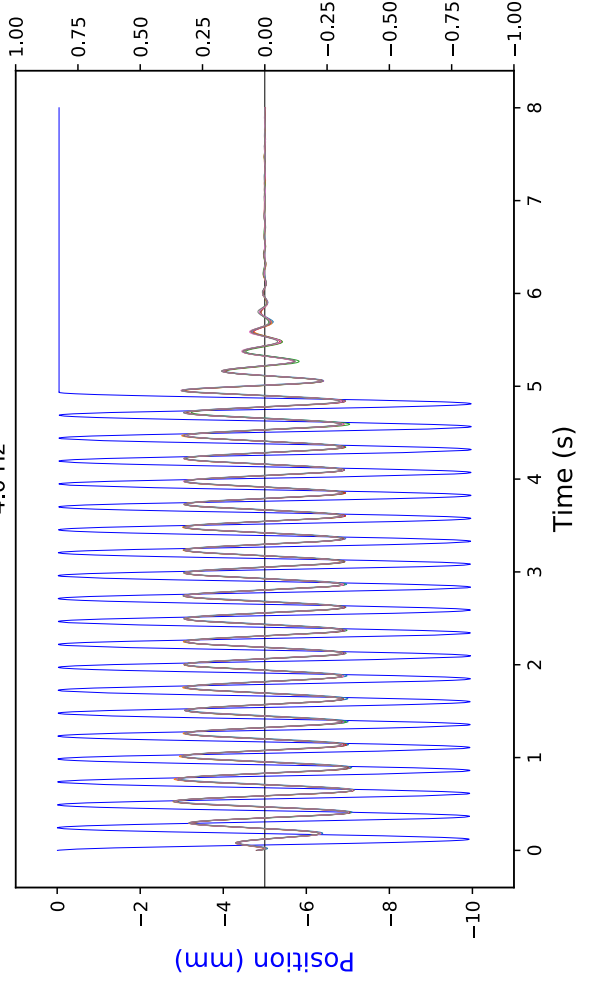
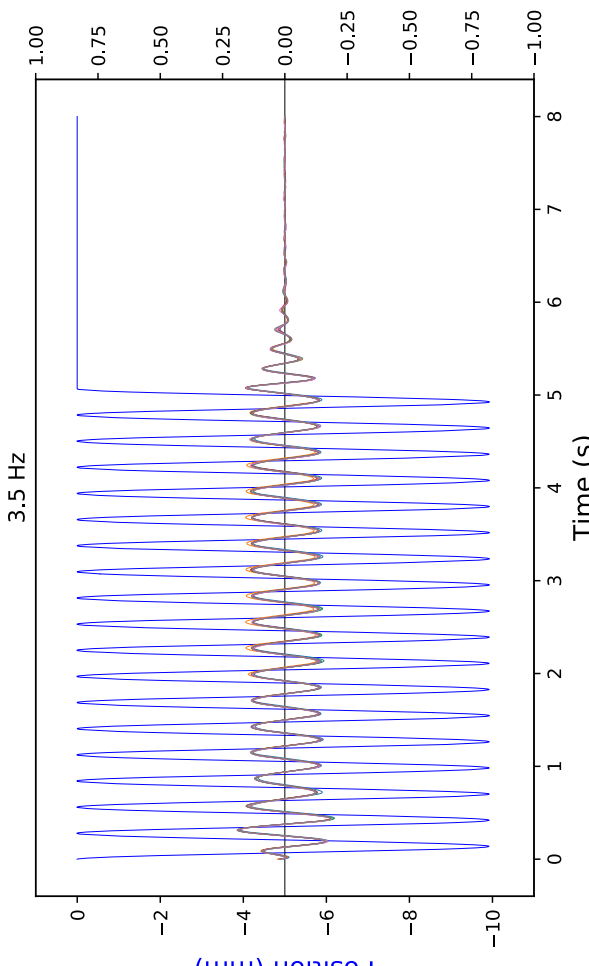
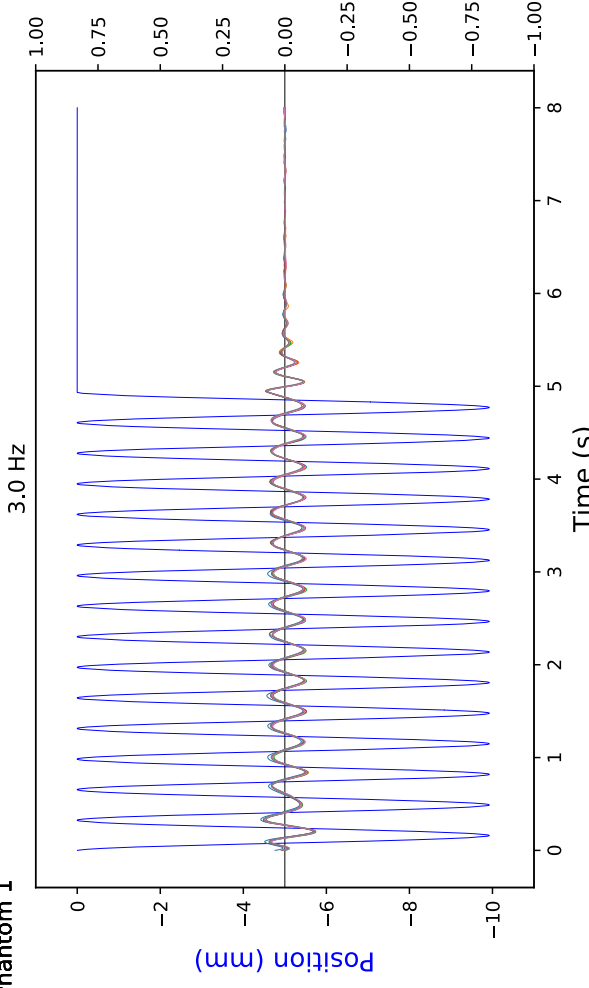
We found that oscillations stabilized in all trials after 3.0 s and subtracted consecutive positive and negative peak values until 4.8 s, to calculate the peak-to-peak amplitude A . Models took the settling time τ to entrain. We measured the settling time with the peak-to-peak amplitude A as reference; we identified the earliest peak amplitude $\leq 0.9A$ tracing backwards from 3 s. The zero crossing immediately after the earliest peak finishes the entrainment phase. The steady phase starts at the end of the entrainment phase and finishes when the motor is switched off at 5 s. We calculated the phase shift ϕ between the actuator and model oscillation by cross-correlation. In the damping phase, the model oscillates at a damped oscillation frequency f_d after the motor is turned off. We obtain the damped oscillation frequency f_d by spectrum analysis in all but model-5, and 7. The data was too noisy for model-5 and 7, and we manually calculated f_d from the first two cycles of the damping phase. We further investigate the model's damping behaviour by calculating the decay rate ζ (or the logarithmic decrement) as $\zeta = \ln \frac{x_1 - x_2}{x_3 - x_4}$. Values x_1, x_3 and x_2, x_4 are successive positive and negative peaks, respectively, of two cycles within the damping phase, after motor switch-off. Data was processed in Python v. 3.8 and in Matlab v. 2019a.

References

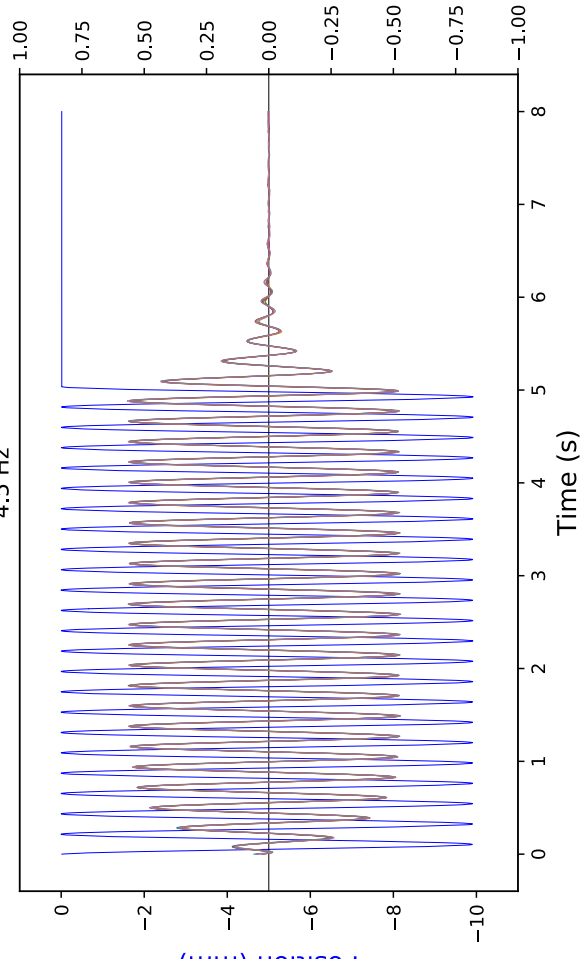
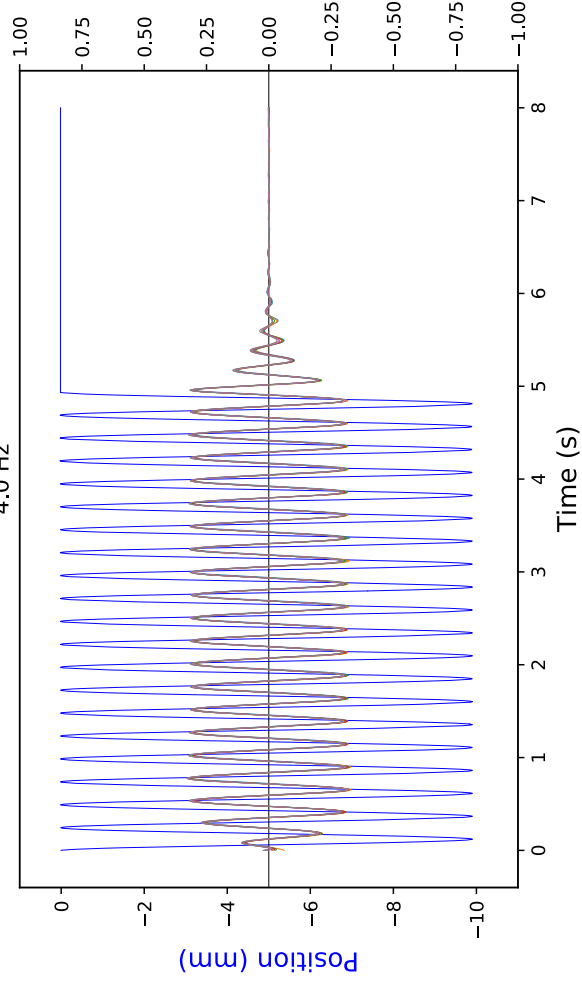
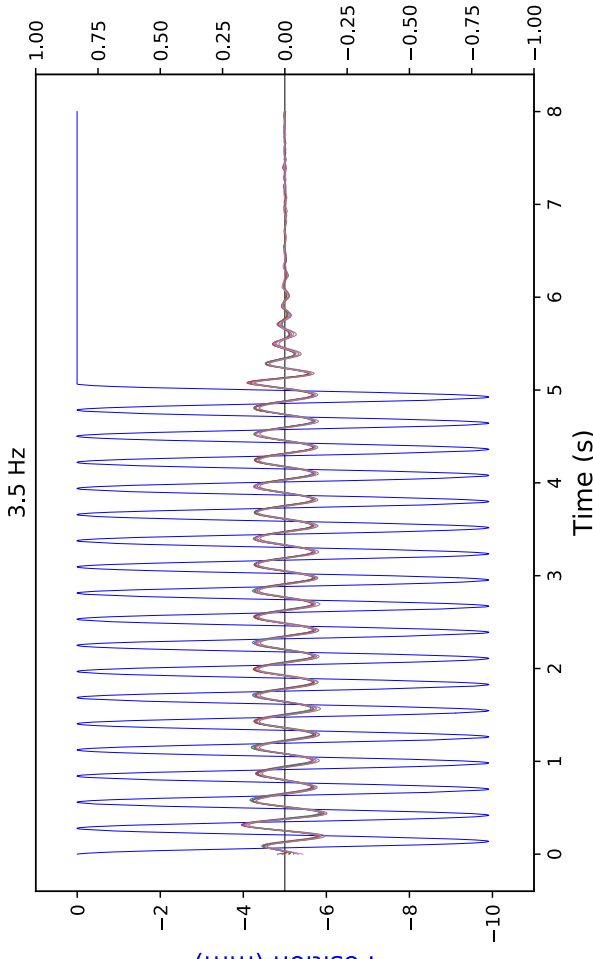
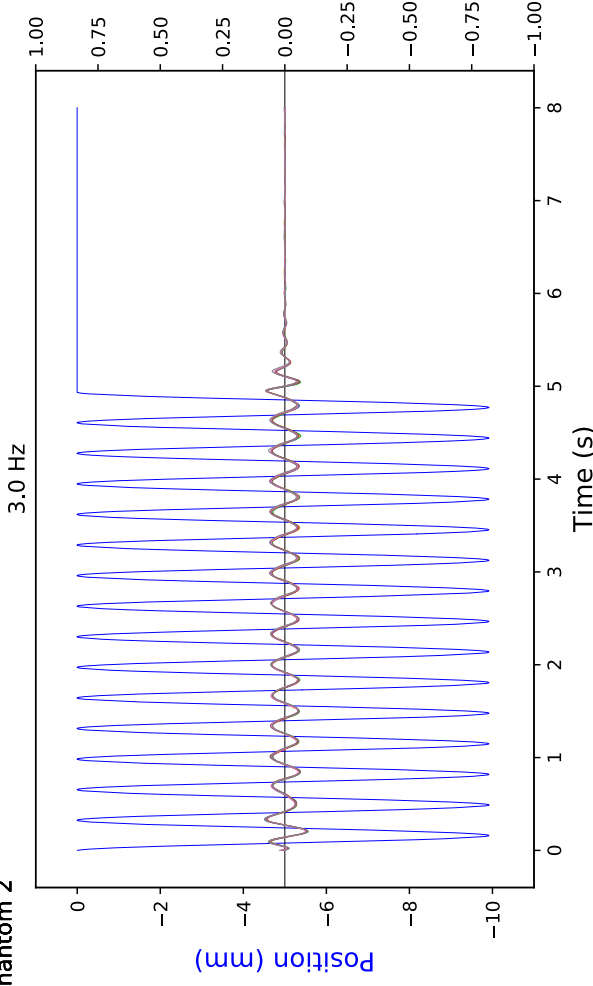
1. Ramo NL, Troyer KL, and Puttlitz CM. Viscoelasticity of spinal cord and meningeal tissues. *Acta biomaterialia* 2018;75:253–62.
2. Clarke EC. Spinal Cord Mechanical Properties. In: *Neural Tissue Biomechanics*. Ed. by Bilston LE. Berlin, Heidelberg: Springer Berlin Heidelberg, 2011:25–40.
3. Hepp J and Badri-Spröwitz A. A Novel Spider-Inspired Rotary-Rolling Diaphragm Actuator with Linear Torque Characteristic and High Mechanical Efficiency. *Soft Robotics* 2021.
4. Kamska V, Daley M, and Badri-Spröwitz A. 3D Anatomy of the Quail Lumbar Spinal Canal—Implications for Putative Mechanosensory Function. *Integrative Organismal Biology* 2020;2.
5. Thomas JH. Fluid dynamics of cerebrospinal fluid flow in perivascular spaces. *Journal of The Royal Society Interface* 2019;16:20190572.

6. Stanchak KE, French C, Perkel DJ, and Brunton BW. The Balance Hypothesis for the Avian Lumbosacral Organ and an Exploration of Its Morphological Variation. *Integrative Organismal Biology* 2020;2.
7. Necker R. Specializations in the Lumbosacral Spinal Cord of Birds: Morphological and Behavioural Evidence for a Sense of Equilibrium. *European Journal of Morphology* 1999;37:211–4.
8. Software T. Tracker Video Analysis and Modeling Tool for Physics Education.

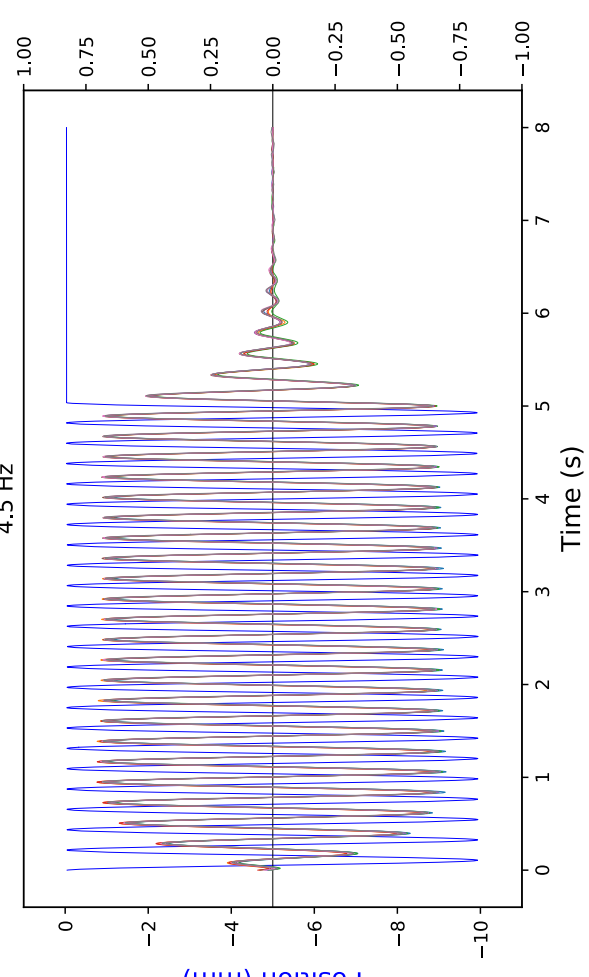
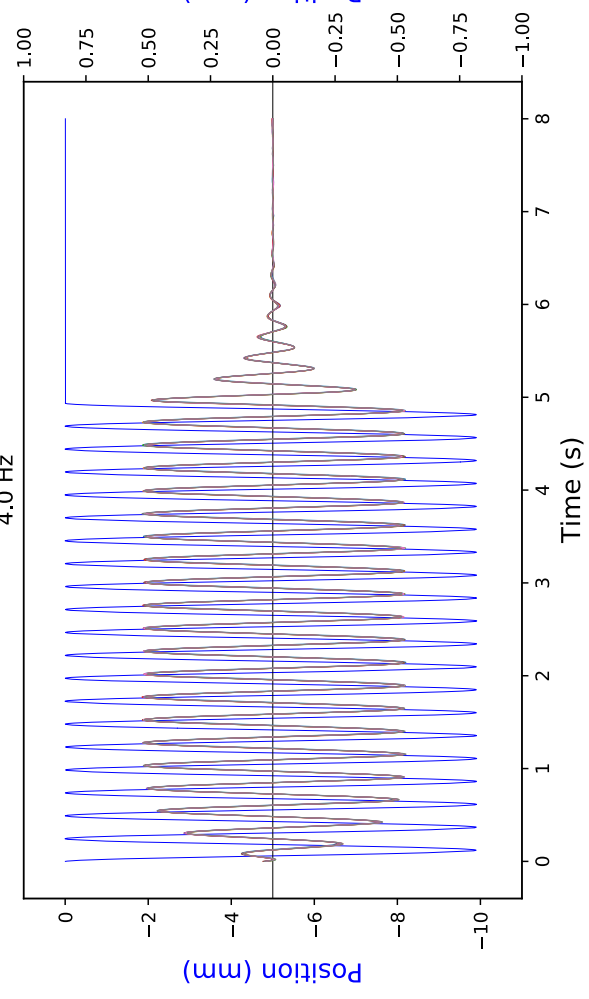
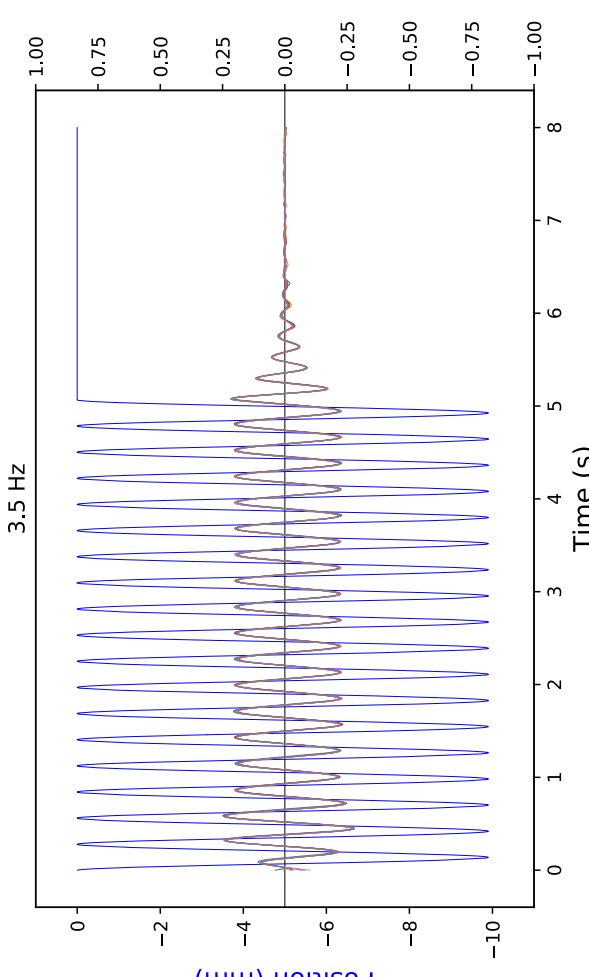
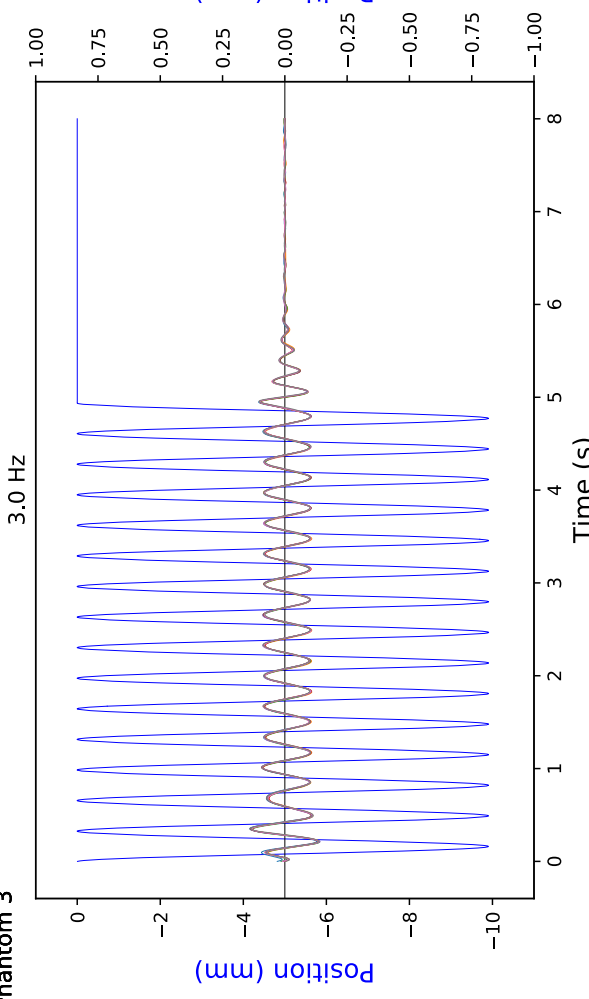
Phantom 1



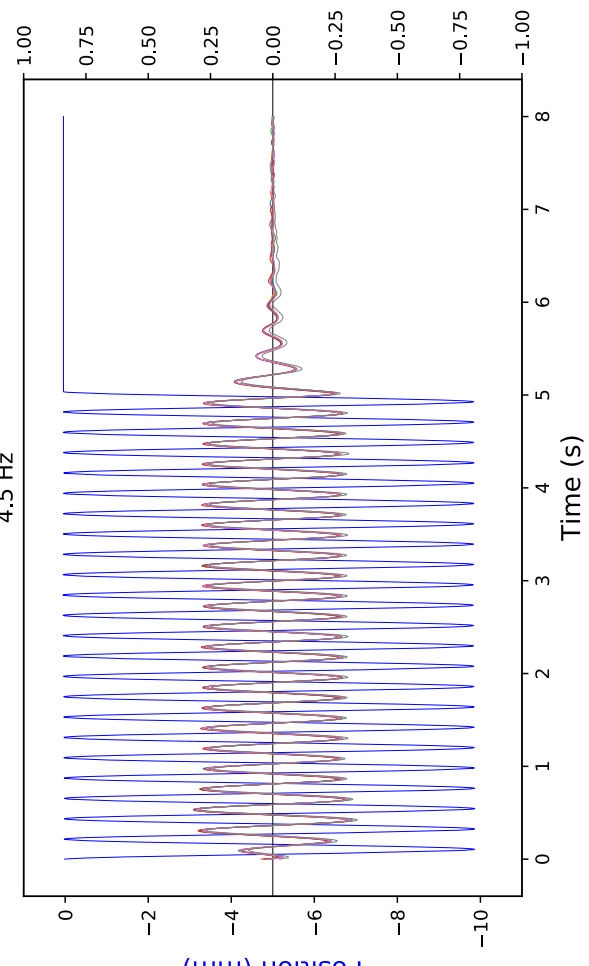
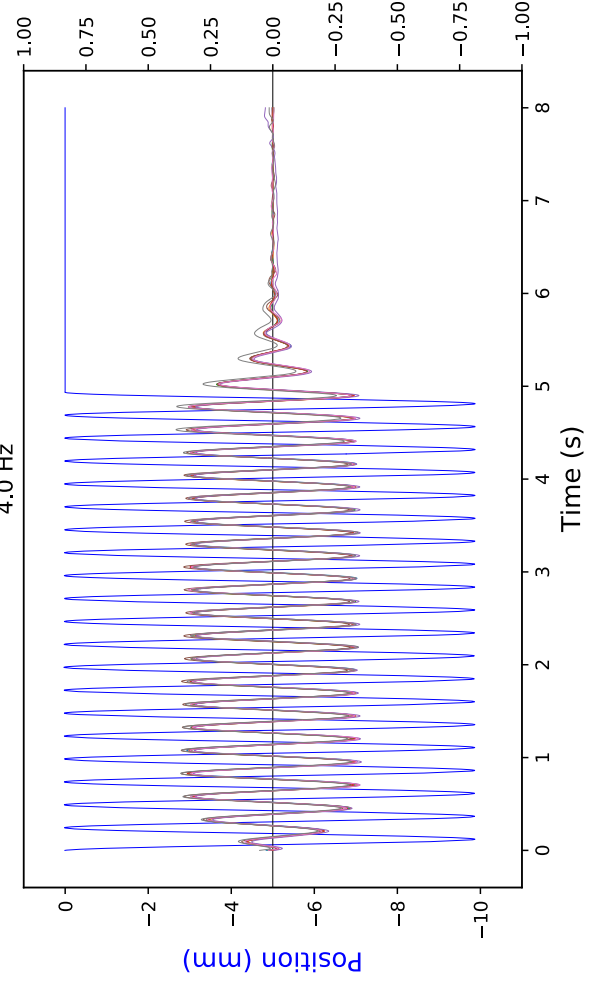
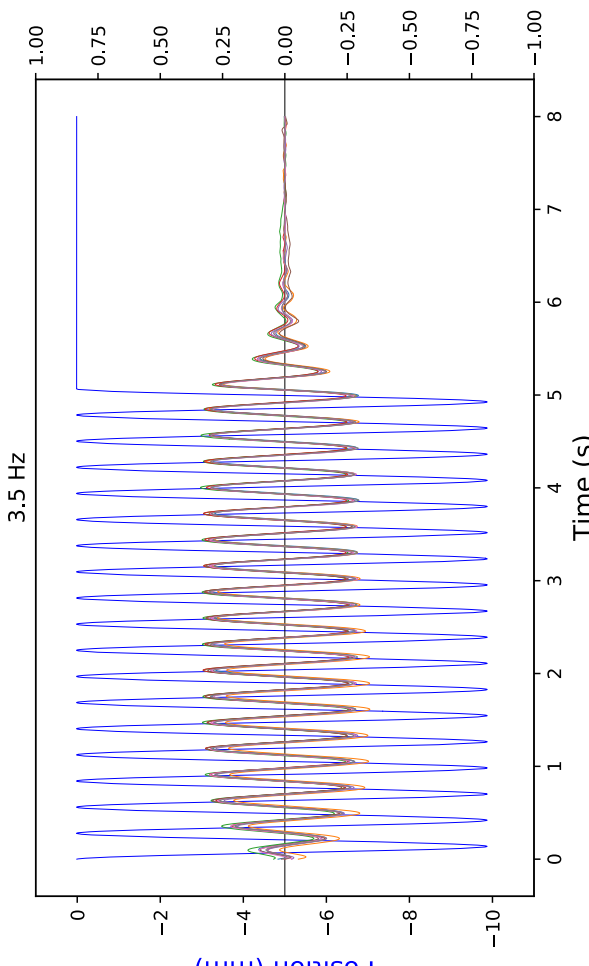
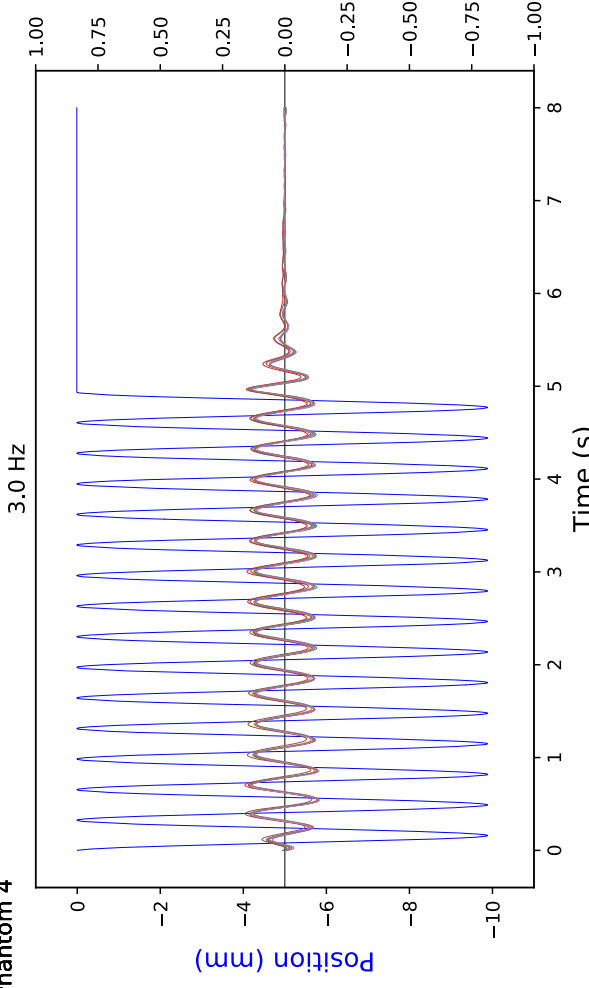
Phantom 2



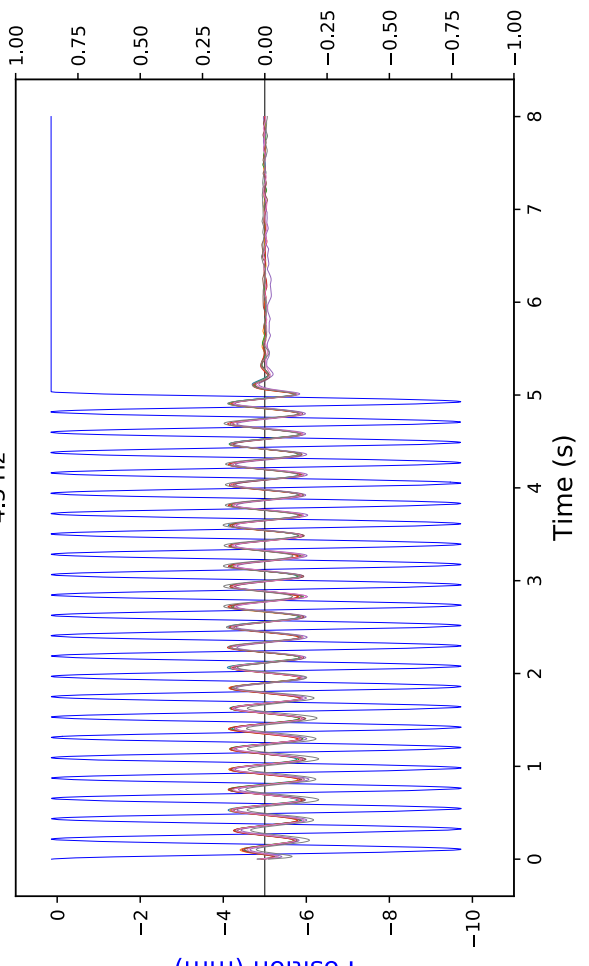
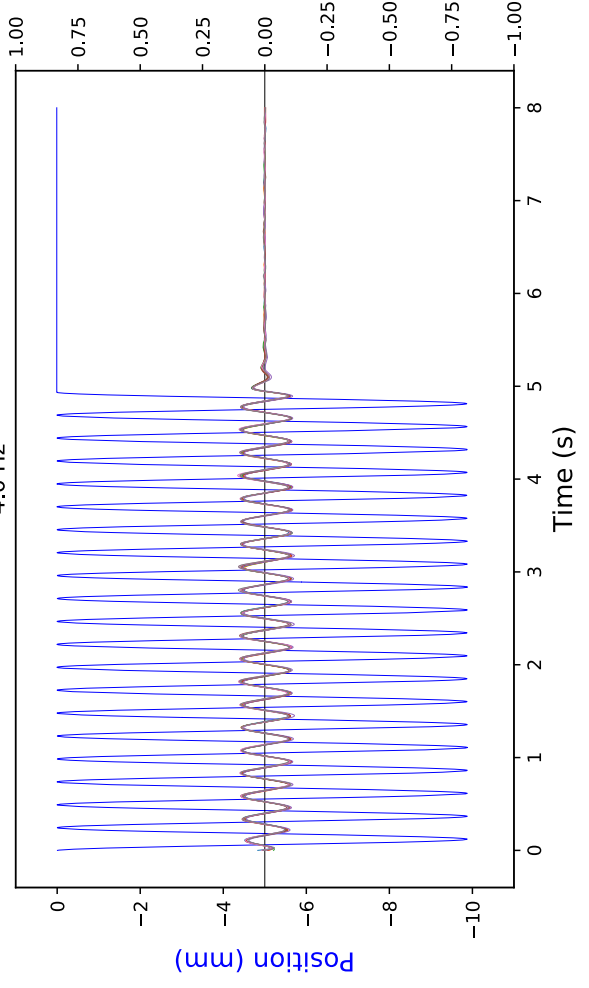
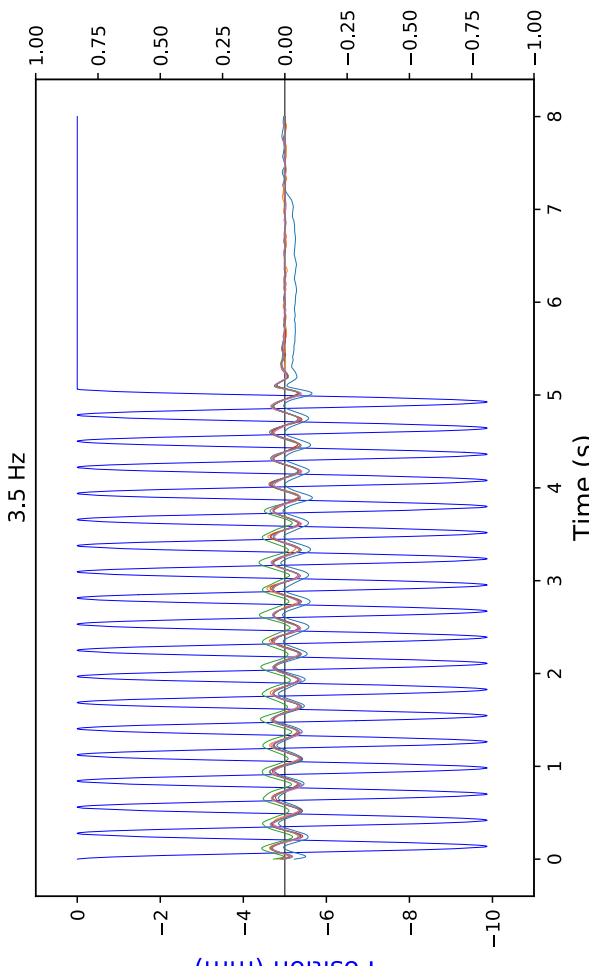
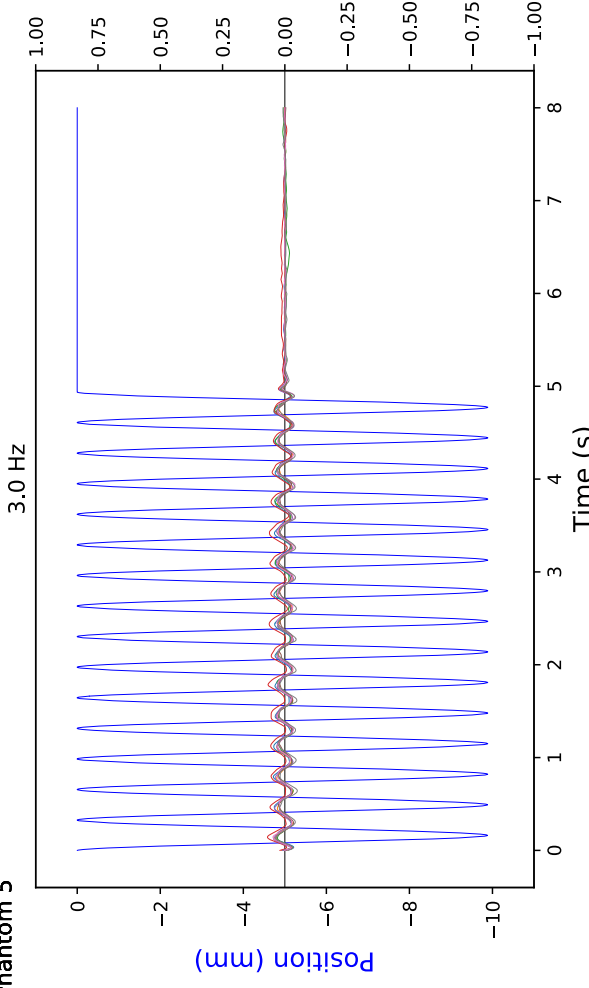
Phantom 3



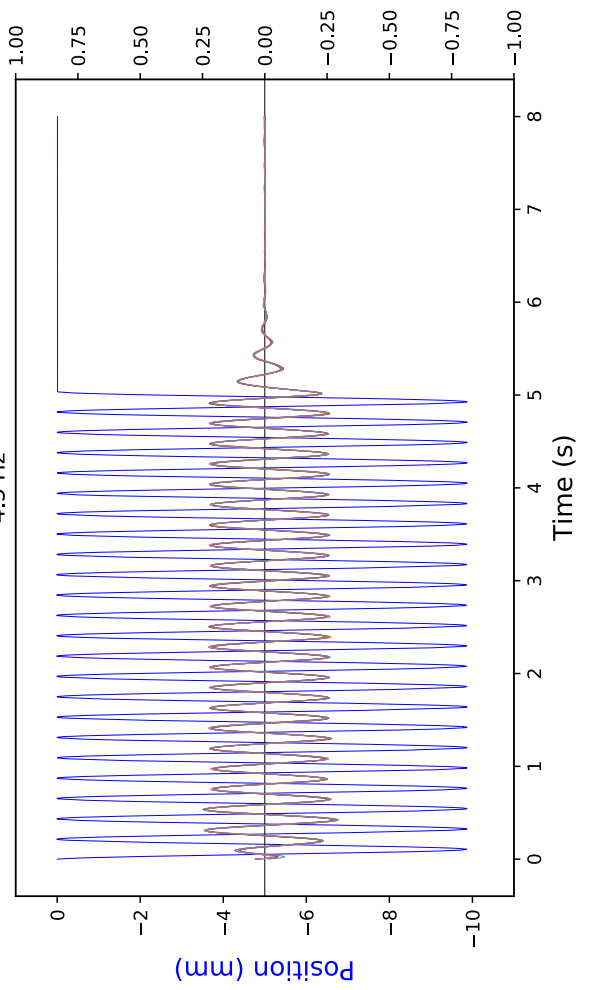
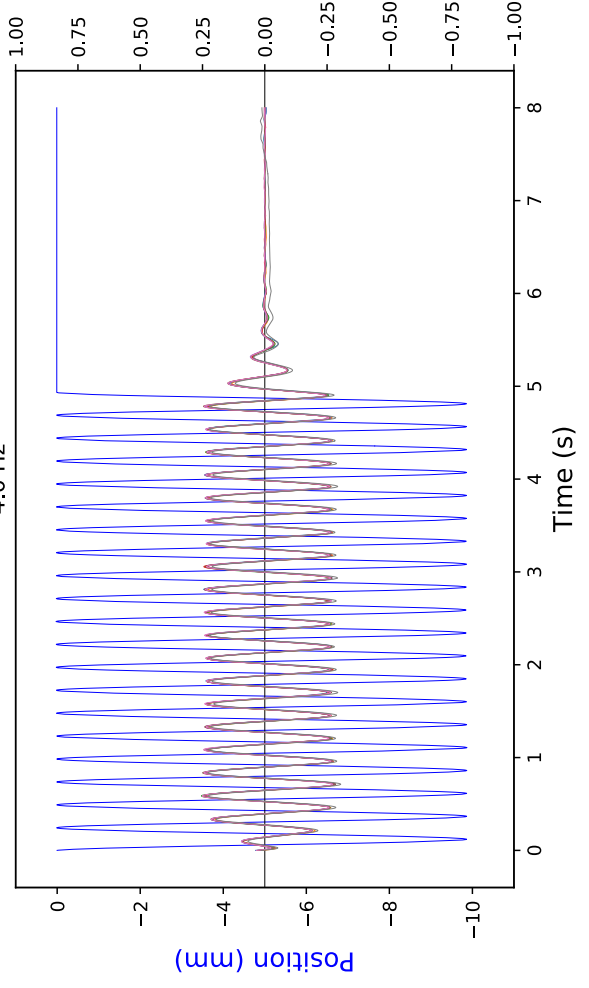
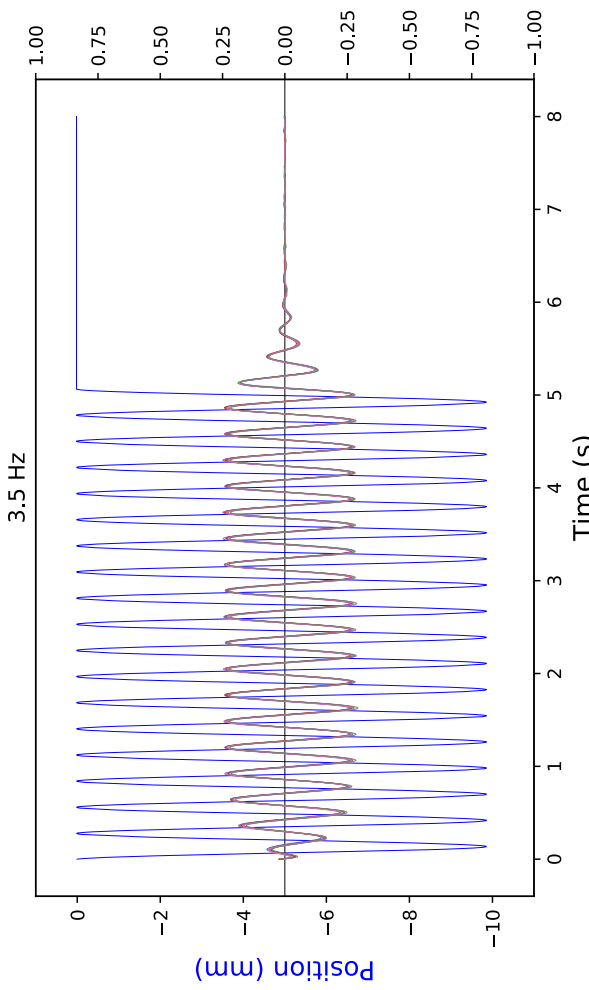
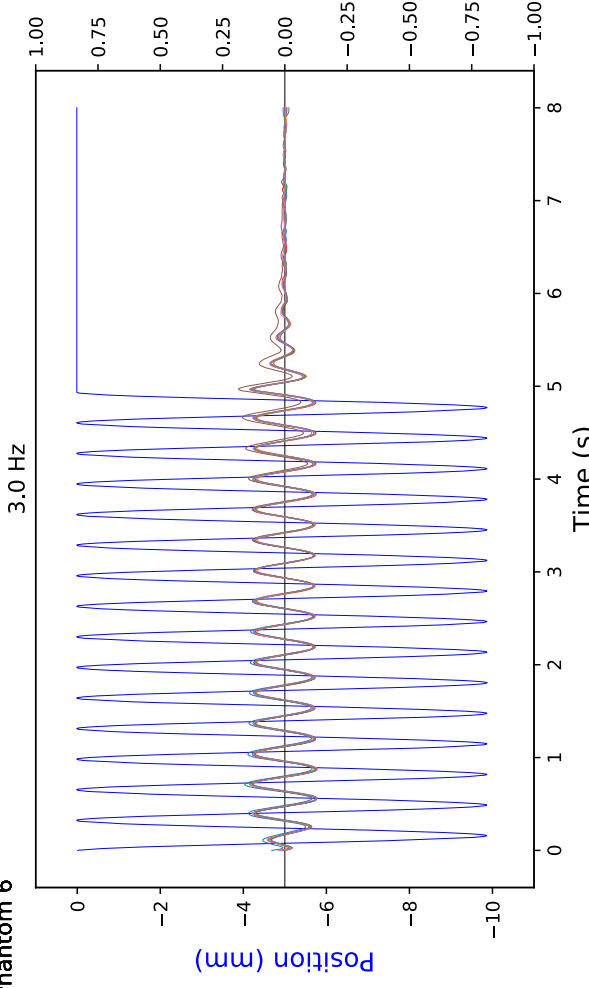
Phantom 4



Phantom 5



Phantom 6



Phantom 7

